AD-A142 802 AXIAL-CONDUCTANCES ANGULAR FILTER INVESTIGATION(U) 1/3
HAZELTINE CORP GREENLAWN NY P W HANNAN ET AL. APR 84
6519 RADC-TR-84-80 F19628-81-C-0067

UNCLASSIFIED F/G 9/5 NL

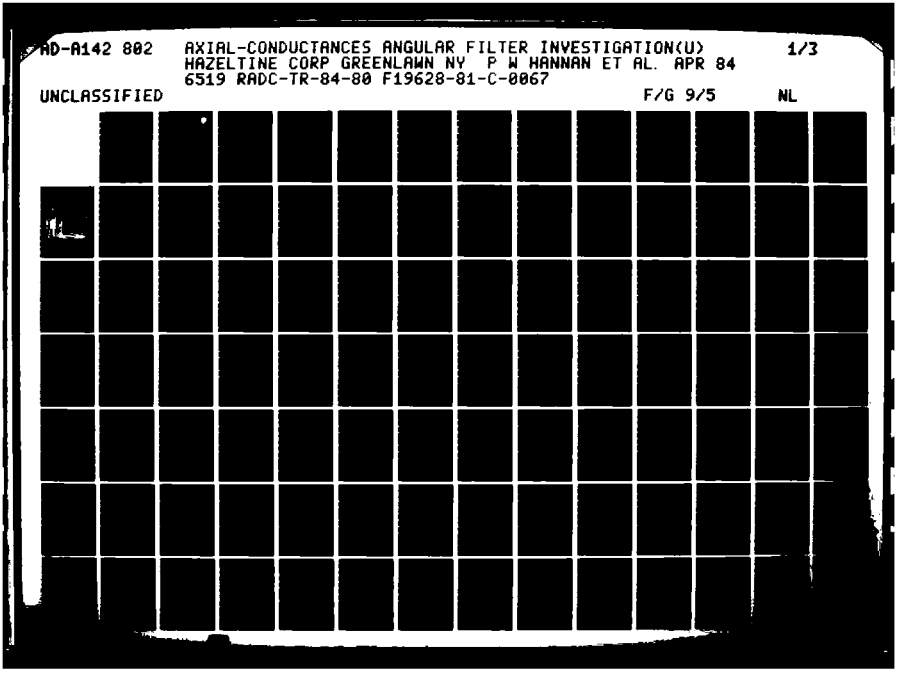

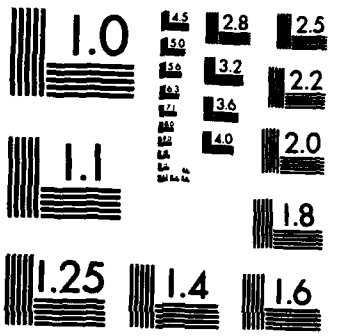

MICROCOPY RESOLUTION TEST CHART
NATIONAL BUREAU OF STANDARDS-1963-A

RADC-TR-84-80
Final Technical Report
April 1984

AXIAL-CONDUCTANCES ANGULAR FILTER INVESTIGATION

Hazeltine Corporation

Peter W. Hannan
John F. Pedersen

APPROVED FOR PUBLIC RELEASE; DISTRIBUTION UNLIMITED

ROME AIR DEVELOPMENT CENTER
Air Force Systems Command
Griffiss Air Force Base, NY 13441

This report has been reviewed by the RADC Public Affairs Office (PA) and is releasable to the National Technical Information Service (NTIS). At NTIS it will be releasable to the general public, including foreign nations.

APPROVED: Peter R Franchi

PETER R. FRANCHI
Project Engineer

APPROVED: Allan C Schell

ALLAN C. SCHELL
Chief, Electromagnetic Sciences Division

FOR THE COMMANDER: John A. Ritz

JOHN A. RITZ
Acting Chief, Plans Office

If your address has changed or if you wish to be removed from the RADC mailing list, or if the addressee is no longer employed by your organization, please notify RADC (EEAA), Hanscom AFB MA 01731. This will assist us in maintaining a current mailing list.

Do not return copies of this report unless contractual obligations or notices on a specific document requires that it be returned.

UNCLASSIFIED

SECURITY CLASSIFICATION OF THIS PAGE

REPORT DOCUMENTATION PAGE

1a. REPORT SECURITY CLASSIFICATION UNCLASSIFIED	1b. RESTRICTIVE MARKINGS N/A
2a. SECURITY CLASSIFICATION AUTHORITY N/A	3. DISTRIBUTION/AVAILABILITY OF REPORT Approved for public release; distribution unlimited
2b. DECLASSIFICATION/DOWNGRADING SCHEDULE N/A	
4. PERFORMING ORGANIZATION REPORT NUMBER(S) Report #6519	5. MONITORING ORGANIZATION REPORT NUMBER(S) RADC-TR-84-80
6a. NAME OF PERFORMING ORGANIZATION Hazeltine Corporation 6b. OFFICE SYMBOL (If applicable)	7a. NAME OF MONITORING ORGANIZATION Rome Air Development Center (EEAA)
6c. ADDRESS (City, State and ZIP Code) Greenlawn NY 11740	7b. ADDRESS (City, State and ZIP Code) Hanscom AFB MA 01731
8a. NAME OF FUNDING/SPONSORING ORGANIZATION Rome Air Development Center 8b. OFFICE SYMBOL (If applicable) EEAA	9. PROCUREMENT INSTRUMENT IDENTIFICATION NUMBER F19628-81-C-0067
8c. ADDRESS (City, State and ZIP Code) Hanscom AFB MA 01731	10. SOURCE OF FUNDING NOS. PROGRAM ELEMENT NO. 61102F; PROJECT NO. 4600; TASK NO. 14; WORK UNIT NO. 74
11. TITLE (Include Security Classification) AXIAL-CONDUCTANCES ANGULAR FILTER INVESTIGATION	
12. PERSONAL AUTHOR(S) Peter W. Hannan & John F. Pedersen	
13a. TYPE OF REPORT Final 13b. TIME COVERED FROM Apr81 TO Sep83	14. DATE OF REPORT (Yr., Mo., Day) April 1984 15. PAGE COUNT 246
16. SUPPLEMENTARY NOTATION N/A	

17. COSATI CODES			18. SUBJECT TERMS (Continue on reverse if necessary and identify by block number)
FIELD	GROUP	SUB. GR.	Angular Filter Spatial Filter Axial Conductance
17	02		
09	01		

19. ABSTRACT (Continue on reverse if necessary and identify by block number)

This report describes the concept, analysis, design, construction, and tests of an angular filter using an axial-conductance medium. The filter provides rejection that increases with incidence angle in the E plane. It is essentially invisible at broadside incidence, does not have critical tolerances on dimensions or materials, and operates over a wide frequency band. Analysis of an ideal homogeneous axial-conductance medium shows that the optimum value for the axial loss tangent is unity. With this value, the homogeneous medium provides approximately 8 dB of absorptive rejection per wavelength of filter thickness at a 45 E-plane incidence angle. Analysis of a practical inhomogeneous axial-conductance medium shows that some loss is introduced at broadside incidence, and that two types of waves can exist in the medium when only one wave is incident at an oblique angle.

When the practical medium has dimensions that are properly chosen, its broadside loss can be negligible, and its rejection versus incidence angle can approximate that of the ideal medium. Tests of inhomogeneous samples in simulator wave guide confirm these analytical

20. DISTRIBUTION/AVAILABILITY OF ABSTRACT UNCLASSIFIED/UNLIMITED ☒ SAME AS RPT. ☐ DTIC USERS ☐	21. ABSTRACT SECURITY CLASSIFICATION UNCLASSIFIED
22a. NAME OF RESPONSIBLE INDIVIDUAL Peter R. Franchi	22b. TELEPHONE NUMBER (Include Area Code) (617) 861-3067 22c. OFFICE SYMBOL EEAA

DD FORM 1473, 83 APR EDITION OF 1 JAN 73 IS OBSOLETE.

UNCLASSIFIED

SECURITY CLASSIFICATION OF THIS PAGE

Item #19 continued

results.

A screen printing method for depositing thick-film resistive ink on thin dielectric sheets has been investigated. With this method a 5x5 foot angular filter, designed for operation at 10 GHz, has been constructed containing over 70,000 axial-conductance elements.

Tests of the 5x5 foot tilter rejection versus incidence angle give results similar to the analytical results and show that the filter provides useful angular rejection over a frequency band from 5 to 20 GHz. An additional test with grating/reflector antenna combination indicates that the absorptive rejection mechanism of this filter provides freedom from troublesome antenna/filter interactions.

CONTENTS

CONTENTS (Continued)

ILLUSTRATIONS

ILLUSTRATIONS (Continued)

ILLUSTRATIONS (Continued)

ILLUSTRATIONS (Continued)

ILLUSTRATIONS (Continued)

SECTION 1

INTRODUCTION

An angular filter is a device which passes or rejects an electromagnetic wave depending on the angle of incidence of this wave relative to the filter surface. Typically, the angular filter passes waves incident at and near broadside (normal incidence), and provides rejection that increases with angle of incidence away from broadside. Such a filter offers the potential for reducing sidelobes in the radiation patterns of directive antennas.

Several types of angular filters (also called spatial filters) have been investigated in the past. A new type of angular filter is described in this report. Features of this filter are its wide frequency band of operation, and its insensitivity to tolerances of construction.

This report describes an investigation of the new angular filter conducted by Hazeltine for RADC. First, the basic approach for this filter is outlined (Section 2). Then (Section 3) an analysis is made of an ideal form of the filter.

Next, a practical form of the filter is described and analyzed (Section 4). Then (Section 5) measurements of various samples of the practical filter in waveguides simulating various angles of incidence are presented.

The construction of a 5 x 5 foot filter panel is described (Section 6). Figure 1-1 shows this filter panel. Tests of this filter over a range of frequencies and incidence angles are presented (Section 7). Finally, (Section 8) the conclusions reached from this investigation are summarized.

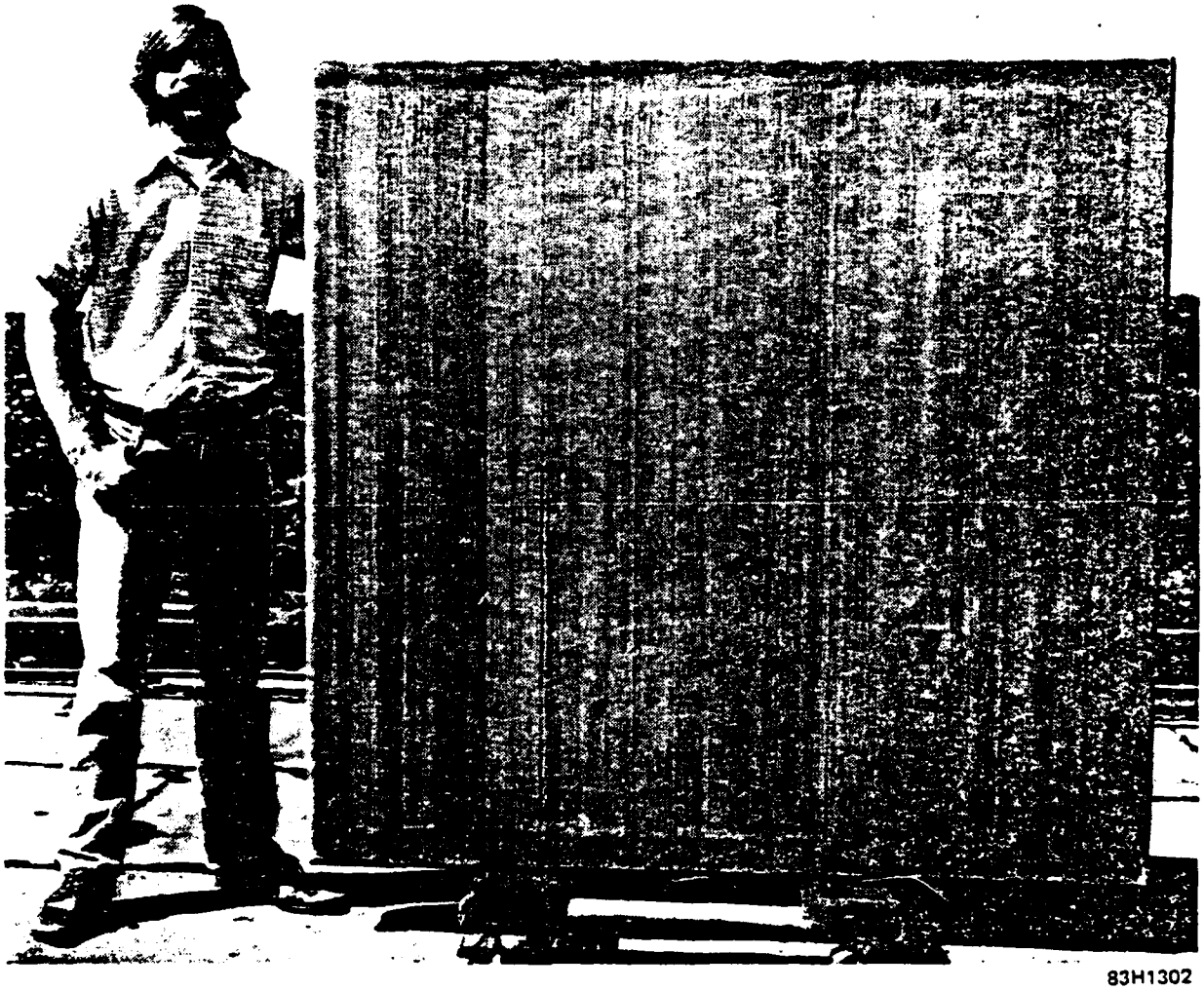

Figure 1-1. 5 x 5 Foot Axial-Conductance Angular Filter

SECTION 2

THE AXIAL-CONDUCTANCE ANGULAR FILTER

2.1. BACKGROUND

Angular filters comprising layers of dielectric have been synthesized and analyzed by Mailloux (Ref. 1). Raytheon, under contract to RADC, has extended this synthesis and has tested an experimental model of a dielectric filter (Ref. 2, 3).

Angular filters utilizing layers of metal grids have been proposed by Schell et al (Ref. 4) and studied by Mailloux (Ref. 5). Experiments with some perforated-metal layered filters have been performed by Rope and Tricoles

---

Ref. 1 - R.J. Mailloux, "Synthesis of Spatial Filters with Chebyshev Characteristics", IEEE Trans. Antennas and Propagation, pp. 174-181; March, 1976.

Ref. 2 - J.H. Pozgay, S. Zamoscianyk, L.R. Lewis, "Synthesis of Plane Stratified Dielectric Slab Spatial Filters Using Numerical Optimization Techniques", Final Technical Report RADC-TR-76-408 by Raytheon Co., December, 1976.

Ref. 3 - J.H. Pozgay, "Dielectric Spatial Filter Experimental Study", Final Technical Report RADC-TR-78-248 by Raytheon Co., November, 1978.

Ref. 4 - A. C. Schell et al, "Metallic Grating Spatial Filter for Directional Beamforming Antenna" AD-D002-623; April, 1976.

Ref. 5 - R.J. Mailloux, "Studies of Metallic Grid Spatial Filters", IEEE AP-S Int. Symp. Digest, p. 551; 1977

(Refs. 6, 7). Mailloux and Franchi have analyzed and tested experimental models of metal-grid filters (Refs. 8, 9).

Further investigation of metal-grid angular filters has been performed by Hazeltine, under contract to RADC. This work (Refs. 10-13) culminated in a 5 x 5 foot filter panel containing four metal-grid layers. Tests of this panel confirmed its predicted performance and demonstrated its capability for rejecting antenna sidelobes beyond angles of about 30^{O}.

Ref. 6 - E. L. Rope, G. Tricoles, O-C Yue, "Metallic Angular Filters for Array Economy", IEEE AP-S Int. Symp. Digest, pp. 155-157; 1976.

Ref. 7 - E. L. Rope, G. Tricoles, "An Angle Filter Containing Three Periodically Perforated Metallic Layers", IEEE AP-S Int. Symp. Digest, pp. 818-820; 1979.

Ref. 8 - R. J. Mailloux and P.R. Franchi, "Metal Grid Angular Filters for Sidelobe Suppression", RADC-TR-79-10; January 1979.

Ref. 9 - P. R. Franchi, R. J. Mailloux, "Theoretical and Experimental Study of Metal Grid Angular Filters for Sidelobe Suppression", IEEE Trans. Antennas and Propagation, pp. 445-450; May 1983.

Ref. 10 - P. W. Hannan, P. L. Burgmyer, "Metal-Grid Spatial Filter", Interim Technial Report RADC-TR-79-295 by Hazeltine Corp., July 1980.

Ref. 11 - P. W. Hannan and J. F. Pedersen, "Investigation of Metal-Grid Angular Filters", Proceedings of the 1980 Antenna Applications Symposium, Allerton Park, Illinois; September 1980.

Ref. 12 - P. W. Hannan, J. F. Pedersen, "Metal-Grid Spatial Filter", Final Technical Report RADC-TR-81-282, by Hazeltine Corp., November 1981

Ref. 13 - J. F. Pedersen, P. W. Hannan, "A Metal-Grid 5 x 5 Foot Angular Filter", IEEE AP-S Int. Symp. Digest, pp. 471-474; 1982.

The metal-grid angular filter investigations outlined above have shown that such filters are practical and can offer improved performance (reduced wide-angle sidelobes) when added to an antenna. However, these investigations have also shown that such filters have certain limitations.

One limitation of metal-grid filters is the inherent relation between the angular characteristic and the frequency characteristic of the filter. Typically this results in a useful frequency bandwidth that is not very wide.

Another limitation, inherent in the resonant nature of such filters, is the need to construct them with tight dimensional tolerances. Failure to hold sufficiently tight tolerances can result in variations of transmission phase across the filter aperture for incidence angles within the filter angular passband. Such phase variations can create unwanted sidelobes in the pattern of the antenna/filter combination.

A third limitation of such filters is that they reject power by reflection rather than by absorption. This reflected power can return to the antenna that is associated with the filter, and then may reflect again to yield unwanted sidelobes within the angular passband of the filter.

An ideal angular filter could be considered as one that retains the good features of metal-grid filters but avoids the limitations noted above. First, an ideal angular filter should have an angular rejection characteristic that is

independent of frequency. Second, an ideal angular filter should be inherently invisible at broadside incidence, so that tight dimensional tolerances are not needed to obtain error-free transmission through the filter at broadside incidence. Third, an ideal angular filter should provide rejection by absorption rather than by reflection.

The axial-conductance angular filter described in this report represents an attempt to achieve the three objectives defined above.

2.2. THE AXIAL-CONDUCTANCE CONCEPT

Consider a filter panel consisting of a closely-spaced array of thin rods or strips oriented in the axial direction as shown in Figure 2-1. These thin axial elements are neither good conductors nor good insulators, but rather, provide a certain amount of conductance (or resistance) in the axial direction.

Now consider an electromagnetic wave incident on this filter in the E plane of incidence. As indicated in Figure 2-2, the axial component of electric field in this wave is proportional to sin θ, where θ is the angle of incidence away from broadside. If we assume that this is also true within the filter medium, then the axial current I in the filter should also be proportional to sin θ. Since this current flows through resistive elements, there is power dissipated within the filter. This dissipated power should be proportional to I^2 and hence proportional to $\sin^2\theta$.

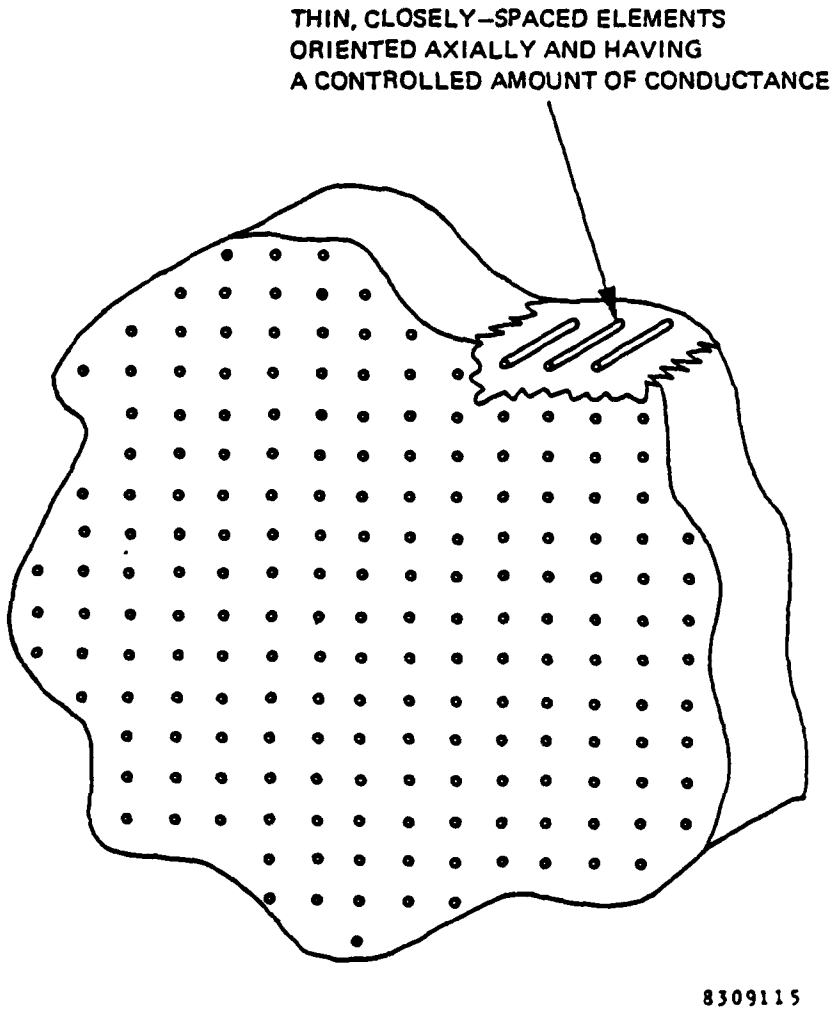

Figure 2-1. Basic Configuration of Axial-Conductance Angular Filter

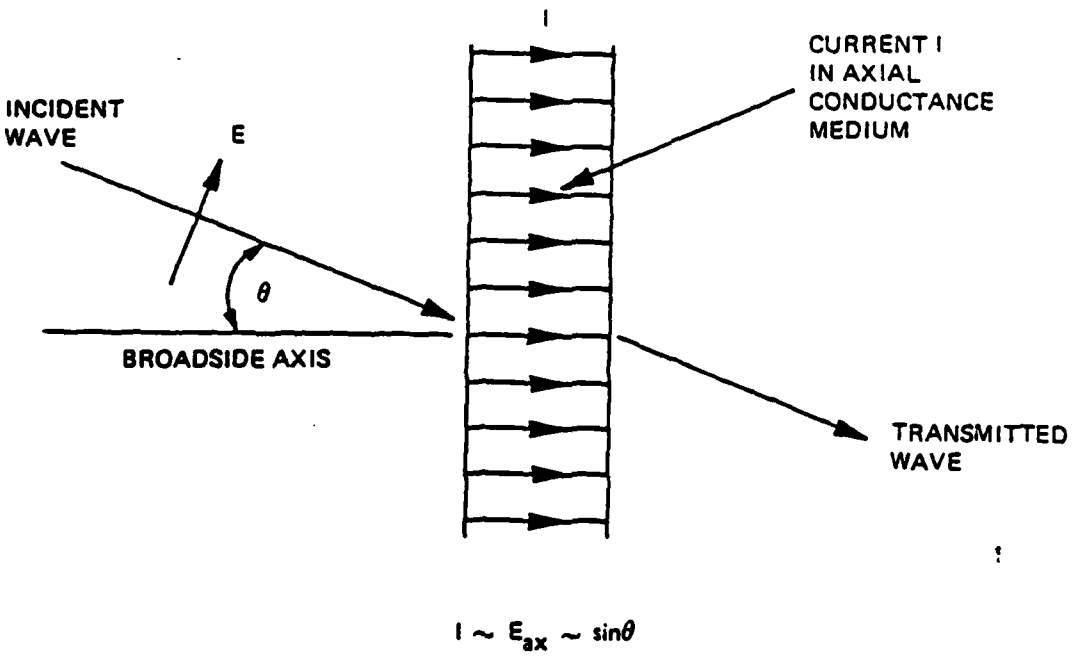

Figure 2-2. Simplified Viewpoint for Axial-Conductance Filter

This heuristic analysis neglects to account for the effect of the axial-conductance medium on the incident wave, and it does not relate the dissipated power to the incident power. Nevertheless, as will be shown in later sections of this report, the $\sin^2\theta$ proportionality turns out to be a fairly good approximation for the dissipative loss of an axial-conductance angular filter that is designed for optimum performance.

2.3. FEATURES AND LIMITATIONS ANTICIPATED FOR AN AXIAL-CONDUCTANCE ANGULAR FILTER

Assuming that the $\sin^2\theta$ proportionality represents the dissipative loss of an axial-conductance filter, we can expect that such a filter should provide continuously increasing rejection with incidence angle in the E plane. This desirable result does not always occur with other types of angular filters. For example, the multilayer dielectric filter is subject to Brewster-angle effects in the E plane of incidence, and the crossed metal-grid filter may provide little or no rejection near grazing incidence in the E plane (see Ref. 10, pp. 75, 81, 84, and Ref. 12, Figure 4-3).

Another feature that can be anticipated for the axial-conductance filter is that it should be inherently invisible at broadside incidence. This is a result of its thin axially-oriented elements which have essentially no effect when the electric field is perpendicular to them. Such a filter, when placed in the aperture of a narrow-beam antenna, should have only a small risk of harming the main beam or raising the nearby sidelobes.

A corollary of this inherent broadside invisibility is that the axial-conductance filter does not have critical tolerances on dimensions or materials. Variations of filter thickness or resistance values do not affect the amplitude or phase of the main-beam power passing through the filter near broadside incidence, so no new sidelobes are created. Only the wide-angle rejection value would be affected, which is not a critical factor.

Still another feature that can be anticipated for the axial-conductance filter is that its rejection of incident power will occur primarily by means of absorption. Reflection from the filter for most angles of incidence will tend to be fairly small. This reduces the chance that rejected power will return to the antenna and then be re-reflected to create new sidelobes.

Finally, it can be anticipated that the axial-conductance filter would provide all of the above features over a wide frequency band. Since its operation does not depend on a resonance or a grating-lobe phenomenon, it is not strongly affected by a change of frequency. As will be shown later, there is a certain relation between wide-angle rejection and frequency, but this can still permit a wide useful frequency band of operation.

The features mentioned in the previous paragraphs involve some limitations that do not occur with other types of angular filters. One limitation of the axial-conductance filter is that it provides rejection versus angle only in the E plane of incidence. Another limitation is that a sharp increase of rejection with incidence angle (i.e., a sharp cutoff) is not obtainable, unless some resonant or

frequency-sensitive mechanism is incorporated into the filter medium. Even with these limitations, the positive features of the axial-conductance filter make it worthy of consideration for use either alone or in combination with another filter.

Figure 2-3 summarizes the anticipated features and limitations discussed above for the axial-conductance angular filter.

FEATURES

- PROVIDES CONTINUOUSLY INCREASING REJECTION WITH INCIDENCE ANGLE IN E PLANE
- IS INHERENTLY INVISIBLE AT BROADSIDE INCIDENCE (NEGLIGIBLE LOSS, REFLECTION OR INSERTION PHASE)
- DOES NOT HAVE CRITICAL TOLERANCES ON DIMENSIONS OR MATERIALS
- REJECTION IS PROVIDED PRIMARILY BY AN ABSORPTION MECHANISM
- ABOVE FEATURES ARE PROVIDED OVER A WIDE FREQUENCY BAND

LIMITATIONS

- PROVIDES REJECTION ONLY IN E PLANE OF INCIDENCE
- A SHARP INCREASE OF REJECTION VS ANGLE IS NOT OBTAINABLE UNLESS WIDEBAND PERFORMANCE IS SACRIFICED

8309110

Figure 2-3. Features and Limitations of Axial-Conductance Angular Filter

SECTION 3

ANALYSIS OF IDEAL HOMOGENEOUS MEDIUM

3.1 INTRODUCTION

The heuristic analysis given in Section 2.2 is not only inaccurate, it also does not provide answers to several important questions. One question is: what value of axial conductance gives the most rejection at some angle of incidence? Another question is: what thickness of angular filter is needed to provide a certain value of rejection at some angle? A third question is: how does the rejection at some angle vary over a wide frequency band? An analysis that provides answers to these questions is needed.

The axial-conductance angular filter that was shown in Figure 2-1 uses thin, closely-spaced, axially-oriented resistive elements. If we let the thickness and the spacing of these elements become infinitesimal, then we have a homogeneous medium that provides a certain conductance σ_{ax} in the axial direction, but zero conductance in the transverse directions. This is the simplest medium to analyze, and it will be seen to generally yield the best performance.

The remainder of this section contains an analysis of this ideal homogeneous medium. (In a later section of the report, the more practical inhomogeneous medium is analyzed.) Figure 3-1 indicates the essential characteristics of the ideal homogeneous axial-conductance medium.

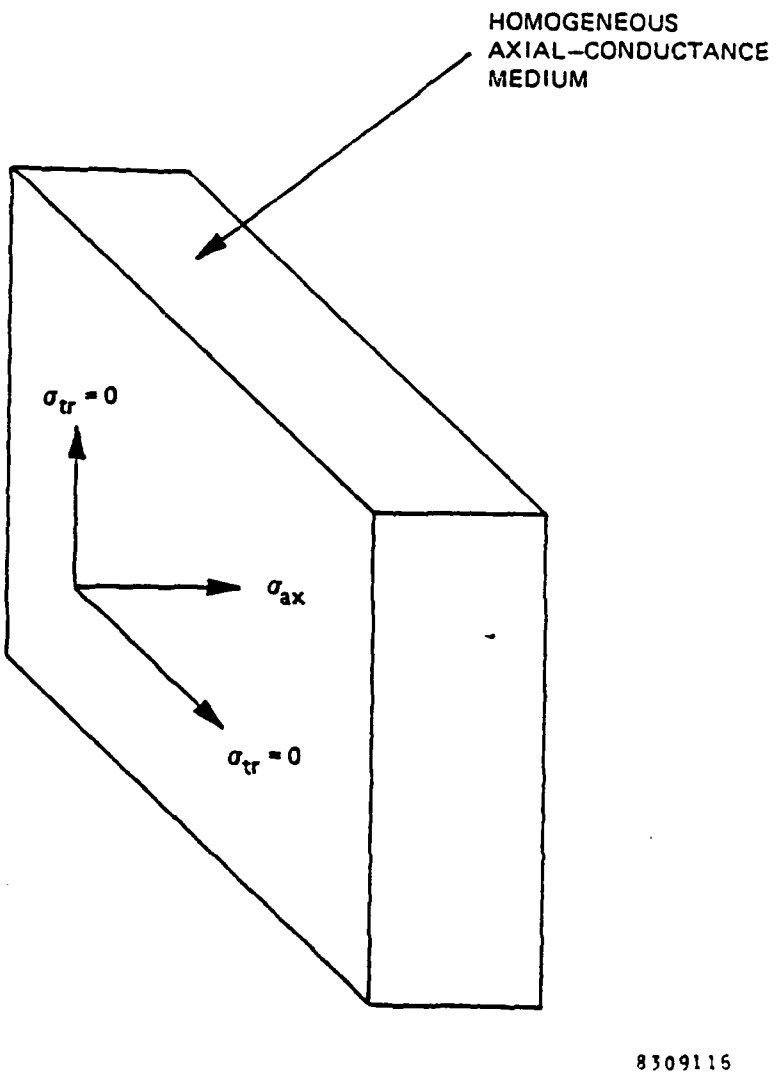

Figure 3-1. Ideal Homogeneous Axial-Conductance Filter

3.2 BASIC FORMULAS

We wish to determine the attenuation and the reflection of a homogeneous axial-conductance medium as a function of incidence angle (θ), axial conductance (σ_{ax}), and frequency. The medium is assumed here to have free-space permittivity (ε_o); a later subsection will consider a more general case.

Figure 3-2 defines the geometry in which a plane wave, polarized with E in the plane of incidence, is incident on a semi-infinite slab of homogeneous axial-conductance material. In this material the electric and magnetic fields are given by:

$$\begin{aligned} \underline{E} &= (\underline{i}\, E_x + \underline{k}\, E_z) \exp j\,(\omega t - k_x x - k_z z) \\ \underline{H} &= (\underline{j}\, H_y) \exp j\,(\omega t - k_x x - k_z z) \end{aligned} \tag{1}$$

The transverse wavenumber k_x in the medium must be the same as it is in free space, therefore:

$$k_x = \frac{2\pi}{\lambda} \sin\theta \tag{2}$$

Maxwell's equations are:

$$\begin{aligned} \Delta \times \underline{E} &= -\mu_o \frac{\partial \underline{H}}{\partial t} \\ \Delta \times \underline{H} &= \varepsilon_o \frac{\partial \underline{E}}{\partial t} + \underline{J} \end{aligned} \tag{3}$$

and the current density (J) in the axial-conductance medium is:

$$\underline{J} = \underline{k}\, J_z = \underline{k}\, \sigma_{ax}\, E_z \tag{4}$$

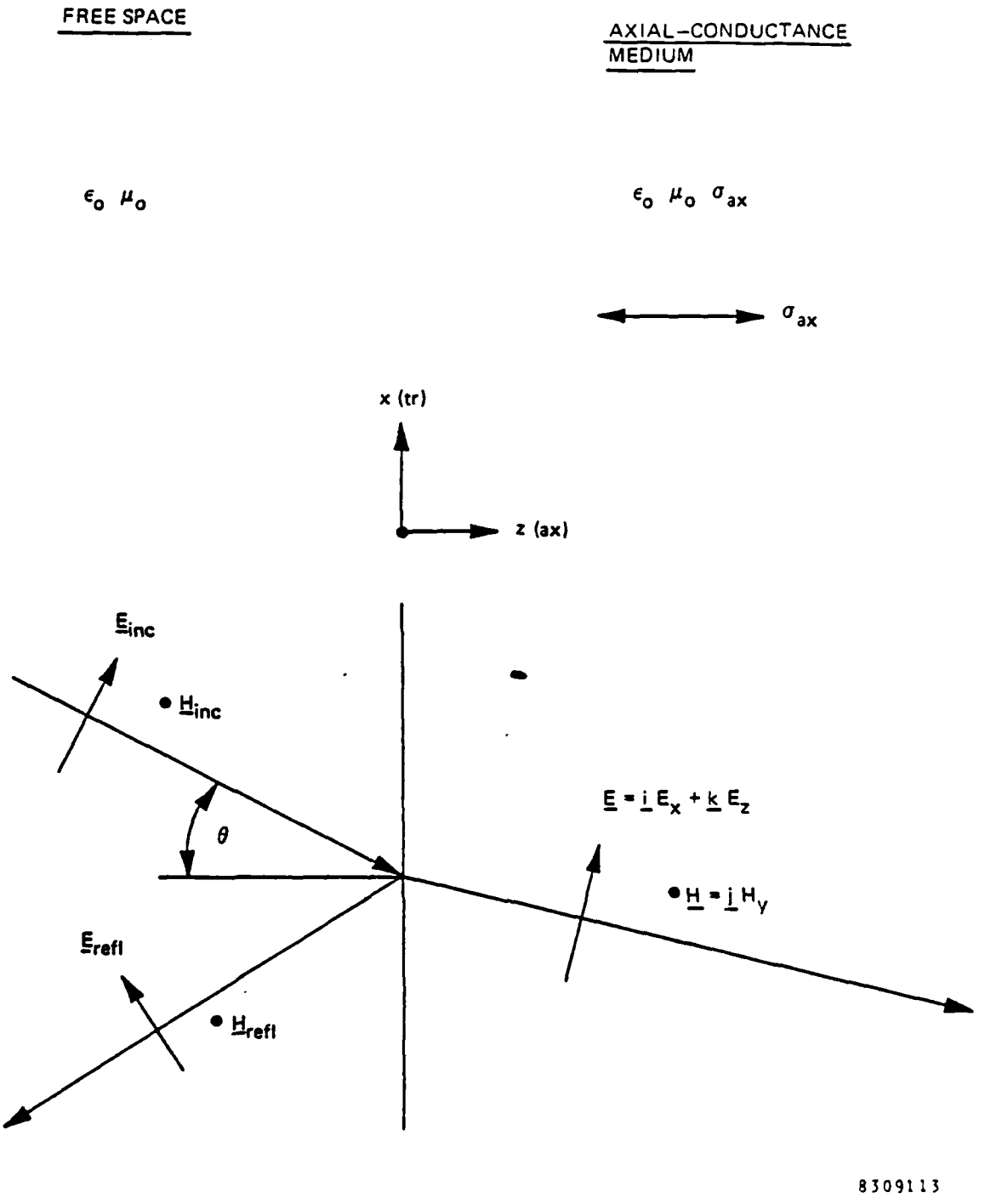

Figure 3-2. Geometry for Analysis of Homogeneous Medium

Putting (1) and (4) into (3) gives:

$$k_z E_x - k_x E_z = \omega\mu_o H_y$$

$$k_z H_y = \omega\varepsilon_o E_x \qquad (5)$$

$$jk_x H_y = (j\omega\varepsilon_o + \sigma_{ax}) E_z$$

Eliminating the field components in (5) yields:

$$k_z^2 = \omega^2 \mu_o \varepsilon_o - \frac{k_x^2}{1 - j \frac{\sigma_{ax}}{\omega\varepsilon_o}} \qquad (6)$$

Now substituting (2) for k_x in (6) and recalling that $2\pi/\lambda = \omega(\mu_o \varepsilon_o)^{1/2}$ we obtain:

$$k_z^2 = \left(\frac{2\pi}{\lambda}\right)^2 \left[1 - \frac{\sin^2\theta}{1 - j \frac{\sigma_{ax}}{\omega\varepsilon_o}} \right] \qquad (7)$$

This is the basic relation describing propagation in the homogeneous axial-conductance medium as a function of incidence angle, axial conductance, and frequency.

It is helpful to define an axial loss tangent (D) as follows:

$$D = \frac{\sigma_{ax}}{\omega\varepsilon_o} \qquad (8)$$

The parameter D will be used instead of σ_{ax} throughout most of this report. Substituting (8) into (7) yields:

$$k_z^2 = \left(\frac{2\pi}{\lambda}\right)^2 \left[1 - \frac{\sin^2\theta}{1 - j\,D}\right] \tag{9}$$

The axial wavenumber (k_z) can be separated into its two components, attenuation constant (α) and phase constant (β):

$$k_z = \beta - j\alpha \tag{10}$$

Applying (10) to (9) yields:

$$\alpha = -\frac{2\pi}{\lambda}\ \mathrm{Im}\left[1 - \frac{\sin^2\theta}{1 - j\,D}\right]^{1/2} \tag{11}$$

$$= \frac{2\pi}{\lambda}\left[\frac{1 + D^2 - \sin^2\theta}{2\,(1 + D^2)}\left(\sqrt{1 + \left(\frac{D\sin^2\theta}{1 + D^2 - \sin^2\theta}\right)^2} - 1\right)\right]^{1/2}$$

$$\beta = \frac{2\pi}{\lambda}\ \mathrm{Re}\left[1 - \frac{\sin^2\theta}{1 - j\,D}\right]^{1/2} \tag{12}$$

$$= \frac{2\pi}{\lambda}\left[\frac{1 + D^2 - \sin^2\theta}{2\,(1 + D^2)}\left(\sqrt{1 + \left(\frac{D\sin^2\theta}{1 + D^2 - \sin^2\theta}\right)^2} + 1\right)\right]^{1/2}$$

The attenuation constant (α) is the quantity of most interest, because it tells how much dissipative rejection an

angular filter should provide at various incidence angles, for a given thickness and axial loss tangent (D) of the medium. This subject will be discussed further in subsection 3.3.

Another quantity of interest is the impedance of the axial-conductance medium. This determines how much reflection should be expected from the input face of the angular filter. The impedance of the medium (Z_{medium}) is:

$$Z_{medium} = \frac{E_x}{H_y} \tag{13}$$

From the middle equation of (5) we have:

$$k_z H_y = \omega\varepsilon_o E_x \tag{14}$$

Therefore:

$$Z_{medium} = \frac{k_z}{\omega\varepsilon_o} \tag{15}$$

Recalling that $\omega\varepsilon_o = 2\pi/\lambda Z_o$ we can write:

$$Z_{medium} = \frac{k_z \lambda Z_o}{2\pi} \tag{16}$$

Now define an input impedance ratio (Z') as:

$$Z' = \frac{Z_{medium}}{Z_{space}} \tag{17}$$

and recall that for E-plane incidence:

$$Z_{space} = Z_o \cos \theta \tag{18}$$

Combining (16), (17), and (18) gives:

$$Z' = \frac{k_z}{\frac{2\pi}{\lambda} \cos \theta} \tag{19}$$

Now substituting (9) for k_z yields:

$$Z' = \frac{\left(1 - \frac{\sin^2 \theta}{1 - j D}\right)^{1/2}}{\cos \theta} \tag{20}$$

This relation for the input impedance ratio enables the reflection from the input face of the angular filter to be calculated as a function of incidence angle for any specified value of the axial loss tangent (D). This subject will be discussed further in subsection 3.3. Simple relations for the magnitude and phase of this input impedance ratio are:

$$|Z'| = \frac{1}{\cos\theta}\left[\frac{\cos^4\theta + D^2}{1 + D^2}\right]^{1/4} \qquad (21)$$

$$\angle Z' = -\frac{1}{2}\arctan\left(\frac{D\sin^2\theta}{1 + D^2 - \sin^2\theta}\right)$$

3.3 BASIC RESULTS

(a) Optimum Value for D

Having derived formulas for the attenuation constant and input impedance ratio, it is now possible to answer the questions mentioned earlier. One such question is: what value of the axial loss tangent (D) gives the greatest rejection for the angular filter?

To answer this quantitatively, it is necessary to specify the incidence angle in some way. A particularly good way is to let the incidence angle approach zero. Optimizing D for greatest attenuation (α) when θ approaches zero should yield an axial-conductance medium giving the fastest increase of α with increasing θ near broadside incidence.

For small θ, equation (11) simplifies to the following:

$$\alpha(\theta \to 0) = \frac{\pi}{\lambda}\,\frac{D}{1 + D^2}\,\theta^2 \qquad (22)$$

The value of D giving the maxium $\alpha(\theta \to 0)$ in (22) is:

$$D_{opt} = 1 \qquad (23)$$

This simple result should not be too surprising. When D = 0 the medium is absent, and there is no attenuation. When D = ∞ the medium has perfect axial conductivity, and the attenuation is also zero. A value of D intermediate between 0 and ∞ should give maximum attenuation. When D = 1 the conductance equals the capacitive susceptance of free space; this condition often coincides with some benchmark such as a transition or an optimum.

It is instructive to plot the ratio of the small-angle attenuation α for any value of D to the α at the same angle when D = 1. This is done in Figure 3-3. It is seen that D can deviate from unity over a considerable range without causing a major decrease of $\alpha(\theta \to 0)$. This result indicates that tolerances on D need not be tight when an axial-conductance angular filter is constructed.

(b) Filter Rejection Versus Angle

Another question that was mentioned earlier is: what thickness of angular filter is needed to provide a certain value of rejection at some angle? This question can be answered by computing attenuation versus θ using equation (11). The results of this computation are shown in Figure 3-4 for several values of D. In this figure, the attenuation is given in dB per wavelength thickness of the axial-conductance medium.

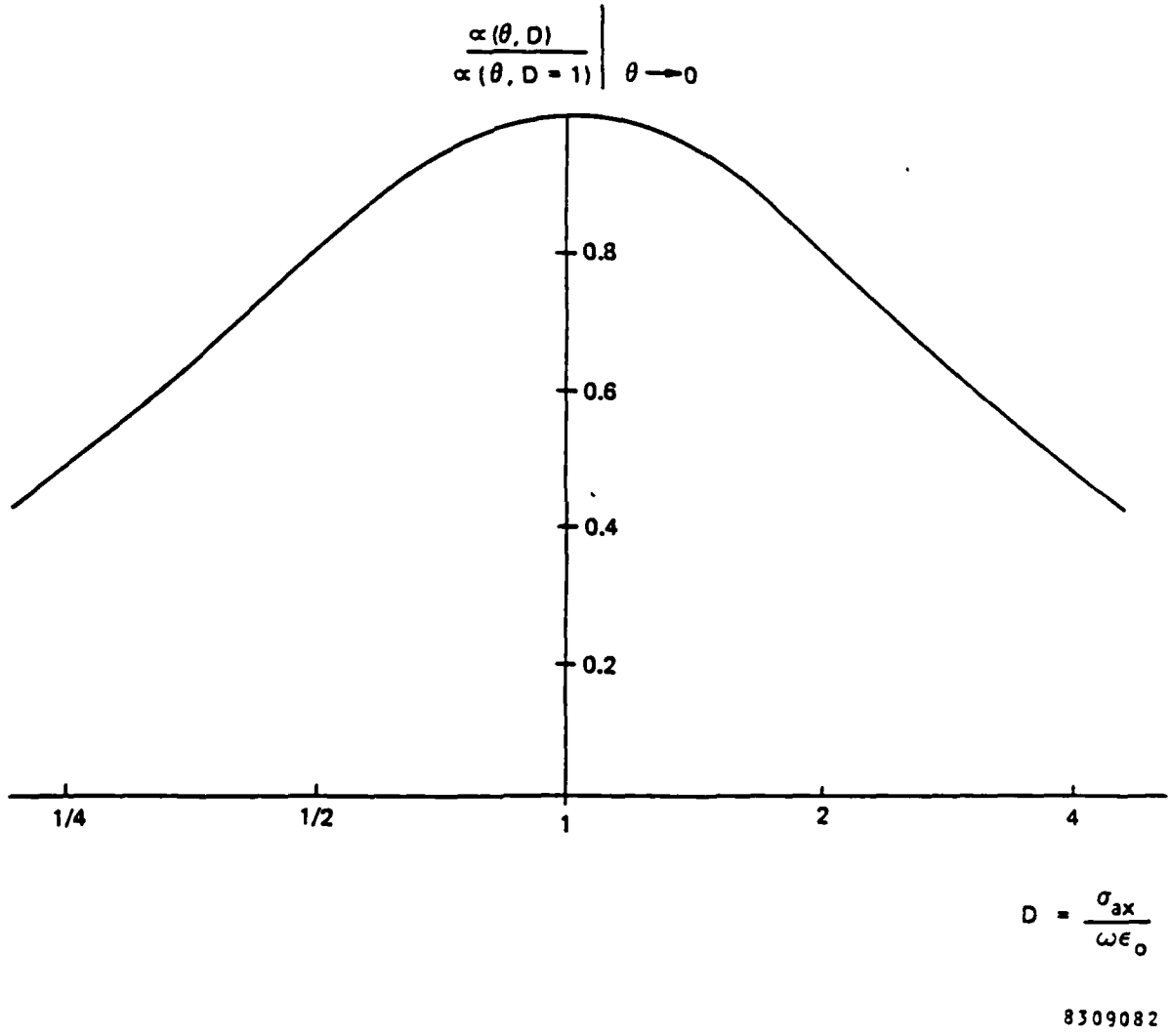

Figure 3-3. Small-Angle Attenuation Ratio vs D

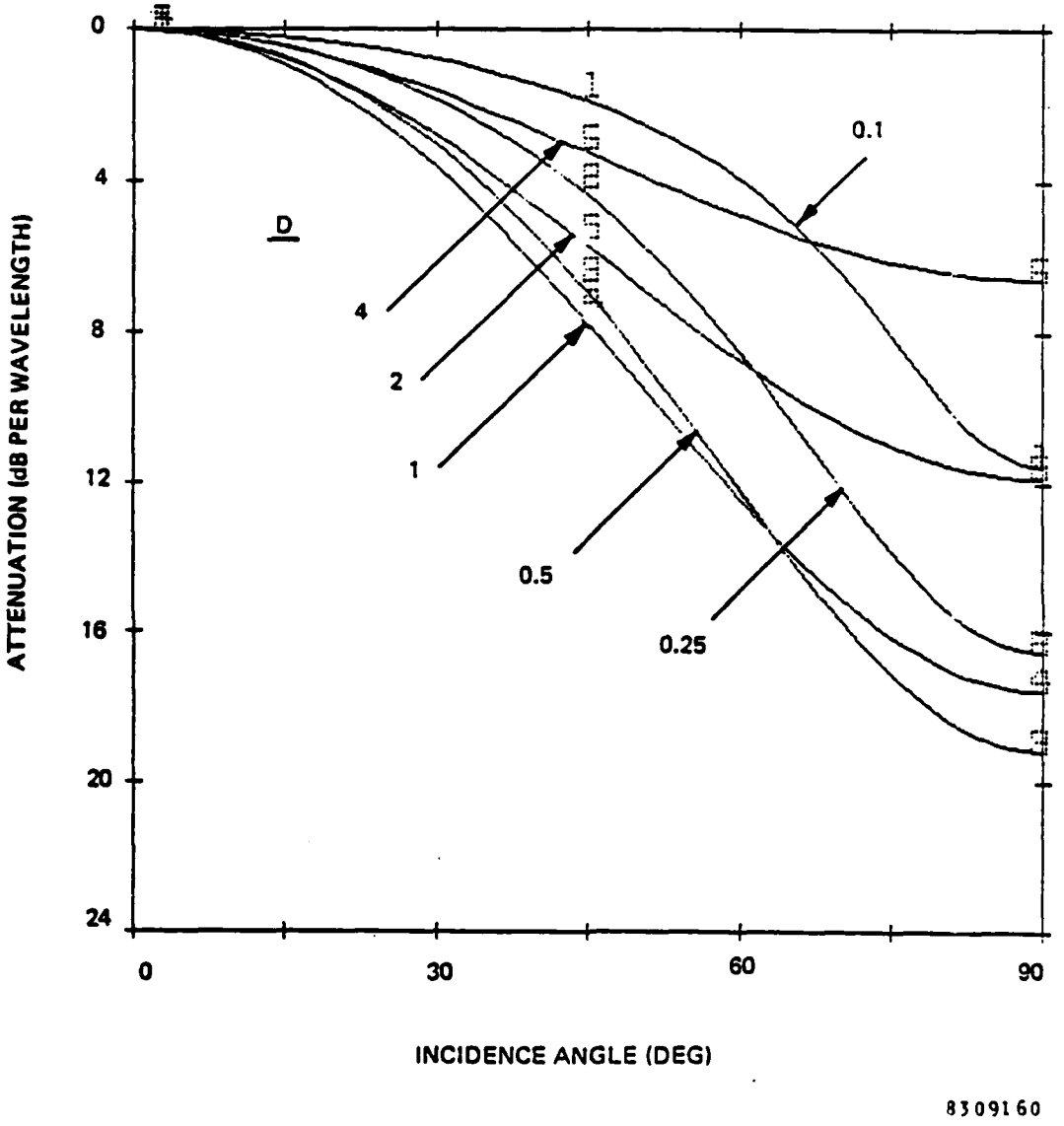

Figure 3-4. Attenuation vs Incidence Angle for Various D Values

Inspection of Figure 3-4 reveals several things. First, a comparison of the several curves at small incidence angles confirms that D = 1 gives the greatest attenuation at small angles. Second, the D = 1 case gives almost, but not quite, the greatest attenuation near 90° incidence. Third, the shape of the curves, as well as their level, is not the same for different values of D.

The curves of Figure 3-4 give essentially the angular rejection characteristic of a filter using an axial-conductance medium. For example, with a medium having D = 1, a rejection of almost 8 dB would be obtained for a wavelength-thick filter at 45° incidence. For a filter two wavelengths thick, almost 16 dB would be obtained at 45°.

At 90°, the attenuation for the D = 1 case is about twice the value at 45°. In addition, there would be a substantial reflection loss near 90°; this is discussed later in this section. There is no indication in any of the curves of Figure 3-4 that the filter rejection might decrease with increasing angle (as it can with some other types of angular filter).

Near 0° incidence, the filter attenuation characteristic is inherently square-law with angle, as was shown by equation (22). For a filter two wavelengths thick, the attenuation of the homogeneous axial-conductance medium would be less than 0.1 dB over a ± 3° range of incidence angles centered on broadside. Thus a pencil-beam antenna having a beamwidth of 3° or less should have virtually no change of peak gain when operated with such a filter over its aperture.

The shape of the curves in Figure 3-4 is of some interest. To compare the shapes for different values of D, the attenuation of each curve can be normalized to its value at 90° incidence. Figure 3-5 shows the resulting set of curves. Also shown is a $\sin^2\theta$ curve. It is evident that for values of D equal to unity or more, the $\sin^2\theta$ curve gives a good approximation to the actual shape of the α versus θ curve. The approximation becomes poor for values of D much less than unity.

(c) Filter Rejection Versus Frequency

A third question that was mentioned earlier is: how does the rejection at some angle vary over a wide frequency band? The answer to this question is contained in equations (11) and (22), and in the curves of Figure 3-4. In all three, it is evident that the basic factor is attenuation per wavelength of the medium. Thus, for a filter having a specified thickness (in inches), the principal term is a linear increase of attenuation with frequency.

A secondary term also exists because D is inversely proportional to frequency. However if D is set to unity at midband, the variation of D that would occur over a frequency band as much as two octaves wide would still have only a relatively small effect on attenuation (see, for example, Figure 3-3). This is another case in which the non-critical nature of D is helpful.

(d) The Phase Constant and Refraction

Equation (12) gives the phase constant (β) as a function of θ and D. It is interesting to consider the curves of β versus θ presented in Figure 3-6, as obtained from

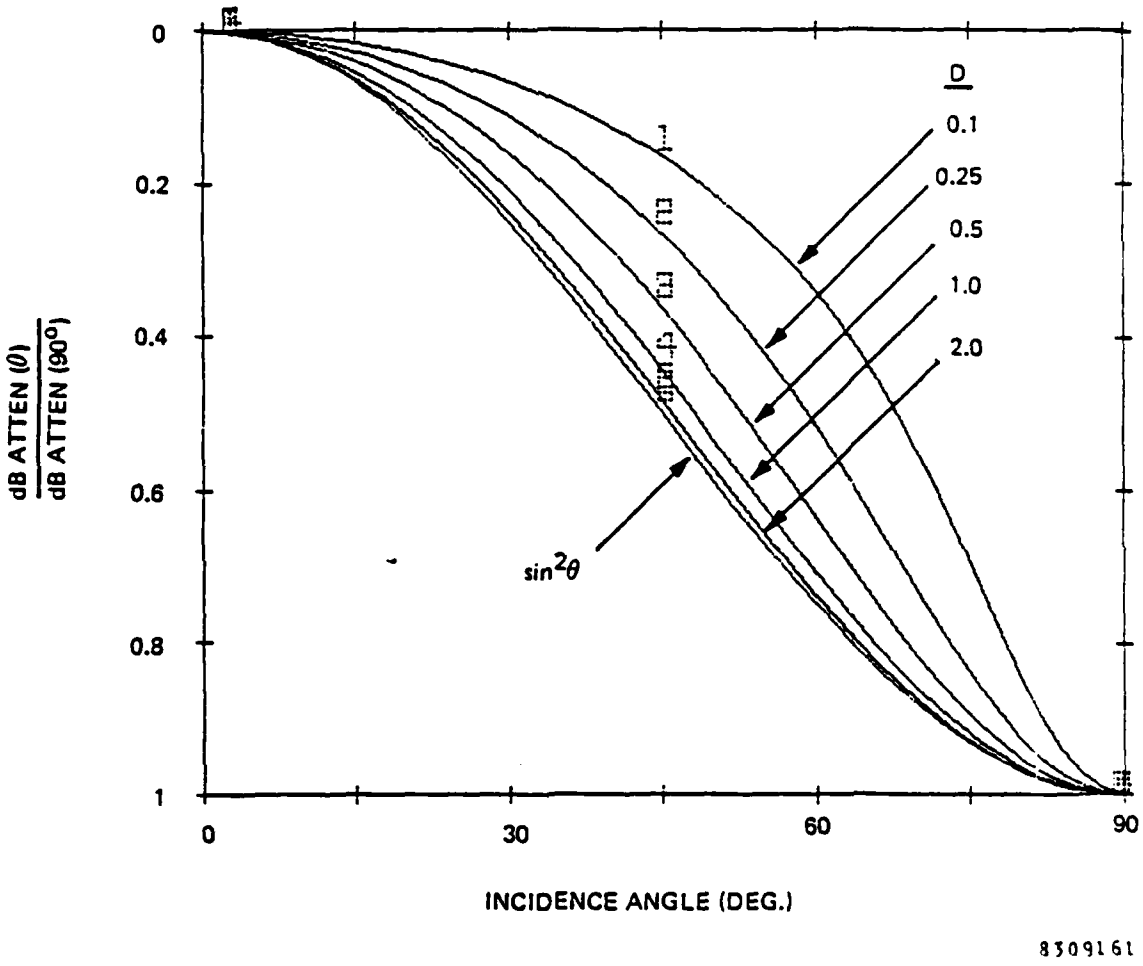

Figure 3-5. Normalized Attenuation vs Incidence Angle for Various D Values

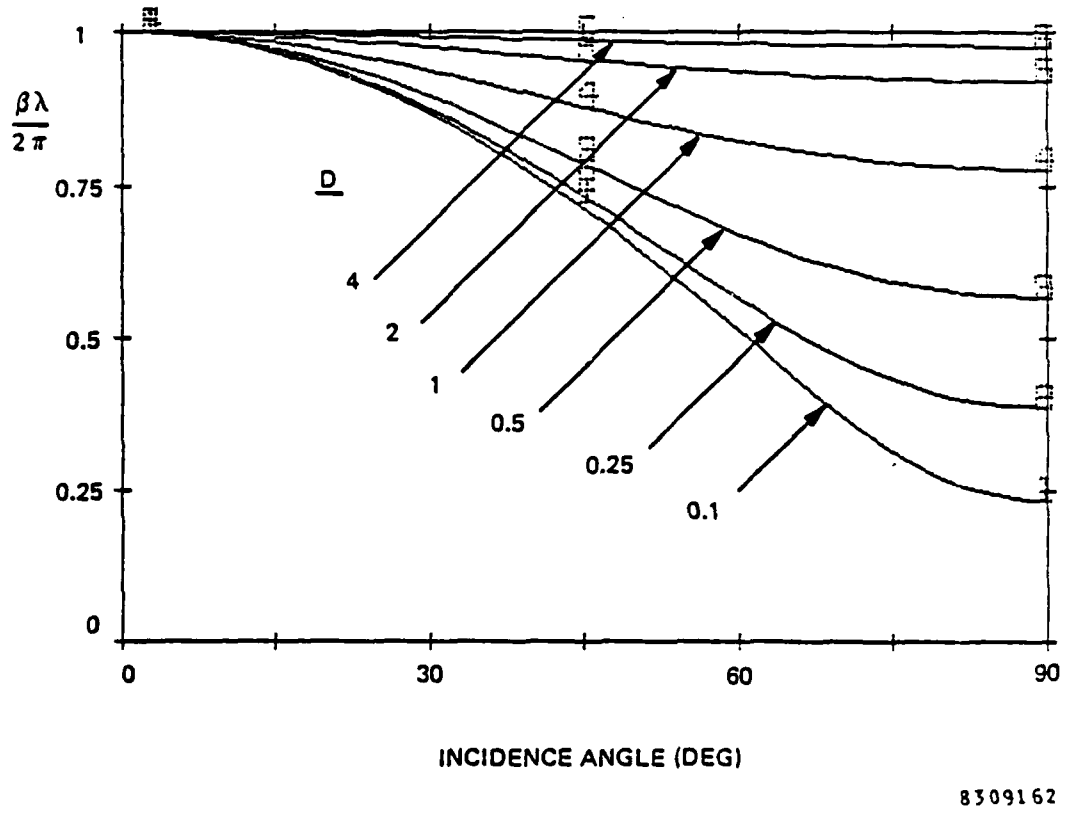

Figure 3-6. Relative Phase Constant vs Incidence Angle for Various D Values

(12). In this figure, β is normalized to $2\pi/\lambda$. At small incidence angles the medium is essentially invisible, so $\beta\lambda/2\pi$ is essentially unity. However at large incidence angles β decreases in a manner that depends on the value of D.

If D were zero, the medium would be absent, and $\beta\lambda/2\pi$ would equal cos θ. The curves for smaller values of D show a trend in this direction. If D were infinite, the medium would constrain the power flow to exactly the axial direction, and $\beta\lambda/2\pi$ would equal unity for all values of θ. The curves for larger values of D show a trend in this direction.

The direction of wave propagation inside the medium can be considered as the direction that is perpendicular to planes of constant phase in the medium. (These planes do not correspond to the planes of constant amplitude, which are parallel to the input face.) The angle between this propagation direction and the normal to the input face is designated θ_m. This angle is related to the incidence angle θ and to β by the following:

$$\theta_m = \arctan\left(\frac{2\pi \sin \theta}{\lambda\beta}\right) \qquad (24)$$

The difference between θ_m and θ can be considered to be the refracting effect of the medium. Figure 3-7 gives curves of θ_m versus θ for various values of D. As might be expected, when D is small there is not much refraction, and θ_m is nearly equal to θ. For large values of D the wave is almost completely constrained and for θ near 90° the value of θ_m approaches 45°.

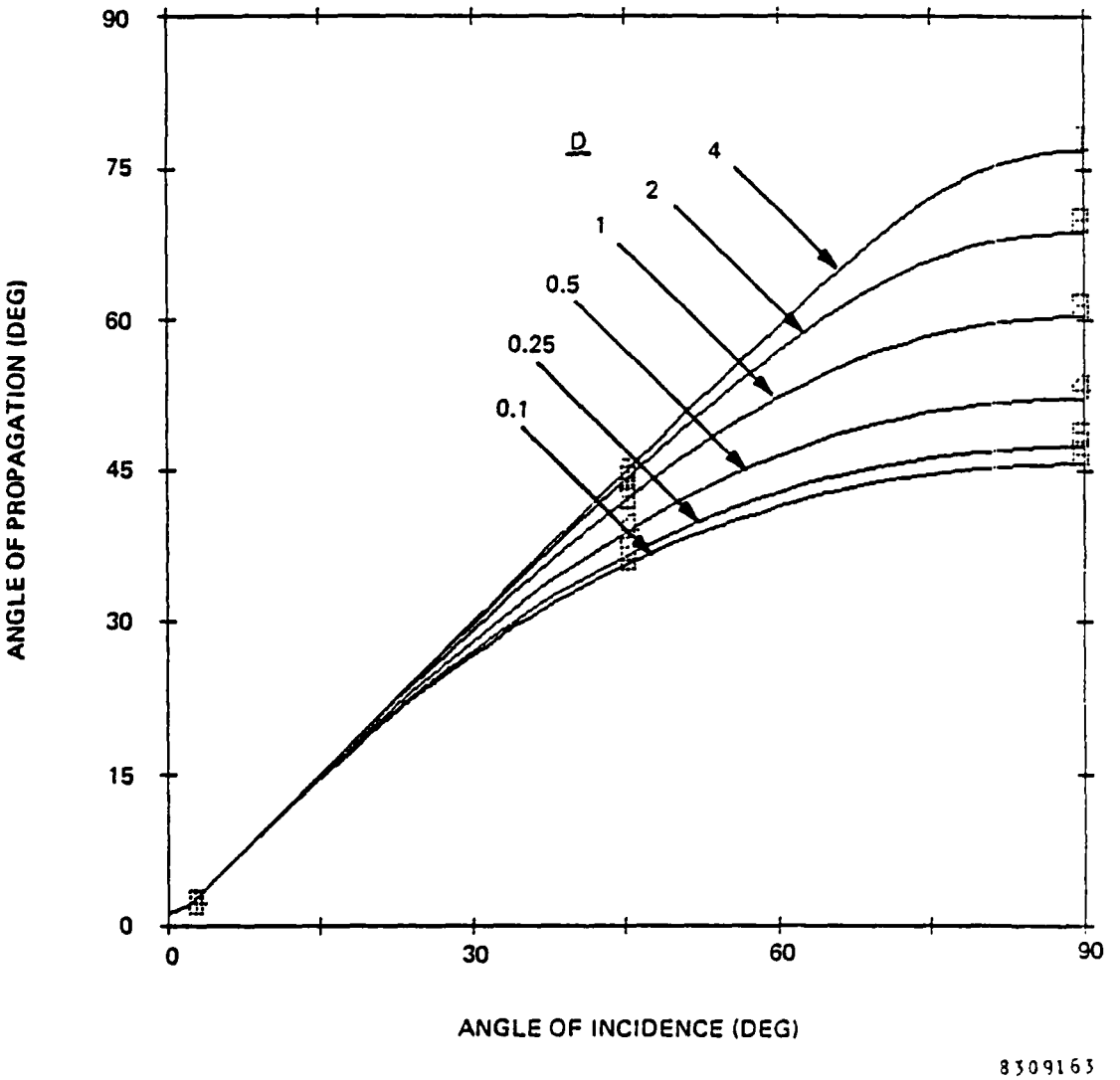

Figure 3-7. Propagation Angle vs Incidence Angle for Various D Values

(e) Impedance and Reflection versus Angle

The magnitude of the input impedance ratio versus incidence angle is shown for several values of D in Figure 3-8. It is seen that for D = 1 the impedance magnitude is only moderately different from the case of D = ∞. The latter case has $|Z'| = \sec\theta$ as can be seen in equation (21). The impedance magnitude becomes large only for large angles of incidence.

The phase of the input impedance versus incidence angle is shown for several values of D in Figure 3-9. For D = 1 this phase becomes -22.5° for grazing incidence. The maximum possible value for this phase is -45°, which is approached at grazing incidence when D approaches zero.

The reflection-coefficient magnitude $|\rho|$ vs. incidence angle is shown for several values of D in Figure 3-10. Again, the curve for D = 1 is not very different from the curve for D = ∞. The latter case has $|\rho| = \tan^2(\theta/2)$.

It is appropriate to consider how much contribution to filter rejection the reflection is likely to make. Suppose that an axial-conductance angular filter is sufficiently thick that its attenuation substantially isolates the input-face and output-face reflections from each other. In this case the two reflection losses add in dB. Figure 3-11 shows the total reflection loss versus incidence angle for several values of D. It is seen that in the range of incidence angles from 0° to over 60°, the contribution of reflection loss to the filter rejection is small, and can probably be neglected. Only very close to grazing incidence does the reflection loss become substantial.

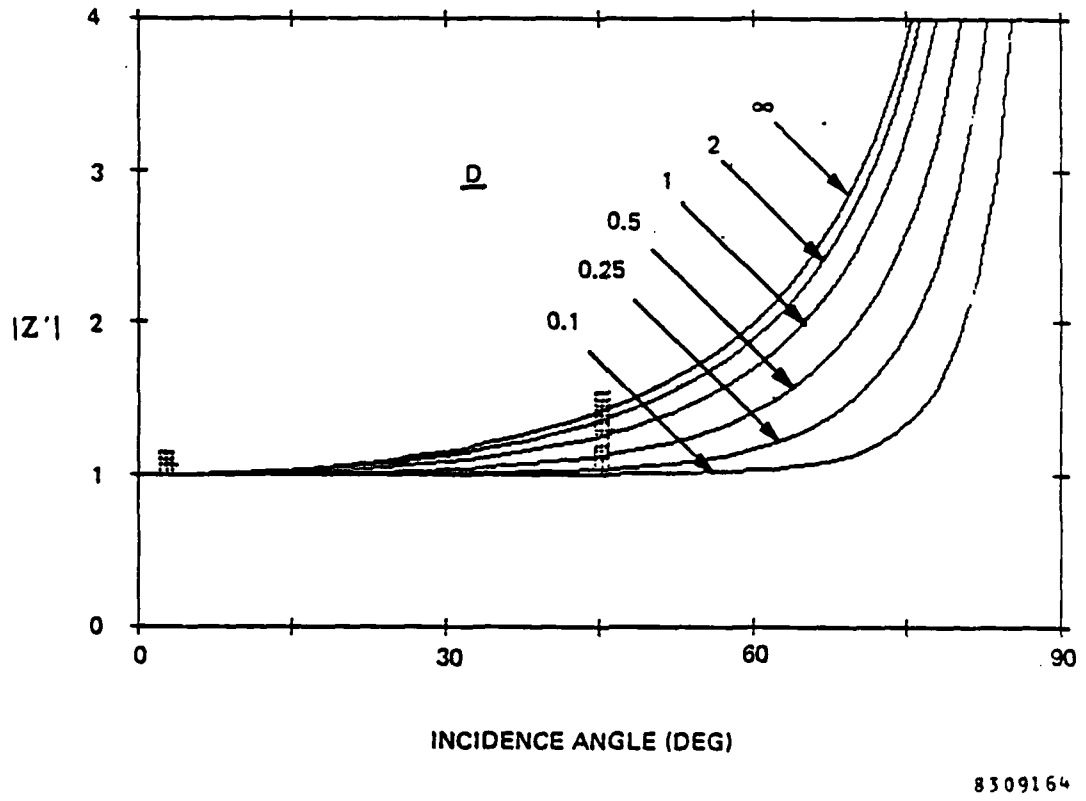

Figure 3-8. Magnitude of Input Impedance Ratio vs Incidence Angle for Various D Values

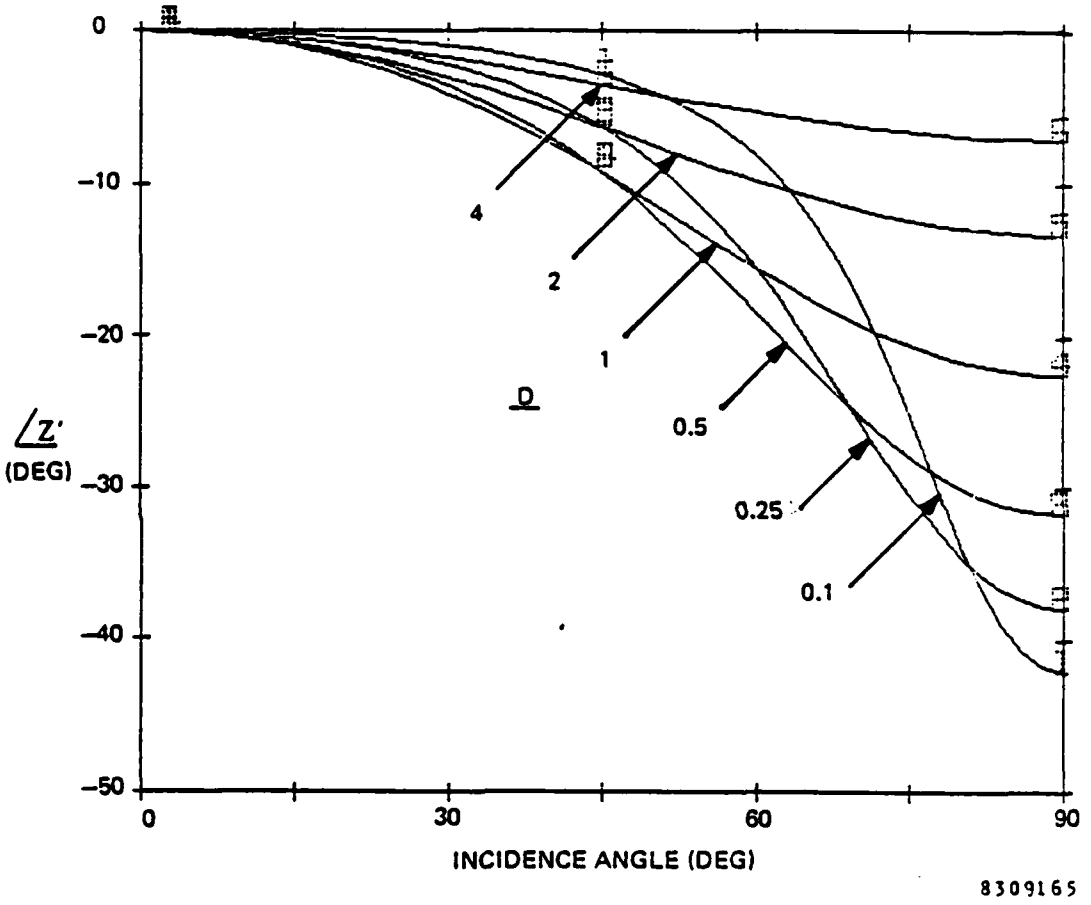

Figure 3-9. Phase of Input Impedance Ratio vs Incidence Angle for Various D Values

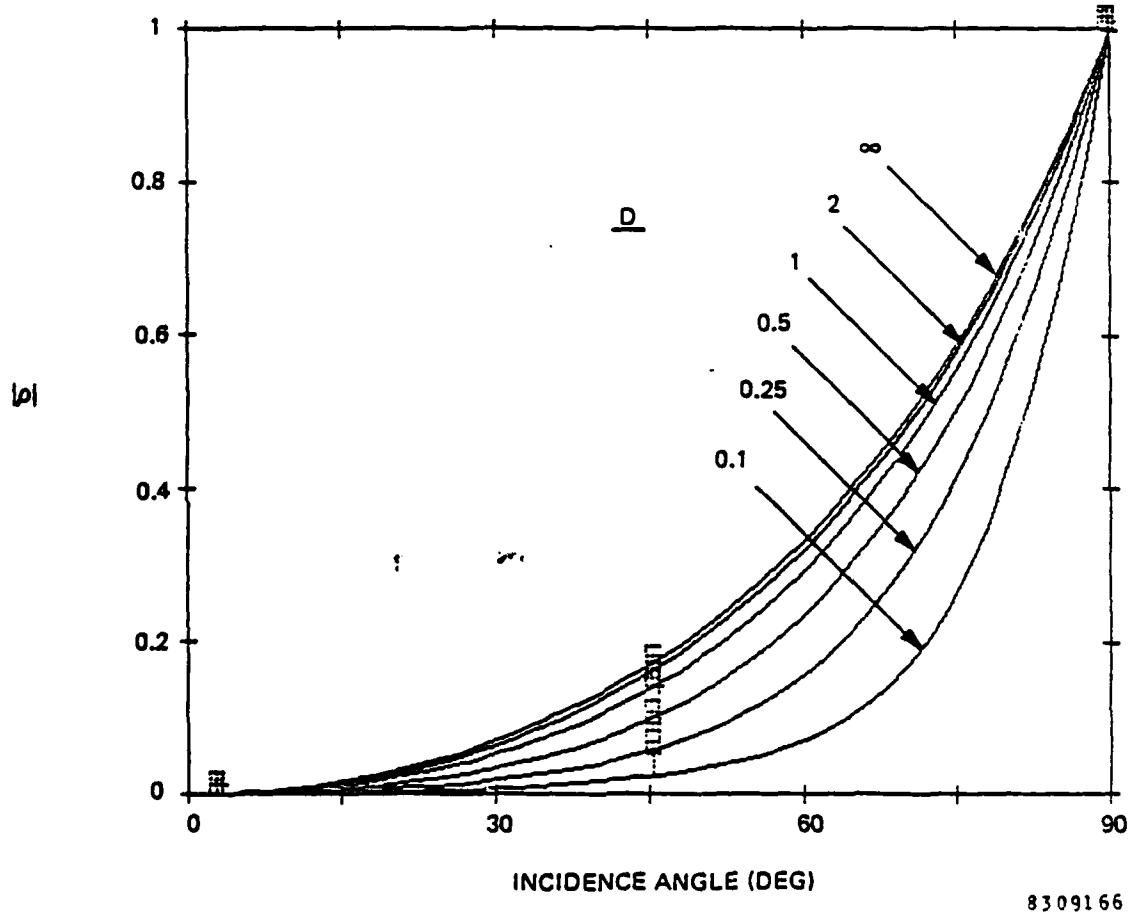

Figure 3-10. Reflection Coefficient Magnitude vs Incidence Angle for Various D Values

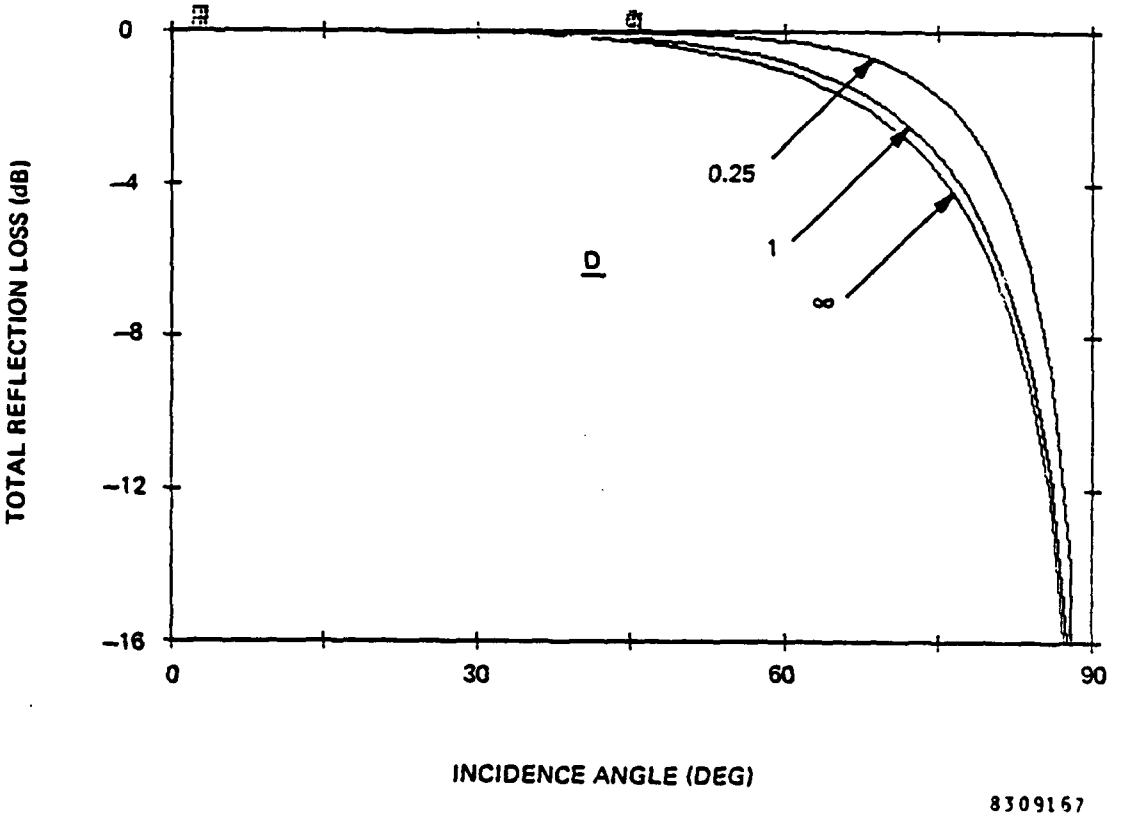

Figure 3-11. Total Reflection Loss vs Incidence Angle for Various D Values

(f) Matching The Impedance

Earlier in this report it was mentioned that an ideal angular filter would provide all of its rejection by absorption, and would be nonreflecting for all angles of incidence. The curves of Figure 3-10 come close to this objective at small incidence angles but not at large angles. It is interesting to see whether a still closer approximation to the ideal nonreflecting filter is possible, without destroying one or more of the other good features of the axial-conductance filter.

An impedance-matching layer on each face of the filter might be designed to increase the range of incidence angles over which the filter has low reflection. However, this matching layer must be designed to be inherently invisible at broadside incidence in order to preserve the wideband invisibility of the filter at broadside. An approach for accomplishing this is to use axial-conductance material for the matching layer as well as for the filter.

As an example of such a matching layer, a design is presented that yields a second angle of perfect match near 40° (the first angle is 0°). This matching layer is 0.4 wavelengths thick and has D = 0.3 (the filter has D = 1). Figure 3-12 shows the resulting curve of reflection versus angle, together with the original (unmatched) curve. A substantial reduction of reflection from 0° to 45° incidence is observed.

If a larger angular range for very low reflection were desired, a thicker and more complex matching layer could be considered. Matching over a wide frequency bandwidth could also be included in the design. The ultimate design might

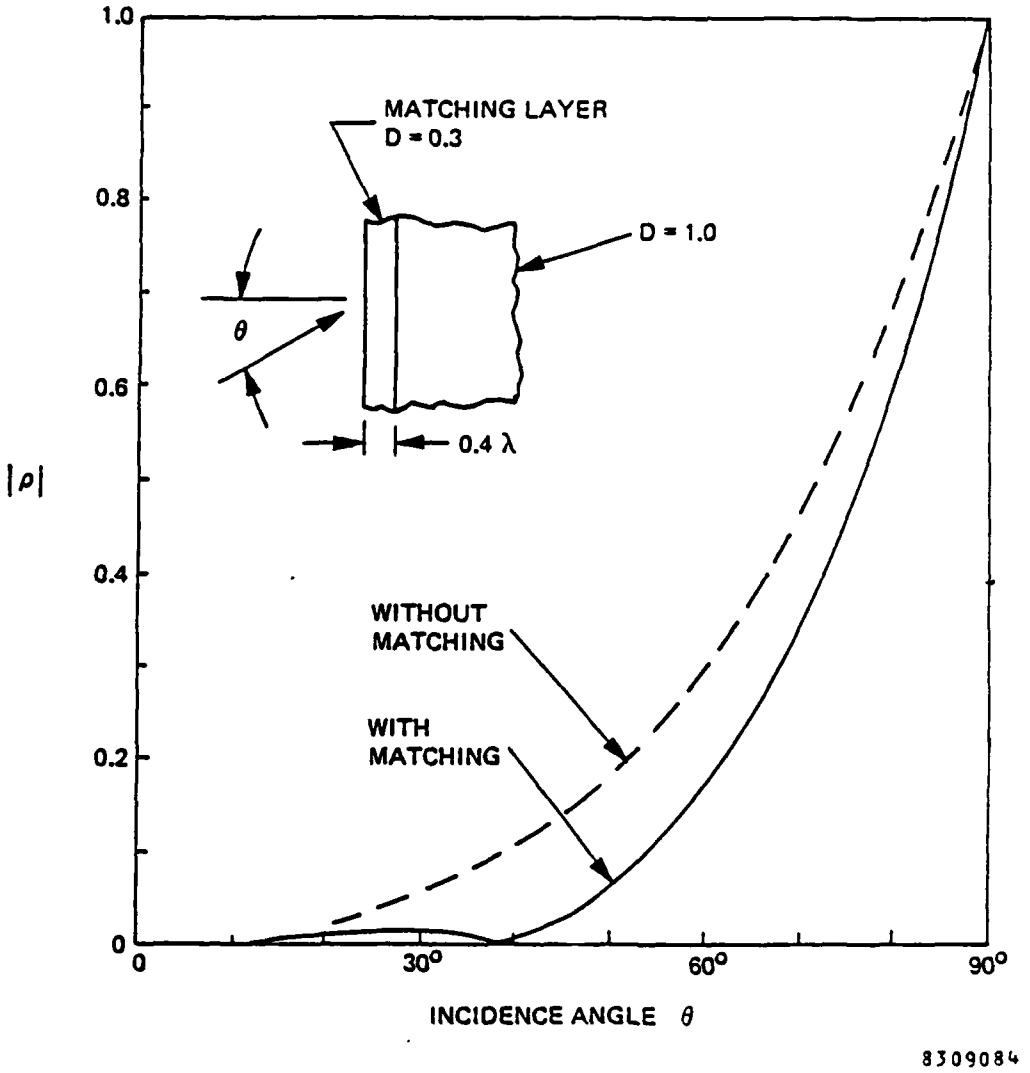

Figure 3-12. Reflection Coefficient Magnitude vs Incidence Angle With a Matching Layer

be thick layer having a smoothly-tapered increase of D. It is noteworthy that this matching layer contributes to the absorptive rejection provided by the filter, because it uses an axial-conductance medium.

3.4 FORMULAS FOR ANISOTROPIC DIELECTRIC

The analysis and results given in subsections 3.2 and 3.3 assume that the axial-conductance medium has the permittivity of free space (ε_o). In this subsection a more general case is considered in which the permittivity of the medium differs from that of free space, and also may be different for the transverse and the axial directions. The transverse and axial permittivities are designated ε_{tr} and ε_{ax} respectively. The geometry is defined in Figure 3-13.

With this anistropic dielectric, Maxwell's equations given in equation (3) now become:

$$\Delta \times \underline{E} = - \mu_o \frac{\partial \underline{H}}{\partial t}$$

$$\Delta \times \underline{H} = \frac{\partial}{\partial t} (\underline{i}\, \varepsilon_{tr} E_x + \underline{k}\, \varepsilon_{ax} E_z) + \underline{J} \qquad (25)$$

Following steps similar to those leading to equation (9), we now obtain:

$$k_z^2 = \left(\frac{2\pi}{\lambda}\right)^2 \frac{\varepsilon_{tr}}{\varepsilon_o} \left[1 - \frac{\sin^2\theta}{\frac{\varepsilon_{ax}}{\varepsilon_o} - j\, D} \right] \qquad (26)$$

where $D = \frac{\sigma_{ax}}{\omega \varepsilon_o}$ as before.

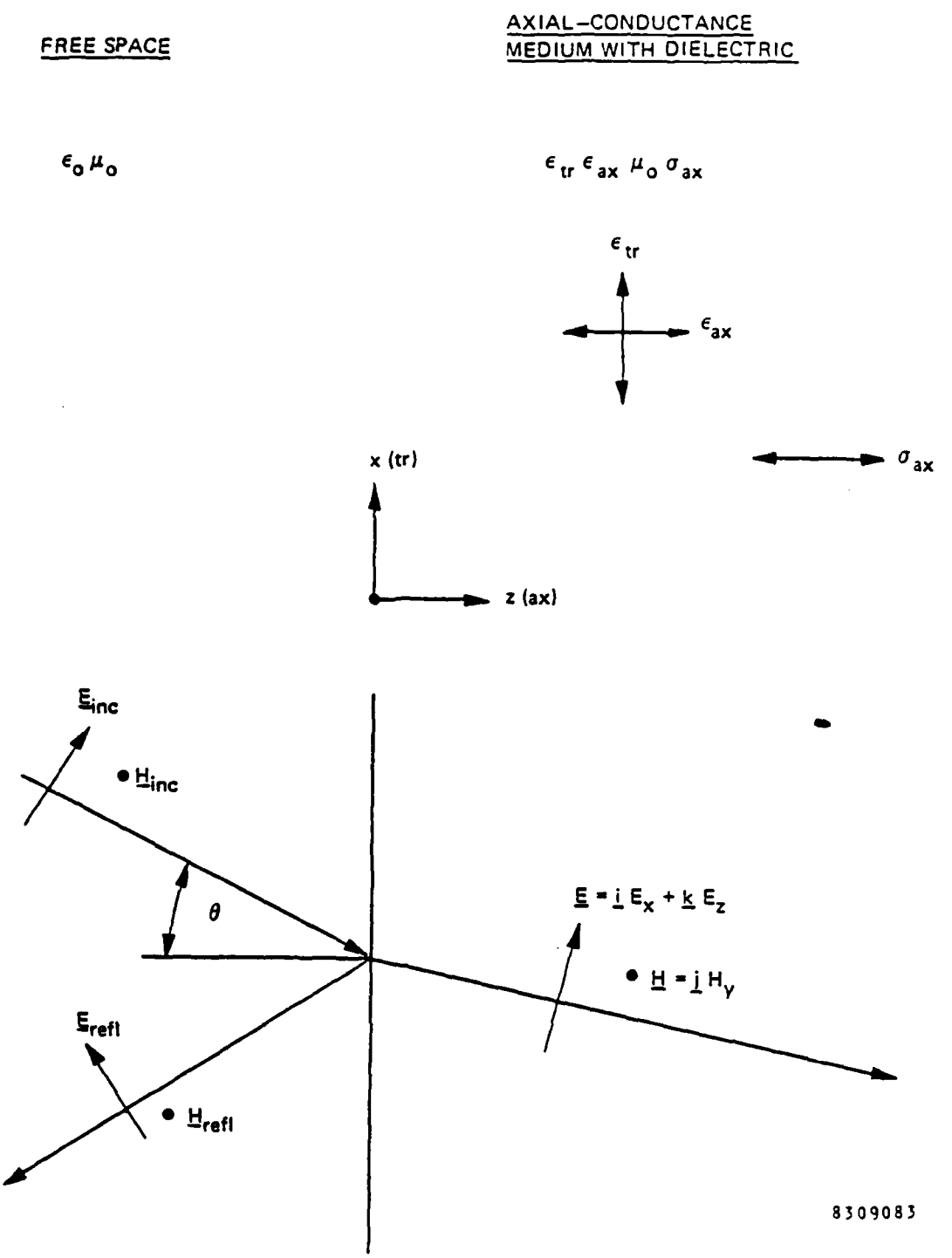

Figure 3-13. Geometry for Analysis of Anisotropic-Dielectric Homogeneous Medium

For convenience, we define the transverse and axial dielectric constants ε'_{tr} and ε'_{ax} :

$$\varepsilon'_{tr} = \frac{\varepsilon_{tr}}{\varepsilon_o} \qquad \varepsilon'_{ax} = \frac{\varepsilon_{ax}}{\varepsilon_o} \tag{27}$$

Equation (26) now becomes:

$$k_z^2 = \left(\frac{2\pi}{\lambda}\right)^2 \varepsilon'_{tr} \left[1 - \frac{\sin^2\theta}{\varepsilon'_{ax} - jD} \right] \tag{28}$$

Separating k_z into its two components according to (10) yields:

$$\alpha = -\frac{2\pi}{\lambda} \sqrt{\varepsilon'_{tr}} \; \mathrm{Im}\left[1 - \frac{\sin^2\theta}{\varepsilon'_{ax} - jD} \right]^{1/2} \tag{29}$$

$$= \frac{2\pi}{\lambda} \sqrt{\varepsilon'_{tr}} \left[\frac{1 + \left(\frac{D}{\varepsilon'_{ax}}\right)^2 - \frac{\sin^2\theta}{\varepsilon'_{ax}}}{2\left[1 + \left(\frac{D}{\varepsilon'_{ax}}\right)^2\right]} \left(\sqrt{1 + \left(\frac{\frac{D}{\varepsilon'_{ax}} \quad \frac{\sin^2\theta}{\varepsilon'_{ax}}}{1 + \left(\frac{D}{\varepsilon'_{ax}}\right)^2 - \frac{\sin^2\theta}{\varepsilon'_{ax}}} \right)^2} - 1 \right) \right]^{1/2}$$

$$\beta = \frac{2\pi}{\lambda} \sqrt{\varepsilon'_{tr}} \; \mathrm{Re}\left[1 - \frac{\sin^2\theta}{\varepsilon'_{ax} - jD} \right]^{1/2} \tag{30}$$

$$= \frac{2\pi}{\lambda} \sqrt{\varepsilon'_{tr}} \left[\frac{1 + \left(\frac{D}{\varepsilon'_{ax}}\right)^2 - \frac{\sin^2\theta}{\varepsilon'_{ax}}}{2\left[1 + \left(\frac{D}{\varepsilon'_{ax}}\right)^2\right]} \left(\sqrt{1 + \left(\frac{\frac{D}{\varepsilon'_{ax}} \quad \frac{\sin^2\theta}{\varepsilon'_{ax}}}{1 + \left(\frac{D}{\varepsilon'_{ax}}\right)^2 - \frac{\sin^2\theta}{\varepsilon'_{ax}}} \right)^2} + 1 \right) \right]^{1/2}$$

The significance of these formulas will be discussed in subsection 3.5.

The impedance of the anisotropic-dielectric axial-conductance medium can also be obtained. Following steps similar to those leading to equation (19), the input impedance ratio now becomes:

$$Z' = \frac{k_z}{\frac{2\pi}{\lambda}\ \varepsilon'_{tr} \cos\ \theta} \tag{31}$$

Substituting (28) for k_z yields:

$$Z' = \frac{\left[1 - \frac{\sin^2\theta}{\varepsilon'_{ax} - jD}\right]^{1/2}}{\sqrt{\varepsilon'_{tr}}\ \cos\ \theta} \tag{32}$$

The significance of this formula will also be discussed in subsection 3.5.

3.5 RESULTS FOR ANISOTROPIC DIELECTRIC

(a) Effect of Dielectric at Small Angles

For small θ, equation (29) simplifies to the following:

$$\alpha(\theta \to 0) = \frac{\pi}{\lambda} \frac{\frac{D}{\varepsilon'_{ax}}}{1 + \left(\frac{D}{\varepsilon'_{ax}}\right)^2} \frac{\sqrt{\varepsilon'_{tr}}}{\varepsilon'_{ax}}\ \theta^2 \tag{33}$$

The value of D giving the maximum $\alpha(\theta \to 0)$ in (33) is:

$$D_{opt} = \varepsilon'_{ax} \tag{34}$$

An equivalent relation is:

$$\frac{\sigma_{ax\ opt}}{\omega\ \varepsilon_{ax}} = 1 \tag{35}$$

Now let us compare the maximum attenuation at a small θ for this case against the maximum attenuation at the same θ for the non-dielectric case. From (33) and (34) versus (22) and (23) is obtained:

$$\frac{\max\ \alpha(\theta \to 0)\ \text{dielectric}}{\max\ \alpha(\theta \to 0)\ \text{no dielectric}} = \frac{\sqrt{\varepsilon'_{tr}}}{\varepsilon'_{ax}} \tag{36}$$

From the above simple relation, the following statements can be made for a dielectric-loaded axial-conductance filter:

1) increasing the <u>transverse</u> dielectric constant should yield an <u>increase</u> in the filter rejection,

2) increasing the <u>axial</u> dielectric constant should greatly <u>decrease</u> the filter rejection that is available,

3) increasing the dielectric constant of <u>isotropic</u> dielectric should <u>decrease</u> the filter rejection that is available.

While these statements are based on the small-angle case given by (36), they are generally valid for any incidence angle. It should also be noted that if an axial-conductance medium could be made to have an effective axial dielectric constant less than unity, (36) indicates that a filter using such a medium might have enhanced rejection. This is considered further in Section 4.

The impedance for small θ is also of interest. For an axial-conductance medium with no dielectric, equation (20) showed that for small θ, the input impedance ratio was approximately unity, and there was virtually no reflection. However with dielectric loading, equation (32) evaluated for small θ becomes:

$$Z'(\theta \to 0) = \frac{1}{\sqrt{\varepsilon'_{tr}}} \tag{37}$$

Thus, when the transverse dielectric constant of the axial-conductance medium is greater than unity, the medium creates a reflection even at broadside incidence.

Assuming that a filter having no reflection at broadside is desired, an impedance-matching section that is effective at broadside incidence would be needed. Such a matching section might be simple, but it would inevitably introduce some limitation on frequency bandwidth and sensitivity to tolerances. This is the price that would be paid for the increased rejection that occurs when the transverse dielectric constant of the axial-conductance medium is greater than unity.

(b) Examples of Dielectric Effect at All Angles

To illustrate the effect of dielectric on the angular behavior of the axial-conductance medium, three examples are given. The first is the reference case of no dielectric (unity dielectric constants). The second is with a transverse dielectric constant of 4, and an axial dielectric constant of unity. Both cases have D = 1 for optimum small-angle attenuation. The third case has an isotropic dielectric with dielectric constant of 4, and with D = 4 for optimum small-angle attenuation.

The attenuation versus θ as computed from equation (29) is shown for the three examples in Figure 3-14. As expected, the transverse-dielectric case has exactly $(\varepsilon'_{tr})^{1/2}$ times the attenuation of the no-dielectric case. The isotropic-dielectric case has approximately $1/(\varepsilon')^{1/2}$ times the attenuation of the no-dielectric case at small angles, and even less attenuation at large angles.

The phase constant versus θ as computed from equation (30) is shown for the three examples in Figure 3-15. The transverse-dielectric case has exactly $(\varepsilon'_{tr})^{1/2}$ times the phase constant of the no-dielectric case. The isotropic-dielectric case has a phase constant $(\varepsilon')^{1/2}$ times that of the no-dielectric case at broadside incidence, but deviates somewhat from this ratio at large angles of incidence.

The propagation angle θ_m within the medium is shown versus θ for the three examples in Figure 3-16. The dielectric cases exhibit more refraction than the no-dielectric case, as would be expected.

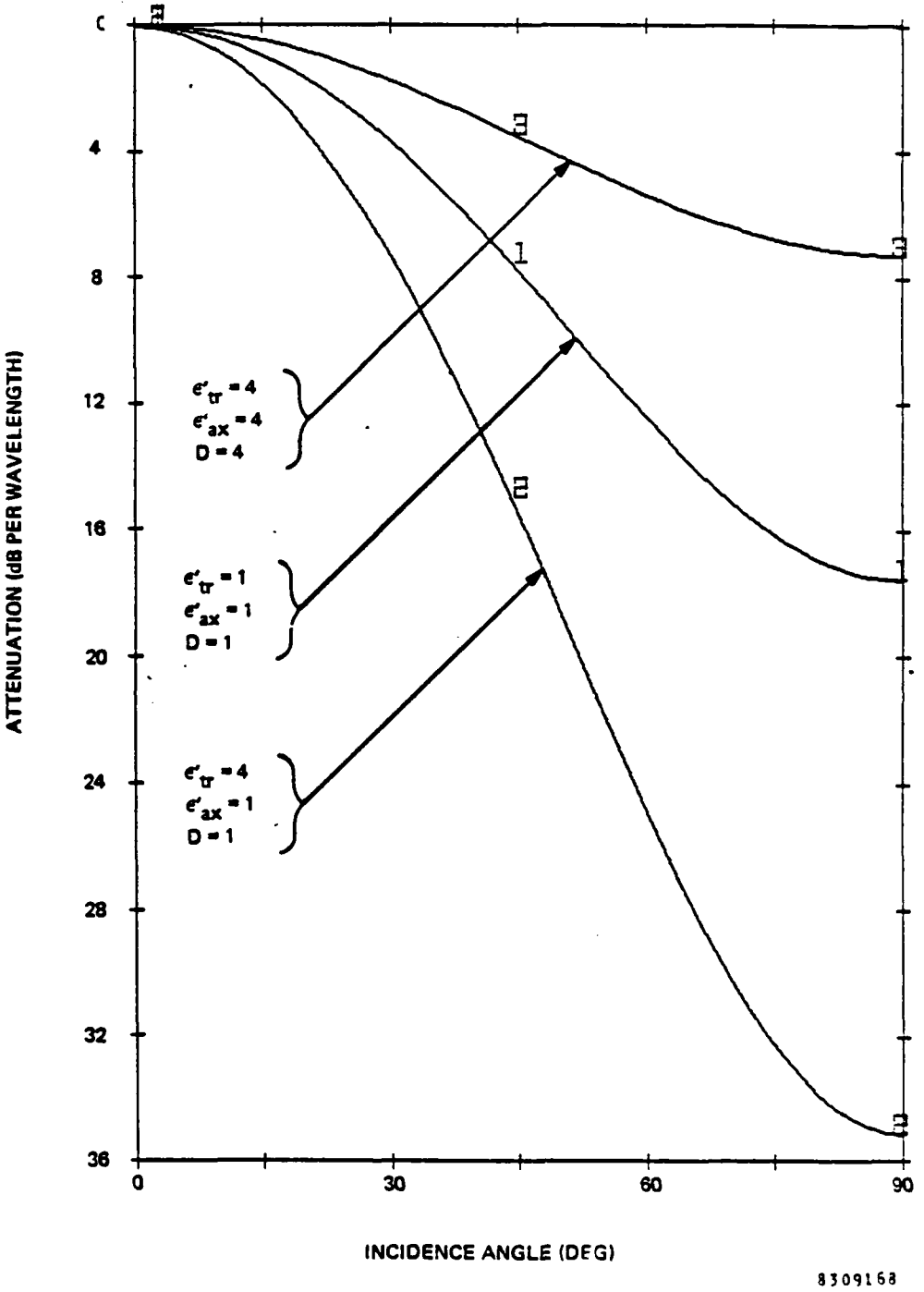

Figure 3-14. Attenuation vs Incidence Angle for Three Dielectric Cases

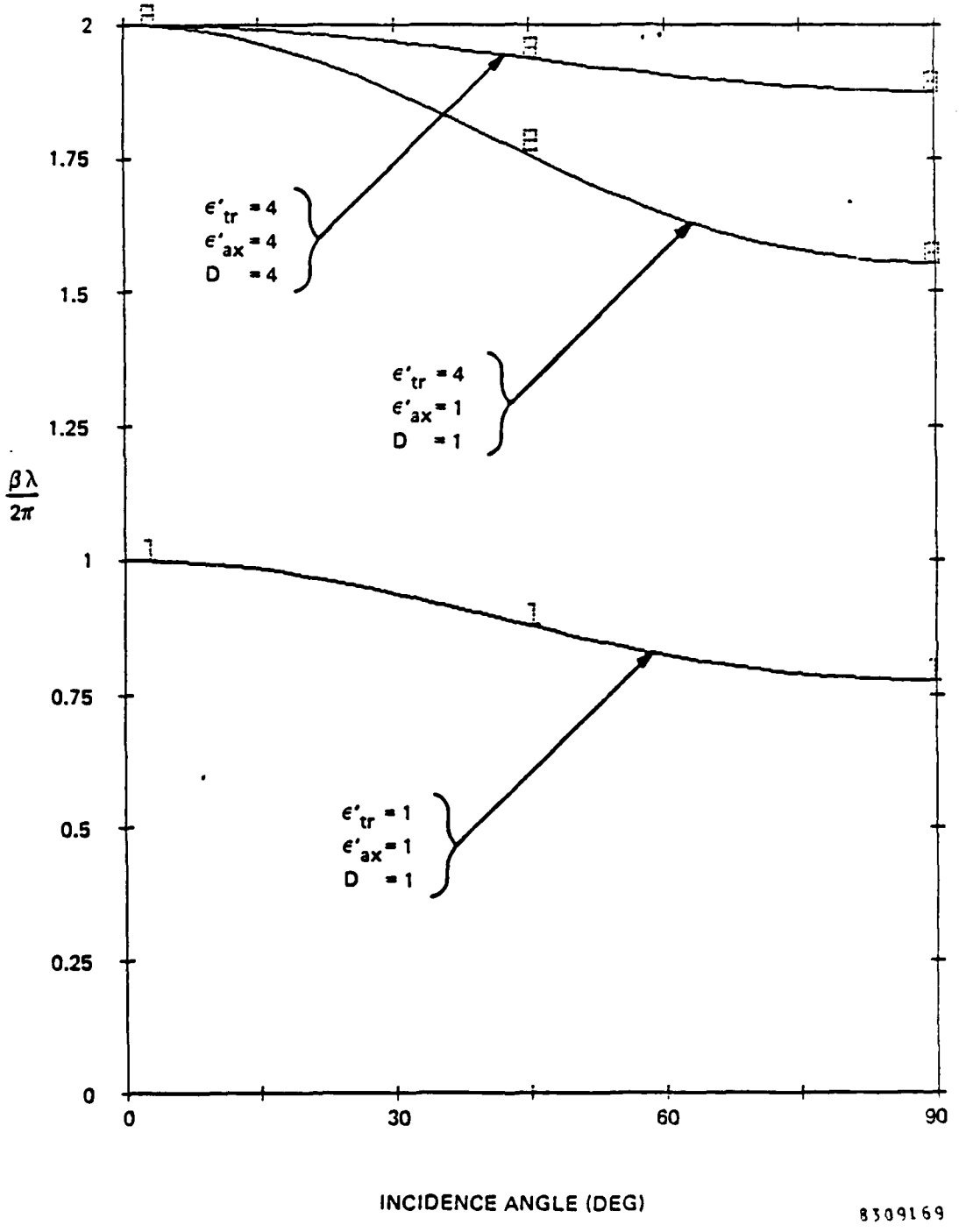

Figure 3-15. Relative Phase Constant vs Incidence Angle for Three Dielectric Cases

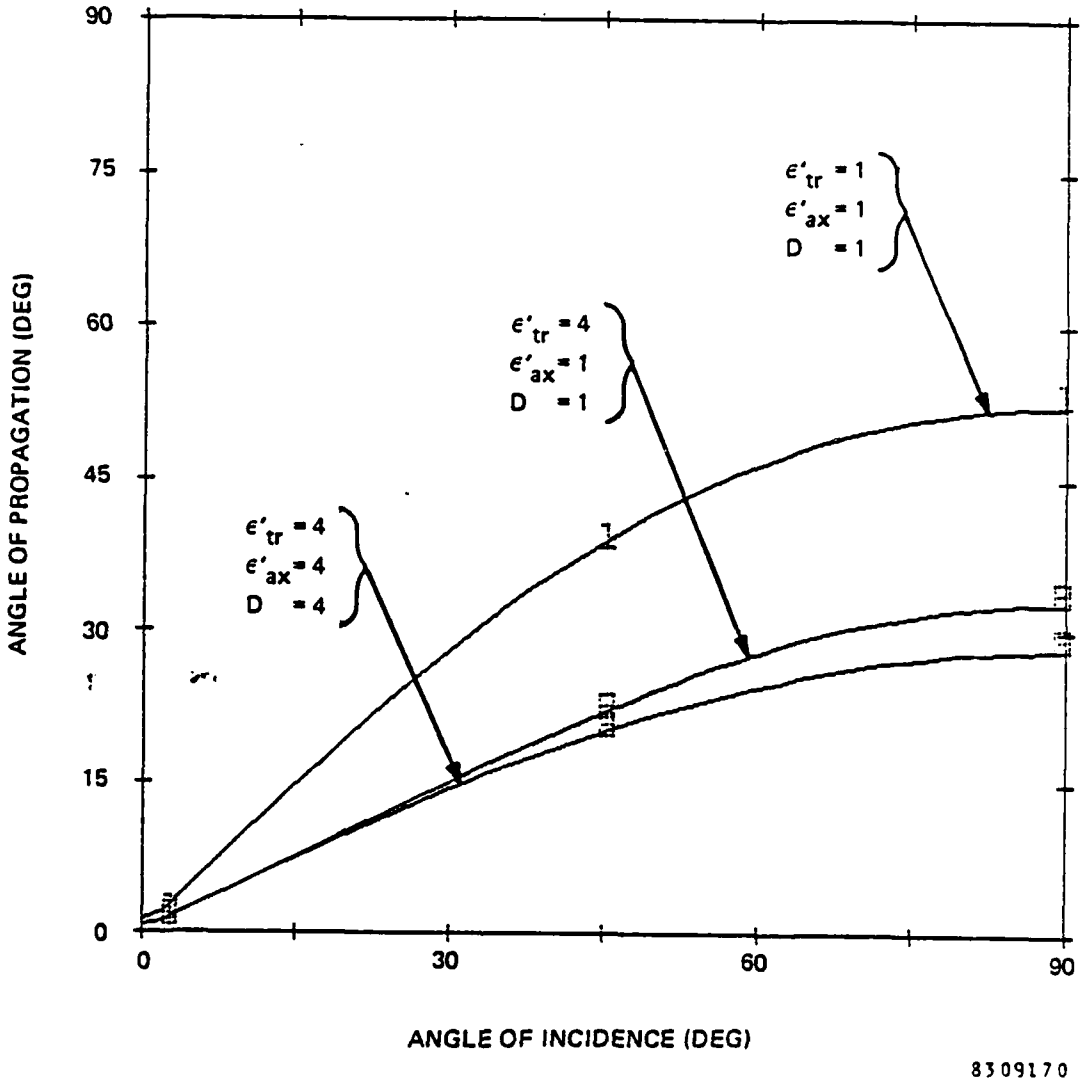

Figure 3-16. Propagation Angle vs Incidence Angle for Three Dielectric Cases

The magnitude of the input impedance ratio versus θ as computed from (32) is shown for the three examples in Figure 3-17. The transverse-dielectric case has exactly $1/(\varepsilon'_{tr})^{1/2}$ times the impedance magnitude of the no-dielectric case. The isotropic-dielectric case has $1/(\varepsilon')^{1/2}$ times the impedance magnitude of the no-dielectric case at broadside incidence, but deviates somewhat from this ratio at large angles of incidence.

The reflection coefficient magnitude versus θ is shown for the three examples in Figure 3-18. As expected, the dielectric cases have a non-zero reflection at broadside incidence. To obtain zero reflection at broadside, a broadside-impedance-matching section would be needed as was mentioned earlier.

3.6 DISCUSSION

The essential properties of an axial-conductance angular filter have been determined, based on use of an ideal homogeneous axial-conductance medium. An optimum value for the axial loss tangent (D) of the medium has been derived; it is unity. With this value the filter rejection is maximized, and variations of D with construction tolerances and with frequency are non-critical.

The homogeneous axial-conductance medium provides an attenuation that is zero at broadside incidence, and that increases monotonically with E-plane incidence angle (θ). This increase is approximately proportional to $\sin^2\theta$. At 45° incidence the attenuation is approximately 8 dB per wavelength of filter thickness. The attenuation for any specified filter thickness is essentially proportional to frequency over a wide frequency range.

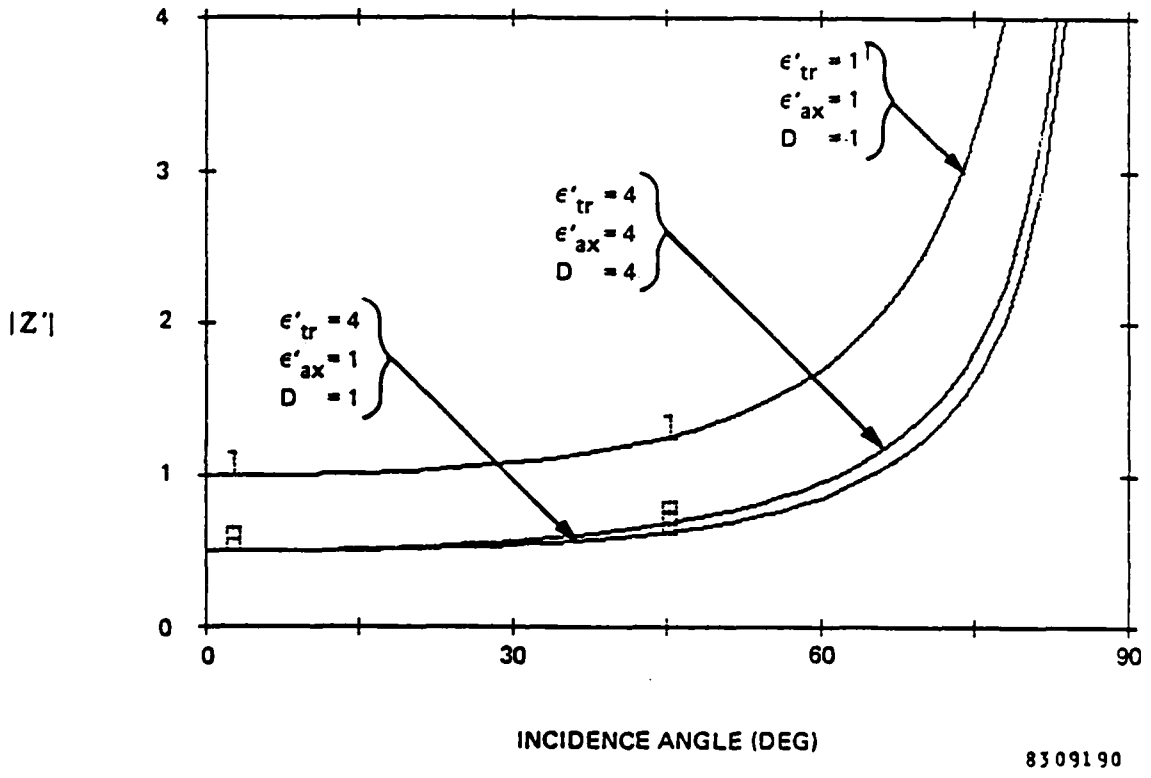

Figure 3-17. Magnitude of Input Impedance Ratio vs Incidence Angle for Three Dielectric Cases

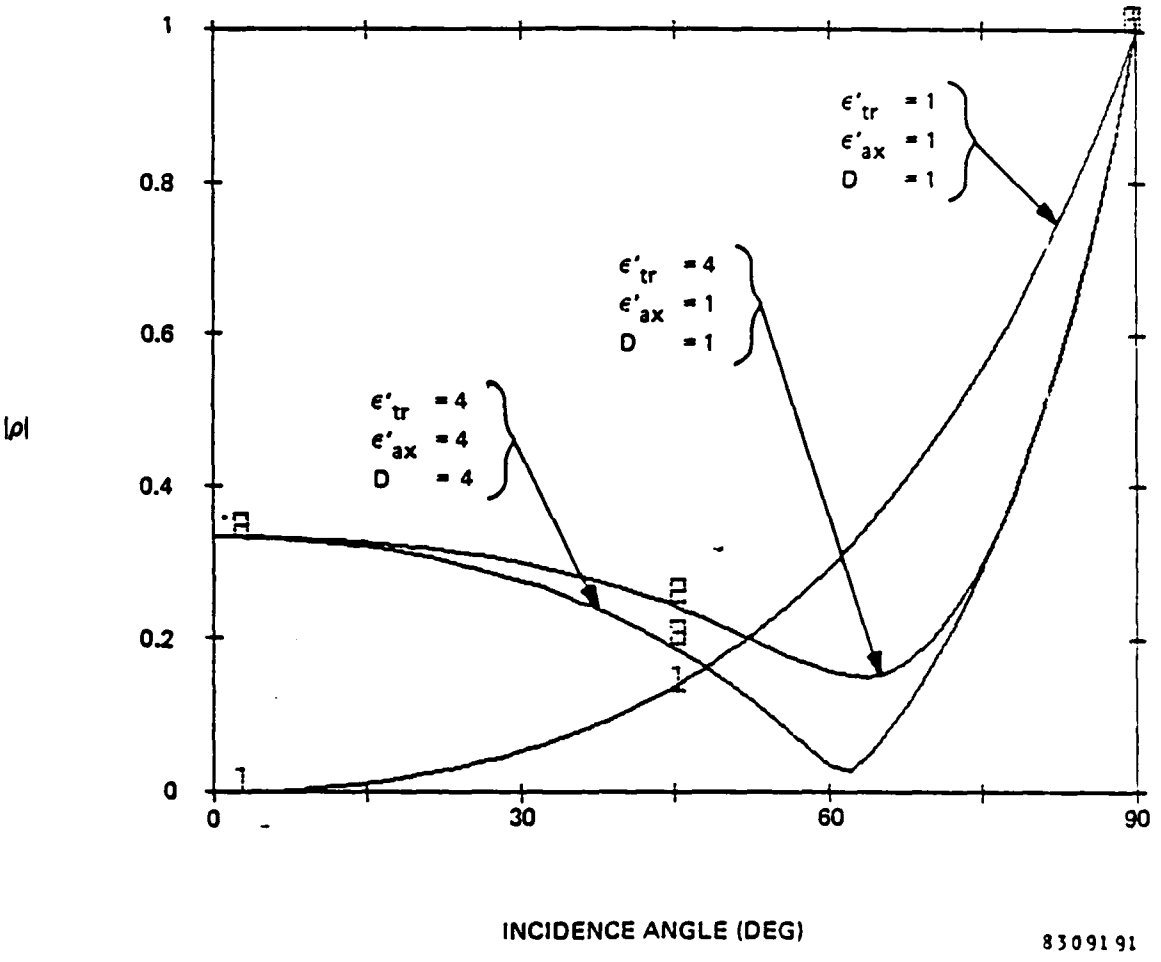

Figure 3-18. Reflection Coefficient Magnitude vs Incidence Angle for Three Dielectric Cases

The basic homogeneous axial-conductance medium is invisible to a wave incident at broadside. As incidence angle increases in the E plane, the reflection coefficient gradually increases, and goes to unity at grazing incidence. The reflection loss becomes substantial only near grazing incidence. If desired, the medium can be impedance matched at angles other than broadside without destroying the inherent wideband match at broadside.

The inclusion of dielectric in the axial-conductance medium modifies its performance. Isotropic dielectric reduces the attenuation that is available from a given thickness. Transverse dielectric, however, increases the attenuation. Either type of dielectric creates some reflection at broadside incidence, and may need to be impedance matched at broadside.

The homogeneous form of axial-conductance medium is an ideal form, and can be considered to be a reference standard against which more practical inhomogeneous forms are compared. If an inhomogeneous axial-conductance medium has very thin, very closely-spaced conductance elements, its performance should closely approximate that of the homogeneous medium. A significant question is: at what element spacing and element thickness does the performance of the inhomogeneous medium deviate substantially from that of the ideal homogeneous medium? This question, as well as others relating to the design and performance of the inhomogeneous medium, are addressed in Section 4.

SECTION 4

ANALYSIS OF PRACTICAL INHOMOGENEOUS MEDIUM

There are three aspects relating to the inhomogeneous axial-conductance medium that are considered in this section. First, the configuration and basic design of the medium is described (subsection 4.1). Next, the potential loss of this medium at broadside incidence is analyzed and discussed (subsection 4.2). Then, the angular response of the inhomogeneous medium is analyzed and discussed (subsection 4.3).

4.1 CONFIGURATION AND DESIGN

The inhomogeneous axial-conductance medium comprises an array of thin resistance elements oriented in the axial direction, as was indicated in Figure 2-1. A basic requirement for this medium is that it provide the desired value of axial loss tangent (D).

It is helpful to define a quantity R_λ as the resistance (in ohms) across a cube having wavelength sides. The quantity R_λ is equal to the axial resistivity divided by wavelength, and hence equals $1/\sigma_{ax}\lambda$. Recalling the definition of D in equation (8), the relation between R_λ and D is then obtained:

$$R_\lambda = \frac{60 \text{ ohms}}{D} \tag{38}$$

If a value of unity for D is wanted, then the medium should provide a resistance of 60 ohms in the axial direction between opposite faces of a wavelength cube.

The resistance elements can have any convenient cross-sectional shape; we have selected thin strips because they can be produced by printed-circuit techniques. Figure 4-1 shows an array of resistance strips comprising the inhomogeneous axial-conductance medium. The array lattice is square with spacing s, and the width of each strip is w.

It is assumed that the strips are very thin, and that their resistance behavior can be defined in terms of the surface resistance R_s (in ohms per square) of the strip material. The following relation can then be easily derived:

$$R_\lambda = \left(\frac{s}{\lambda}\right)^2 \cdot\frac{\lambda}{w} \; R_s \qquad (39)$$

Combining (38) and (39) yields a formula for R_s in terms of D and the array/strip dimensions:

$$R_s = \frac{60 \text{ ohms}}{D} \; \frac{\lambda}{s} \; \frac{w}{s} \qquad (40)$$

As an example, suppose that $s/\lambda = 0.2$ and $w/s = 0.2$, and a value of unity for D is wanted. Equation (40) then yields 60 ohms per square as the surface resistance needed for the strip material.

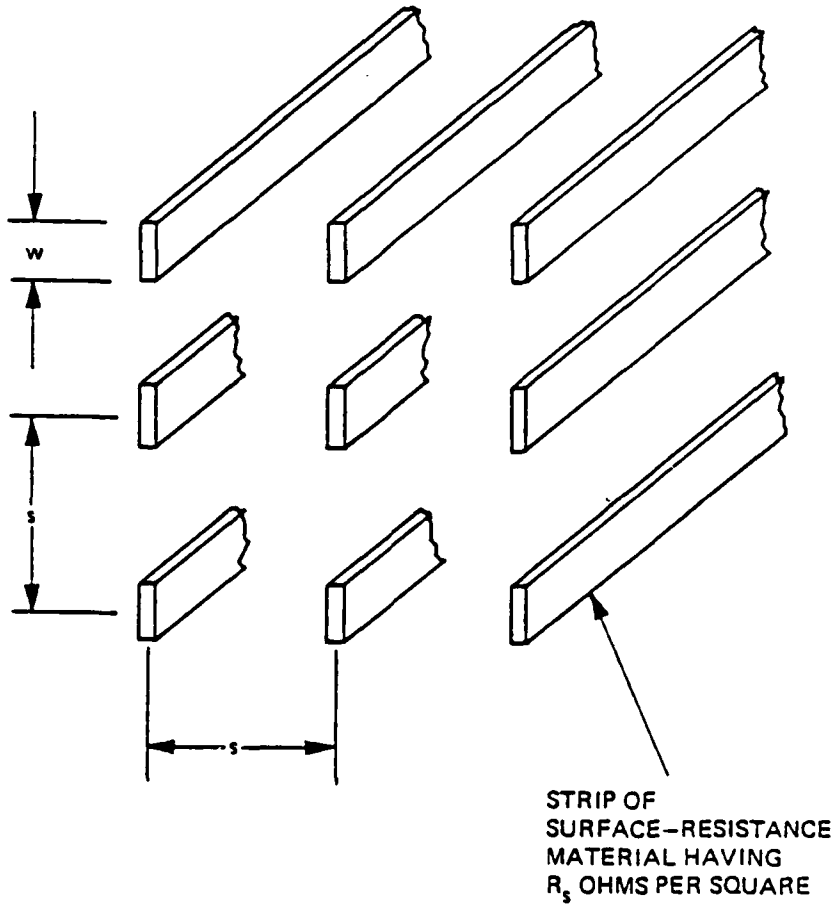

Figure 4-1. Inhomogeneous Axial-Conductance Medium Dimensions

The choice of particular values for s/λ and w/s depends on how these parameters affect both the loss at broadside incidence and the angular response of the filter. These aspects are examined in subsections 4.2 and 4.3.

4.2 LOSS AT BROADSIDE INCIDENCE

The homogeneous axial-conductance medium has no attenuation at broadside incidence. However, the inhomogeneous medium can have a substantial attenuation at broadside incidence if its transverse dimensions are not sufficiently small.

There are two components for the broadside loss. One component results from the electric (E) field of the incident wave. The other component results from the magnetic (H) field of the wave. These two components of the broadside loss are discussed separately below.

(a) E-Field Broadside Loss

If the electric field of the incident wave has a component parallel to the width (w) dimension of the resistance strips, there will be a current induced across the width of the strip. Since the strip has resistance, this transverse current will cause a loss.

The following analysis is made to determine the essential relation between this loss and the dimensions of the strip medium. At broadside incidence, the strips introduce a capacitive susceptance in parallel with that of free space. This effect is equivalent to that of an artificial-dielectric medium comprising metal strips. If the strip width (w) is assumed to be small compared with the

strip spacing (s), and the spacing is assumed to be small compared with the wavelength, a simple approximate formula can be stated for the capacitive susceptance (B_1) introduced by the strip medium relative to that of free space (B_o). This relation, based on the refractive index of metal-strip artifical dielectric (Ref. 14) is:

$$\frac{B_1}{B_o} = \frac{\pi}{4} \left(\frac{w}{s}\right)^2 \tag{41}$$

where the strip dimension w is assumed to be oriented parallel to the electric field of the incident wave. Let both B_o and B_1 be defined as the capacitive susceptances across a cubic cell having a side s. The free-space susceptance across this cell is:

$$B_o = \omega \varepsilon_o s = \frac{2\pi s}{\lambda Z_o} \tag{42}$$

Combining (41) and (42) yields the capacitive susceptance introduced by the strip medium per periodic cubic cell:

$$B_1 = \frac{\pi^2}{2} \frac{1}{Z_o} \frac{s}{\lambda} \left(\frac{w}{s}\right)^2 \tag{43}$$

Ref. 14 - J. Brown, "Microwave Lenses", Methuen and Co. Ltd., London, page 41; 1953.

The current in the susceptance B_1 is related to the current that flows transversely in the strips. Since the strips are made of resistance material, there is a resistance (R_1) in series with the susceptance B_1. The equivalent circuit representing the E-field effect of the resistance strips at broadside incidence is therefore a series R-C circuit in parallel with the C of free space, as indicated at the lower left side of Figure 4-2.

The series resistance R_1 for the periodic cubic cell is determined in two steps. First, the effective transverse resistance R_w for a strip in the cubic cell is stated:

$$R_w = \frac{2}{3} \; R_s \; \frac{w}{s} \tag{44}$$

where the 2/3 factor accounts for the non-uniform current across the strip (see Appendix A). Then, a factor based on conformal transformation of the strip geometry by H. A. Wheeler (see Appendix A) is applied to account for the ratio of strip transverse current to current in the susceptance B_1. This factor yields:

$$R_1 = \left(\frac{4}{\pi} \; \frac{s}{w} \right)^2 \; R_w \tag{45}$$

In most cases of interest, R_1 is small compared with $1/B_1$, and the transverse current is nearly independent of R_1. For these typical cases the equivalent circuit indicated at the lower right side of Figure 4-2 has a shunt conductance G_1 that is obtained by the approximation:

$$G_1 = R_1 \; B_1^2 \tag{46}$$

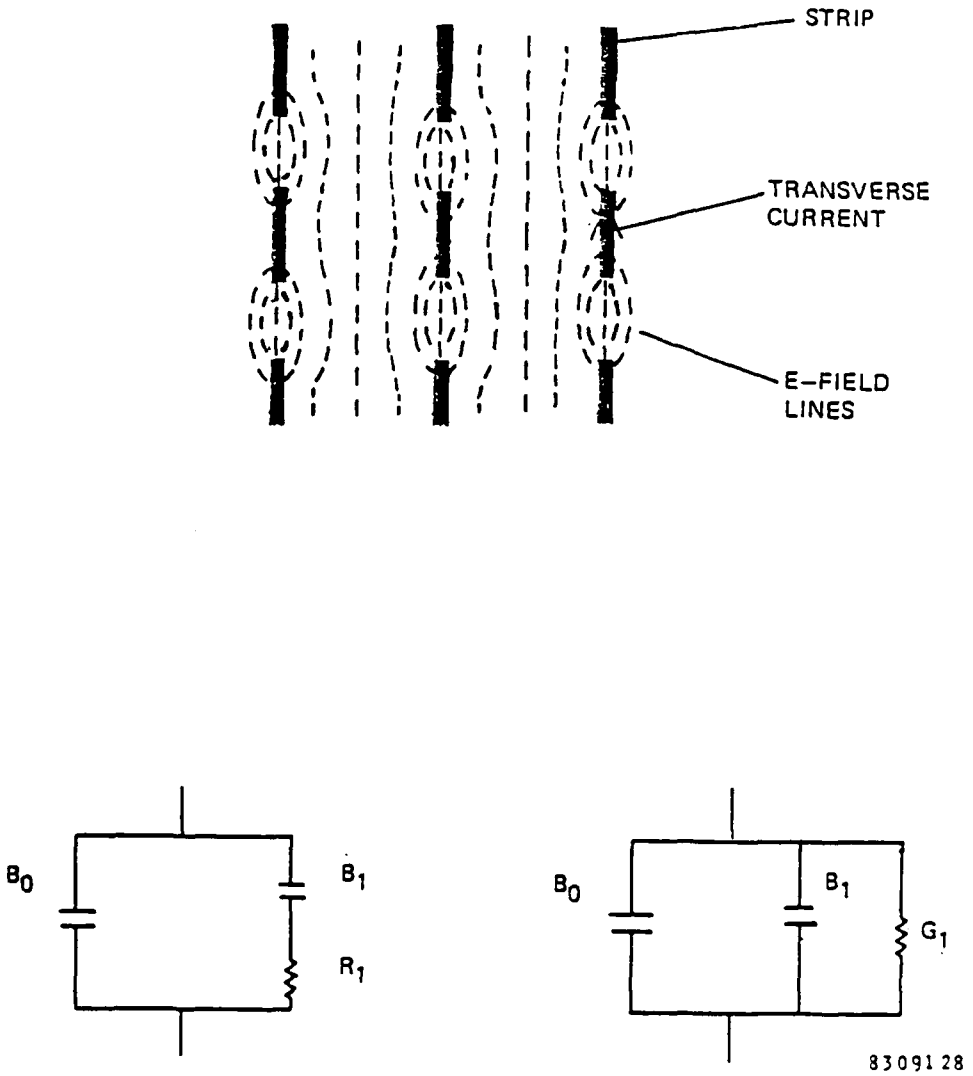

Figure 4-2. E-Field Broadside Loss Analysis

Combining (43), (44), (45) and (46) yields:

$$G_1 = \frac{8\pi^2}{3} \frac{R_s}{Z_o^2} \left(\frac{s}{\lambda}\right)^2 \left(\frac{w}{s}\right)^3 \tag{47}$$

The attenuation constant $\alpha(E,0^o)$ for E-field loss at broadside incidence is approximately:

$$\alpha(E,0^o) = \frac{\pi}{\lambda} \frac{G_1}{B_o + B_1} = \frac{\pi}{\lambda} \frac{G_1}{B_o} \tag{48}$$

where B_1 can usually be neglected because it is small compared with B_o. Combining (42), (47) and (48) this attenuation constant becomes:

$$\alpha(E,0^o) = \frac{4\pi^2}{3\lambda} \frac{R_s}{Z_o} \frac{s}{\lambda} \left(\frac{w}{s}\right)^3 \tag{49}$$

The surface resistance (R_s) can be replaced by the axial loss tangent (D) of the strip medium by using equation (40), yielding:

$$\alpha(E,0^o) = \frac{2\pi}{3\lambda} \frac{1}{D} \left(\frac{w}{s}\right)^4 \tag{50}$$

This is the approximate relation between the parameters of the strip medium and the resulting E-field loss at broadside incidence.

As an example, consider a strip medium having D = 1 and w/s = 0.2. Application of equation (50) yields an E-field broadside loss of about 0.03 dB per wavelength of medium thickness. This loss is probably small enough to be negligible in most applications. However, as w/s is increased beyond 0.2, the loss rapidly increases to a significant amount.

One of the approximations made in this analysis is that of equation (46), which is based on the assumption that R_1B_1 is much smaller than unity. For the case of D = 1 and w/s = 0.2 the value for R_1B_1 is 0.03. Therefore the approximation that the transverse current is independent of R_1 is a good one for this case. For substantially larger values of w/s this approximation is not as good. However, we are unlikely to use much larger values of w/s because the H-field loss (as well as the E-field loss) is likely to become too large, as discussed in the following paragraphs.

(b) H-Field Broadside Loss

If the magnetic field of the incident wave has a component perpendicular to the plane of a resistance strip, there will be a circulating axial current induced in the strip. Since the strip has resistance, this circulating current will cause a loss.

To determine the essential relation between this loss and the dimensions of the strip medium, an analysis is made for the case in which the circulating current is limited only by the resistance of the strip, and not by its inductance. This is equivalent to assuming that the magnetic field of the incident wave goes through the strip

unimpeded, which is a good approximation when the strip resistance is large and its width is small. This assumption is a conservative one because it yields a value for broadside loss that could be larger, but not smaller, than the actual loss.

Consider a short segment Δl of one strip, as indicated at the top of Figure 4-3. The magnetic flux Φ through a rectangular portion of the segment bounded by $\pm x$ is:

$$\Phi = \mu_o H \; 2x \; \Delta l \tag{51}$$

where H is the magnetic field strength of the incident wave, and the strip is assumed to be oriented perpendicular to the magnetic field. The magnitude of the voltage V induced around this rectangle is:

$$V = \omega\Phi = \frac{2\pi}{\lambda} \; Z_o H \; 2x \; \Delta l \tag{52}$$

The current resulting from this induced voltage is essentially a circulating axial current, as indicated at the bottom of Figure 4-3. The resistance around this loop of current for an incremental width dx is:

$$R = R_s \; \frac{2l}{dx} \tag{53}$$

The power dissipated for this incremental width is therefore:

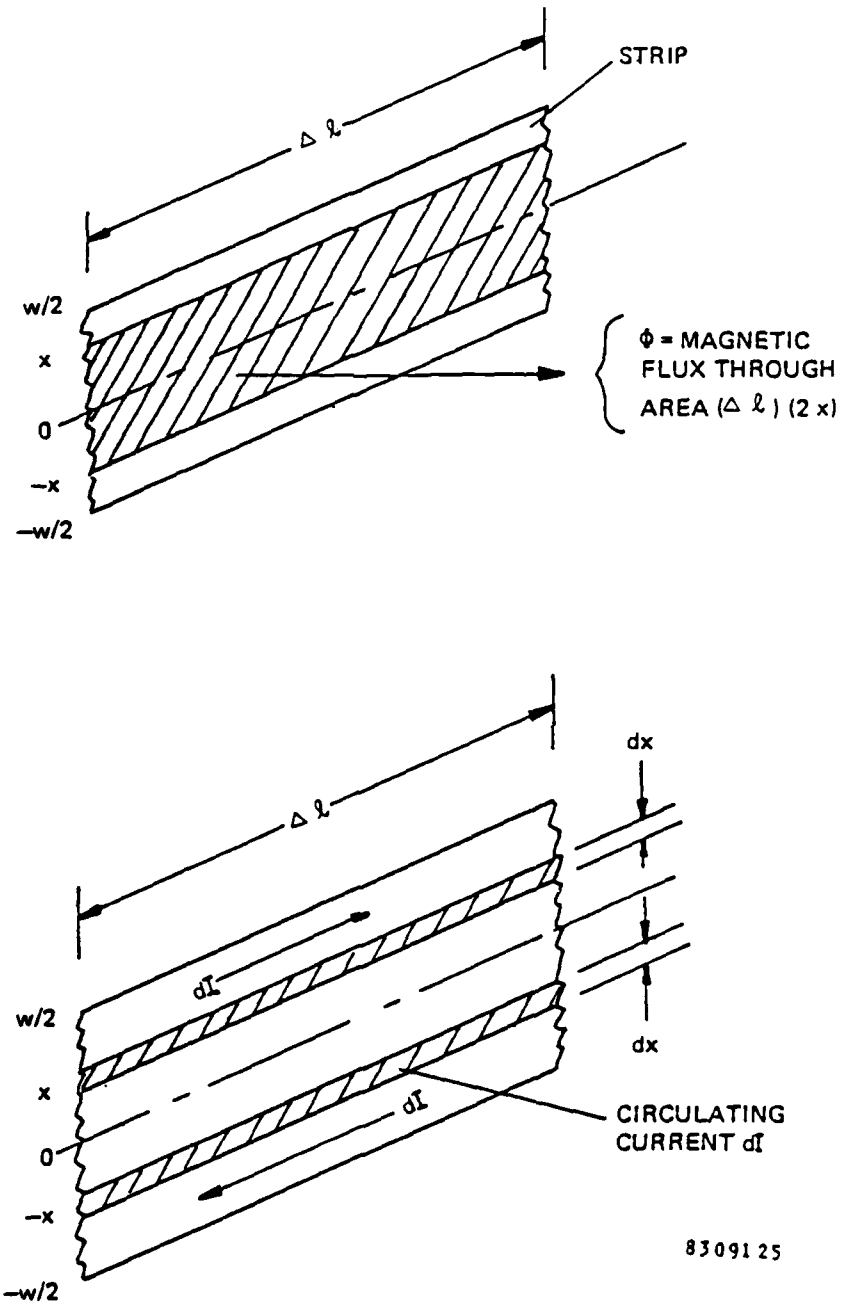

Figure 4-3. H-Field Broadside Loss Analysis

$$dP_{dis} = \frac{V^2}{R} = \frac{8\pi^2 Z_o^2 H^2 \Delta l \, x^2 \, dx}{R_s \lambda^2} \tag{54}$$

The total power dissipated for the strip segment is then:

$$P_{dis} = \int dP_{dis} = \frac{8\pi^2 Z_o^2 H^2 \Delta l}{R_s \lambda^2} \int_0^{w/2} x^2 \, dx \tag{55}$$

$$= \frac{\pi^2}{3} \frac{Z_o^2}{R_s} H^2 \frac{w^3 \Delta l}{\lambda^2}$$

The wave power P_{inc} that is incident on the broadside area alloted to this one strip in the array of strips is:

$$P_{inc} = Z_o H^2 s^2 \tag{56}$$

The ratio of P_{dis} to P_{inc} is then:

$$\frac{P_{dis}}{P_{inc}} = \frac{\pi^2}{3} \frac{Z_o}{R_s} \frac{w^3 \Delta l}{\lambda^2 s^2} \tag{57}$$

The attenuation constant $\alpha(H,0^o)$ for H-field loss at broadside incidence is approximately:

$$\alpha(H,0^{o}) = \frac{1}{2} \frac{P_{dis}}{P_{inc}} \frac{1}{\Delta l} \tag{58}$$

Combining (57) and (58), this attenuation constant becomes:

$$\alpha(H,0^{o}) = \frac{\pi^2}{6} \frac{Z_o}{R_s} \frac{w^3}{\lambda^2 s^2} \tag{59}$$

Replacing the surface resistance (R_s) by the axial loss tangent (D) of the strip medium by using equation (40) yields:

$$\alpha(H,0^{o}) = \frac{\pi^3}{3\lambda} D \left(\frac{w}{\lambda}\right)^2 \tag{60}$$

This is the approximate relation between the parameters of the strip medium and the resulting H-field loss at broadside incidence.

As an example, consider a strip medium having D = 1 and $w/\lambda = 0.04$. Application of equation (60) yields an H-field broadside loss of about 0.15 dB per wavelength of medium thickness. While this is a small loss, it is not negligible in many applications. It is therefore desirable to design and construct the strip medium of an axial-conductance angular filter so that w/λ is less than about 0.04. The example given in subsection 4.1, in which

$s/\lambda = 0.2$ and $w/s = 0.2$, corresponds to the case of $w/\lambda = 0.04$, and is thus about at the limit of strip size for small broadside loss.

An approximation made in the above analysis is that the magnetic field of the incident wave passes through the strips undiminished. This is a good approximation when the strip resistance is large enough to limit the circulating current to a small fraction of the current that would exist with perfectly-conducting strips. It is estimated that for D near unity and for an s/λ less than about 1/3 the approximation is reasonably good. For much larger values of D or s/λ the approximation would be not as good, and the actual loss would be substantially less than the value computed from equation (60). Of course, if D were infinite the actual loss would be zero while the computed value would be infinite.

(c) Summary of Broadside Losses

The two components of broadside loss, as obtained from equations (49) and (60), are shown as a function of w/s and s/λ in Figure 4-4. While these results are not accurate when w/s and s/λ are not small, they still can show useful trends. It is evident from the curves that in most cases of interest it is the H-field loss, rather than the E-field loss, that predominates. Also evident is the fairly rapid change from negligible loss to significant loss as a function of dimensions or wavelength.

The curves of Figure 4-4 are given for the case of $D = 1$. As shown in equations (49) and (60), a larger value of D would decrease the E-field loss but would increase the H-field loss, and vice-versa. It should also be mentioned

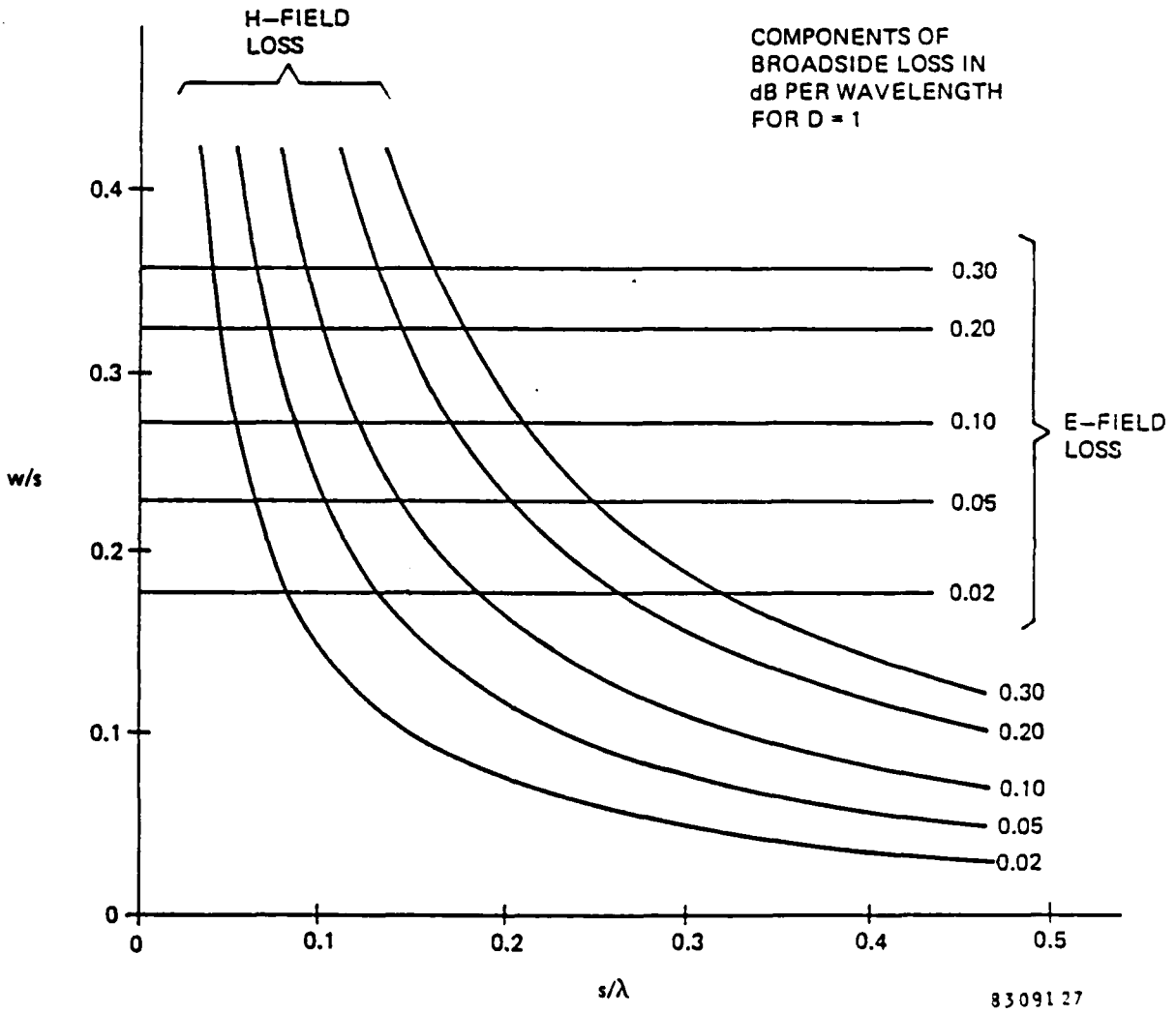

Figure 4-4. Broadside Loss Analysis Summary

that equations (50) and (60) were derived assuming that the surface resistance (R_s) is the same in the transverse and axial directions. If this is not the case, then the two different values for R_s should be used as appropriate in equations (49) and (59). For example, an unusually large transverse R_s would increase the E-field loss, while the H-field loss would remain dependent only on the axial R_s or D.

To summarize, the width of the resistance strips that comprise a practical inhomogeneous axial-conductance medium must be limited in order to limit the loss at broadside incidence. When D = 1, each of the two components of broadside loss is less than about 0.05 dB per wavelength in the medium if w/s and w/λ are less than 0.23 and 0.023 respectively. Larger values of w rapidly increase the broadside loss.

4.3 ANGULAR RESPONSE OF INHOMOGENEOUS MEDIUM

When designing the practical inhomogeneous medium, the selection of particular values for s/λ and w/s depends not only on how the broadside loss is affected, but also on how these parameters affect the angular response of the medium. Intuitively, one would expect that if s/λ is very small, the angular response of the medium would closely approximate that of the ideal homogeneous medium analyzed in Section 3. The questions is: how large can s/λ be before the angular performance deviates substantially from that of the ideal homogeneous case? Another question is: in what way does the angular performance differ from that of the ideal homogeneous medium?

In the following, an analysis is made with the objective of answering these questions. The analysis is based on a modification of the homogeneous analysis to account for the essential effect of the inhomogeneous structure. Every opportunity is taken to apply simplifying concepts and approximations in order to obtain results expeditiously. The derivation of the formulas is described in subsection (a). Results obtained from these formulas are then given in subsection (b).

(a) Formulas for Inhomogeneous Medium

The concept upon which this analysis of the inhomogeneous medium is based is that the essential effect of the inhomogeneous structure is the introduction of inductance. The axial current is no longer distributed uniformly over the transverse dimension of the medium, but instead is confined to discrete regions formed by the array of strips. The loops of magnetic field enclosing the current strips create an inductance in series with the resistance of the strips.

The first step in the analysis is to obtain a quantitative relation between the inductance and the variables that affect it. This process is complicated by the effect of the E-plane incidence angle and the attenuation that occurs in the medium. The inductance is considered to be distributed homogeneously throughout the medium so that it can be applied to the formulas previously derived for the homogeneous medium.

The inductive susceptance B_o of a single layer of closely-spaced, perfectly-conducting strips at normal incidence (Ref 15) is approximately:

$$\frac{B_o}{Y_o} = - \frac{\lambda}{s \ln\left(\frac{2s}{\pi w}\right)} \tag{61}$$

where s is the spacing between the strips and w is the strip width. Normal incidence in this case means that the incident wave is traveling in a direction perpendicular to the plane of the single layer of strips.

Now consider an infinite set of such layers having a separation s between adjacent layers. If s is much smaller than the wavelength, the layer susceptances can be assumed to add in parallel. The net inductive reactance $X_{\lambda o}$ between the opposite faces of a cube having wavelength sides is then approximately:

$$X_{\lambda o} = \frac{s}{\lambda} \frac{1}{B_o} \tag{62}$$

This relation neglects cutoff-mode interactions between layers, which is a good approximation when the

---

Ref. 15 - G.G. MacFarlane, "Surface Impedance of an Infinite Parallel-Wire Grid at Oblique Angles of of Incidence", JIEE, Vol. 93, Pt 3A, pp 1523-1527; 1946.

layer-to-layer spacing is equal to or greater than the spacing between strips in each layer. Combining (61) and (62) yields:

$$X_{\lambda o} = Z_o \left(\frac{s}{\lambda}\right)^2 \ln\left(\frac{2s}{\pi w}\right) \tag{63}$$

The above relation gives the approximate inductive reactance across a wavelength cube of the strip medium for a wave at normal incidence to the layers.

For a wave incident at an oblique angle in the E plane of incidence, the relation becomes more complicated. For convenience, the angle θ_E is defined as the angle of incidence relative to the plane of a layer of strips; it is the complement of θ, the latter having been defined relative to the input face of the angular filter. The inductive susceptance $B(\theta_E)$ of a single layer of closely-spaced perfectly-conducting strips for an incidence angle θ_E is the E plane of incidence is approximately:

$$\frac{B(\theta_E)}{Y_{space}(\theta_E)} = \frac{B_o}{Y_o} \frac{\cos \theta_E}{1 - \frac{1}{e} \sin^2 \theta_E} \tag{64}$$

where the parameter e is the excess capacitance ratio of a general strip configuration relative to a simple strip. For simple straight strips in free space, the parameter e is unity. For other configurations e may be larger than unity, corresponding to strips having excess capacitance per unit

length (without a corresponding decrease in inductance per unit length). An example of this is a crossed-wire grid in which e = 2 because it has twice the surface area (Ref. 16, 10). Formula (64) is given here without proof, but can be inferred from Reference 16, or can be derived from a transmission-line viewpoint of a conducting grid.

Now the inductive reactance X_λ across a wavelength cube of the strip medium can be obtained from (64) by the same process as before, yielding:

$$X_\lambda(\theta_E) = Z_{space} \left(\frac{s}{\lambda}\right)^2 \ln\left(\frac{2s}{\pi w}\right) \frac{1 - \frac{1}{e}\sin^2\theta_E}{\cos\theta_E} \qquad (65)$$

Recalling that for E-plane incidence $Z_{space} = Z_o \cos\theta_E$ this becomes:

$$X_\lambda(\theta_E) = Z_o \left(\frac{s}{\lambda}\right)^2 \ln\left(\frac{2s}{\pi w}\right) \left[1 - \frac{1}{e}\sin^2\theta_E\right] \qquad (66)$$

Ref. 16- M.I.Kontorovich, V. Yu Pretun'kin, N.A.Yesepkina, M.I. Astrakhan, "The Coefficient of Reflection of a Plane Electromagnetic Wave from a Plane Wire Mesh", Radio Engineering and Electronic Physics (USSR), Vol. 7, No. 2, pp 222-231; February 1962.

This gives the inductive reactance in ohms across a wavelength cube of the strip medium for any incidence angle (θ_E) in the E plane of incidence.

The axial-conductance medium attenuates the wave that travels through it. Therefore θ_E is not a real angle but becomes a complex number for this medium. Formula (66) must therefore be appropriately generalized so that it applies within the attenuating medium. This is done by assuming the following relation between sin θ_E and k_z:

$$\sin \theta_E = \frac{k_z}{k} \tag{67}$$

where $k = 2\pi/\lambda$. Inserting (67) into (66) gives:

$$X_\lambda(k_z) = Z_o \left(\frac{s}{\lambda}\right)^2 \ln\left(\frac{2s}{\pi w}\right) \left[1 - \frac{1}{e}\left(\frac{k_z}{k}\right)^2\right] \tag{68}$$

The derivation that yielded (64) indicates that this substitution provides a valid result for an attenuating medium, as well as for a lossless medium. For convenience, the first few factors in (68) can be replaced by the reactance $X_{\lambda o}$ as given in (63):

$$X_\lambda(k_z) = X_{\lambda o} \left[1 - \frac{1}{e}\left(\frac{k_z}{k}\right)^2\right] \tag{69}$$

Since k_z is in general complex, the reactance X_λ is also likely to be a complex quantity. This can be seen by writing k_z^2 in terms of β and α:

$$k_z^2 = \beta^2 - \alpha^2 - 2j\beta\alpha \tag{70}$$

Inserting (70) into (69) gives:

$$X_\lambda(\alpha,\beta) = X_{\lambda o}\left[1 - \frac{1}{e}\frac{\beta^2 - \alpha^2}{k^2} + j\frac{1}{e}\frac{2\beta\alpha}{k^2}\right] \tag{71}$$

This is the complex reactance across a wavelength cube of the strip medium, as a function of β and α in the medium.

The total impedance $Z_{1\lambda}$ across a wavelength cube of the strip medium is the series combination of this complex reactance with the resistance of the strip medium across a wavelength cube; the latter is designated R_λ and was given in formula (38). Thus:

$$Z_{1\lambda} = R_\lambda + jX_\lambda \tag{72}$$

Combining (71) and (72) gives:

$$Z_{1\lambda}(\alpha,\beta) = R_\lambda - X_{\lambda o}\frac{1}{e}\frac{2\beta\alpha}{k^2} + jX_{\lambda o}\left[1 - \frac{1}{e}\frac{\beta^2 - \alpha^2}{k^2}\right] \tag{73}$$

The real and imaginary parts of $Z_{1\lambda}$ are separated into a new resistance $R_{1\lambda}$ and a new reactance $X_{1\lambda}$ giving:

$$R_{1\lambda}(\alpha,\beta) = R_\lambda \left[1 - \frac{x_o}{e} \frac{2\beta\alpha}{k^2} \right] \tag{74}$$

$$X_{1\lambda}(\alpha,\beta) = R_\lambda \, x_o \left[1 - \frac{1}{e} \frac{\beta^2 - \alpha^2}{k^2} \right]$$

where the parameter x_o is defined as:

$$x_o = \frac{X_{\lambda o}}{R_\lambda} = 2\pi D \left(\frac{s}{\lambda}\right)^2 \ln\left(\frac{2s}{\pi w}\right) \tag{75}$$

as obtained from (63) and (38).

An equivalent circuit for the axial parameters of the inhomogeneous medium can be described, as shown in Figure 4-5(A). It comprises the series combination of the axial resistance and axial inductive reactance, in parallel with the axial capacitive susceptance of the dielectric material (or of free space if there is no such material). Each of the three elements is assumed to be distributed uniformly throughout the medium, which is an approximation that is reasonable when the spacing s is small compared with the wavelength in the dielectric.

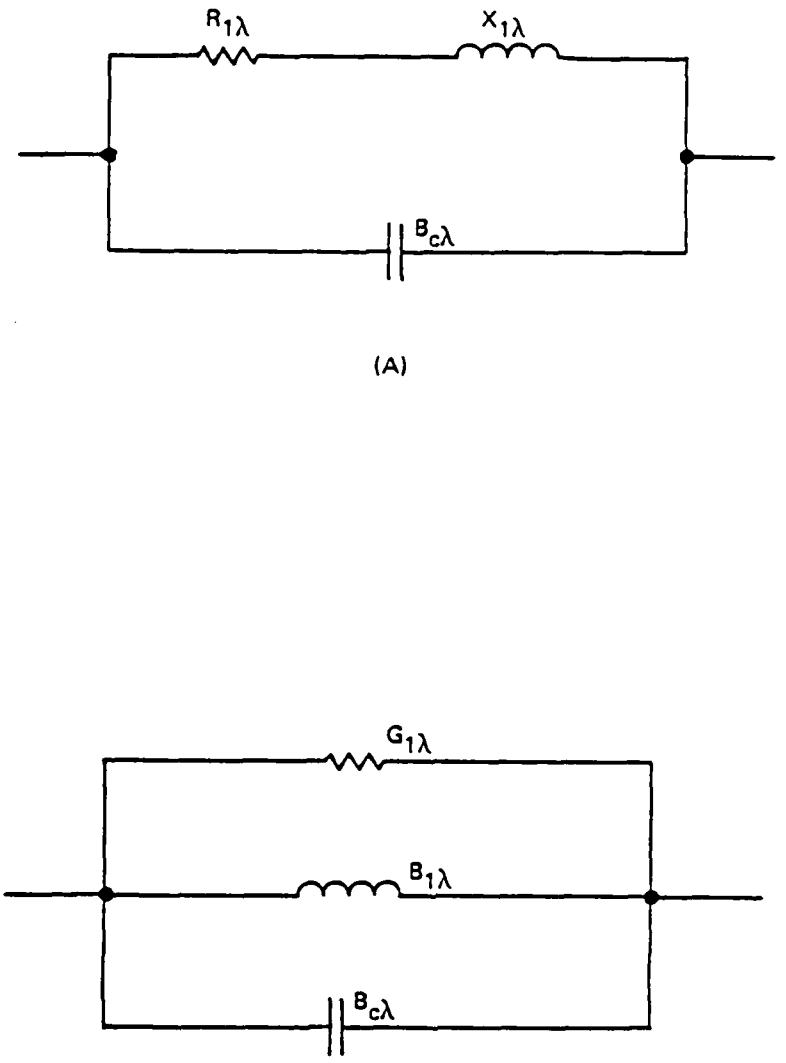

Figure 4-5. Equivalent Circuits for Axial Parameters of Inhomogeneous Medium

The equivalent circuit can be transposed into an all-parallel circuit, as shown in Figure 4-5(b). The shunt inductive susceptance $B_{1\lambda}$ becomes:

$$B_{1\lambda}(\alpha,\beta) = \frac{-1}{R_{1\lambda}} \cdot \frac{x_1}{1 + x_1^2} \tag{76}$$

where the parameter x_1 is defined as:

$$x_1(\alpha,\beta) = \frac{X_{1\lambda}}{R_{1\lambda}} \tag{77}$$

From (74), the parameter x_1 equals:

$$x_1(\alpha,\beta) = x_o \frac{1 - \frac{1}{e}\frac{\beta^2 - \alpha^2}{k^2}}{1 - \frac{x_o}{e}\frac{2\beta\alpha}{k^2}} \tag{78}$$

The shunt inductive susceptance $B_{1\lambda}$ in mhos can be written in terms of D by combining (76), (74) and (38):

$$B_{1\lambda}(\alpha,\beta) = \frac{-D}{60\left[1 - \frac{x_o}{e}\frac{2\beta\alpha}{k^2}\right]} \cdot \frac{x_1}{1 + x_1^2} \tag{79}$$

In the equivalent circuit of Figure 4-5, the axial capacitive susceptance $B_{c\lambda}$ is the susceptance across a wavelength cube of the dielectric material in the axial direction. This susceptance in mhos is:

$$B_{c\lambda} = \frac{\varepsilon'_{ax}}{60} \tag{80}$$

The inductive susceptance $B_{l\lambda}$ can be added to the capacitive susceptance $B_{c\lambda}$ to obtain the net susceptance. An <u>effective</u> axial dielectric constant can be defined as:

$$\varepsilon'_{lax}(\alpha,\beta) = \frac{\text{net susceptance}}{\text{space susceptance}} = \frac{B_{c\lambda} + B_{l\lambda}}{\frac{1}{60}} \tag{81}$$

where all susceptances are defined across a wavelength cube. Combining (79), (80) and (81), this effective axial dielectric constant becomes:

$$\varepsilon'_{lax}(\alpha,\beta) = \varepsilon'_{ax} - \frac{D\, x_1}{\left[1 + x_1^2\right]\left[1 - \frac{x_o}{e}\frac{2\beta\alpha}{k^2}\right]} \tag{82}$$

It is seen that when x_1 is greater than zero, the effective axial dielectric constant is reduced. This is consistent with the familiar result that a medium comprising conducting rods or strips can be a phase-advance medium for the case of a wave with electric field parallel to the rods.

In the transposed equivalent circuit of Figure 4-5(b), the shunt conductance $G_{1\lambda}$ becomes:

$$G_{1\lambda}(\alpha, \beta) = \frac{1}{R_{1\lambda}} \frac{1}{1 + x_1^2} \tag{83}$$

By analogy to (38), an <u>effective</u> axial loss tangent D_1 can be defined as:

$$D_1 = 60\, G_{1\lambda} \tag{84}$$

Combining (84) with (83) and (74) yields:

$$D_1(\alpha, \beta) = \frac{D}{\left[1 + x_1^2\right]\left[1 - \frac{x_o}{e}\frac{2\beta\alpha}{k^2}\right]} \tag{85}$$

The above analysis has derived relationships for the effective axial dielectric constant ε'_{1ax} and the effective axial loss tangent D_1 for an inhomogeneous axial-conductance medium comprising closely-spaced resistance strips. Now these two parameters can be substituted for the original ones (ε'_{ax} and D) in equation (28). This substitution yields:

$$k_z^2 = \left(\frac{2\pi}{\lambda}\right)^2 \varepsilon'_{tr}\left[1 - \frac{\sin^2\theta}{\varepsilon'_{1ax} - jD_1}\right] \tag{86}$$

An alternate form of (86) is more convenient:

$$\left(\frac{k_z}{k}\right)^2 = \varepsilon'_{tr}\left[1 - \frac{\frac{\sin^2\theta}{\varepsilon'_{1ax}}\left(1 + j\,\frac{D_1}{\varepsilon'_{1ax}}\right)}{1 + \left(\frac{D_1}{\varepsilon'_{1ax}}\right)^2}\right] \tag{87}$$

Separating (87) into real and imaginary components by (70) yields:

$$\frac{\beta^2 - \alpha^2}{k^2} = \varepsilon'_{tr} - \frac{\varepsilon'_{tr}\,\frac{\sin^2\theta}{\varepsilon'_{1ax}}}{1 + \left(\frac{D_1}{\varepsilon'_{1ax}}\right)^2} \tag{88}$$

$$\frac{2\beta\alpha}{k^2} = \varepsilon'_{tr}\,\frac{\frac{D_1}{\varepsilon'_{1ax}}\,\frac{\sin^2\theta}{\varepsilon'_{1ax}}}{1 + \left(\frac{D_1}{\varepsilon'_{1ax}}\right)^2} \tag{89}$$

We now have five equations (78, 82, 85, 88, 89) with five unknowns (x_1, ε'_{1ax}, D_1, α, β). When values are specified for the medium parameters D, x_o, e, ε'_{tr} and ε'_{ax}, and for the variable θ , these five equations can be solved for the five unknowns. A computer has been programmed to do this, and to plot the resulting α and β as a function of θ.

(b) Angular Response Computed Results

In the graphs to be presented, a set of three curves is shown for each case examined. One curve represents the nominal frequency f_o. Another curve is for a frequency $f = 0.7\ f_o$, and another curve is for $f = 1.4\ f_o$. Thus an octave band is covered by the three curves.

Two of the medium parameters vary with frequency. One of these is D which is inversely proportional to frequency. The other is x_o (see equation 75) which is proportional to frequency. On each graph their values at midband are stated. All of the other medium parameters (e, ε'_{tr} and ε'_{ax}) are assumed to be invariant with frequency.

Examples for D = 1, increasing x_o. The first example given is for $x_o = 0$, which is the homogeneous case. Figure 4-6 shows the attenuation (in dB per wavelength) and the normalized phase constant versus θ for the three frequencies. The results are consistent with those given in Section 3.

The second example is for $x_o = 0.5$, which represents a slightly inhomogeneous medium. Figure 4-7 shows the results for this case. It is seen that the computer has plotted two groups of curves for the phase constant. One group is labeled "A" and the other "B". The A group corresponds to the single group of attenuation curves that are shown. The two groups of phase-constant curves correspond to two different roots of the equations as solved by the computer. Sudden jumps in some of the curves should be disregarded; the computer sometimes jumps from one root to another, or it sometimes fails to find a root.

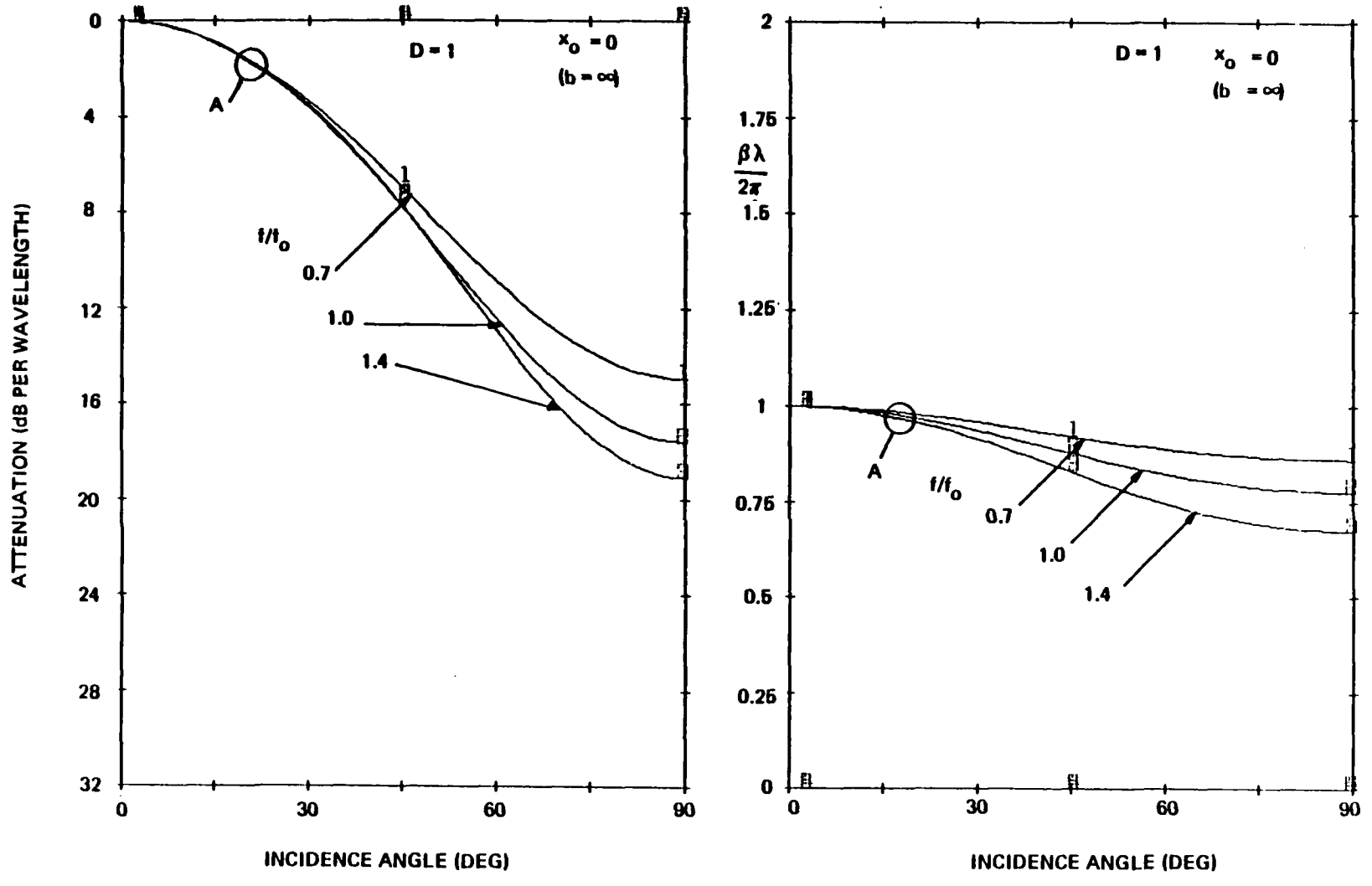

Figure 4-6. Angular Response for D = 1, x_o = 0

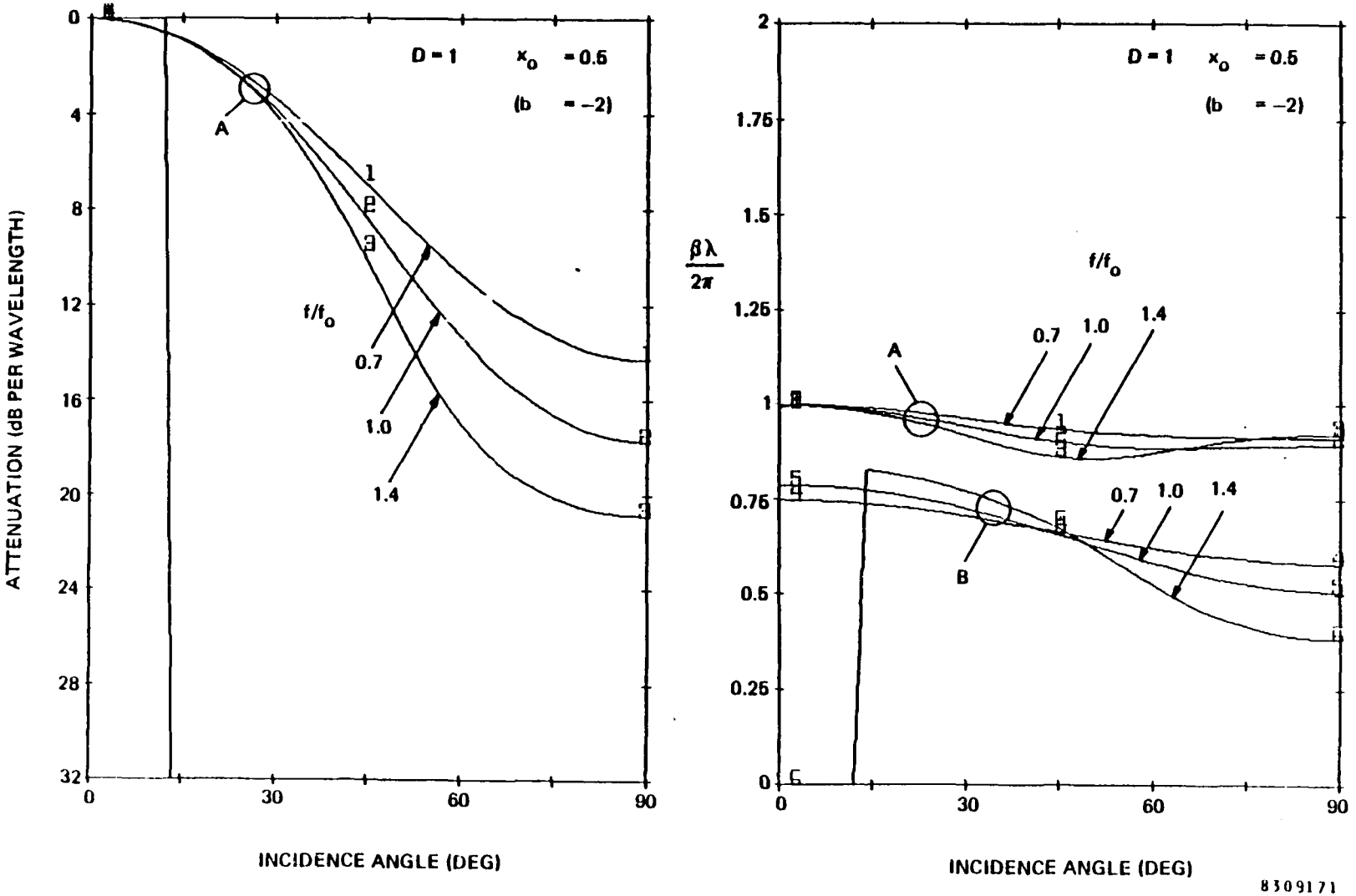

Figure 4-7. Angular Response for D = 1, x_o = 0.5

The third example is for $x_o = 1.0$, which represents a more inhomogeneous medium. Figure 4-8 shows this case. In addition to the two groups of phase-constant curves, there is also seen one new attenuation curve in the B group for the high frequency. This curve has a finite (non-zero) attenuation at $\theta = 0$ (the discontinuity at $\theta = 0$ should be disregarded).

The fourth example is for $x_o = 2.0$, and is given in Figure 4-9. Two attenuation curves in the B group are seen; the attenuation at $\theta = 0$ is less than with the previous example. The A curves show substantially reduced attenuation at large angles.

Explanation of Results. The existence of two solutions for the propagation equations indicates that two wave modes can exist in the inhomogeneous medium. The two waves have quite different characteristics, as shown by the results given above. The wave designed "A" always has zero attenuation at $\theta = 0$ while the wave designated "B" appears to have a non-zero attenuation at $\theta = 0$. For the cases presented above, the B wave has a smaller β and is therefore a relatively fast wave. The B wave appears to have a relatively steep increase of attenuation beyond a certain angle.

Consideration of the actual inhomogeneous medium indicates that the existence of two different waves within the medium is not unreasonable. This is more easily visualized if the strips are assumed to be perfect conductors. One type of wave that might be expected with perfectly-conducting axial strips or wires would be a wave

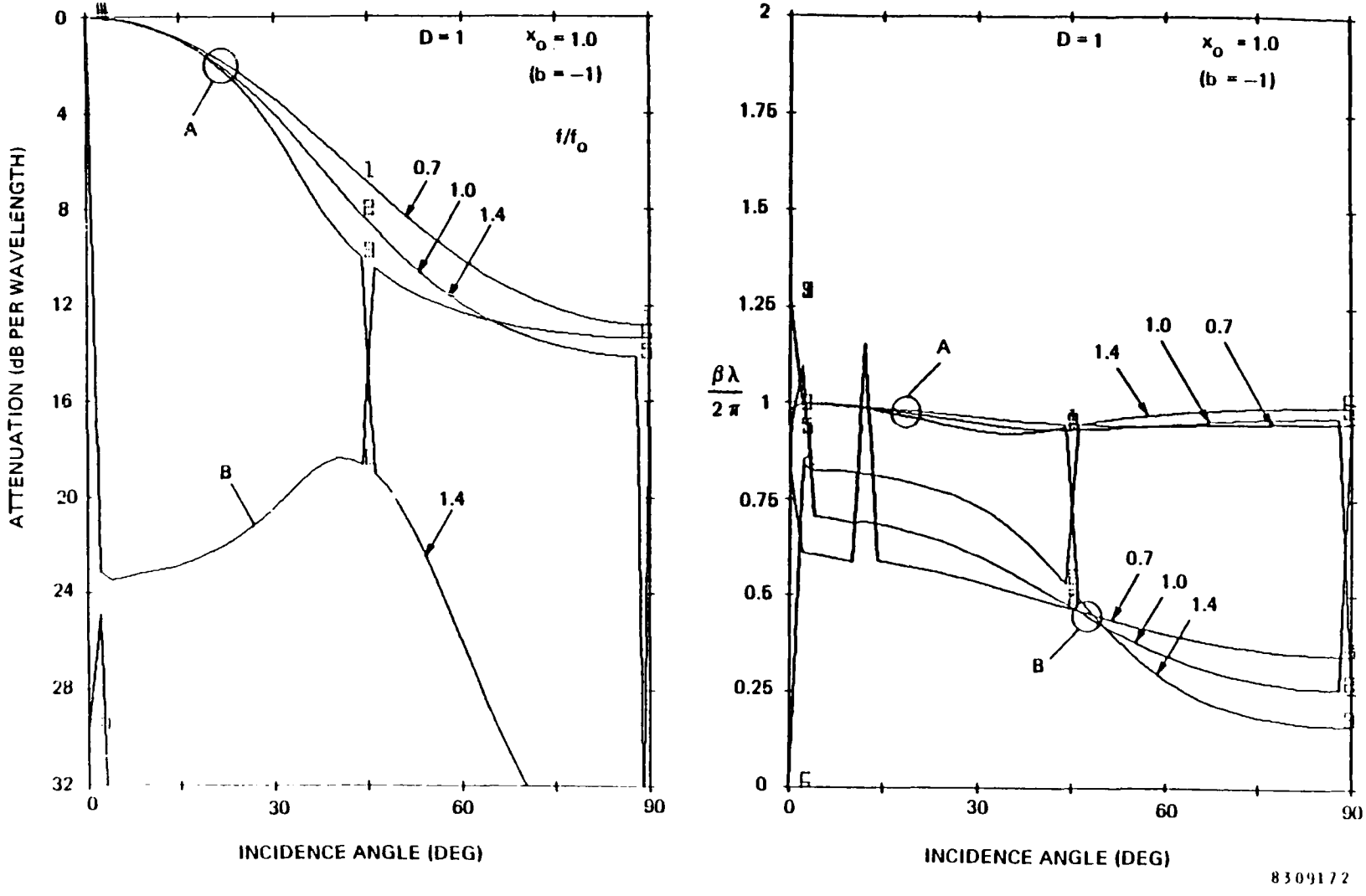

Figure 4-8. Angular Response for D = 1, x_o = 1.0

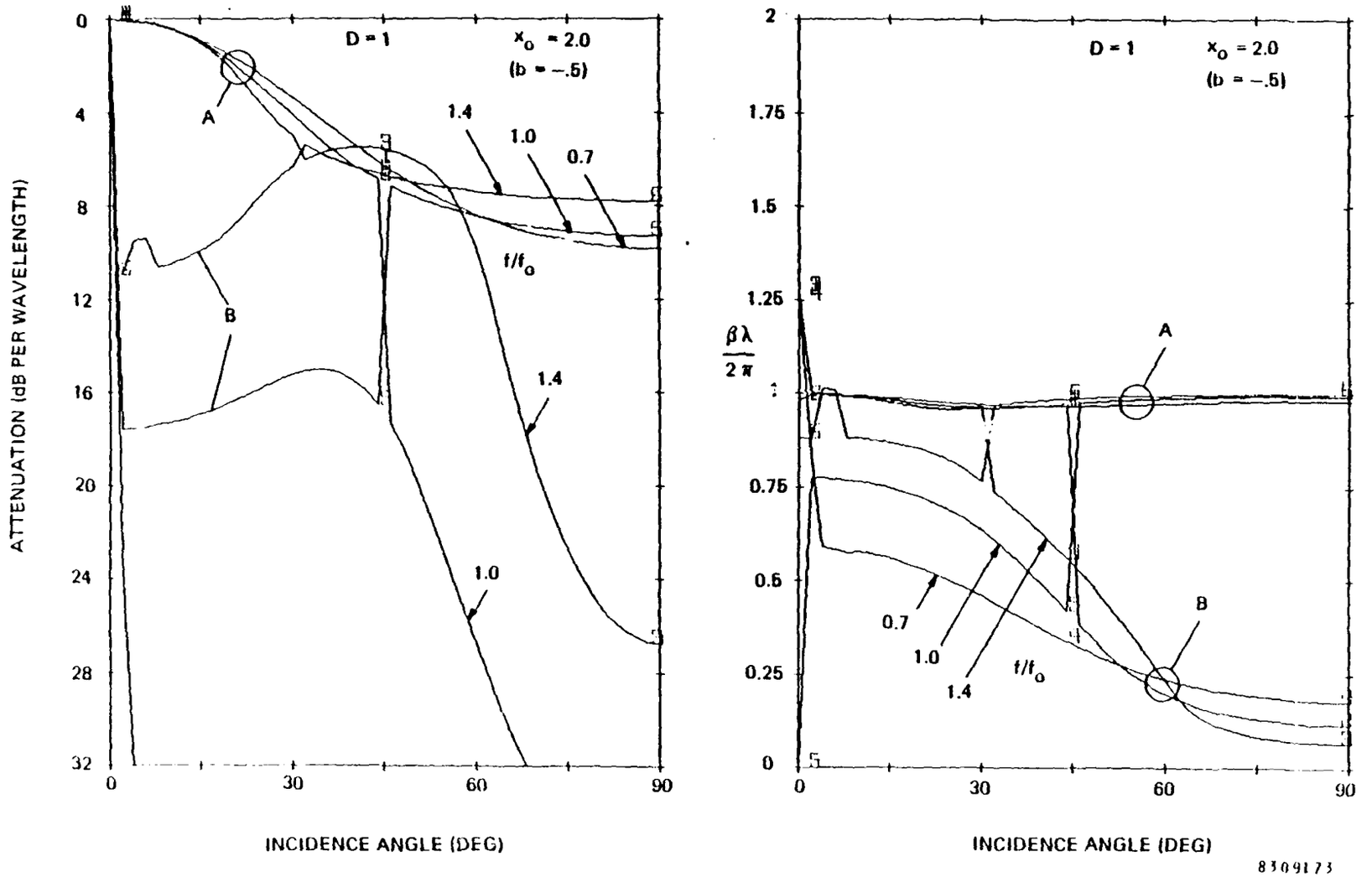

Figure 4-9. Angular Response for D = 1, x_o = 2.0

AD-A142 802 AXIAL-CONDUCTANCES ANGULAR FILTER INVESTIGATION(U) 2/3
HAZELTINE CORP GREENLAWN NY P W HANNAN ET AL. APR 84
6519 RADC-TR-84-80 F19628-81-C-0067

UNCLASSIFIED F/G 9/5 NL

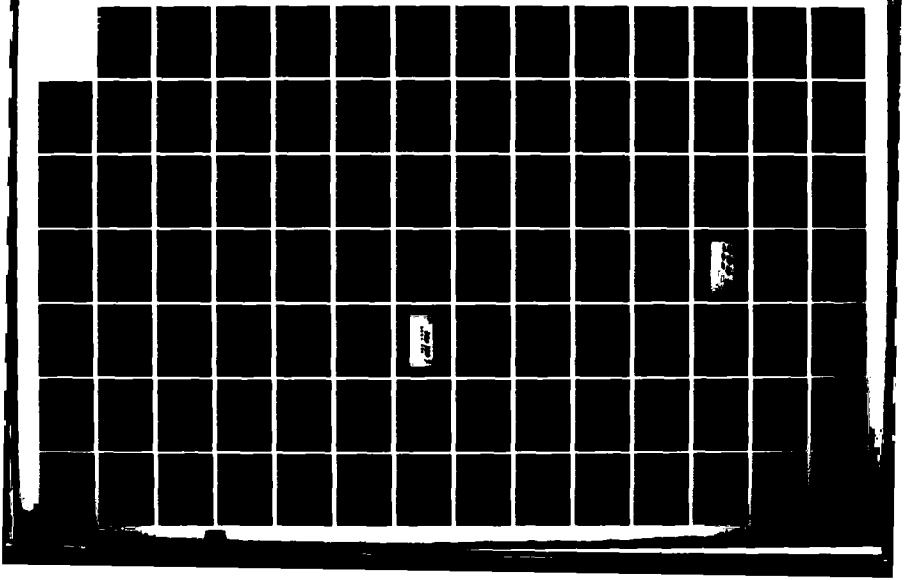

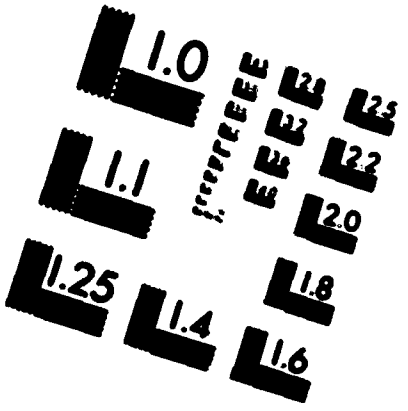

MICROCOPY RESOLUTION TEST CHART
NATIONAL BUREAU OF STANDARDS 1963-A

that is constrained to propagate in the axial direction. This wave would tend to have only transverse electric field.

Another type of wave that might be expected with perfectly conducting strips is one that tends to propagate nearly perpendicular to the strips and to have electric field nearly parallel to the strips. This type of wave should see the conducting strips as a phase-advance medium for propagation in the transverse direction. A cutoff effect, related to the cutoff that occurs in rectangular waveguide, might be expected for such a wave.

To consider further differences between the two waves, some special cases are examined. In this examination, it is convenient to define a parameter b for the inhomogeneous medium as follows:

$$b = \frac{-D}{x_o} = \frac{-60}{X_{\lambda o}} \qquad (90)$$

$$= \frac{-1}{2\pi \left(\frac{s}{\lambda}\right)^2 \ln\left(\frac{2s}{\pi w}\right)}$$

This parameter is simply the inductive susceptance across a wavelength cube of the perfectly-conducting strip medium for a wave at normal incidence to the strip layers, relative to the capacitive susceptance across a wavelength cube of free space. The parameter b is a negative number. The special cases to be examined are given below.

$D = \infty$, $\epsilon'_{tr} = \epsilon'_{ax} = e = 1$. This is the case of a medium comprising simple perfectly-conducting strips in free space. When $D = \infty$ the parameter x_o also becomes infinite but the ratio b remains finite. These quantities have been substituted into equations (78), (82), (85), (88) and (89), yielding the following equation if α is assumed to be zero:

$$2\left(\frac{\beta}{k}\right)^2 = 2 + b - \sin^2\theta \pm (\sin^2\theta - b) \tag{91}$$

When the plus sign is used, (91) yields:

$$\frac{\beta}{k} = 1 \tag{92}$$

This is the A-wave solution, and corresponds to a wave having free-space velocity in the axial direction, independent of the incidence angle θ . Such a wave can be considered totally constrained by the axial medium.

When the minus sign is used, (91) yields:

$$\frac{\beta}{k} = (b + \cos^2\theta)^{1/2} \tag{93}$$

This is the B-wave solution, and corresponds to a wave having greater than free-space velocity in the axial direction, dependent on both b and θ. This wave has a cutoff angle of incidence θ_c above which there is no

propagation in the medium, and β becomes α in (93). The cutoff angle is:

$$\theta_c = \text{arc cos } (-b)^{1/2} \tag{94}$$

When $\theta = 90°$ the medium is cutoff with only an infinitesimal value for b. When $\theta = 0$, the critical (cutoff) value for b is -1. This is reasonable because when b = -1 the inductive susceptance of the conducting-strip medium becomes equal to the capacitive susceptance of free space, and the capacitance is completely tuned out by the inductance. This result for $\theta = 0$ agrees exactly with Brown's result (Ref. 17) for rodded media when s is small compared with the wavelength and when the standard substitution of w/2 for rod diameter is made. Note, however, that in Brown's case the wave is incident onto the <u>side</u> of the conducting rods, but in our case the wave is incident onto the <u>ends</u> of the conducting rods or strips.

Computed results for the B wave when the conductance of the stripe is high are shown in Figure 4-10. Here D = 10 and $x_o = 20$, corresponding to b = -0.5 at midband. From equation (94) this yields a cutoff angle θ_c of 45°. The midband curve in the figure clearly indicates such a cutoff. At $f = 1.4\ f_o$ the value of b becomes -0.25 yielding

---

Ref. 17 - J. Brown, "Artificial Dielectrics Having Refractive Indices Less Than Unity", Proc. IEEE, Vol. 100, Pt 4, pp 51-62; 1953.

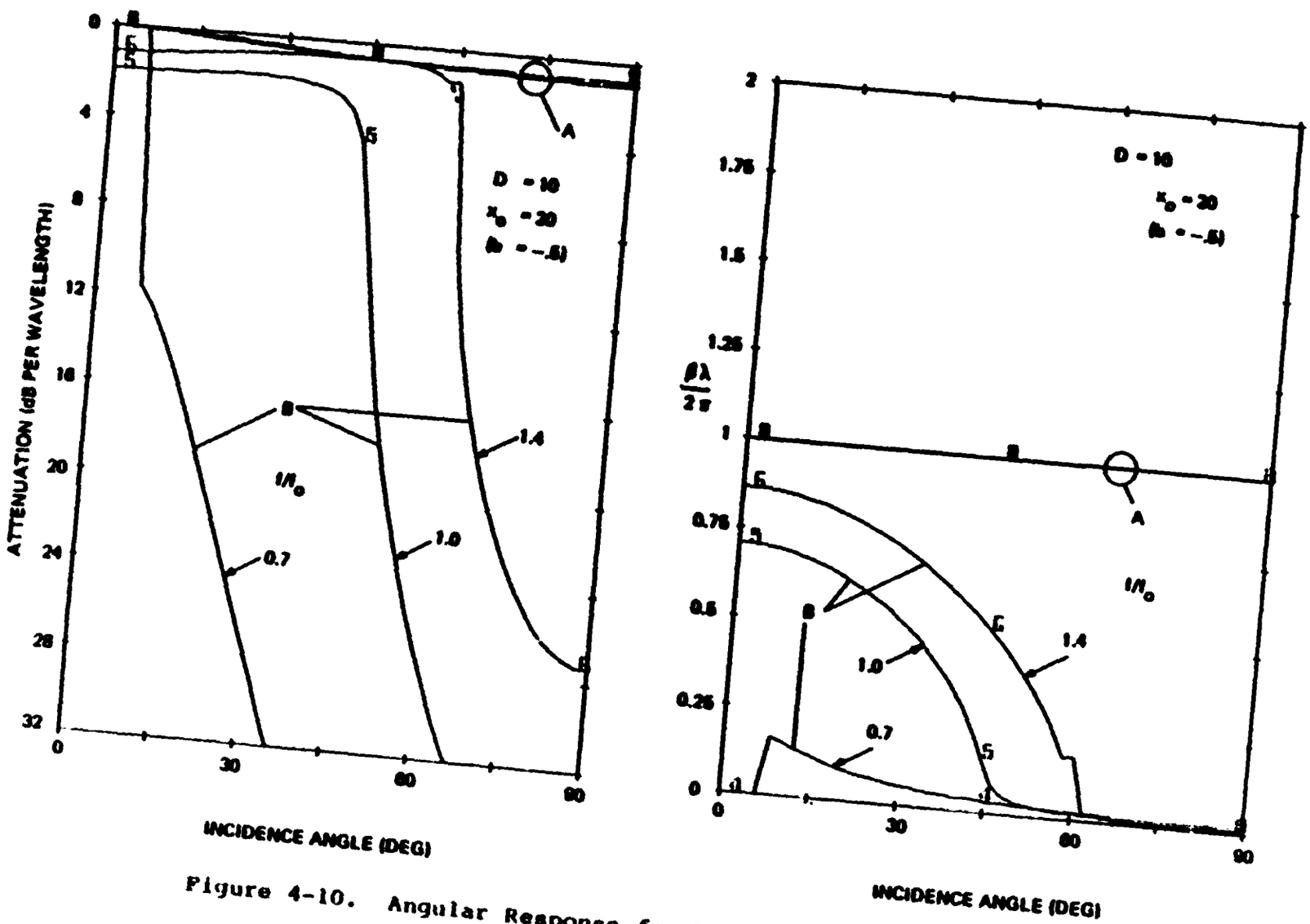

Figure 4-10. Angular Response for D = 10, x_o = 20

a θ_c of 60°. Again, this is quite evident in the figure. At $f = 0.7\ f_o$ the value of b is -1 yielding a ϑ_c of 0°; a hint of this also appears in the incompletely computed curve of the figure.

A comparison of Figure 4-10 (high conductance) with the previous figures (moderate conductance) can be made. In Figure 4-9, for example, the b values are the same as those in Figure 4-10, so the "cutoff" angles are the same. Clearly, the steep attenuation increases seen in the B-wave curves of Figure 4-9 are caused by the cutoff effect shown in Figure 4-10. However, the curves in Figure 4-9 have a much more rounded cutoff because there is substantial dissipative loss present.

Another item of interest in the B-wave attenuation curves of Figures 4-8 and 4-9 is the non-zero attenuation at $\theta = 0$. To quantify this property, another special case is examined in the following paragraphs.

$\underline{\theta \to 0,\ \epsilon'_{tr} = \epsilon'_{ax} = 1.}$ When the incidence angle approaches zero (broadside incidence) the set of equations (78), (82), (85), (88) and (89) can be solved by approximation techniques without resorting to a computer. Two solutions are obtained, corresponding to the two types of waves. One solution is:

$$\frac{\beta(o)}{k} = 1 \tag{95}$$

$$\frac{2\alpha(o)}{k} = \frac{D\left[1 + x_o^2\left(1 - \frac{1}{e}\right)^2\right]\theta^2}{D^2 + \left[1 - Dx_o\left(1 - \frac{1}{e}\right) + x_o^2\left(1 - \frac{1}{e}\right)^2\right]^2} \tag{96}$$

This solution corresponds to the A wave, which always has zero attenuation at $\theta = 0$. Although equation (96) has some interesting features, it will not be examined further at this point.

The other solution is:

$$\frac{2\alpha^2(o)}{ek^2} = \left[(1 + b)^2 + \left(\frac{b}{D}\right)^2\right]^{1/2} - (1 + b) \qquad (97)$$

$$\frac{2\beta^2(o)}{ek^2} = \left[(1 + b)^2 + \left(\frac{b}{D}\right)^2\right]^{1/2} + (1 + b) \qquad (98)$$

This solution corresponds to the B wave. Examination of (97) shows that when b is more negative than -1 (which corresponds to the "cutoff" condition) the attenuation can be large. However, even when b is between 0 and -1 (not "cutoff") the attenuation does not become zero unless D becomes infinite. Values of b and D corresponding to those used in Figures 4-8 and 4-9 yield attenuation values corresponding to those given in the figures at θ approaching zero. In the case of Figure 4-7, equation (47) yields an attenuation greater than the 32 dB per wavelength limit of the graph.

The results given above have clearly established that the <u>B wave has a non-zero attenuation for θ approaching zero</u>. However, simple physical reasoning tells us that an angular filter containing only thin axially-oriented elements should have essentially no attenuation at

broadside incidence. It therefore must be concluded that the B wave is not excited at broadside incidence.

Discussion of Two Waves The analysis presented in this report is based on a representation of the actual inhomogeneous medium by a fictitious homogeneous medium. This approach has yielded the interesting result that there are two different waves that can exist in the inhomogeneous medium when a wave is incident at the "open-end" face of the medium. However, the analysis does not determine the relative amplitude or phase in which the two waves are excited at the input face.

In general, (except at broadside) both waves should be excited at the input face. The two waves typically have different phase constants as well as different attenuation rates, and therefore would be expected to yield a complex and ripply type of decay for the net field as a function of the axial coordinate. Ultimately, at a large axial distance, the wave having the smaller α will predominate. To simplify the situation, then, we can investigate primarily the wave having the smaller α.

Near broadside incidence, the A wave always has a small attenuation, but the B wave typically has a large attenuation. Therefore, near broadside incidence the A wave is typically of most interest.

At larger incidence angles it is possible for the B wave to have less attenuation than the A wave; an example of this is seen in Figure 4-9. This example, however, is one in which x_o is greater than unity, ie, the inductive reactance is greater than the resistance of the strips. This occurs only when the strip spacing (s) is not small

compared with the wavelength, or when the strip width (w) is extremely small compared with the spacing, or when the resistance is unusually small. It should be possible to design the medium so that none of these conditions occurs, thereby avoiding a predominant B wave.

Examples for D = 2, increasing x_o. Figures 4-11 through 4-15 show the attenuation and phase constant versus θ for various x_o values when D = 2. The results are similar to those previously given for D = 1 if the parameter b (rather than x_o) is used for correlation of the two examples. The D = 2 cases yield smaller values of attenuation than did the D = 1 cases, for both the A wave and the B wave.

Examples for D = 0.5, increasing x_o. Figures 4-16 through 4-19 show the attenuation and phase constant versus θ for various x_o values when D = 0.5. These results differ markedly from the previous ones. For x_o = 0.5 (Figure 4-17) the A-wave attenuation at large incidence angles is now greater than it is for x_o = 0 (Figure 4-16). For x_o = 1.0 (Figure 4-18) the curves for midband frequency exhibit a more unusual behavior. The A-wave and B-wave curves meet at about $\theta = 45°$ and appear to have a discontinuity of slope at this junction. This occurs for both the attenuation and the phase-constant curves. A similar phenomenon appears to occur for x_o = 2.0 (Figure 4-19) at about $\theta = 30°$.

Inspection of the phase-constant curves in Figures 4-18 and 4-19 reveals another unusual result. In the previous examples (D = 1, 2) the B wave always had lesser values for β (ie, faster axial phase velocity) than did the A wave. However, in Figure 4-18 a change occurs. At

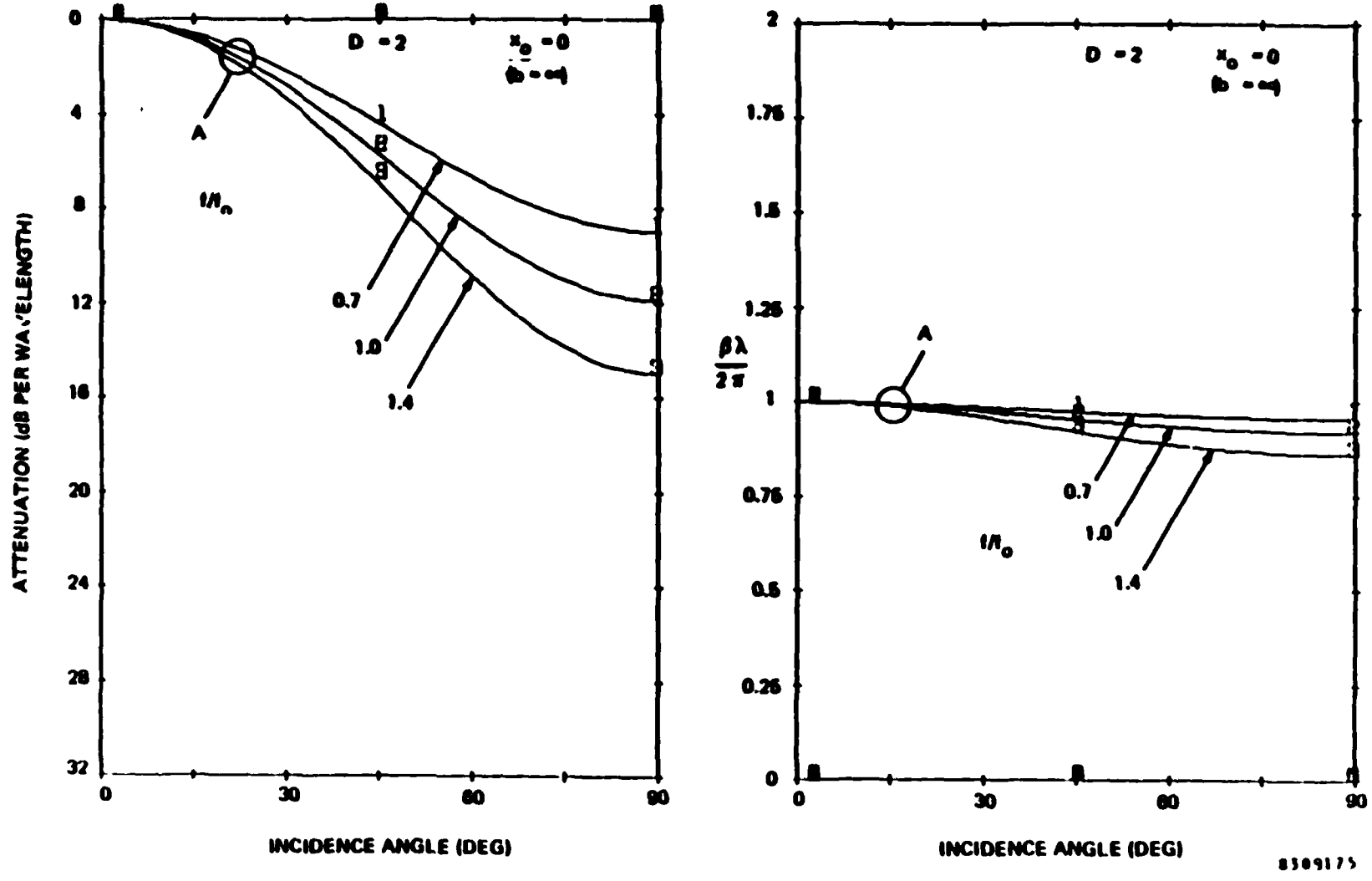

Figure 4-11. Angular Response for D = 2, x_o = 0

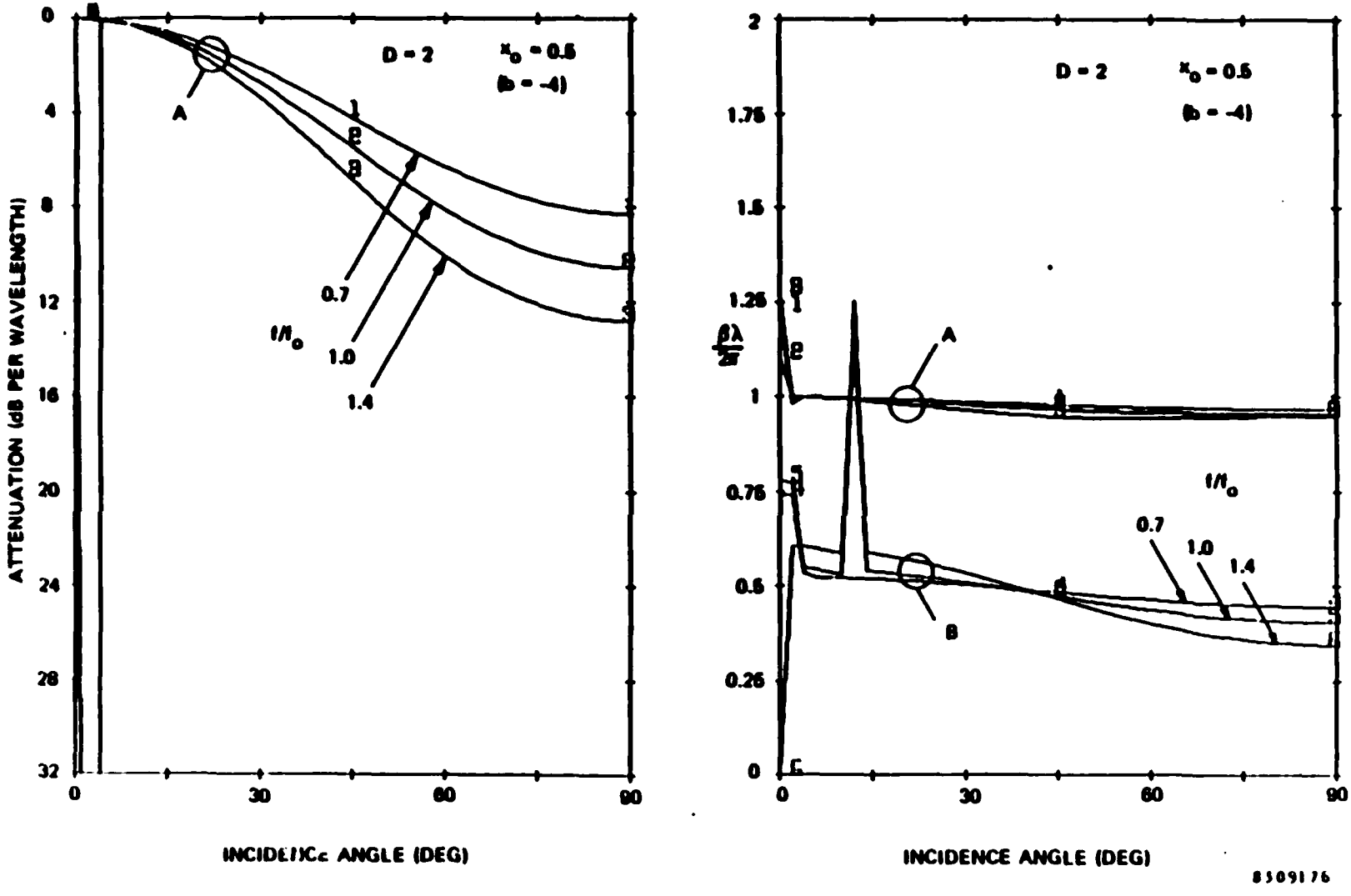

Figure 4-12. Angular Response for D = 2, x_o = 0.5

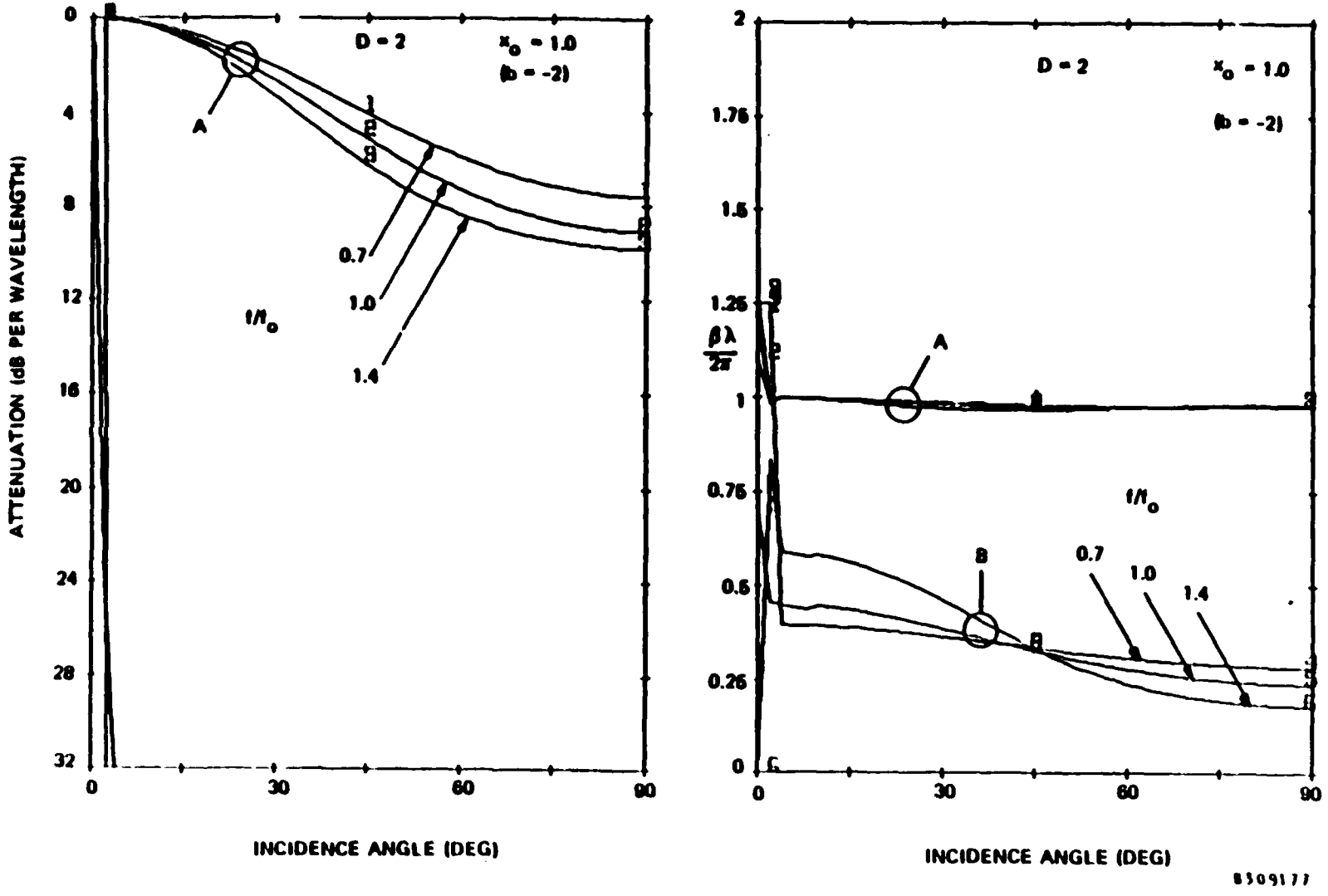

Figure 4-13. Angular Response for D = 2, x_o = 1.0

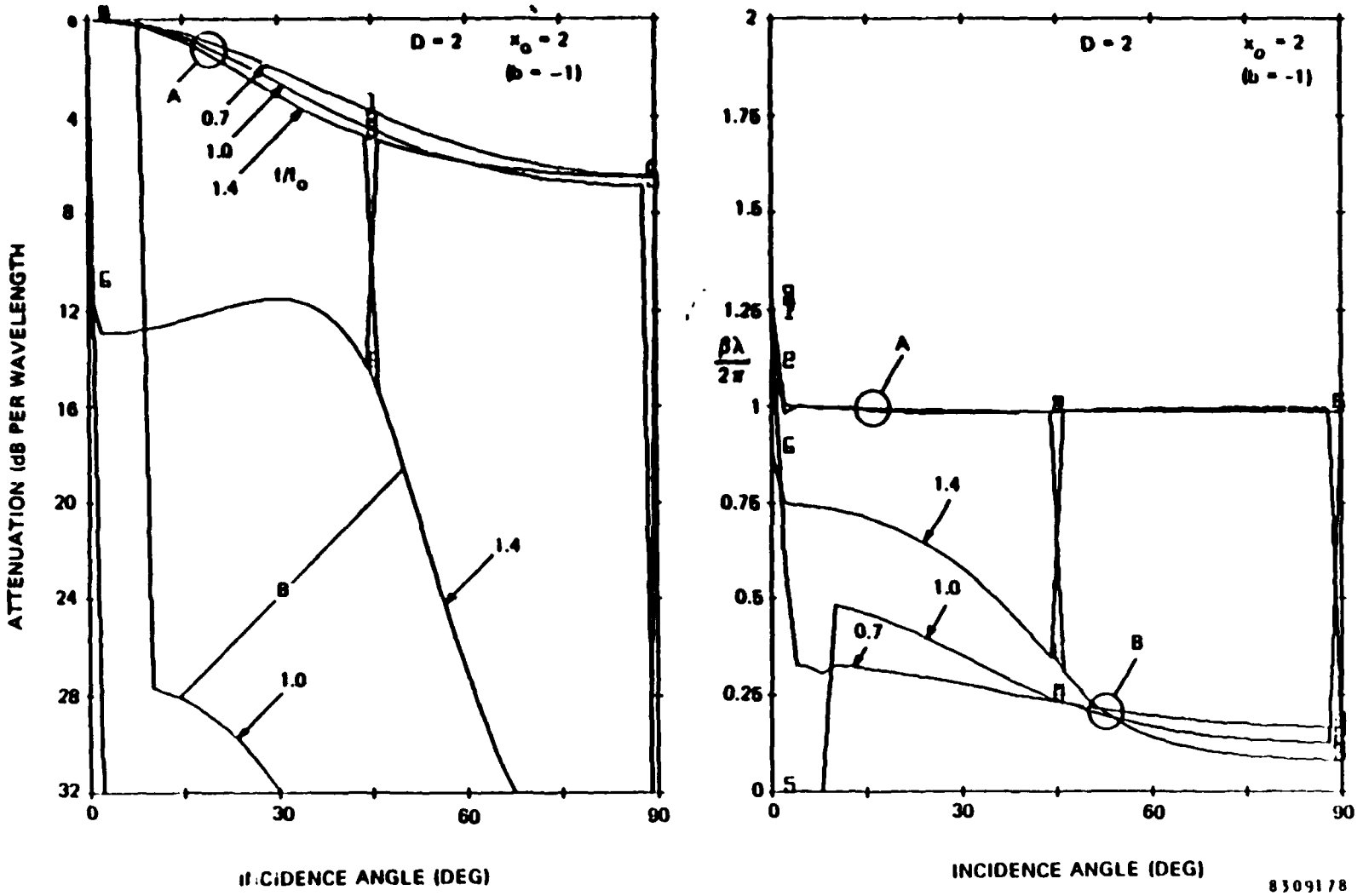

Figure 4-14. Angular Response for D = 2, x_o = 2.0

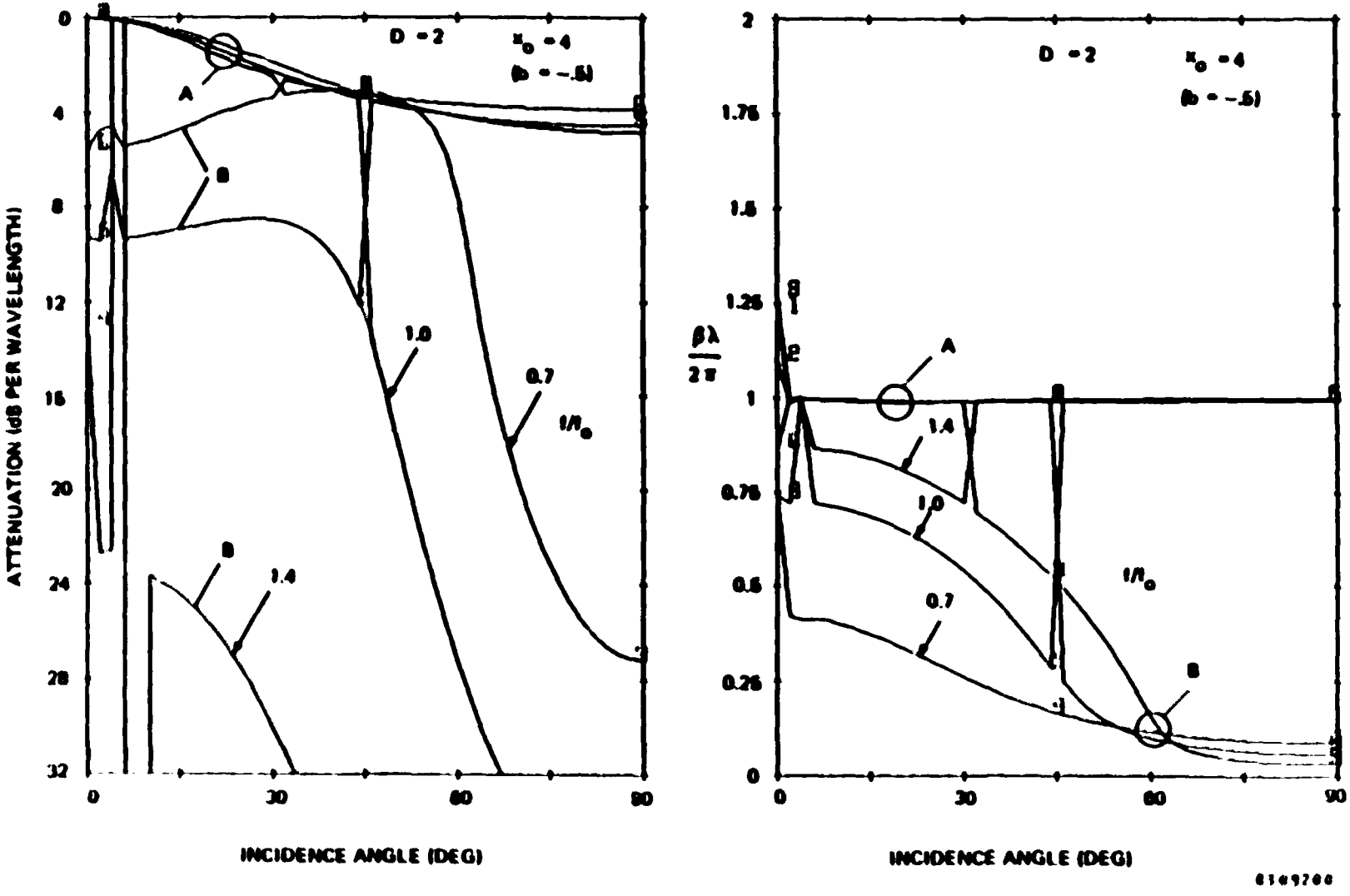

Figure 4-15. Angular Response for D = 2, x_0 = 4.0

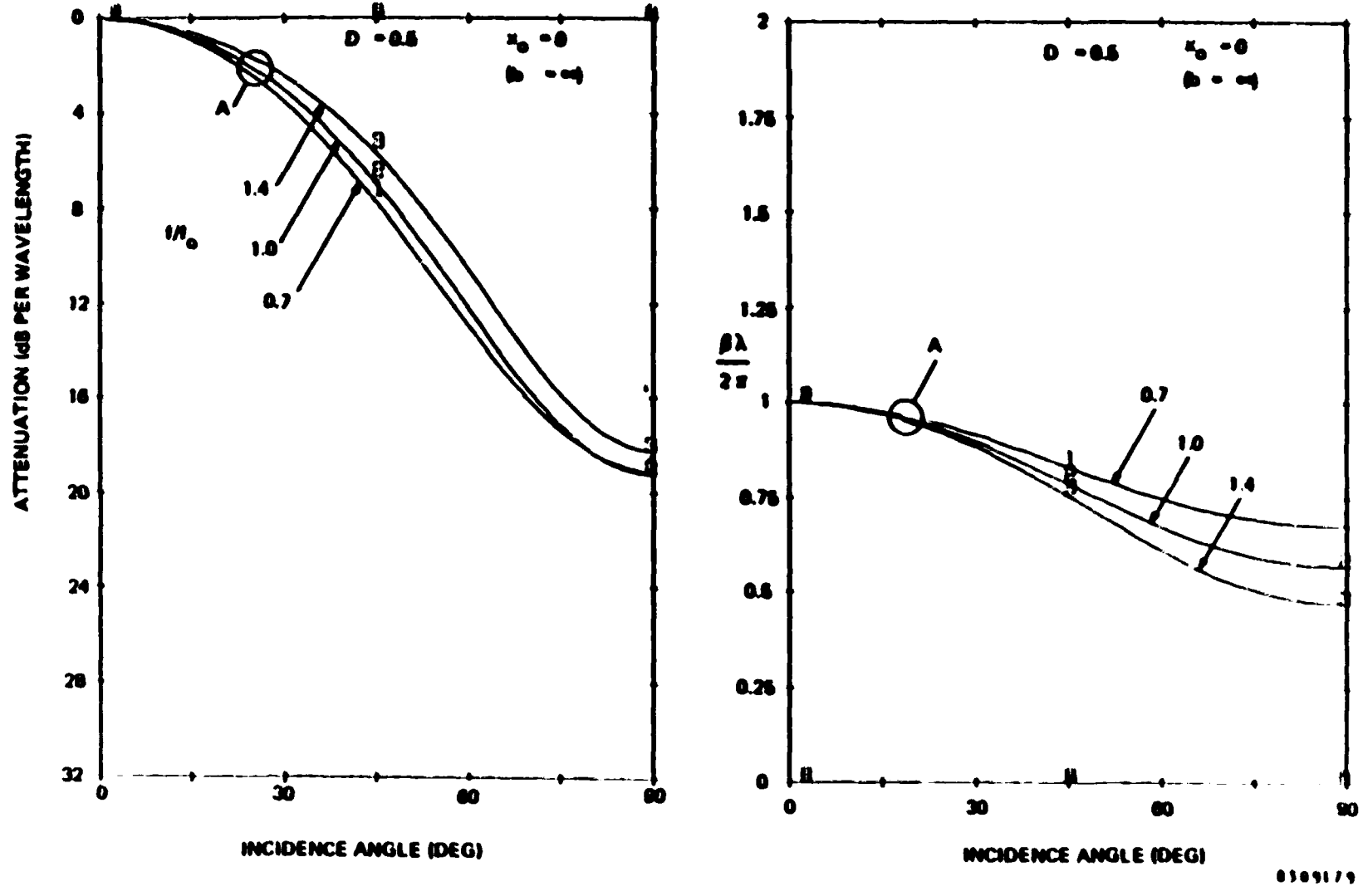

Figure 4-16. Angular Response for D = 0.5, x_o = 0

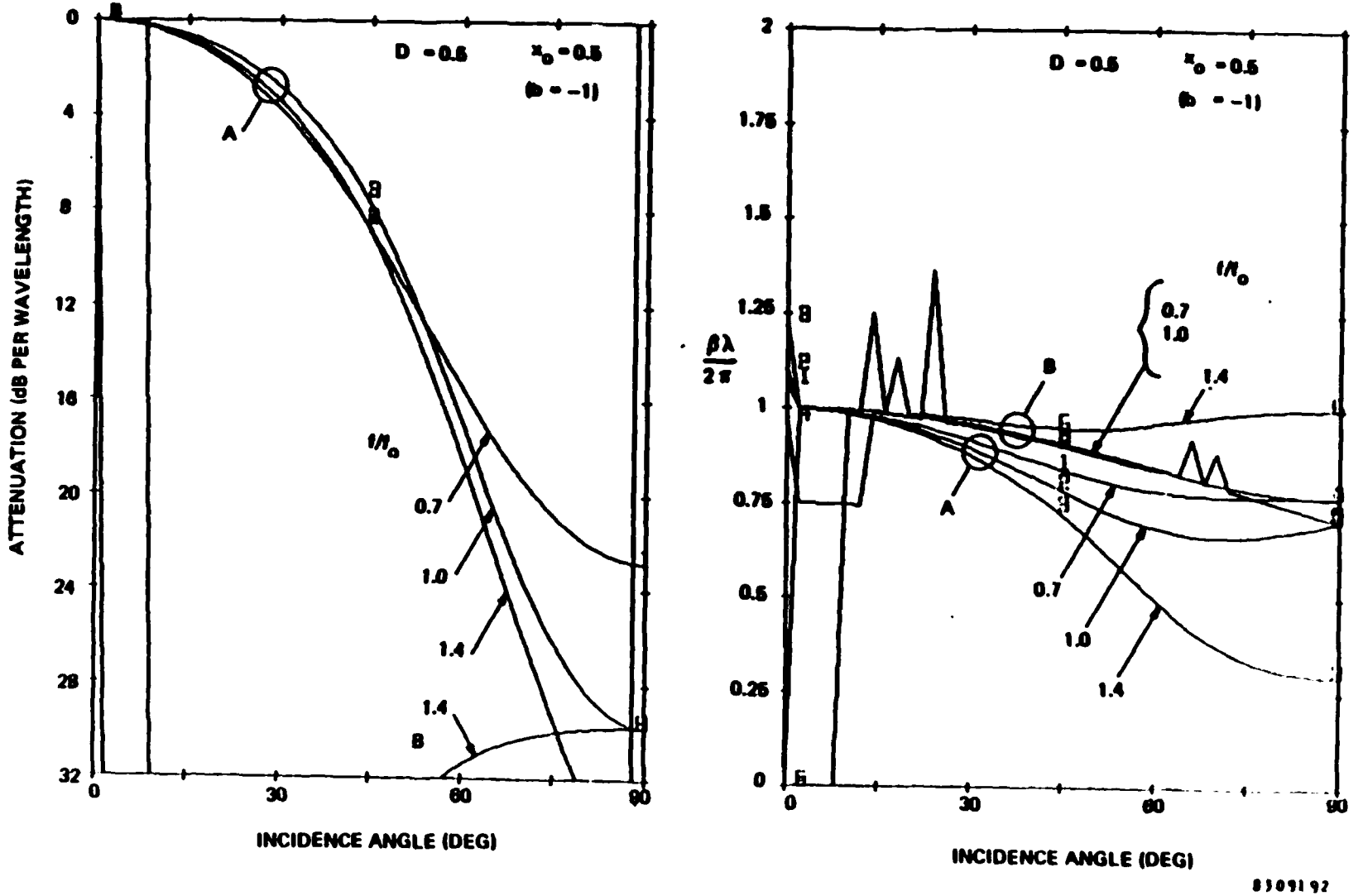

Figure 4-17. Angular Response for D = 0.5, x_o = 0.5

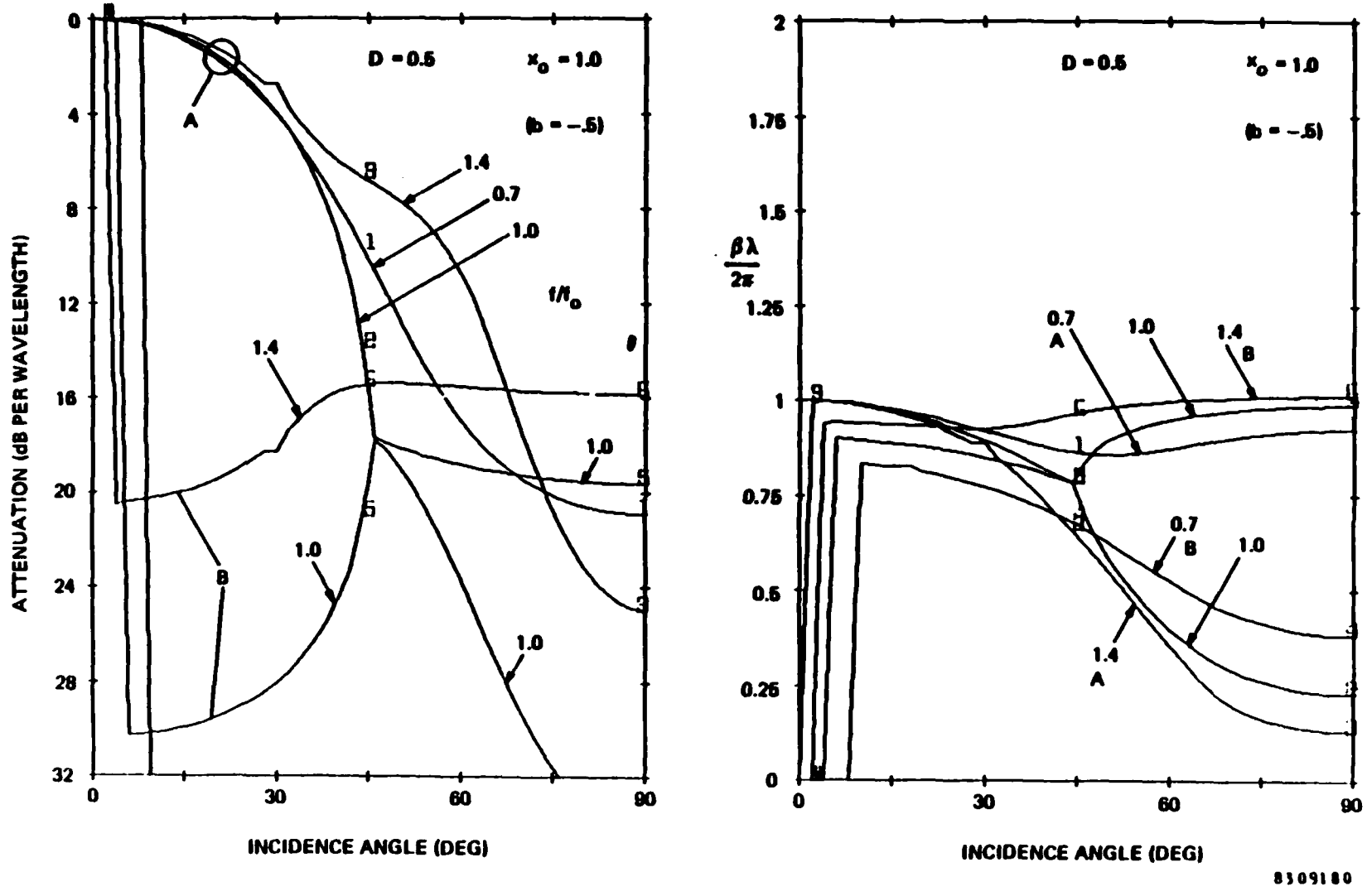

Figure 4-18. Angular Response for D = 0.5, x_o = 1.0

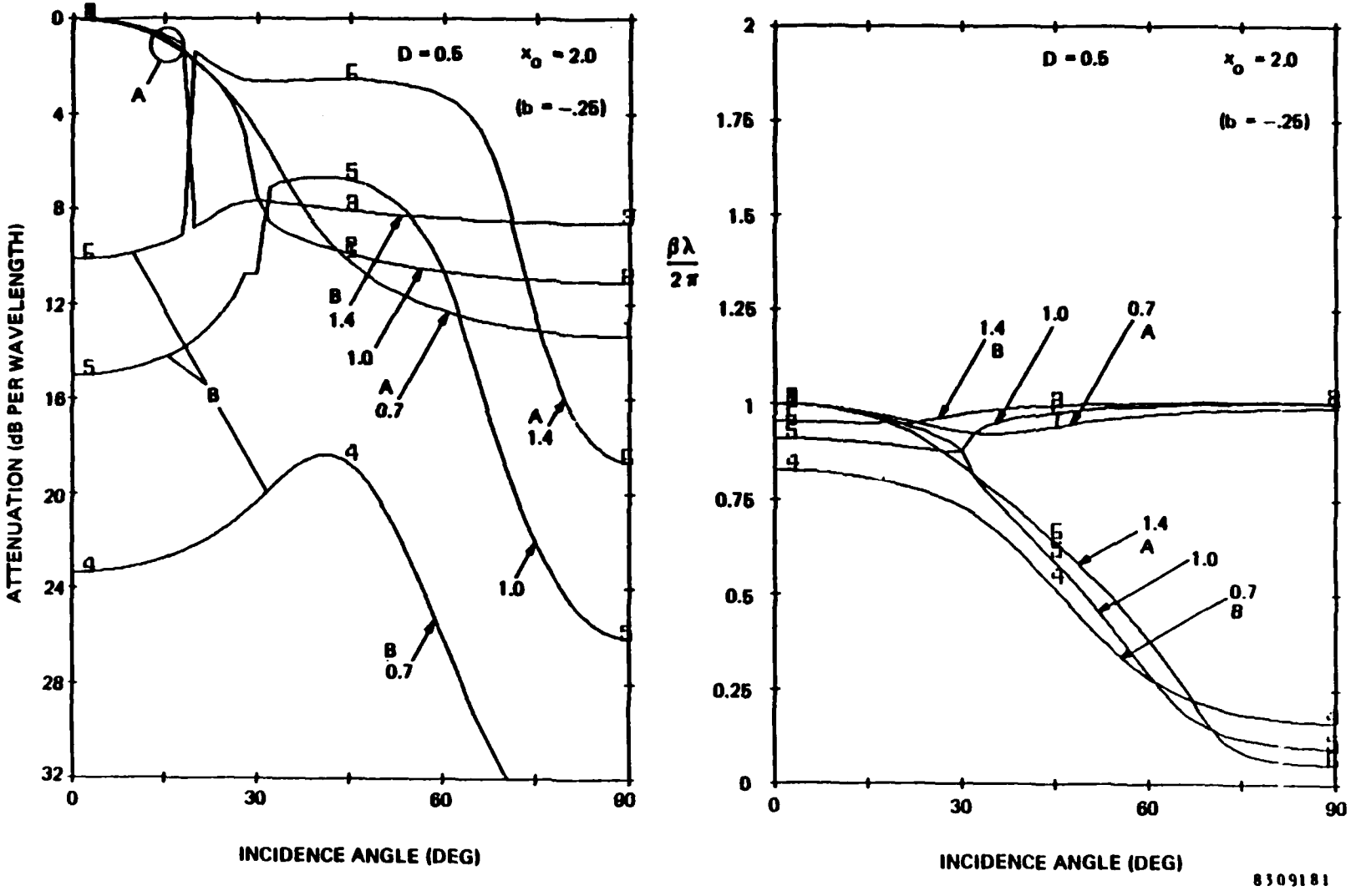

Figure 4-19. Angular Response for D = 0.5, x_o = 2.0

$f = 0.7\ f_o$ the β values are less for the B wave, but at $f = 1.4\ f_o$ the β values are greater for the B wave than for the A wave. For $f = f_o$ the result is not clear; it is obscured by both the closeness of the curves and by the difficulty of identifying the A and B curves beyond the junction point.

A related change with frequency seems to occur for the shape of the attenuation curves in Figures 4-18 and 4-19. At $f = 0.7\ f_o$ the attenuation vs θ curves for the A and B waves have shapes similar to those obtained earlier with $D = 1$ or 2. However, at $f = 1.4\ f_o$ the A-wave curves have a drop beyond the "cutoff angle" that resembles the earlier B-wave drop. Also, at $f = 1.4\ f_o$ the B-wave curve does not drop beyond the "cutoff angle".

The above-mentioned changes with frequency could alternatively be described as changes with the parameter D. At frequencies below f_o the parameter D is greater than the nominal midband value of 0.5, while at frequencies above f_o the value of D is smaller than 0.5. This latter viewpoint is the correct one, as will be seen below.

Examples for $D = 0.25$, increasing x_o. Figures 4-20 through 4-24 show the attenuation and phase constant versus θ for various x_o values when $D = 0.25$. Figure 4-20 shows the $x_o = 0$ case, and appears quite normal. Figure 4-21 shows the results for $x_o = 0.25$: here it is clearly seen that the B wave now has a larger β than does the A wave. Additionally, the B-wave β is greater than unity and does not vary much with incidence angle. Thus the B wave now has an axial phase velocity slower than free-space

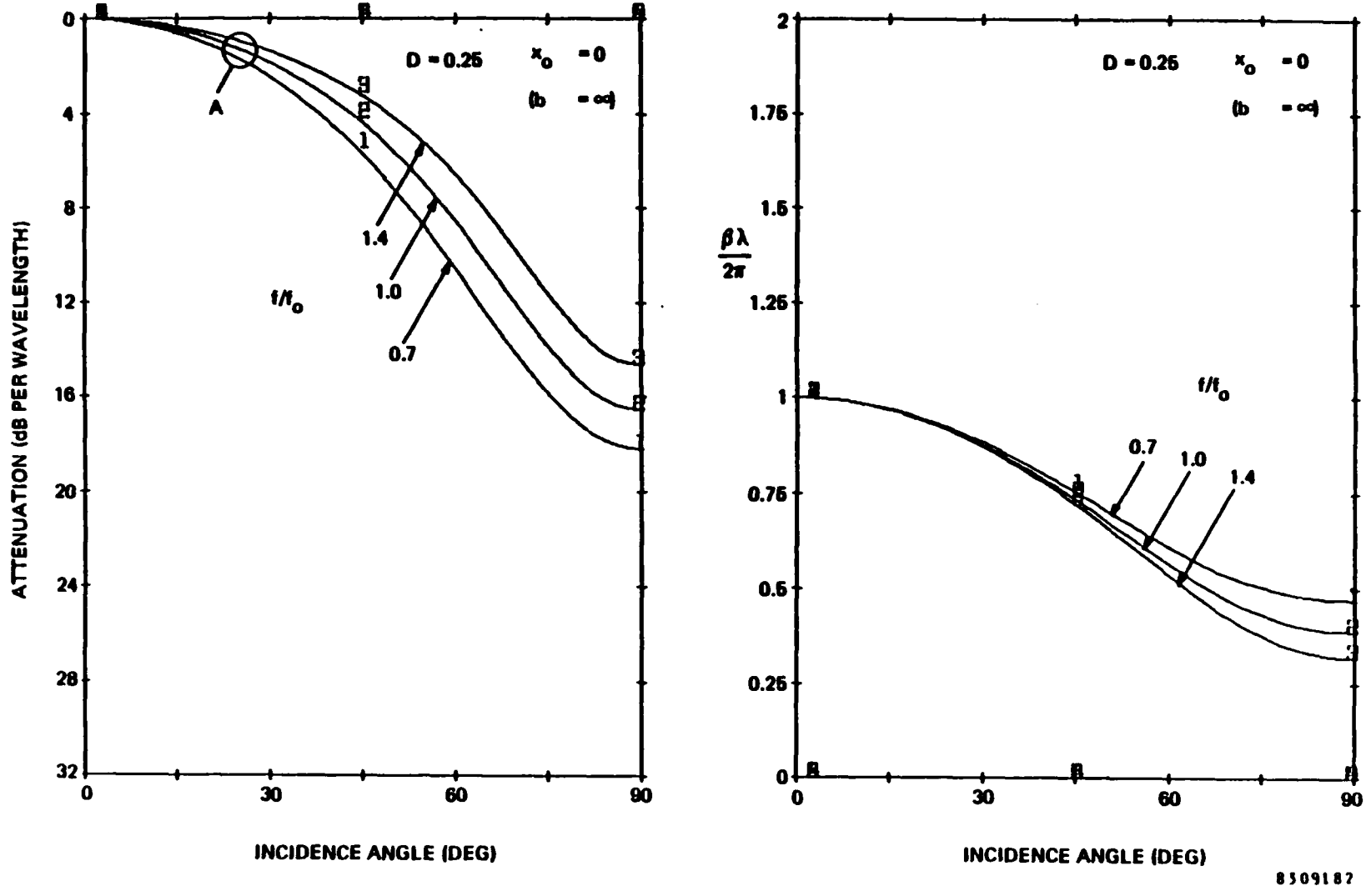

Figure 4-20. Angular Response for D = 0.25, x_o = 0

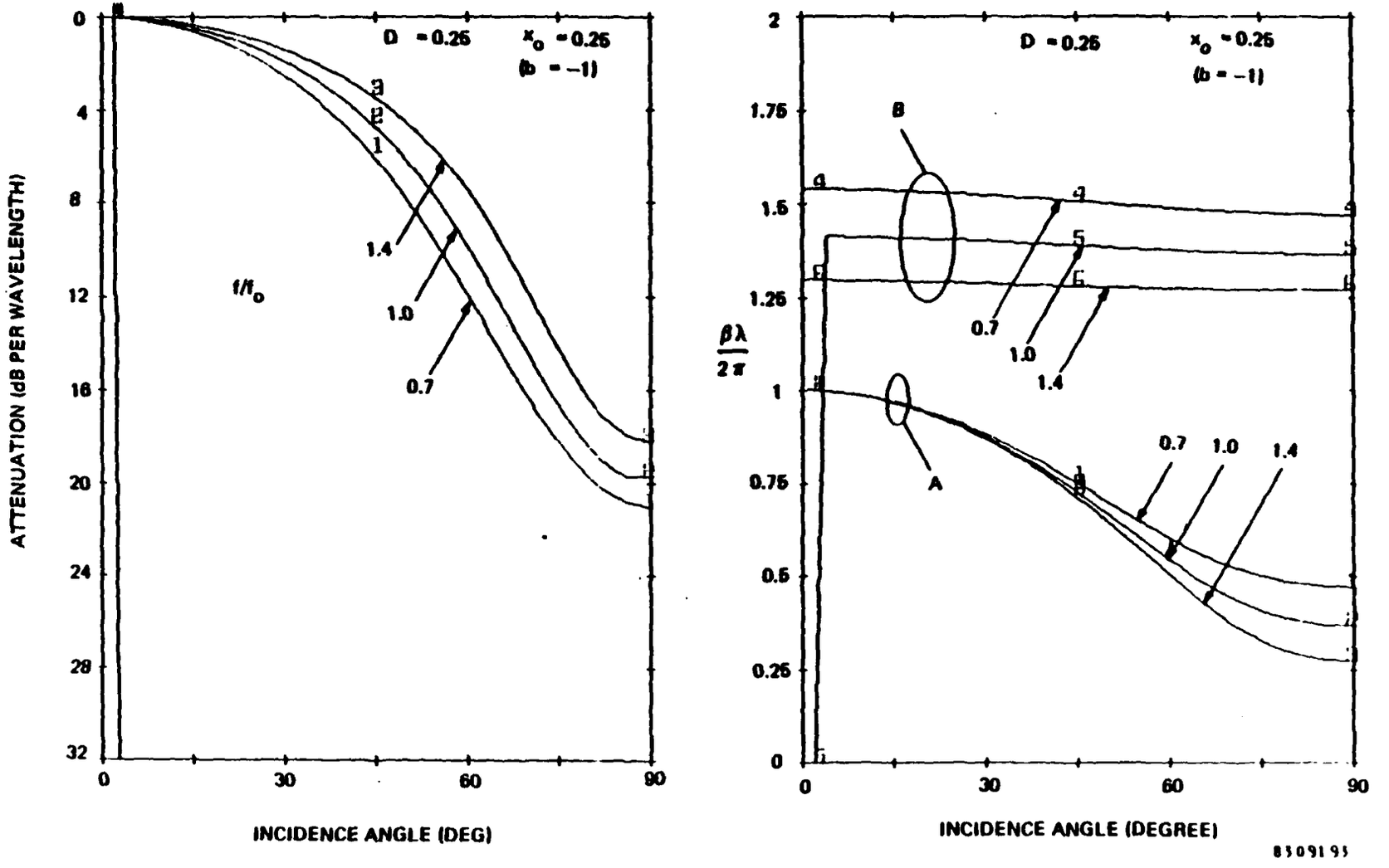

Figure 4-21. Angular Response for D = 0.25, x_o = 0.25

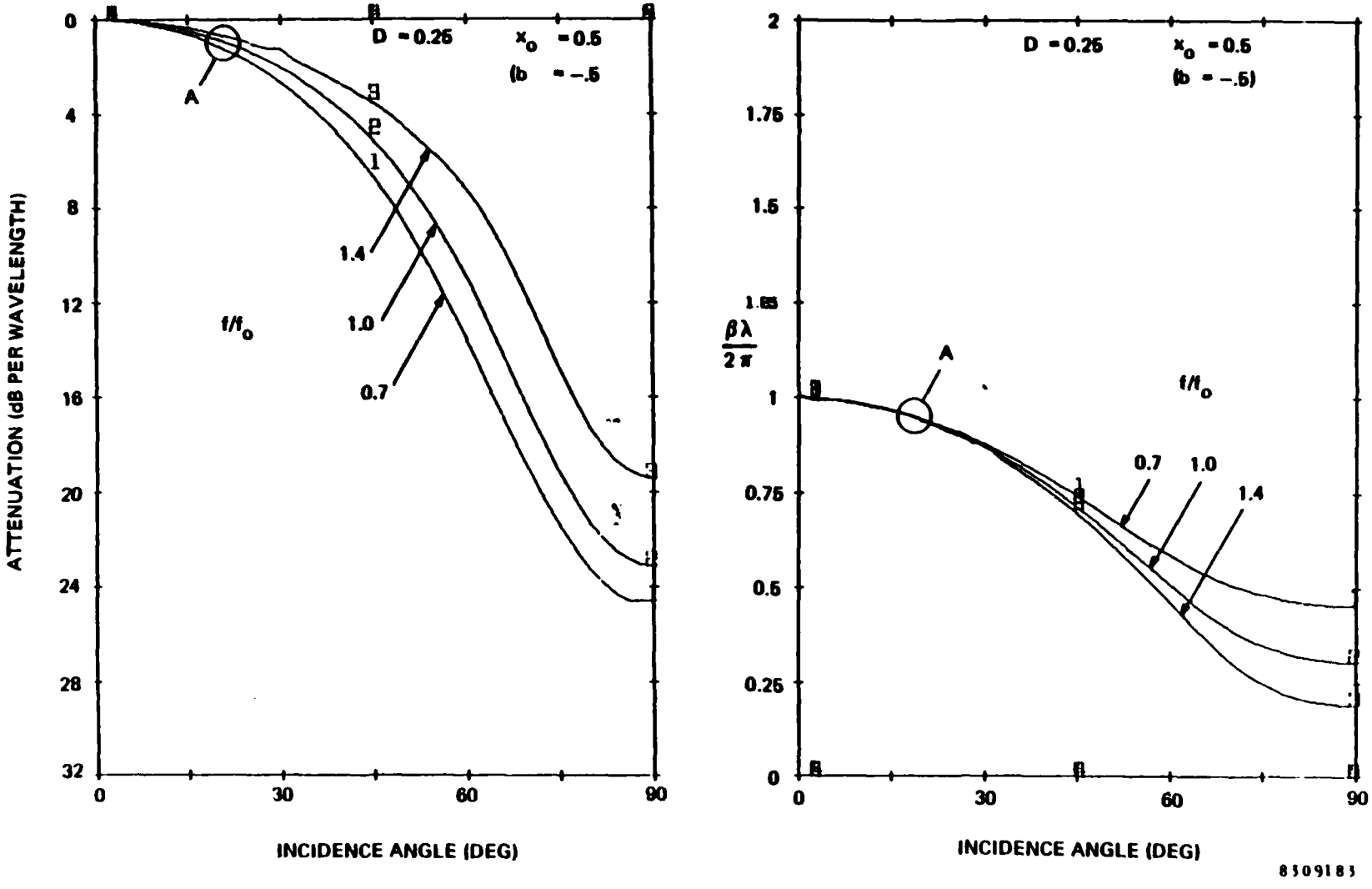

Figure 4-22. Angular Response for D = 0.25, x_o = 0.5

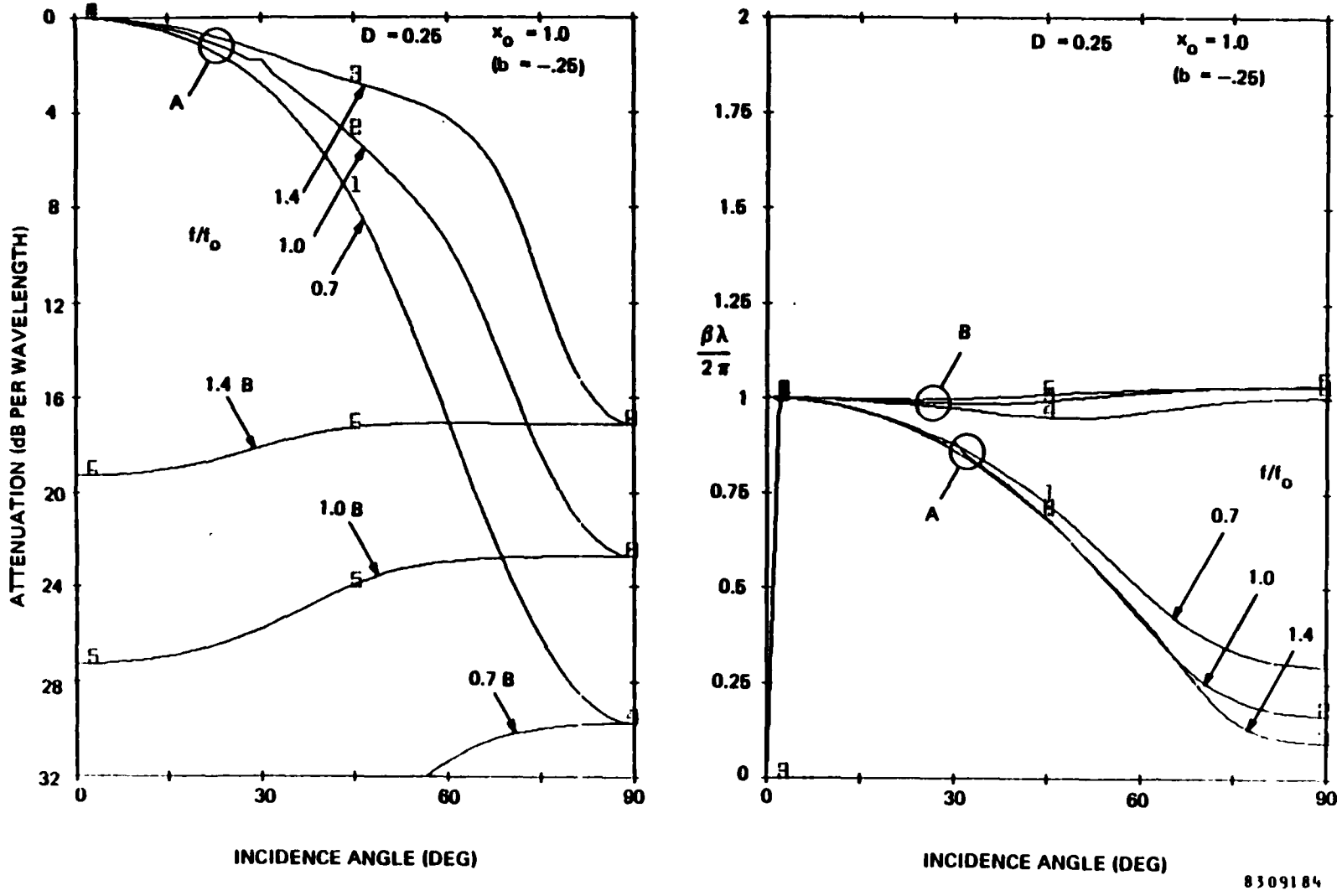

Figure 4-23. Angular Response for D = 0.25, x_o = 1.0

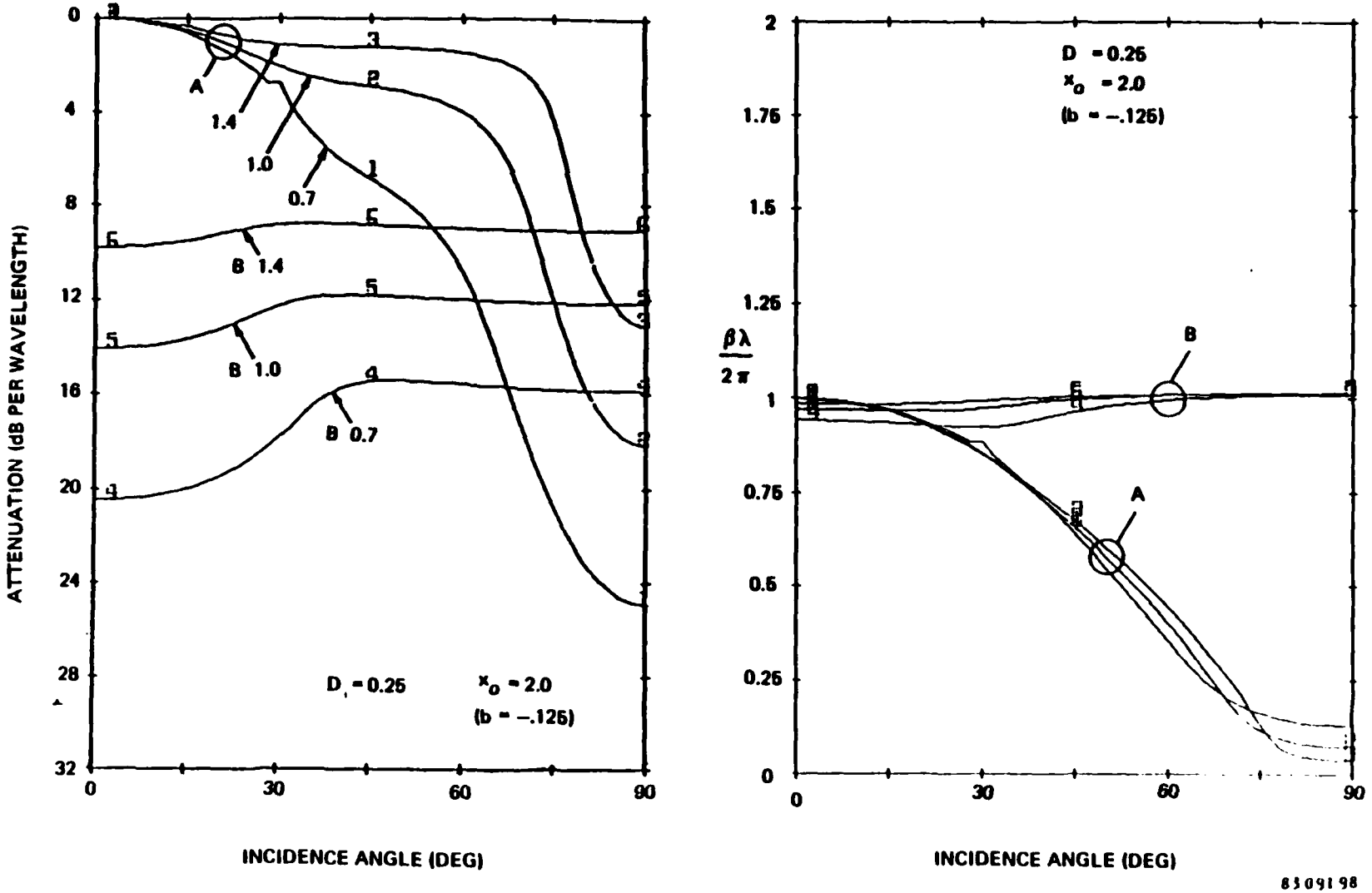

Figure 4-24. Angular Response for D = 0.25, x_o = 2.0

velocity, and apparently is nearly constrained by the axial medium.

Figure 4-22 for $x_o = 0.5$ does not show β curves for the B wave because lack of time did not permit us to follow the procedure needed to have the computer find both roots of the equations in this case. Figure 4-23 for $x_o = 1.0$ has B-wave β curves that have now become nearly unity, indicating that the B wave now has an axial phase velocity close to free-space velocity. This figure also has visible attenuation curves for the B wave; these curves do not drop beyond the "cutoff angle". However, the A-wave curves do evidence some drop beyond the "cutoff angles". Figure 4-24 for $x_o = 2.0$ shows more distinct drops in the A-wave attenuation curves beyond the "cutoff angles".

It is apparent that for D = 0.25, and presumably for all lesser values of D, some of the characteristics of the A and B waves have interchanged when compared with D = 1.0 and greater. For large D the B wave has an α cutoff effect, whereas for small D this effect is seen for the A wave. For large D the β of the B wave is smaller than that of the A wave, whereas for small D the opposite occurs. For large D the β of the A wave becomes nearly unity for large x_o, whereas for small D this happens to the B-wave β .

At an intermediate value of D, ie, when D = 0.5, this interchange is imminent. The interchange of characteristics with frequency in the curves of Figures 4-18 and 4-19, and the apparent discontinuities in some of those curves, evidently resulted from this condition. The discontinuity effect is discussed further below.

Examination of the Discontinuity. The apparent discontinuity of slope that appeared in the $f = f_o$ curves for D = 0.5 (see Figures 4-18 and 4-19) has been investigated further. Figure 4-25 shows an expanded plot of the discontinuity/junction region for the $x_o = 1$ case that appeared in Figure 4-18. The points are calculated by the computer every 0.5° of θ and are connected by straight lines when plotted.

The following conclusions are drawn from curves in Figure 4-25. First, the junction of the A and B curves occurs at exactly the same incidence angle for attenuation and phase constant. Second, this angle is exactly 45°. Third, the slopes appear to be truly discontinuous at the junction point, as nearly as can be determined within the 0.5° granularity of the calculation.

An expanded plot of the discontinuity/junction region for the $x_o = 2$ case that appeared in Figure 4-19 is shown in Figure 4-26. Conclusions similar to those stated above can be drawn. However, in this case, the incidence angle of the junction point is exactly 30°. Also, in this case some of the curves may not have a sharp discontinuity of slope at the junction point.

Further examination of these results, and of the equations derived previously, yields the following observations. The junction point occurs when D = 0.5 and when the variables x_1, D_1 and ϵ'_{1ax} have the following values:

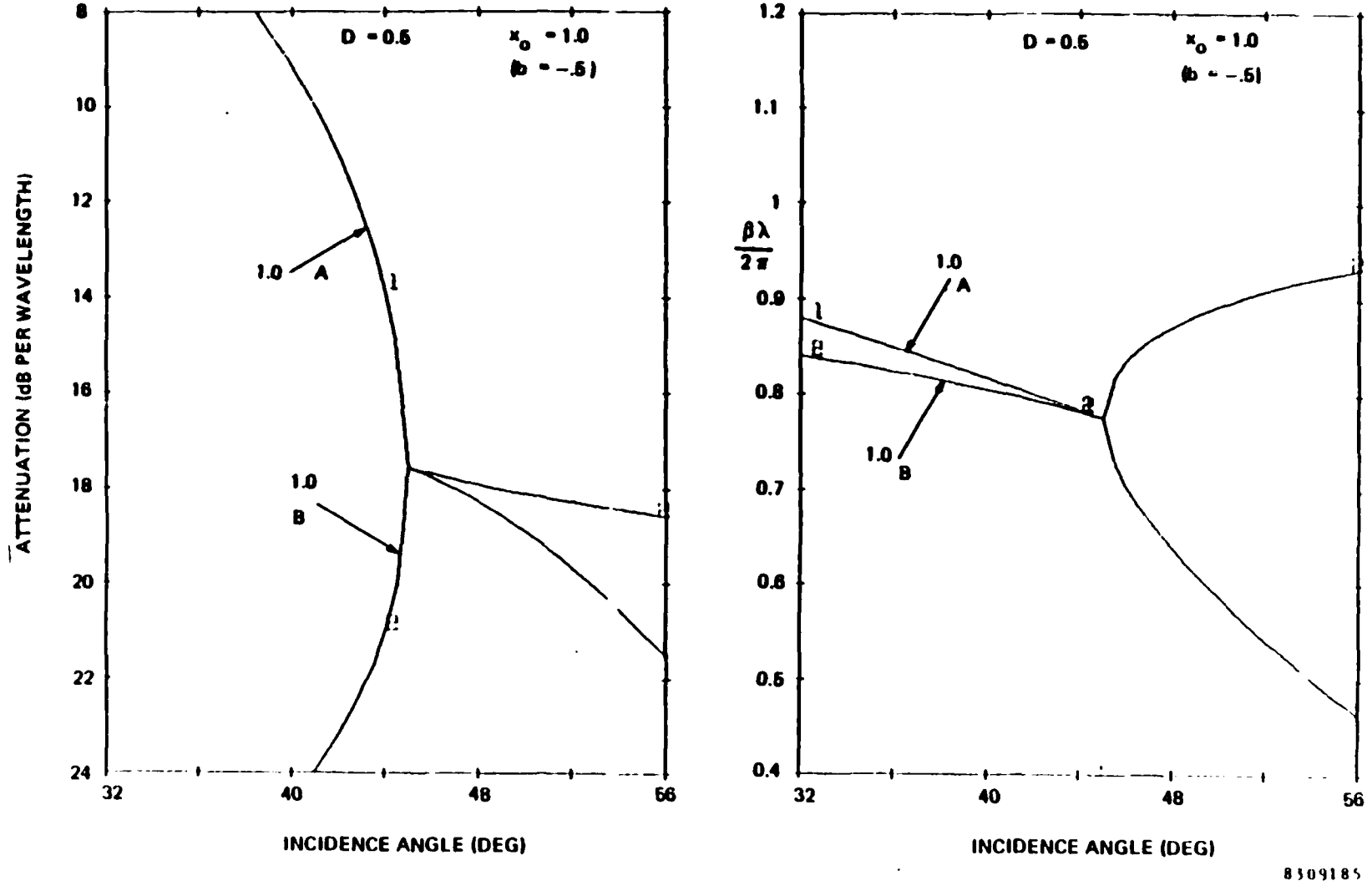

Figure 4-25. Angular Response for D = 0.5, x_o = 1

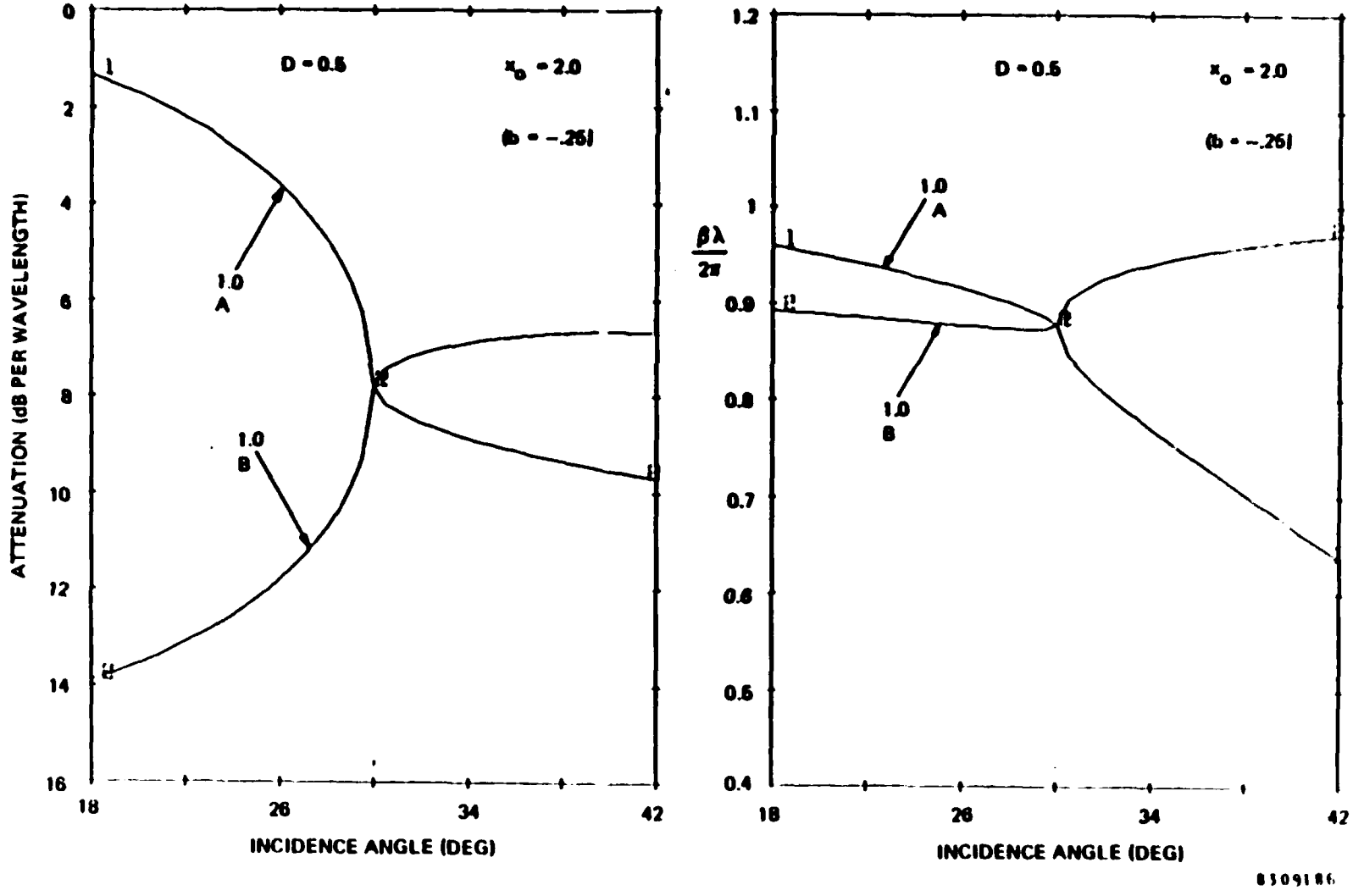

Figure 4-26. Angular Response for D = 0.5, x_o = 2

$$x_1(\alpha,\beta)_p = 1 \qquad (99)$$

$$D_1(\alpha,\beta)_p = 1/2$$

$$\epsilon'_{1ax}(\alpha,\beta)_p = 1/2$$

where the subscript p denotes the special case of the junction point. The values for α and β at the junction point are given by:

$$\frac{2\alpha_p^2}{k^2} = \left[(1+b)^2 + b^2\right]^{1/2} - (1+b) \qquad (100)$$

$$\frac{2\beta_p^2}{k^2} = \left[(1+b)^2 + b^2\right]^{1/2} + (1+b) \qquad (101)$$

where $b = -D/x_o$ as before, and $\epsilon'_{tr} = \epsilon'_{ax} = e = 1$. The incidence angle θ_p of the junction point is:

$$\theta_p = \text{arc sin } (-b)^{1/2} \qquad (102)$$

Therefore the junction point will occur only when b is between -1 and 0.

A basic question regarding the discontinuity/junction in the α and β curves is: does this phenomenon represent a real effect or is it an error or a meaningless quirk in the theory or the mathematics? A definitive answer to this

question has not appeared to us; however, some observations can be made. First, a sharp discontinuity occurring in any measurable quantity as incidence angle is varied would seem to be unlikely for an angular filter that contains dissipative elements. It is possible that some combination of the A and B waves could yield a smoothly-varying net attenuation and phase shift, but this, too, seems unlikely. It appears more likely that the analysis, which is based on the representation of an inhomogeneous medium by a fictitious homogeneous medium containing inductance, is yielding a sharp discontinuity when actually a smooth variation would occur.

Regardless of the precise nature of the junction phenomenon, it seems likely that a significant effect does occur in the vicinity of the junction. At the junction, the two waves have the same properties (attenuation, phase constant, impedance, etc.) and may be identical in all respects. Just before the junction is reached, the A wave attenuation becomes unusually large. Just beyond the junction the assignment of an A or B label to the two curves is difficult, but the curve with less attenuation still has an unusually large attenuation.

These observations lead to the speculation that at incidence angles close to the junction point the angular filter may have an unusually large net attenuation. The large net attentuation would probably occur only over a limited frequency band, because D varies with frequency and therefore deviates from the 0.5 value that yields the junction point. Later in this report, some measurements are presented that appear to confirm this speculation.

Effect of e. So far, the computed results have been shown only for e = 1. The parameter e is the excess capacitance ratio of the strips. Simple straight strips in free space have e = 1. Strips that are loaded with shunt capacitance (without a corresponding decrease of series inductance) have e greater than unity. Although this investigation deals primarily with simple strips having e = 1, some information can be obtained from the analysis for the possible situation in which e is greater than unity.

In equations (78), (82) and (85) for x_1, ε'_{1ax} and D_1, the β^2 , α^2 , and $\beta\alpha$ terms appear over a denominator that contains e. In equations (88) and (89) the β^2, α^2, and $\beta\alpha$ terms appear over a denominator that contains ε'_{tr}. It can be shown that when $e = \varepsilon'_{tr}$ the curves of α and β versus θ retain the same shape and are scaled up by the factor $(\varepsilon'_{tr})^{1/2}$. This holds true for any choice of D and x_o or b.

Figure 4-27 shows the computed results for D = 1, $x_o = 2$, $\varepsilon'_{ax} = 1$, and $e = \varepsilon'_{tr} = 4$. Comparison of these results with those of Figure 4-9 shows that, as expected, the values for attenuation and phase constant have doubled, but the shape of the curves has not changed. This result is analogous to the earlier result for $\varepsilon'_{tr} = 4$ given in Figures 3-14 and 3-15, but is more general because x_o is no longer zero.

A simple way to obtain $e = \varepsilon'_{tr}$ greater than unity while retaining ε'_{ax} close to unity is to embed he resistance strips in transverse layers alternating between thin high-dielectric-constant sheets and thick low-dielectric-constant sheets or free space. With such a configuration the transverse dielectric constant (ε'_{tr}) of the medium without

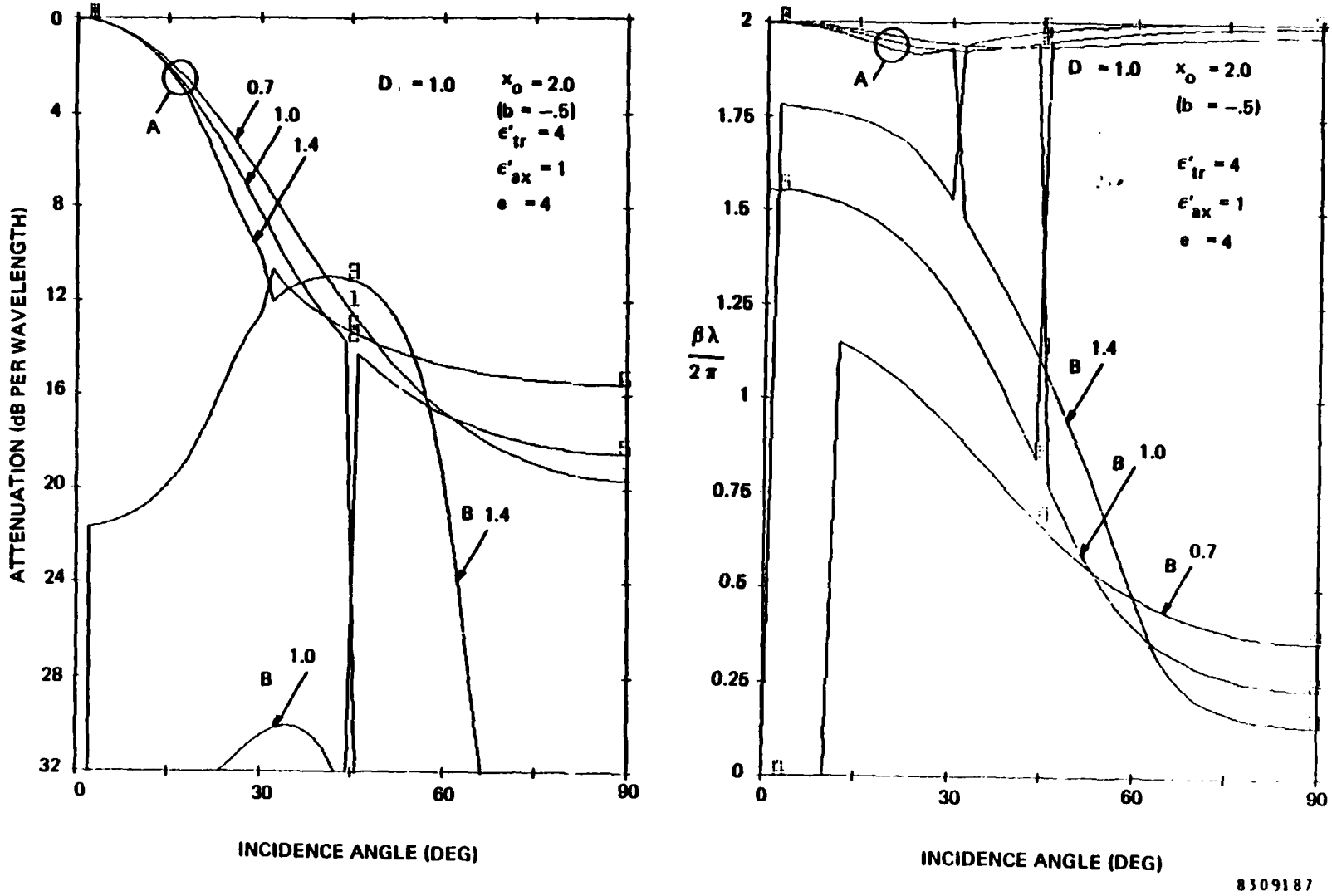

Figure 4-27. Angular Response for D = 1, x_o = 2, ϵ'_{tr} = e = 4

strips and the excess capacitance ratio (e) of the strips are both increased by the same factor.

While the increase of ε'_{tr} together with e yields an increase of attenuation, the increased ε'_{tr} creates a reflection at broadside incidence as discussed in Section 3. It is interesting to consider a case in which only e is greater than unity while ε'_{tr} remains at unity. This might be realized by adding small, lateral conducting elements to straight resistance strips to increase their capacitance. In this case, a change in the shape of the α and β versus θ curves would be expected, but the medium should have essentially no reflection at broadside incidence.

Figure 4-28 shows the results for D = 1, x_o = 2, $\varepsilon'_{tr} = \varepsilon'_{ax} = 1$, and e = 2. Two observations can be made. First, the curves differ substantially from those in Figure 4-9 where e was unity. Second, the A-wave attenuation for the $f = f_o$ and $f = 0.7\ f_o$ curves is enhanced for small incidence angles. In fact, this small-angle attenuation appears to be about twice that of the homogeneous case that was given in Figure 3-4 for D = 1. (A break in one plotted curve near 10° is believed to be a computer difficulty, and the curve can probably be extrapolated to 0° alongside the other two curves.) Third, at large incidence angles, the B-wave attenuation is less than the A-wave attenuation.

The enhanced A-wave attenuation near broadside incidence is of considerable interest. If the incidence angle θ approaches zero the basic set of five equations yield the following for the A-wave when $\varepsilon'_{ax} = 1$:

$$\frac{\beta(o)}{k} = (\varepsilon'_{tr})^{1/2} \qquad (102)$$

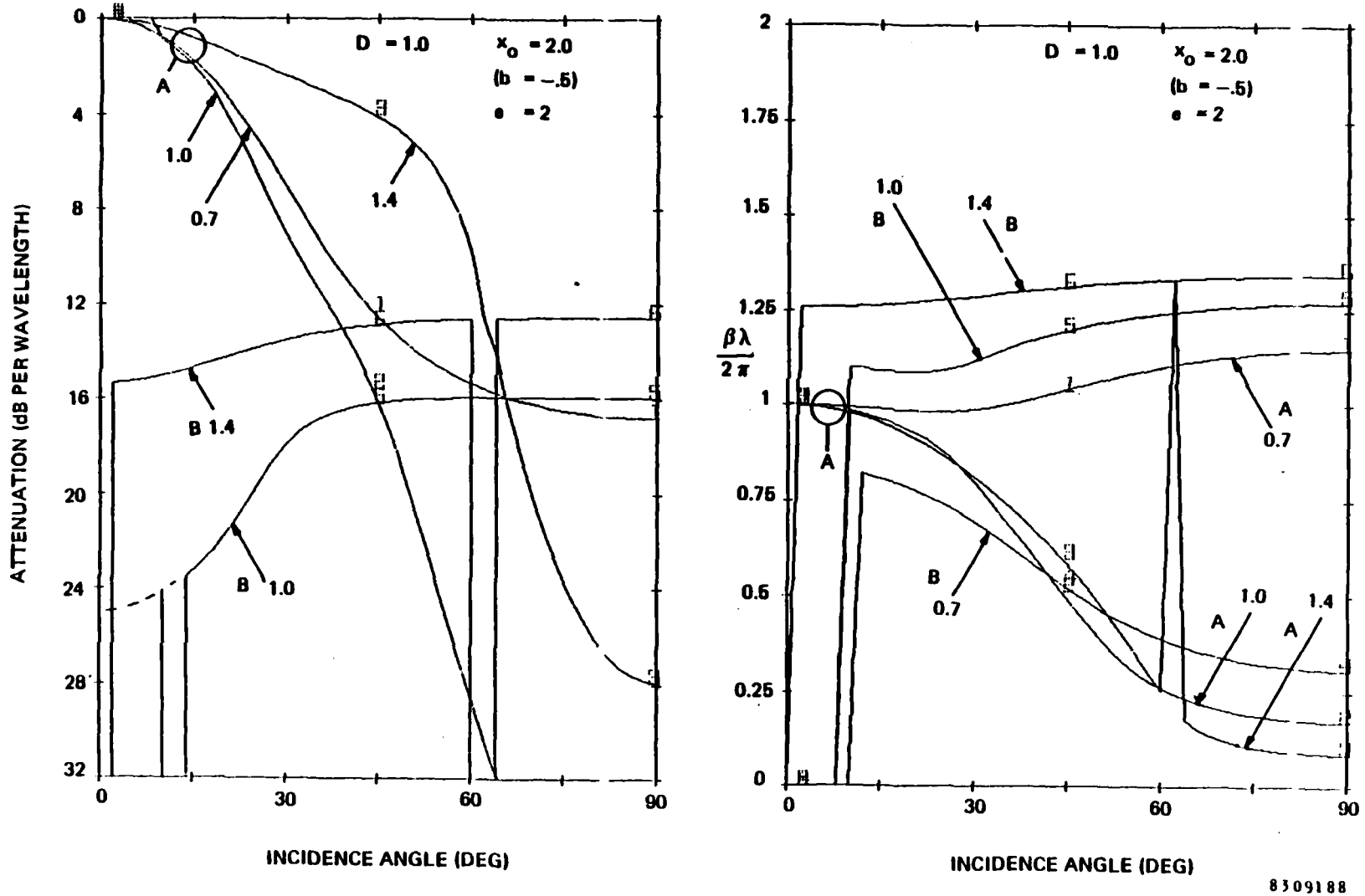

Figure 4-28. Angular Response for D = 1, x_o = 2, e = 2

$$\frac{2\alpha(o)}{k} = \frac{(\varepsilon'_{tr})^{1/2}\, D\left[1 + x_o^2\left(1 - \frac{\varepsilon'_{tr}}{e}\right)^2\right]\theta^2}{D^2 + \left[1 - Dx_o\left(1 - \frac{\varepsilon'_{tr}}{e}\right) + x_o^2\left(1 - \frac{\varepsilon'_{tr}}{e}\right)^2\right]} \qquad (103)$$

It can be seen that when $\varepsilon'_{tr} = e$ the attenuation would be enhanced simply by $(\varepsilon'_{tr})^{1/2}$ as noted in Figure 4-27. However, when $\varepsilon'_{tr} = 1$ but e is greater than unity the attenuation enhancement is more complex, now being dependent on the value of x_o and e (see also equation 96). For the case of Figure 4-28 where $x_o = 2$, $e = 2$, and $D = 1$, the value for $\alpha(o)/k$ for $f = f_o$ is:

$$\frac{\alpha(o)}{k} = \frac{1}{2}\,\theta^2 \quad \text{(for Fig. 4-28 case)} \qquad (104)$$

This can be compared with a reference standard defined as the small-angle attenuation $\alpha_s(o)$ for the homogeneous case in which $x_o = 0$ and $D = 1$ (see Figure 3-3):

$$\frac{\alpha_s(o)}{k} = \frac{1}{4}\,\theta^2 \quad \text{(standard case)} \qquad (105)$$

Thus the small-angle attenuation of the A wave at midband has indeed been doubled by going from the homogeneous standard case to an inhomogeneous case having $x_o = 2$ and $e = 2$.

An examination of equation (103) for the case of $\varepsilon'_{tr} = 1$ leads to an approximate relation that indicates how much A-wave attenuation enhancement at small angles is possible. The maximum enhancement is obtained approximately when:

$$D = x_o\left(1 - \frac{1}{e}\right) \tag{106}$$

When the above relation is satisfied the small-angle A-wave attenuation enhancement at midband is approximately:

$$\frac{\alpha(o)}{\alpha_s(o)} = 2\, x_o\left(1 - \frac{1}{e}\right) = 2D \tag{107}$$

Thus it appears that the small-angle A-wave attenuation could be enhanced as much as desired simply by making D large and x_o (1 - 1/e) large. Of course other properties may be degraded, such as bandwidth, large-angle attenuation, and B-wave attenuation.

An example of greater enhancement of small-angle A-wave attenuation is given in Figure 4-29. This example has $D = 2$, $x_o = 4$, and $e = 2$. For this case, the enhancement ratio $\alpha(o)/\alpha_s(o)$ computes from (107) to be 4 at midband. The midband A-wave curve in Figure 4-29 does indeed have an attenuation at small angles that is about four times the standard attenuation. However, at 30° the A-wave attenuation is only twice that of the standard homogeneous case. At larger angles the B-wave attenuation is less than that of the A wave, and is rather small out to 90°.

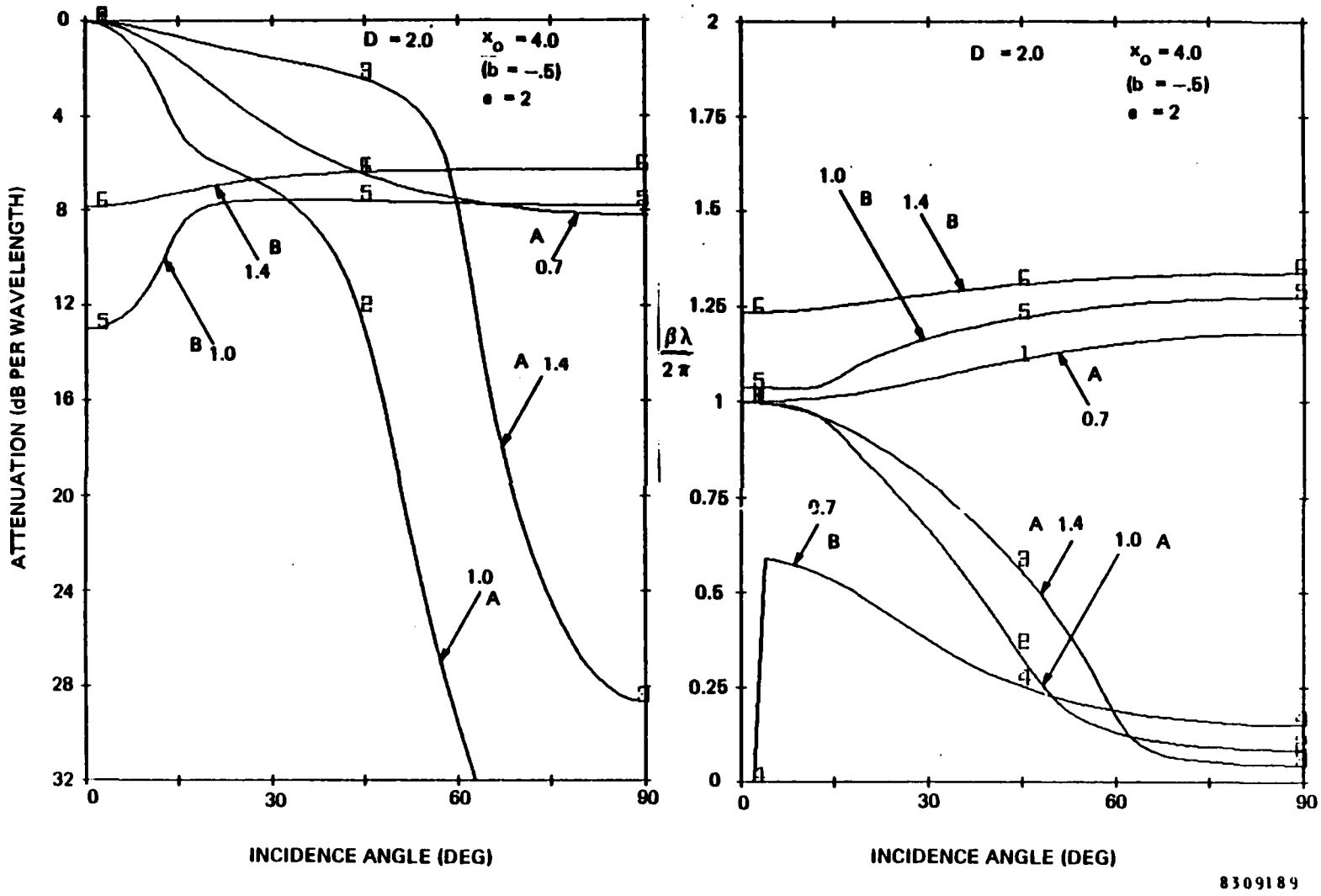

Figure 4-29. Angular Response for D = 2, x_o = 4, e = 2

The $f = 0.7\ f_o$ and $1.4\ f_o$ curves in Figure 4-29 show a much smaller enhancement of the small-angle A-wave attenuation, as well as other deficiencies. This frequency sensitivity is shown more clearly in Figure 4-30, in which the small-angle A-wave attenuation enhancement ratio $\alpha(o)/\alpha_s(o)$ is plotted versus frequency ratio.

This curve illustrates the resonant nature of the enhancement. What is happening here is that the circuit of Figure 4-5 is resonating at broadside incidence. The Q of the resonance is proportional to D, hence the loss at resonance is proportional to D. However, the bandwidth over which high loss is obtained is inversely proportional to Q or D.

It should be mentioned that the effects of excess capacitance discussed in the preceding paragraphs, are highly dependent on the simplifying assumptions made in the analysis of the inhomogeneous medium. Since experiments with a medium having e intentionally made large are beyond the scope of this program, a verification of these theoretical results will not be made. Therefore, the effects of excess capacitance given above should be regarded as unconfirmed potential effects.

Impedance of Inhomogeneous Medium. The input impedance ratio Z' was given by equation (31) in Section 3, and is repeated below in terms of α and β:

$$Z' = \frac{\beta - j\alpha}{k} \frac{1}{\varepsilon'_{tr} \cos \theta} \tag{108}$$

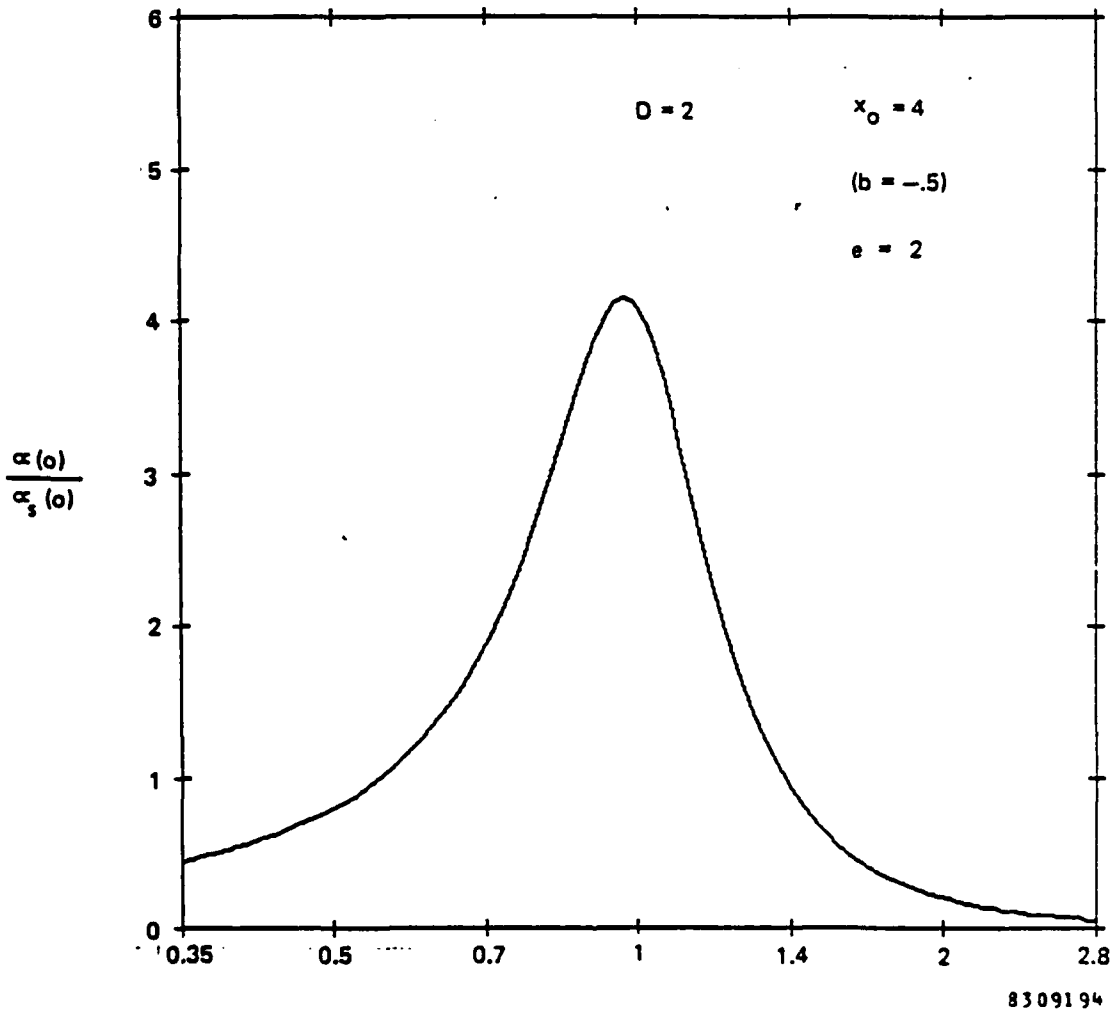

Figure 4-30. Small-Angle Attenuation Ratio vs Frequency Ratio for D = 2, x_o = 4, e = 2

Since α and β versus θ have been computed for each inhomogeneous case, the input impedance ratio versus θ is also available. However, with the inhomogeneous medium there are two waves, and hence, two sets of α and β values to consider. Equation (108) therefore gives two values of input impedance: one assuming only the A wave is present, and the other assuming only the B wave is present. The net input impedance is a combination of the two values that depends on the relative excitation amplitude of the two waves at the input face. Since the relative excitation amplitude is not available from our analysis, the net input impedance is also not available.

The two values of input impedance ratio have been computed for many of the inhomogeneous cases for which α and β have been determined. We have not found this information to be very useful, and therefore, it has not been included in this report. However, one example is included to illustrate the difference between the results for the homogeneous medium and the inhomogeneous medium.

Figure 4-31 shows the magnitude of the input impedance ratio versus θ for the A wave and the B wave at three frequencies, for the case of $D = 1$ and $x_o = 1$, with $\varepsilon'_{tr} = \varepsilon'_{ax} = e = 1$. The three A-wave curves are closely bunched together and are similar to the $D = 1$ curve in Figure 3-8.

One of the three B-wave curves (the midband curve) happens to be very close to the A-wave curves. The other two B-wave curves are displaced, and one of them has a different shape. Most importantly, they do not have a value of unity at broadside incidence. This result reinforces the

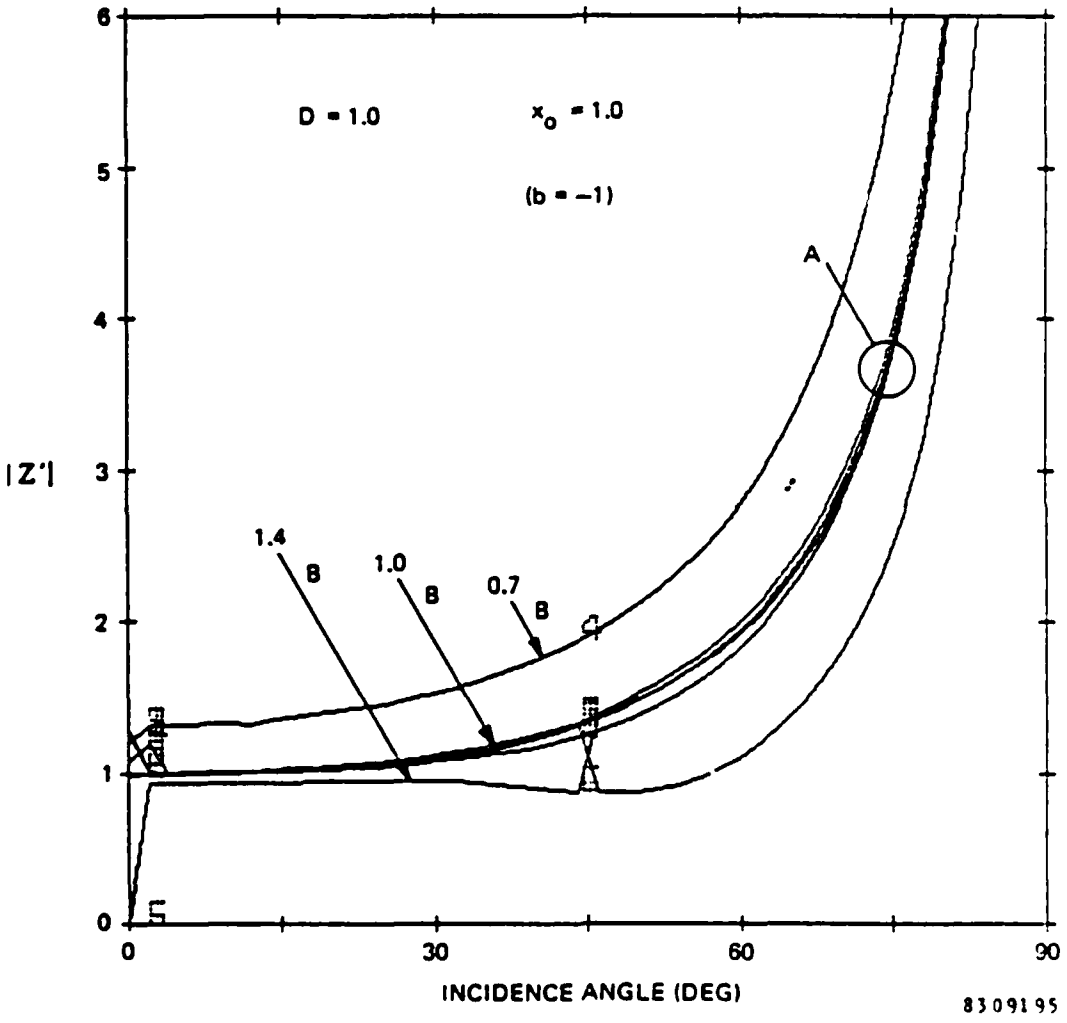

Figure 4-31. Magnitude of Input Impedance Ratio vs Incidence Angle for D = 1, x_o = 1

earlier conclusion that the B-wave excitation must be zero at broadside incidence, based on the viewpoint that the axial medium is essentially invisible at broadside.

Figure 4-32 shows the phase of the input impedance, and Figure 4-33 shows the reflection coefficient magnitude. It is seen that even the midband B-wave curve of reflection coefficient has a substantial value at broadside incidence, because of the non-zero phase of the input impedance at broadside.

(c) Summary of Inhomogeneous Medium Angular Response

An analysis of the inhomogeneous axial-conductance medium has been made, based on the viewpoint that the essential effect of the inhomogeneity is the introduction of inductance in series with the axial resistance. A certain assumption regarding the behavior of this inductance has yielded a set of equations which are solved by computer to provide the attenuation of the medium versus incidence angle.

The analysis has shown that two types of waves can exist in the inhomogeneous medium when only one wave is incident in the E plane. One of these two wave types, called the A type, always has zero attenuation at broadside incidence. The other, called the B type, has a non-zero attenuation for incidence near broadside, and is expected to be unexcited at broadside incidence.

When the axial loss tangent (D) is greater than 0.5 the B wave exhibits a cutoff phenomenon versus frequency and incidence angle, and its axial phase velocity is fast compared with that of the A wave. When D is less than 0.5

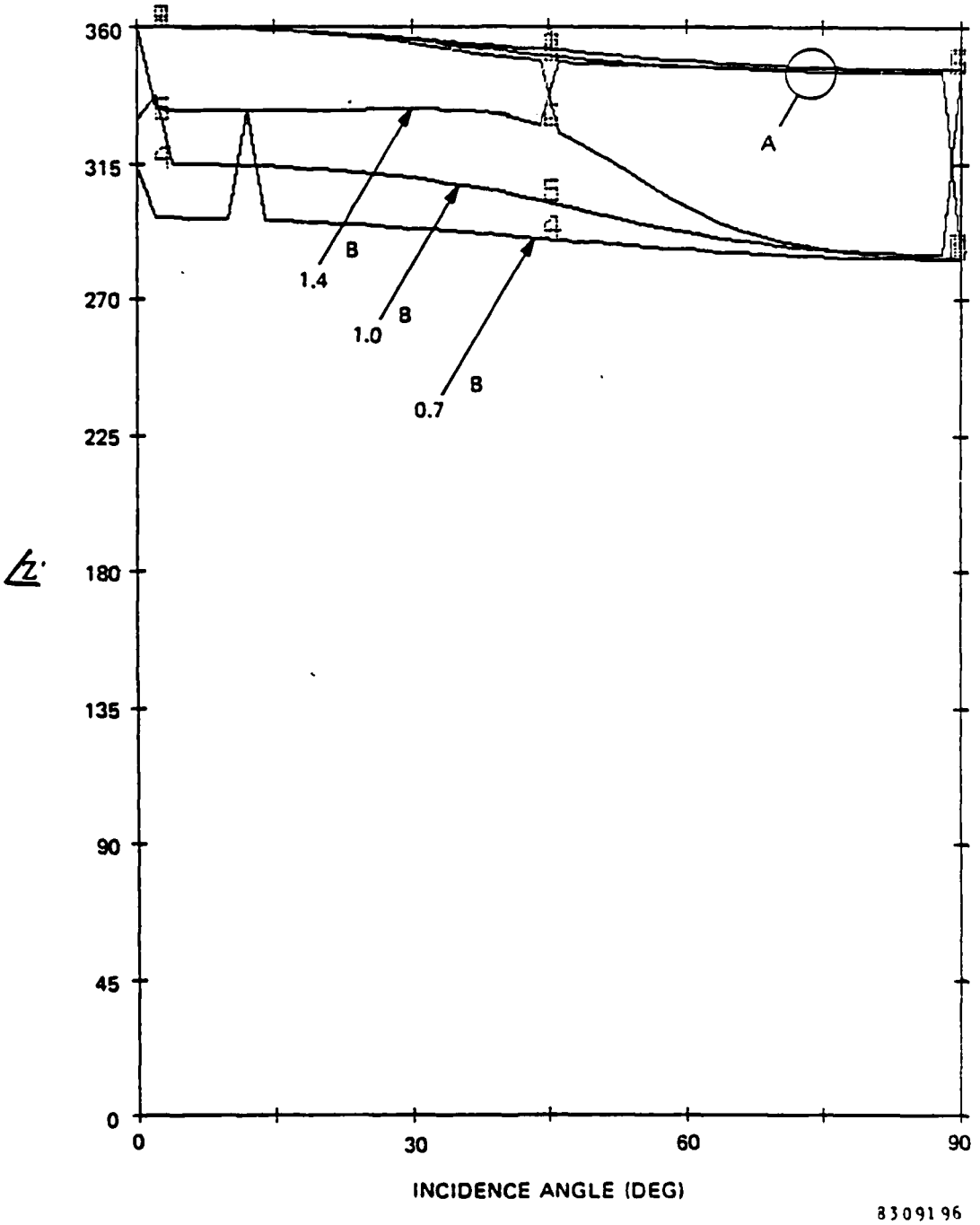

Figure 4-32. Phase of Input Impedance Ratio vs Incidence Angle for D = 1, x_o = 1

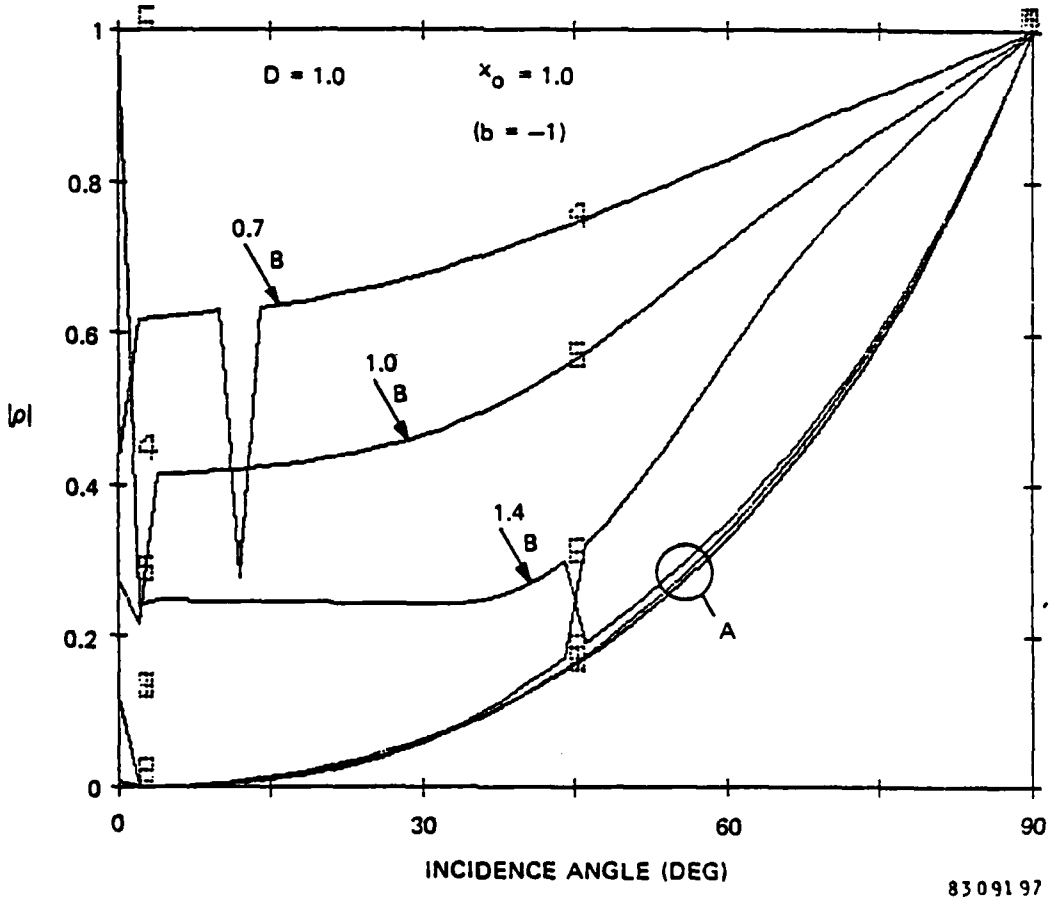

Figure 4-33. Reflection Coefficient Magnitude vs Incidence Angle for D = 1, x_o = 1

the opposite results occur. For D = 0.5 a transition occurs that appears to yield unusually large attenuation for the A wave under certain conditions at particular angles of incidence.

In general, when the spacing (s) of the axial-conductance elements is small, the inductive reactance $X_{\lambda o}$ in series with the axial resistance is small, and the attenuation of the B wave is large. In this case, the overall attenuation of the angular filter is likely to be determined primarily by the A wave. With small $X_{\lambda o}$ the properties of the A wave are not very different from those of the homogeneous medium. Thus, with small spacing the inhomogeneous medium should give angular-filter performance similar to that with the ideal homogeneous medium.

When the spacing is not small the inductive reactance $X_{\lambda o}$ becomes appreciable and the angular response of the inhomogeneous medium can differ significantly from that of the ideal homogeneous medium. The manner in which the response differs depends on the value chosen for D, as discussed earlier. For the case of D = 1, a value of $X_{\lambda o}$ greater than about 60 ohms across a wavelength cube results in substantially decreased attenuation for the A wave, and eventually, a significantly low attenuation for the B wave. These values for $X_{\lambda o}$ correspond to values for $|b|$ of unity or less.

The relation between $X_{\lambda o}$ (or b) and the inhomogeneous medium dimensions s (strip spacing) and w (strip width) was given in equations (63) and (90). For convenience, this relation is plotted in Figure 4-34. It is seen that for values of w/s greater than 0.1, a value of 1/4 or less for s/λ will yield values for $X_{\lambda o}$ less than 60 ohms, as is

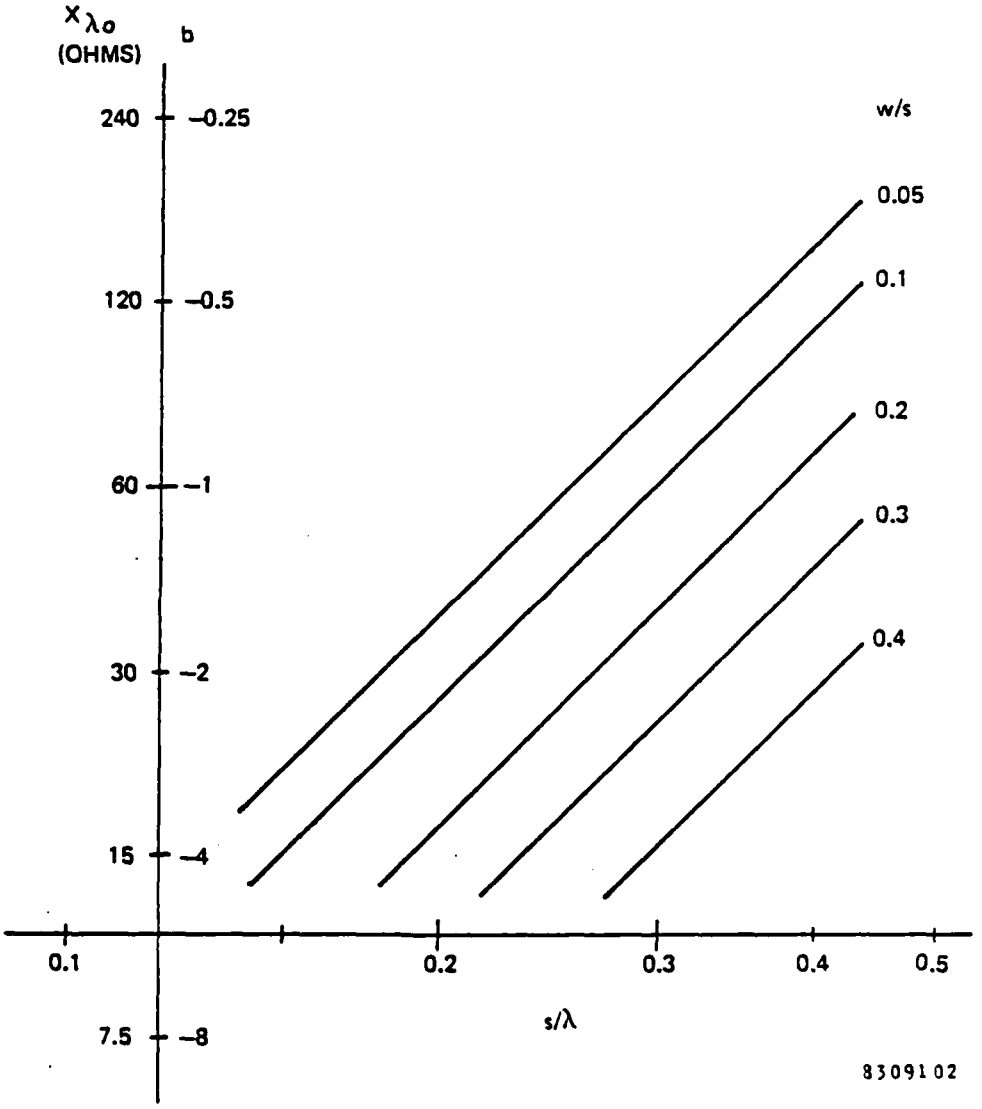

Figure 4-34. Inductive Reactance $X_{\lambda o}$ vs s/λ and w/s

desired. Therefore when D = 1, an inhomogeneous medium having such dimensions might be expected to have an angular response not very different from that of the ideal homogeneous medium.

When the spacing is increased substantially beyond the value noted above, the attenuation of the A wave decreases. The attenuation of the B wave also decreases and eventually may be less than that of the A wave. It seems reasonable to expect that the excitation of the B wave increases with spacing, but this information is not provided by our analysis. If this occurs sufficiently before the B-wave attenuation falls below that of the A wave then the overall attenuation of the angular filter might increase. Eventually as spacing is increased, the overall attenuation should decrease.

If the spacing is increased to $\lambda/2$ or more, then propagating grating lobes may exist. Our analysis does not cover this situation, or the related effect that can occur before such propagation occurs. Therefore as the spacing approaches $\lambda/2$ our analysis may yield inaccurate results.

When the resistance-strip medium is embedded in a dielectric structure having increased transverse dielectric constant (ε'_{tr}) and providing the same increase in the excess capacitance ratio (e) of the strips, the analysis shows that the attenuation of both the A wave and the B wave is increased by $(\varepsilon'_{tr})^{1/2}$ regardless of the value of $X_{\lambda o}$. This increase would come at the price of a reflection at broadside incidence that may require an impedance-matching section.

When only e is increased, as may be accomplished by adding capacitive elements to the resistance strips, the analysis indicates that enhanced attenuation of the A wave can be obtained over a range of incidence angles near broadside. This enhancement occurs only over a limited frequency band but does not create a reflection at broadside incidence.

To summarize, an analysis has been made which indicates that an inhomogeneous medium with closely-spaced resistive-strip elements can yield angular performance similar to that of the ideal homogeneous medium. In an example having D = 1 and w/s greater than 0.1, this desired performance occurs when the spacing is a quarter wavelength or less. Greater spacing may yield more or less attenuation, depending on other parameters and on how the A and B waves combine. Enhanced attenuation is possible by control of the transverse dielectric constant and/or the excess capacitance ratio of the strip medium.

SECTION 5

SIMULATOR TESTS OF AXIAL-CONDUCTANCE SAMPLES

5.1 INTRODUCTION

Before construction of a large angular-filter panel began, a series of samples were made of practical axial-conductance media. These samples have various dimensions (s/λ and w/s) and various D values, and they represent particular construction approaches for the axial-conductance medium. The samples were measured in waveguide to simulate an infinite-size medium at certain incidence angles (Ref. 18, 19).

Two types of simulators were used. One type has wide rectangular waveguide and represents incidence at broadside. The other type has square waveguide operating in the TM-11 mode and provides various angles in the E plane of incidence. Both types had proven to be valuable investigative tools in a previous angular-filter investigation (Ref. 10). The broadside and oblique incidence cases are discussed separately in subsections 5.2 and 5.3.

Ref. 18 - P. W. Hannan and M. A. Balfour, "Simulation of a Phased Array in Waveguide", IEEE Trans. Antennas and Propagation, pp 342-353; May 1965.

Ref. 19 - H. A. Wheeler, "A Survey of the Simulator Technique for Designing a Radiating element in a Phased Array", Phased Array Antenna Symposium, Artech House, pp 132-148; 1970.

5.2 BROADSIDE INCIDENCE SIMULATOR RESULTS

The broadside simulator has a rectangular waveguide operating in the dominant TE-10 mode. The frequency of operation is near 5 GHz. The width of the waveguide is 3.5 inches instead of the 1.8 inches ordinarily used at 5 GHz. This provides a fairly small incidence angle, approximately 20^{o}. Since TE mode is used, the incidence occurs in the H plane, not in the E plane. Therefore, this simulator provides a good approximation to broadside incidence for the axial-conductance media.

Figure 5-1 shows a cross section of the simulator waveguide containing a sample of the axial-conductance medium. The resistance strips are intentionally oriented with their w dimension parallel to the electric field in the waveguide in order to yield the maximum loss. The samples are 5 inches long, which is slightly over two wavelengths at 5 GHz.

Two types of construction for the resistance strips are used for the simulator samples. The first type utilizes commercially-available resistance-card material having particular values for the surface resistance. This material is cut into the desired narrow strips which are then inserted into holes in dielectric foam blocks for support. The second type of construction is the type used for the 5 x 5 foot filter panel. In this case, the resistance strips are printed on thin dielectric sheets, as will be

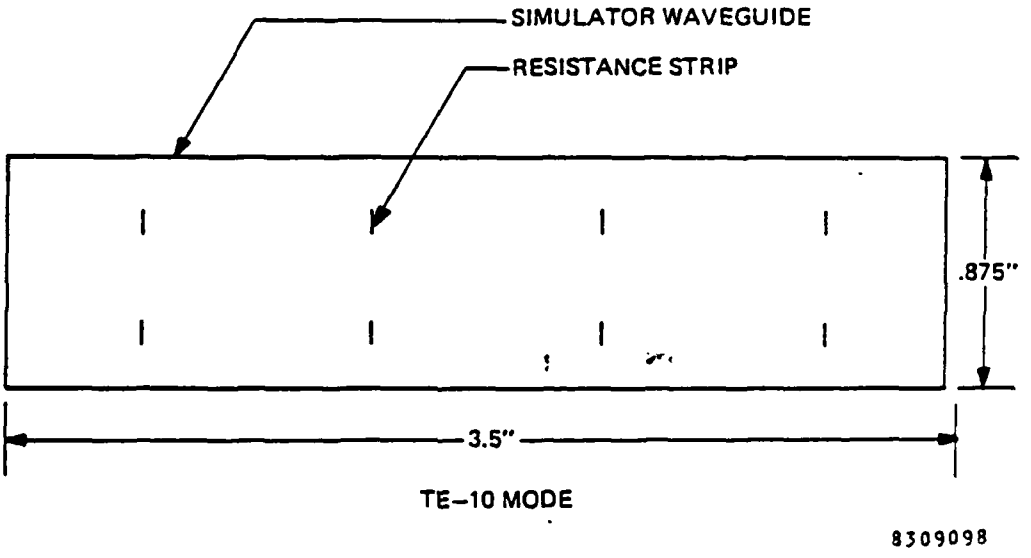

Figure 5-1. Broadside Simulator Cross Section

described in more detail in Section 6. The sheets are then sandwiched between layers of foam. Figure 5-2 shows a group of samples constructed for the broadside simulator.

The simulator waveguide containing a sample is connected at each end to a waveguide taper. One taper leads to a signal generator and calibrated attenuator; the other taper leads to a padded detector and signal-strength meter. The loss of the sample is determined by comparing readings with and without the sample present. The two tapers and some of the other equipment are shown in Figure 5-3.

Each sample is measured at eight frequencies from 4.4 to 5.8 GHz. This permits the averaging of measurement errors as well as providing some information on frequency trends.

Results for Low-Loss Sample. The first sample measured has s/λ and w/s dimensions close to those in the 5 x 5 foot panel. These dimensions are small enough so that the broadside loss is expected to be small.

Figure 5-4 shows the measured loss versus frequency for the first sample. The average loss is approximately 0.2 dB. The dimensions of this sample are $s/\lambda = 0.18$ and $w/s = 0.17$, and its axial loss tangent D is approximately unity. The sum of the E-field and H-field losses calculated from equations (50) and (60) is 0.2 dB, and is primarily H-field loss. Thus, the measured and calculated values agree within measurement accuracy, and the expected small loss is confirmed.

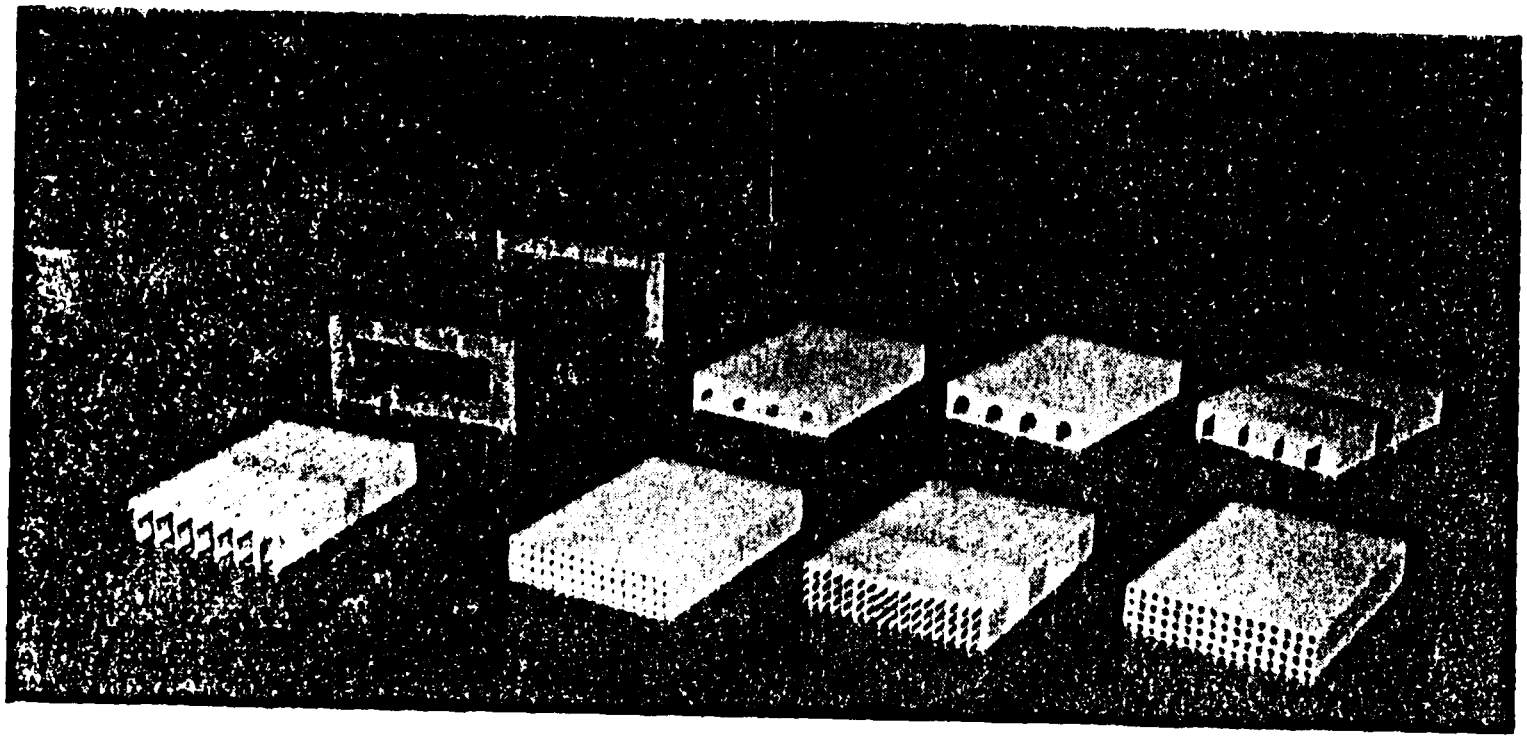

Figure 5-2. Broadside Simulator Samples

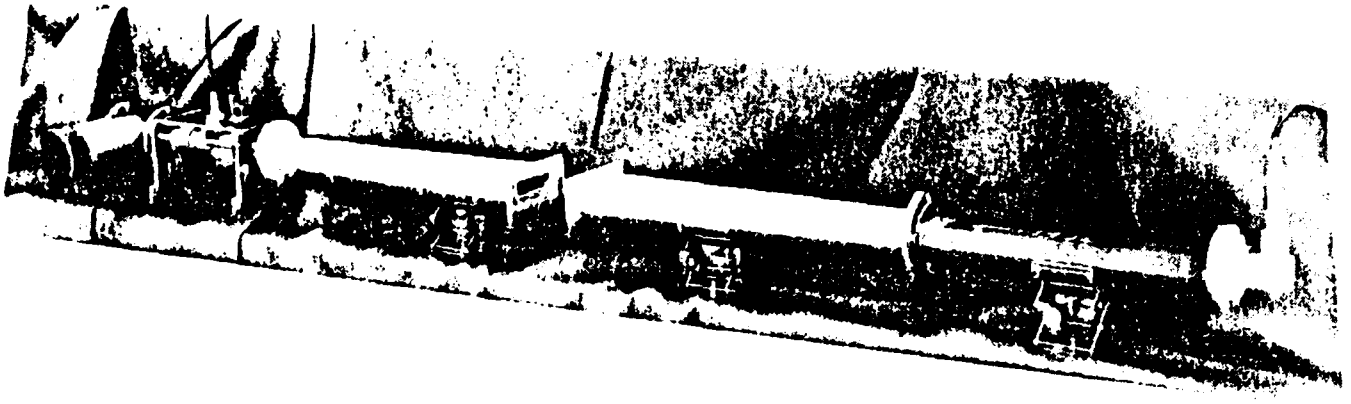

79G3106

Figure 5-3. Broadside Simulator System

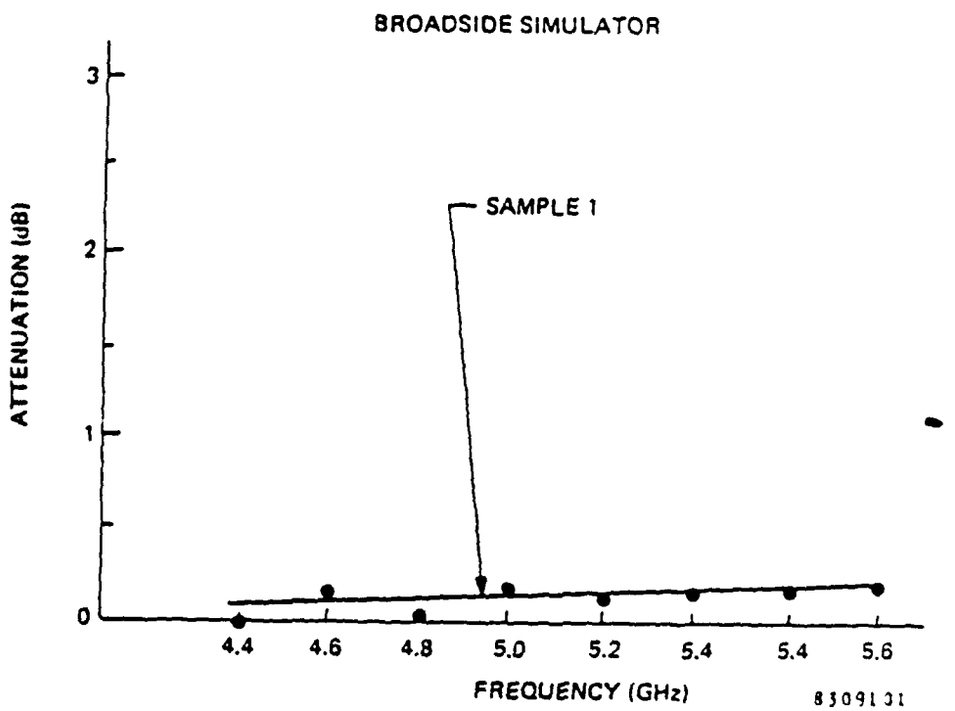

Figure 5-4. Measured Loss of Low-Loss Sample in Broadside Simulator

Results for High-Loss Samples. Since the loss of the first sample is small and is comparable with measurement accuracy, it does not provide a good test of the validity of equations (50) and (60). To accomplish this, a set of samples are constructed with s/λ and w/s large enough to yield a loss much larger than measurement accuracy. Furthermore, these dimensions and the values for D are chosen so that either the E-field or the H-field loss tends to predominate.

Figure 5-5 shows the measured loss for two such samples. The lower curve is for a sample labeled E-2 having $s/\lambda = 0.092$ and $w/s = 0.40$, with $D = 0.5$ at 5.0 GHz. The upper curve is for a sample labeled H-3 having $s/\lambda = 0.37$ and $w/s = 0.40$, with $D = 1$ at 5.0 GHz. Several other samples were also tested.

Figure 5-6 lists the results for seven samples tested in the broadside simulator, including the three shown in Figures 5-4 and 5-5. The sample dimensions and the computed E and H field losses are also given. All data are determined at 5.0 GHz.

It is seen that in most cases the measured loss is somewhat greater than the sum of the computed E-field and H-field losses. However the correlation appears to be sufficiently good that the two distinct relations (50) and (60) for E-field and H-field loss can be considered confirmed as approximations. It should be recognized that most of the samples designed for high loss have dimensions larger than those for which equations (50) and (60) are close approximations.

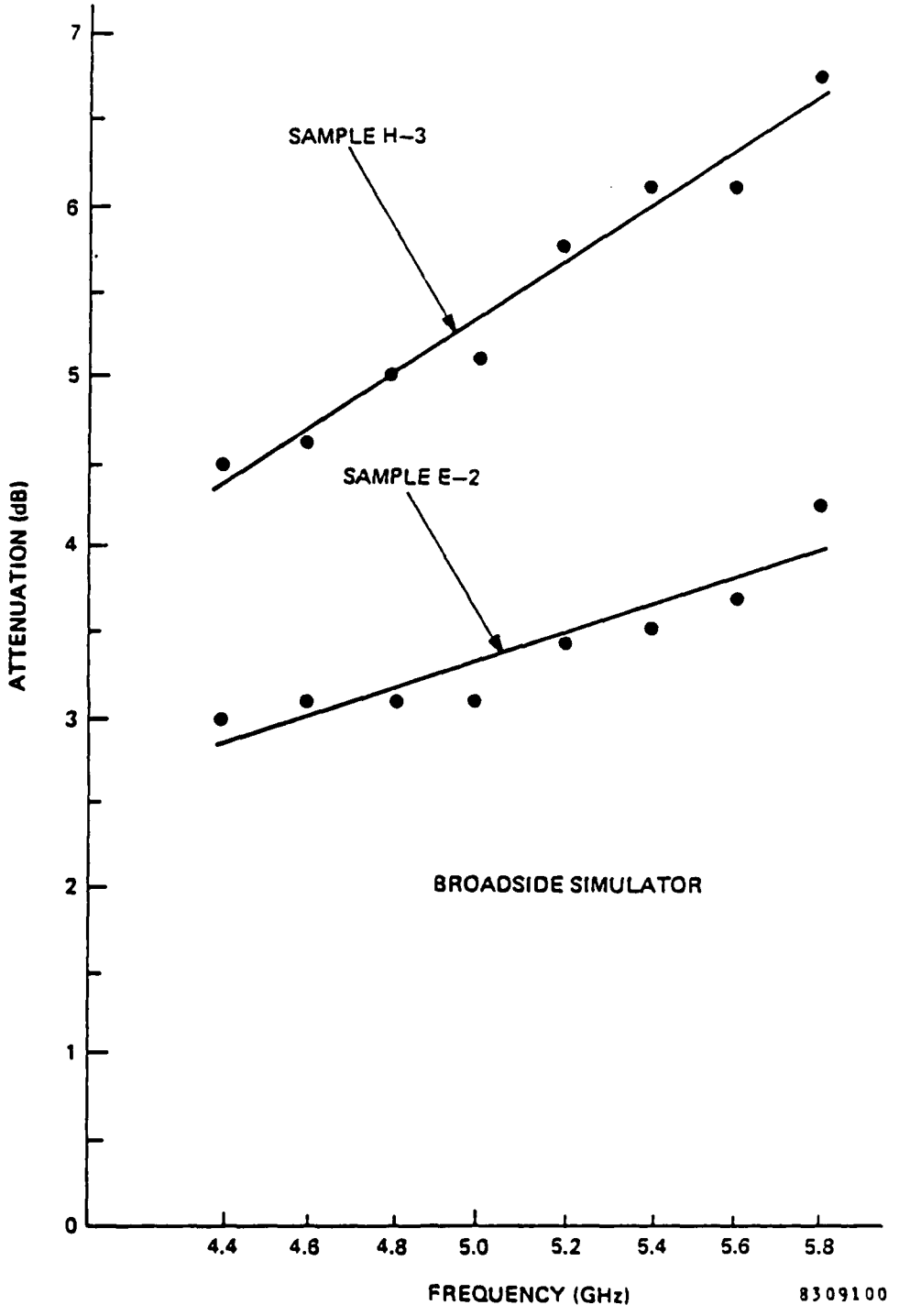

Figure 5-5. Measured Loss of Two High-Loss Samples in Broadside Simulator

SAMPLE	OBJECTIVE	TYPE	s/λ	w/s	w/λ	D	LOSS (dB)			
							CALCULATED			MEAS.
							E	H	E + H	
1	LOW LOSS	PRINT	0.18	0.17	0.034	0.95	0.03	0.2	0.2	0.2
E-1	HIGH E-LOSS	CUT	0.092	0.40	0.037	0.52	1.9	0.1	2.0	2.4
E-2		PRINT	0.092	0.40	0.037	0.50	2.0	0.1	2.1	3.3
E-3		CUT	0.092	0.60	0.055	0.76	6.5	0.4	6.9	8.0
H-1	HIGH H-LOSS	CUT	0.37	0.20	0.075	0.86	0.07	0.84	0.9	0.7
H-2		CUT	0.37	0.40	0.15	0.84	1.2	3.3	4.5	4.7
H-3		PRINT	0.37	0.40	0.15	1.0	1.0	3.9	4.9	5.3

ALL DATA IS AT 5.0 GHz. LOSS IS FOR 5 INCH SAMPLE.

8309099

Figure 5-6. Results for Seven Samples Tested in Broadside Simulator

Two of the "E" samples and two of the "H" samples have similar parameters but use different construction methods. The two "H" samples (H-2 and H-3) give similar measured results. However, the printed "E" sample (E-2) gives a measured loss greater than the cut-card "E" sample (E-1). This difference may be caused by the effective width of the cut resistance cards being smaller than their nominal physical width, or by the transverse current enhancement of the printed sample caused by the thin dielectric substrate, or by both of these effects.

Another characteristic of the broadside loss that appears in the simulator measurements is the increase of broadside loss with frequency. Examples of this increase were evident in Figure 5-5. Inspection of equations (49) and (59) shows that for a given thickness of the axial-conductance medium both the E-field and the H-field broadside losses should be essentially proportional to the square of frequency. The measured results typically show somewhat less variation with frequency, probably caused in part by the natural cutoff effect of the simulator waveguide.

Summary of Broadside Simulator Results. The measurements of inhomogeneous axial-conductance samples in waveguide simulating broadside incidence have verified that small loss at broadside incidence is obtained when w/s and w/λ are made sufficiently small. The measurements have also indicated that equations (50) and (60) for the two components of broadside loss are valid approximations.

5.3 OBLIQUE INCIDENCE SIMULATOR RESULTS

The oblique incidence simulators have square waveguide operating in the TM-11 mode. The TM mode provides incidence in the E plane, as is desired for measurement of the angular rejection behavior of the axial-conductance filter medium. Figure 5-7 shows a cross section of the simulator waveguide containing a sample of the axial-conductance medium. Again, the samples are 5 inches long, or slightly over two wavelengths at 5 GHz.

Figure 5-8 shows a group of samples constructed for the oblique incidence simulators. Again, both the cut-card and the printed types of construction are used for the samples. Two different size samples are seen, corresponding to two different sizes used for the simulator square waveguide. The large size is 2.26 inches square, yielding an incidence angle of approximately 45^{o} at 5 GHz. The smaller size is approximately 1.7 inches square yielding an incidence angle near grazing at 5 GHz. Results from these two sizes are discussed separately in the remainder of this section.

(a) Large Square Simulator Results

The large square simulator provides E-plane incidence angles in the vicinity of 45^{o}. Actually, as frequency is varied from 4.4 to 5.8 GHz, the incidence angle varies from about 54^{o} to about 38^{o}. The TM-11 mode is excited in the square waveguide by an axial probe in the center of the square cross section. This probe is reasonably well matched over the operating frequency band; additionally, adjustable calibrated tuners are employed to obtain a well-matched measurement system.

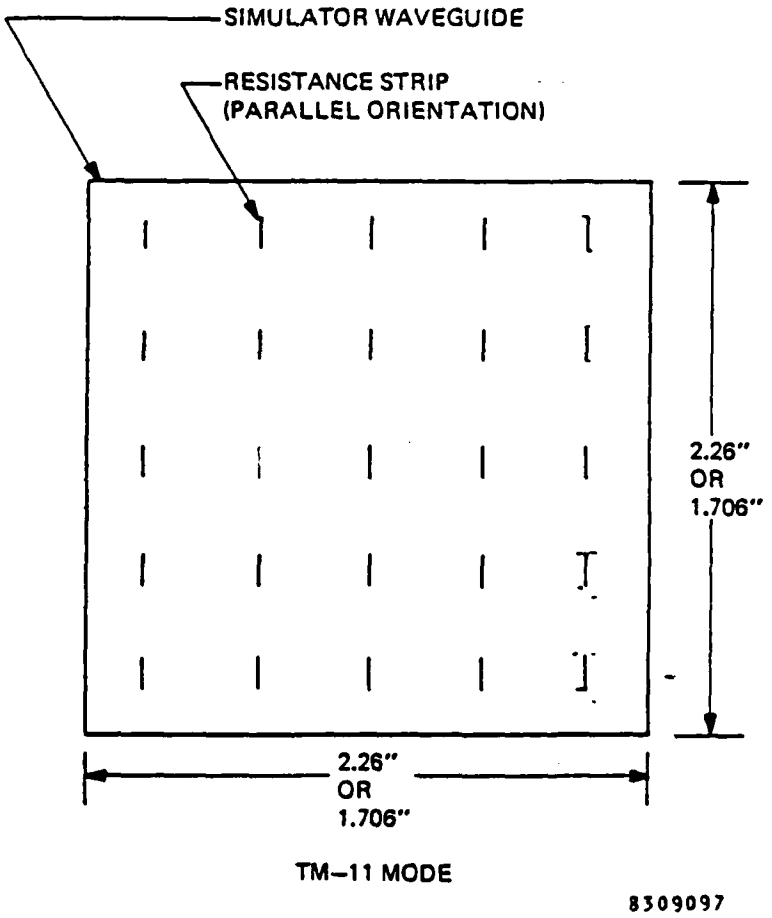

Figure 5-7. Oblique-Incidence Simulator Cross Section

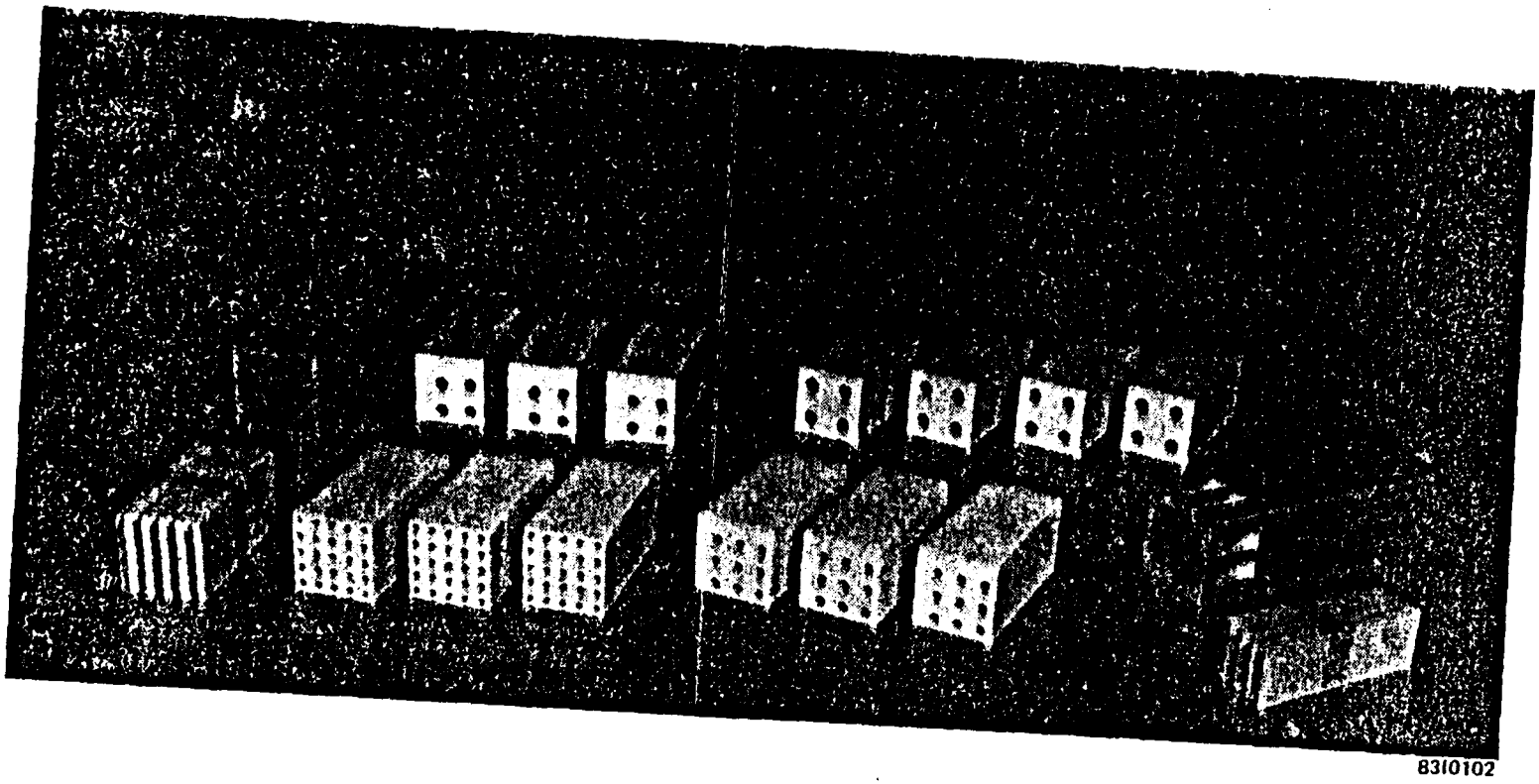

Figure 5-8. Oblique-Incidence Simulator Samples

The two main objectives of the sample measurements in the large square simulator are (1) to see whether closely-spaced resistance strips yield an attenuation at 45° comparable with the attenuation expected of an equivalent homogeneous medium, and (2) how the attenuation changes when the resistance strips are not closely spaced. An additional objective is to measure the impedance behavior of the samples.

Figure 5-9 shows the measured attenuation versus frequency at 0.2 GHz intervals for a printed sample having $s/\lambda = 0.19$ and $w/s = 0.17$, with $D = 0.76$ at 5.0 GHz. Also shown is a computed curve of attenuation that includes both the frequency and the resulting incidence angle in the simulator as inputs to the computation of attenuation. Equation (11) for the ideal homogeneous medium is used for this computation. It is seen that the measured data agrees closely with the curve that is computed for a homogeneous medium.

There are several other samples having the same s/λ but having $w/s = 0.39$. These samples are cut from resistance cards and have several different values of D. Figure 5-10 shows the results for $D = 1.0$. Two sets of data points are shown. For the upper set, the resistance strips are oriented parallel as was shown in Figure 5-7. For the lower set, the strips are individually oriented so that their w dimension is approximately perpendicular to the transverse electric field in the TM-11 mode, as shown in Figure 5-11. This second orientation should eliminate most of the E-field and H-field broadside loss that exists in the first orientation. With $w/s = 0.39$, this sample has a

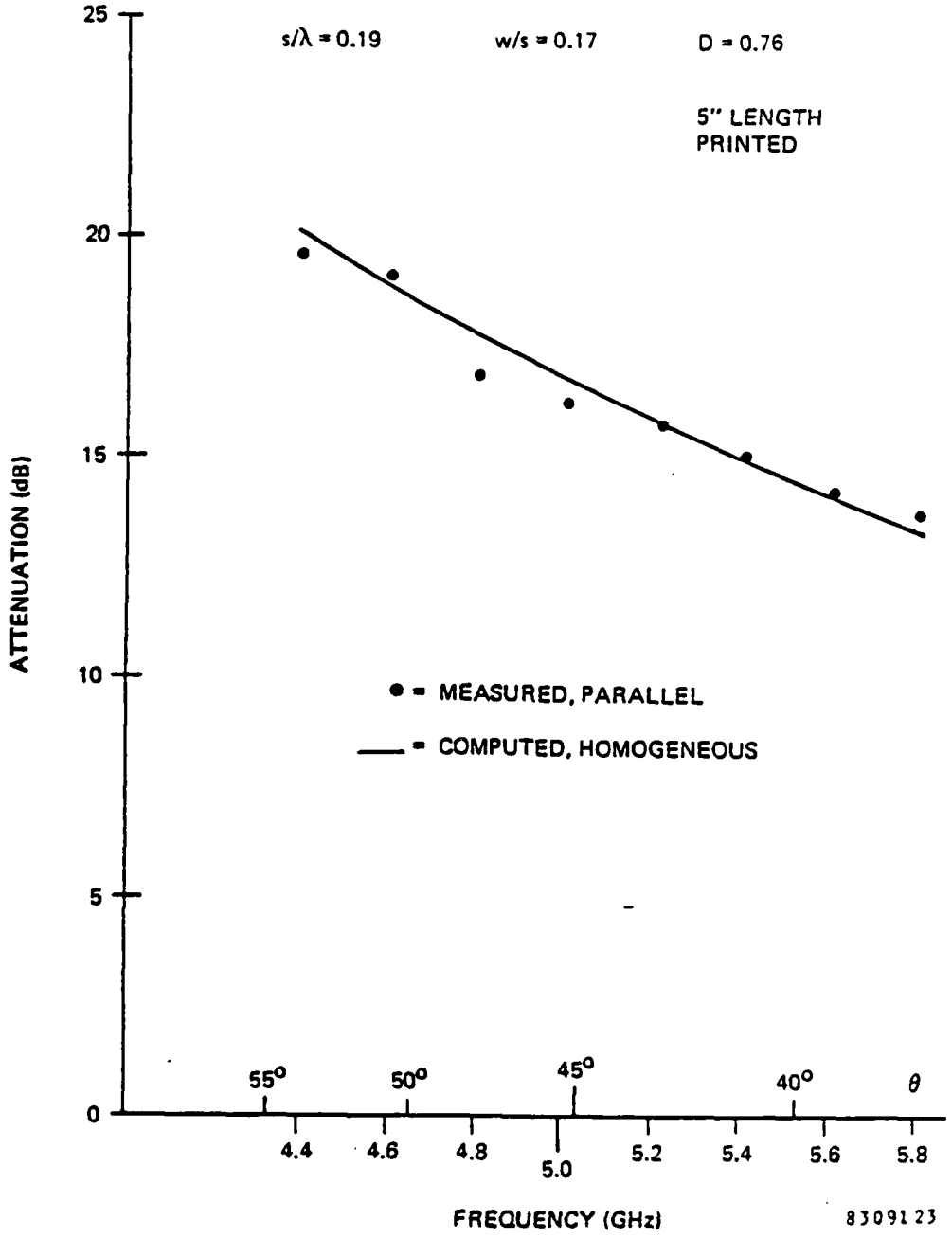

Figure 5-9. Measured Attenuation vs Frequency in Large Square Simulator for $s/\lambda = 0.19$, $w/s = 0.17$, $D = 0.76$

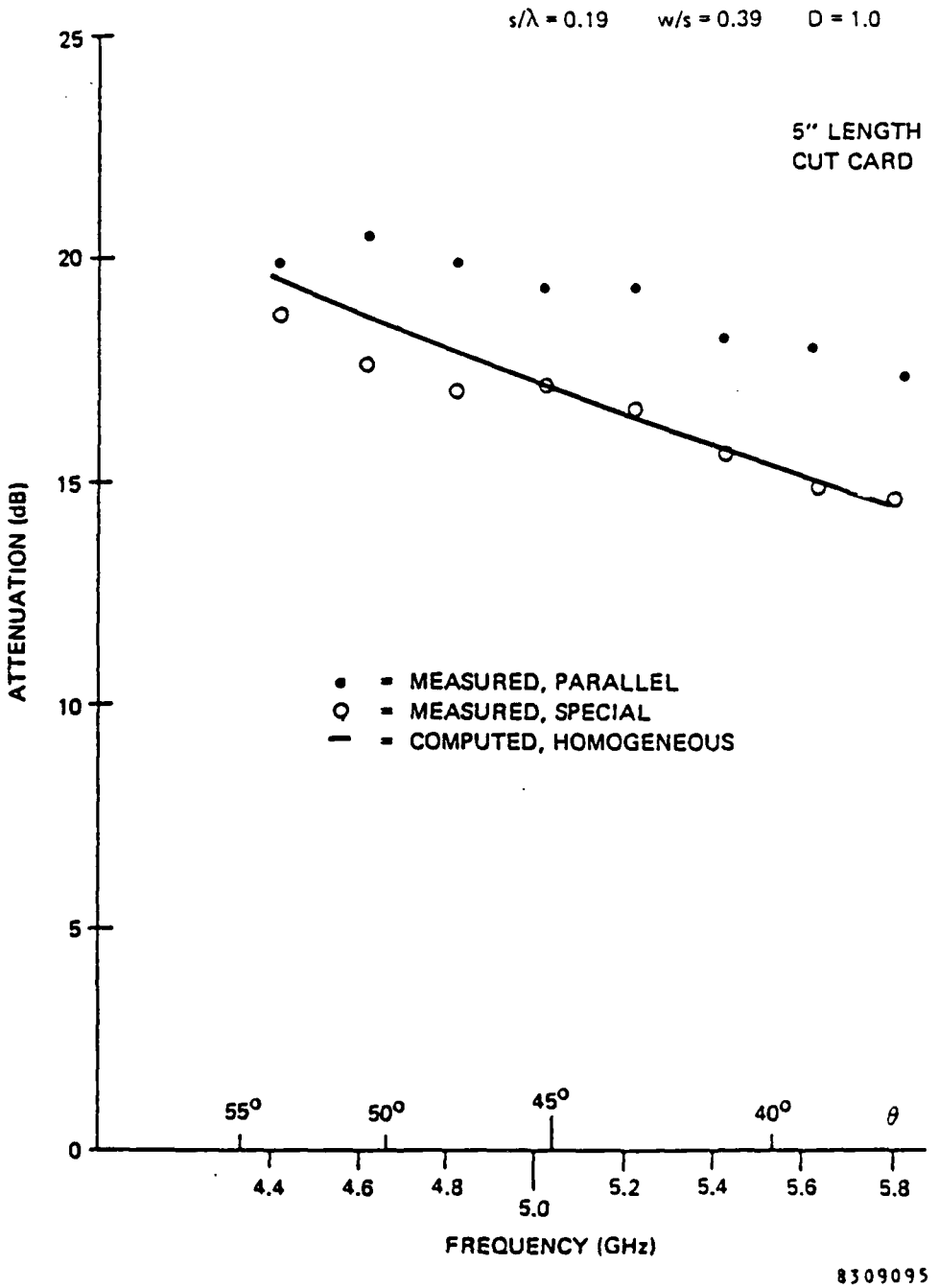

Figure 5-10. Measured Attenuation vs Frequency in Large Square Simulator for $s/\lambda = 0.19$, $w/s = 0.39$, $D = 1.0$

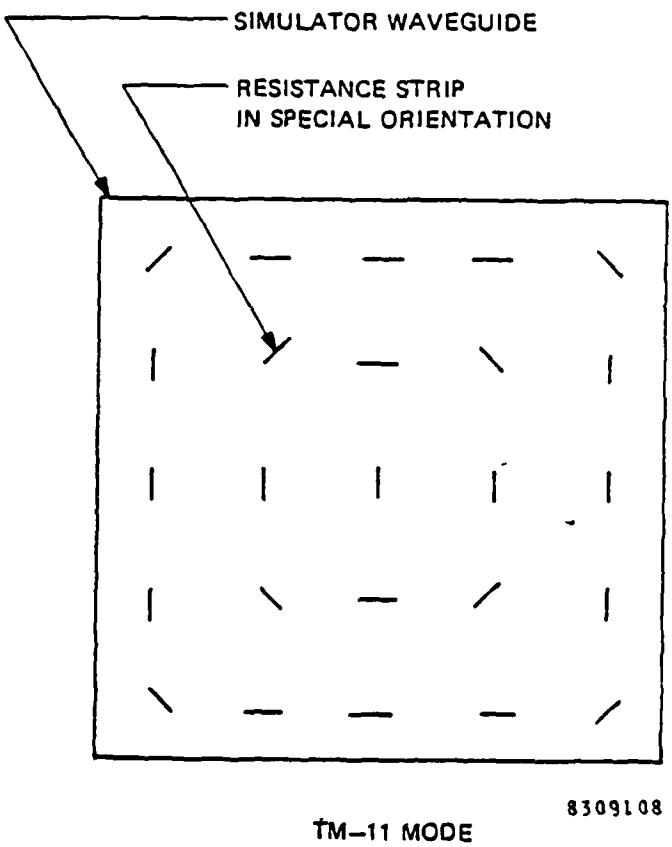

Figure 5-11. Special Orientation of Strips in Oblique-Incidence Simulator

substantial broadside loss. It is seen in Figure 5-10 that the second orientation yields data points close to the calculated curve for a homogeneous medium.

Figures 5-12 and 5-13 show the results for the same s/λ and w/s but D = 0.24 and 4.2, respectively. Of course, with D far from unity the attenuation is substantially reduced. These samples have the w dimensions oriented parallel, and there is a substantial broadside-loss component included in the results. Also, it should be recognized that the value given for D is based on DC measurements of strip resistance, which may not be entirely accurate for giving the effective value for D. With these two factors in mind, a comparison of the data points with the calculated curves for a homogeneous medium shows reasonable agreement.

Figures 5-14, 5-15, and 5-16 show the results for s/λ increased to 0.27, and D = 0.22, 0.91, and 2.6, respectively. Data is shown for the two orientations of the strips. Comparison of the measured points with the curves calculated for a homogeneous medium again shows reasonable agreement, with perhaps somewhat greater values for the measured attenuation at the higher frequencies.

Figures 5-17, 5-18, and 5-19 show the results for s/λ increased to 0.38, with D = 0.19, 0.45, and 0.89, respectively. In the first two cases, the measured attenuation is consistently greater than the attenuation calculated for a homogeneous medium. In the third case, the measured attenuation exhibits an increase with frequency, in contrast to the decrease given by the calculated curve for a homogeneous medium in the simulator waveguide.

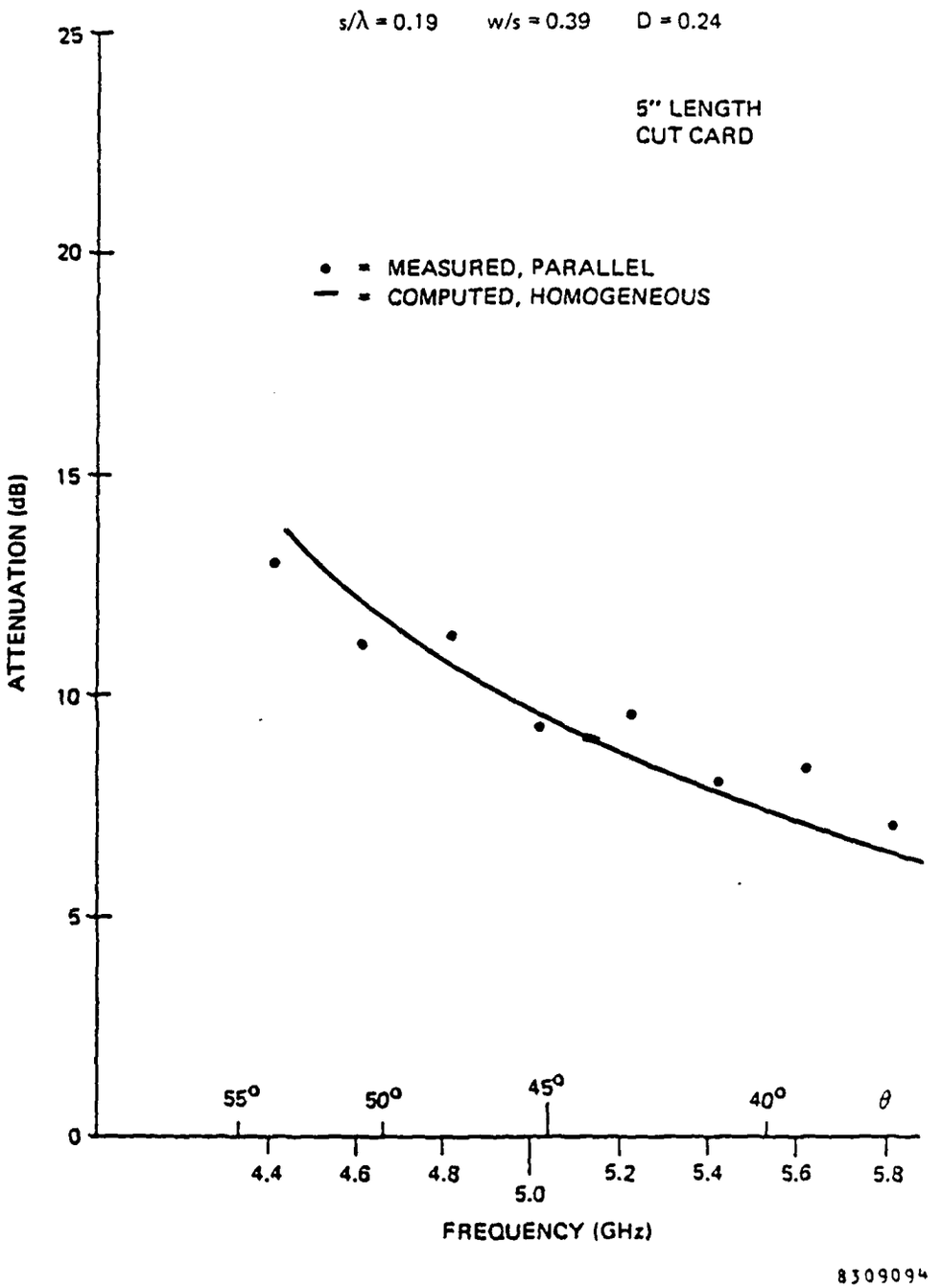

Figure 5-12. Measured Attenuation vs Frequency in Large Square Simulator for $s/\lambda = 0.19$, $w/s = 0.39$, $D = 0.24$

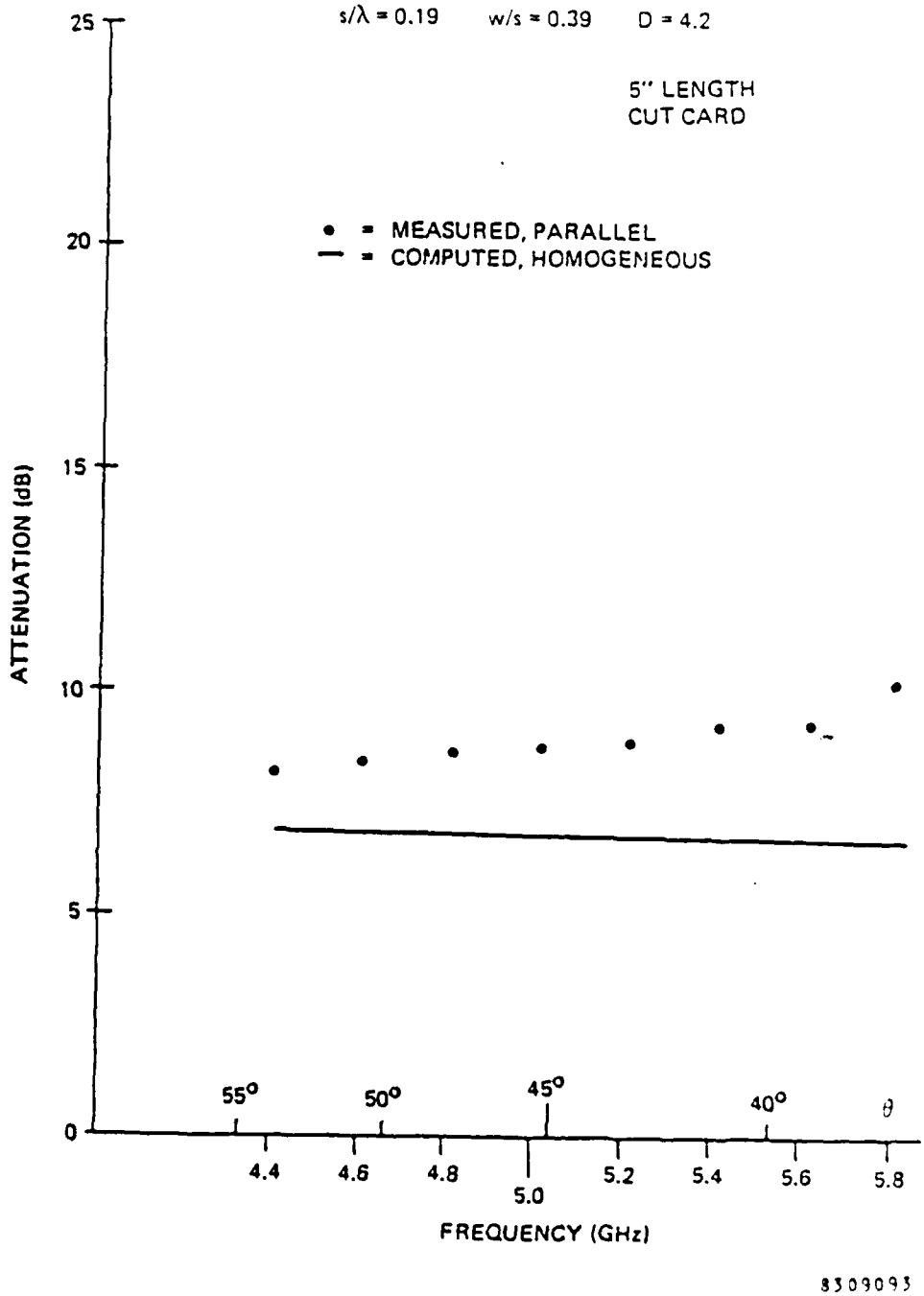

Figure 5-13. Measured Attenuation vs Frequency in Large Square Simulator for $s/\lambda = 0.19$, $w/s = 0.39$, $D = 4.2$

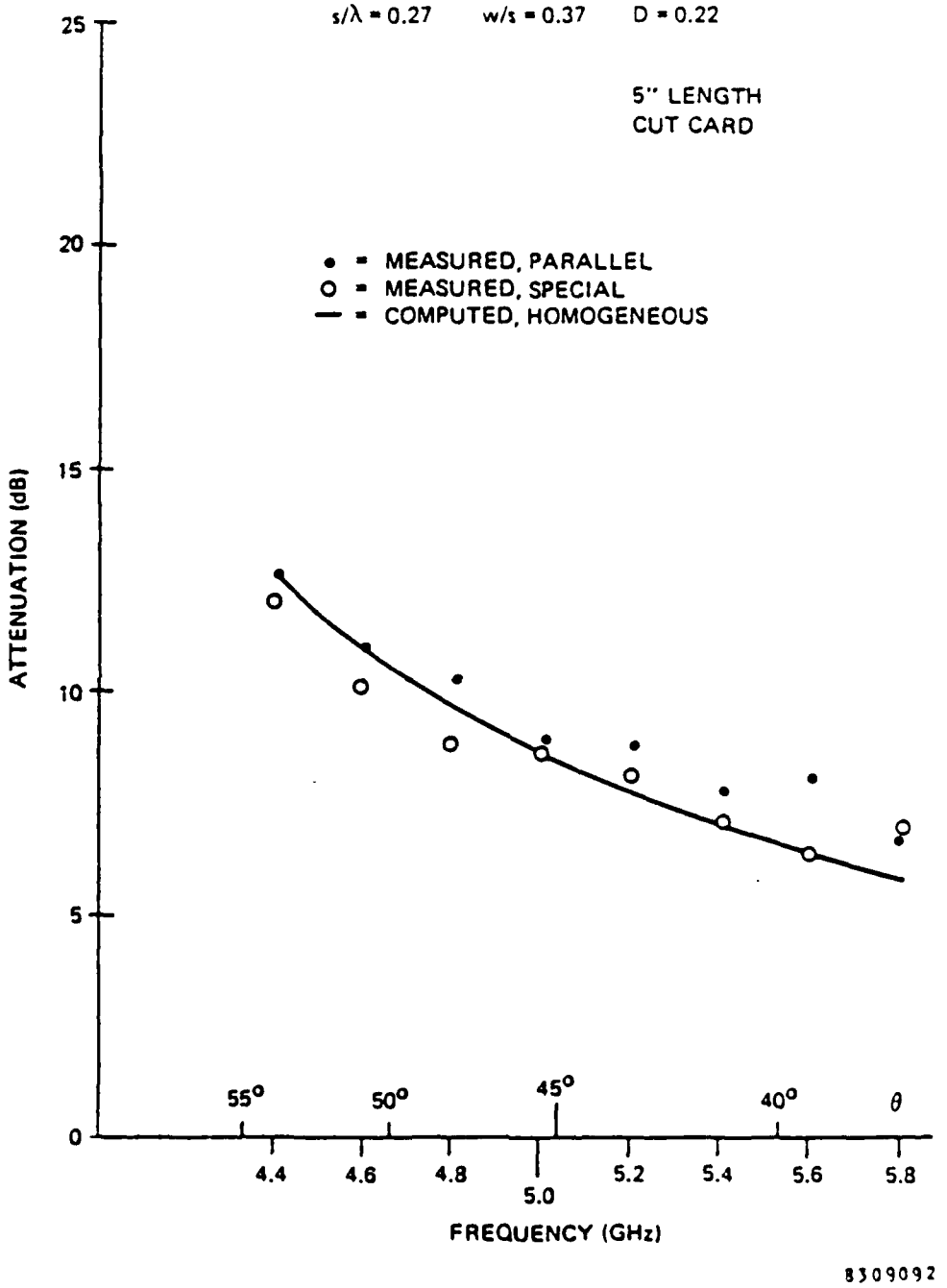

Figure 5-14. Measured Attenuation vs Frequency in Large Square Simulator for $s/\lambda = 0.27$, $w/s = 0.37$, $D = 0.22$

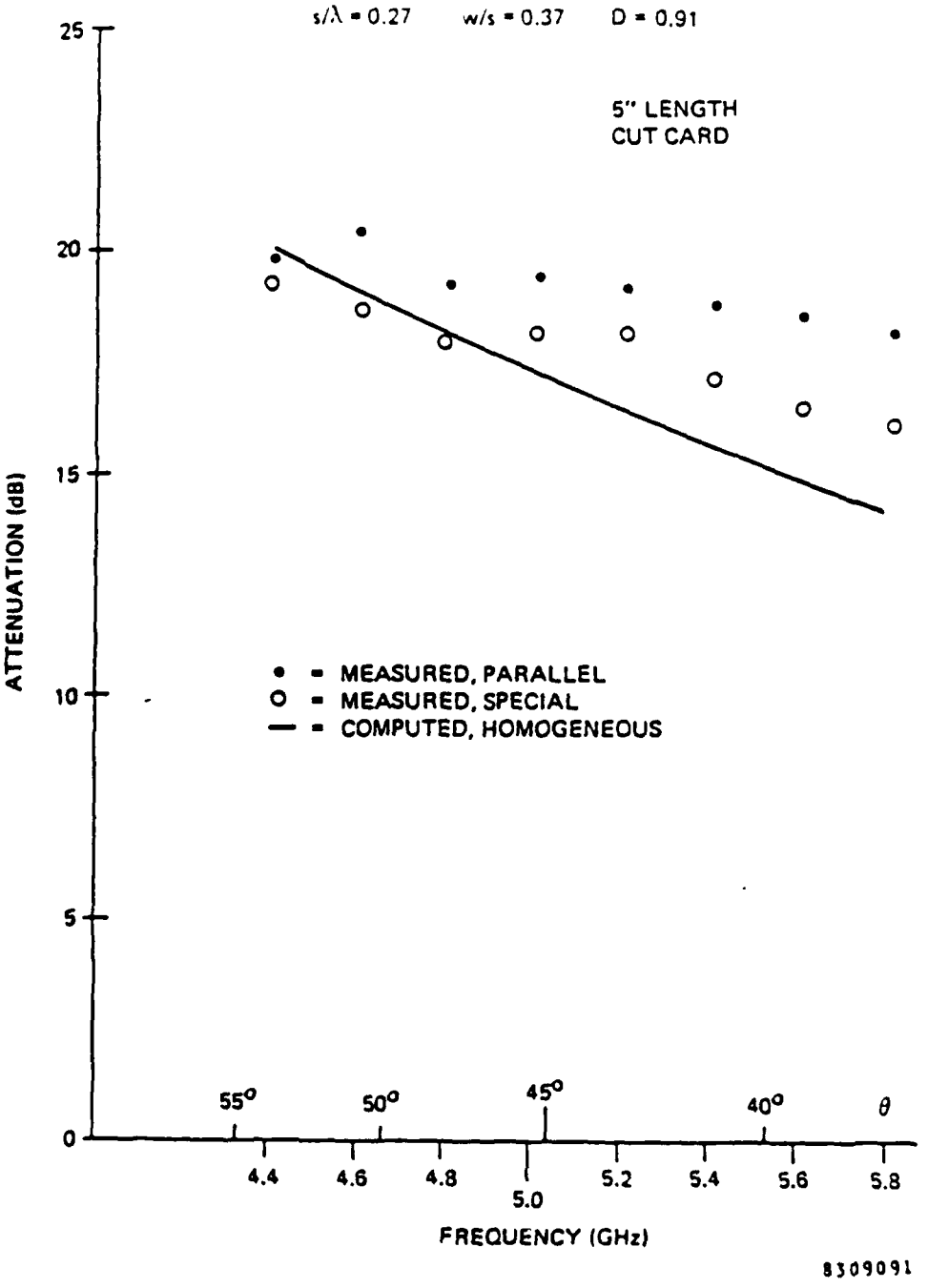

Figure 5-15. Measured Attenuation vs Frequency in Large Square Simulator for $s/\lambda = 0.27$, $w/s = 0.37$, $D = 0.91$

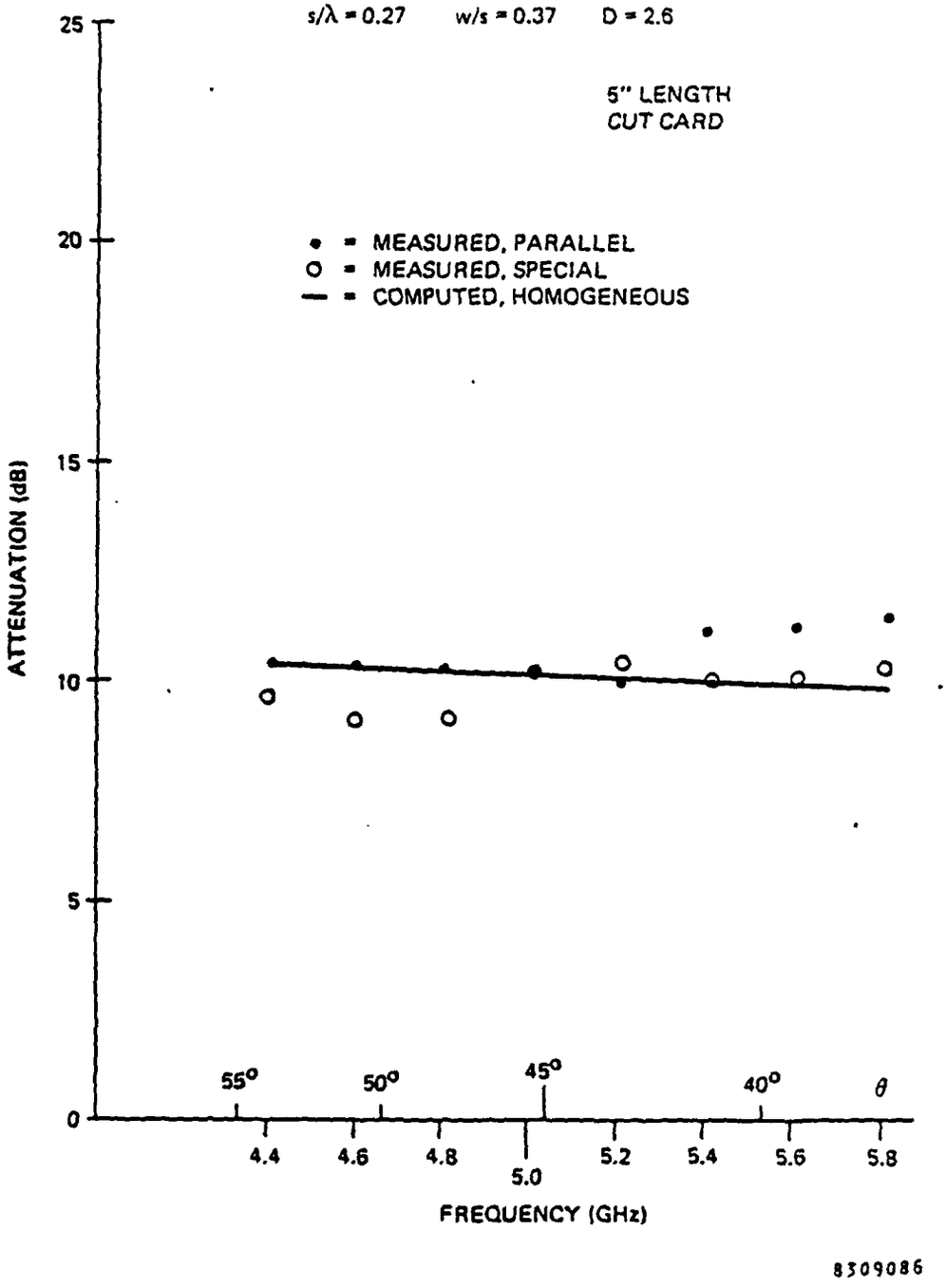

Figure 5-16. Measured Attenuation vs Frequency in Large Square Simulator for $s/\lambda = 0.27$, $w/s = 0.37$, $D = 2.6$

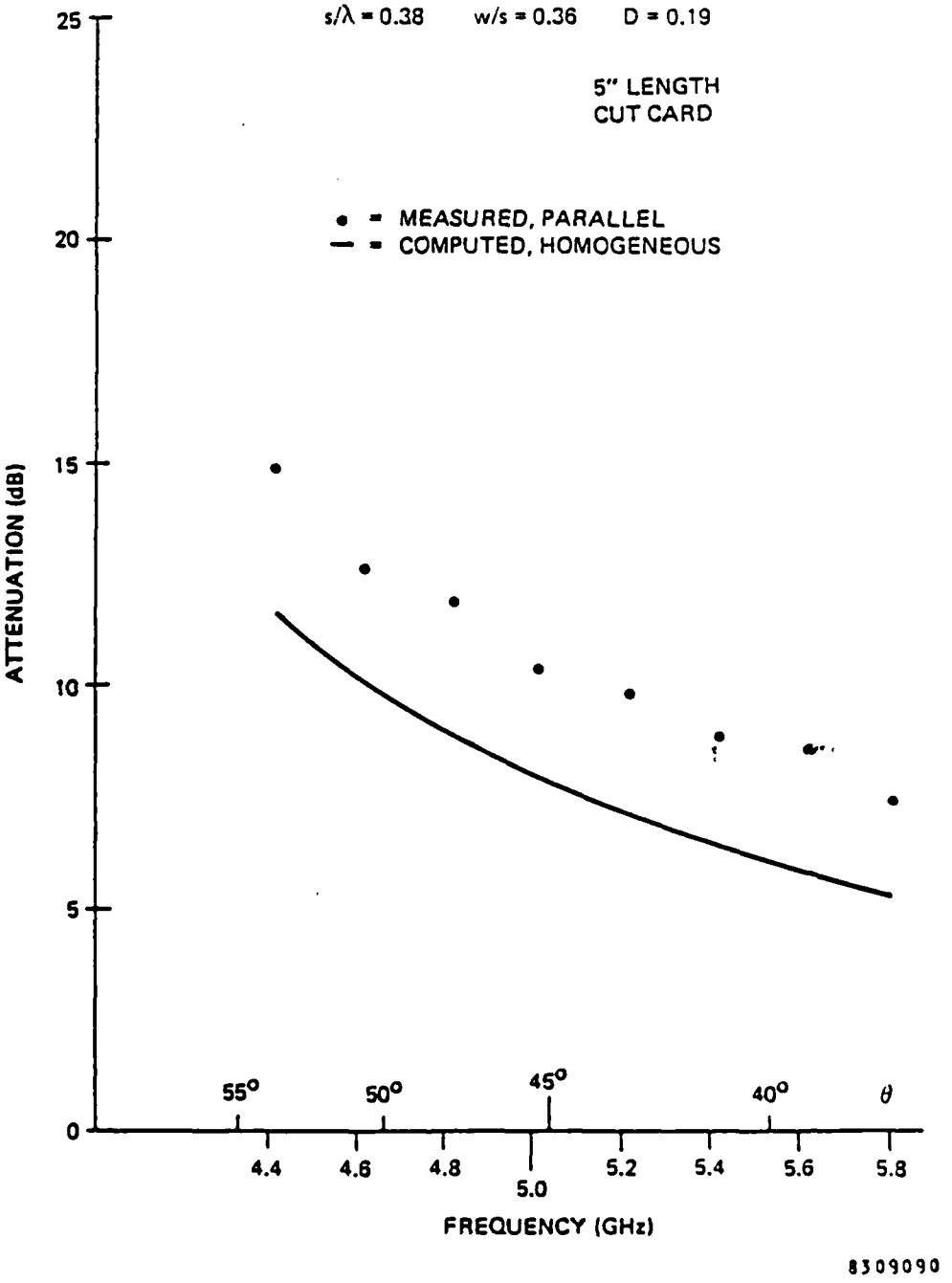

Figure 5-17. Measured Attenuation vs Frequency in Large Square Simulator for $s/\lambda = 0.38$, $w/s = 0.36$, $D = 0.19$

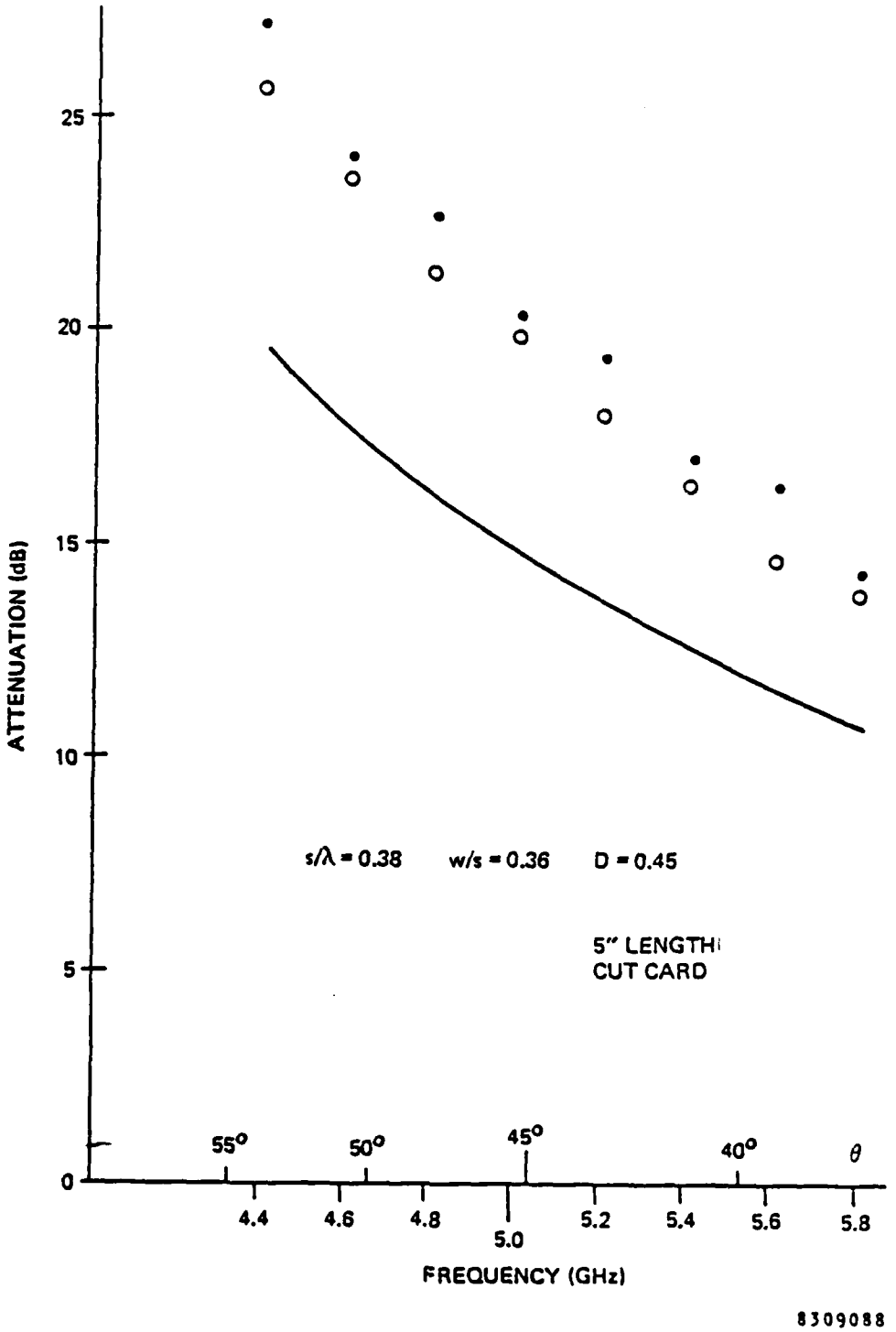

Figure 5-18. Measured Attenuation vs Frequency in Large Square Simulator for $s/\lambda = 0.38$, $w/s = 0.36$, $D = 0.45$

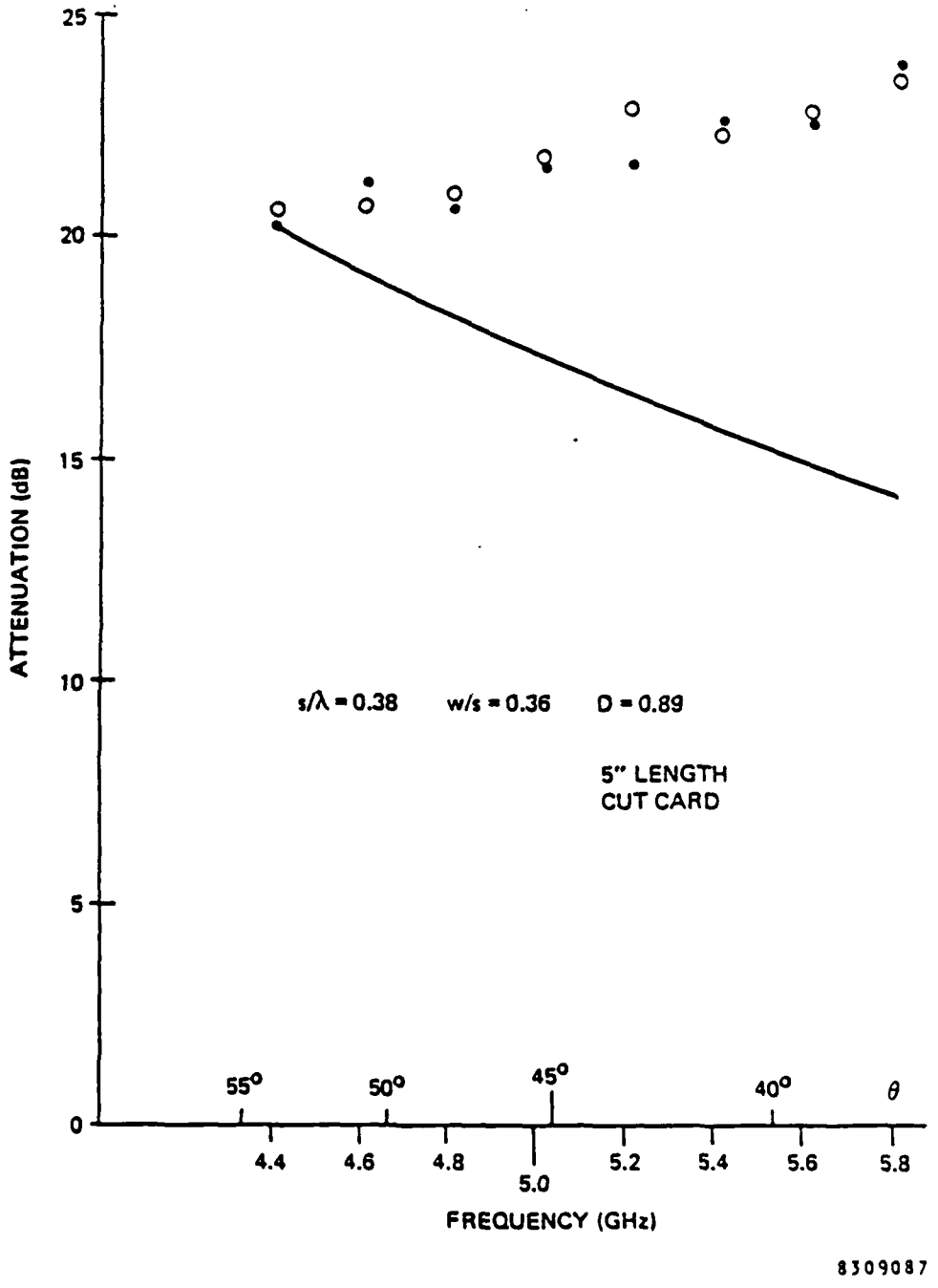

Figure 5-19. Measured Attenuation vs Frequency in Large Square Simulator for $s/\lambda = 0.38$, $w/s = 0.36$, $D = 0.89$

Figures 5-20, 5-21, 5-22 and 5-23 show the results for s/λ increased to 0.48, with D = 0.22, 0.57, 0.76, and 1.2, respectively. For D = 0.22 the measured attenuation is greater than the calculated homogeneous case. However, for D = 0.57 the measured attenuation exhibits a resonant-like response versus frequency and/or incidence angle, with the peak attenuation roughly twice that given by the calculated homogeneous curve.

For D = 0.76 a similar resonant-like response is obtained, but with a smaller enhancement of the attenuation and a somewhat different frequency or angle for peak attenuation. In both resonant-like cases, the parallel orientation of the strips appears to yield substantially greater peak attenuation than does the special orientation. For D = 1.2 the measured attenuation does not exhibit the resonant-like response, but appears to be smaller than that for the calculated homogeneous case.

In addition to attenuation, the VSWR of each sample was measured over the frequency band. Each measured result was compared with the VSWR calculated from equation (20) for a homogeneous medium in the simulator waveguide. Figure 5-24 shows an example of the VSWR results for one sample. It is seen that the measured VSWR points have the same trend as the calculated curve but have somewhat smaller values. This behavior occurs for virtually all of the samples, including those having a resonant-like attenuation response.

Discussion of Large Square Simulator Results. The measurements of samples of the inhomogeneous axial-conductance medium in the large square TM-11 simulator have

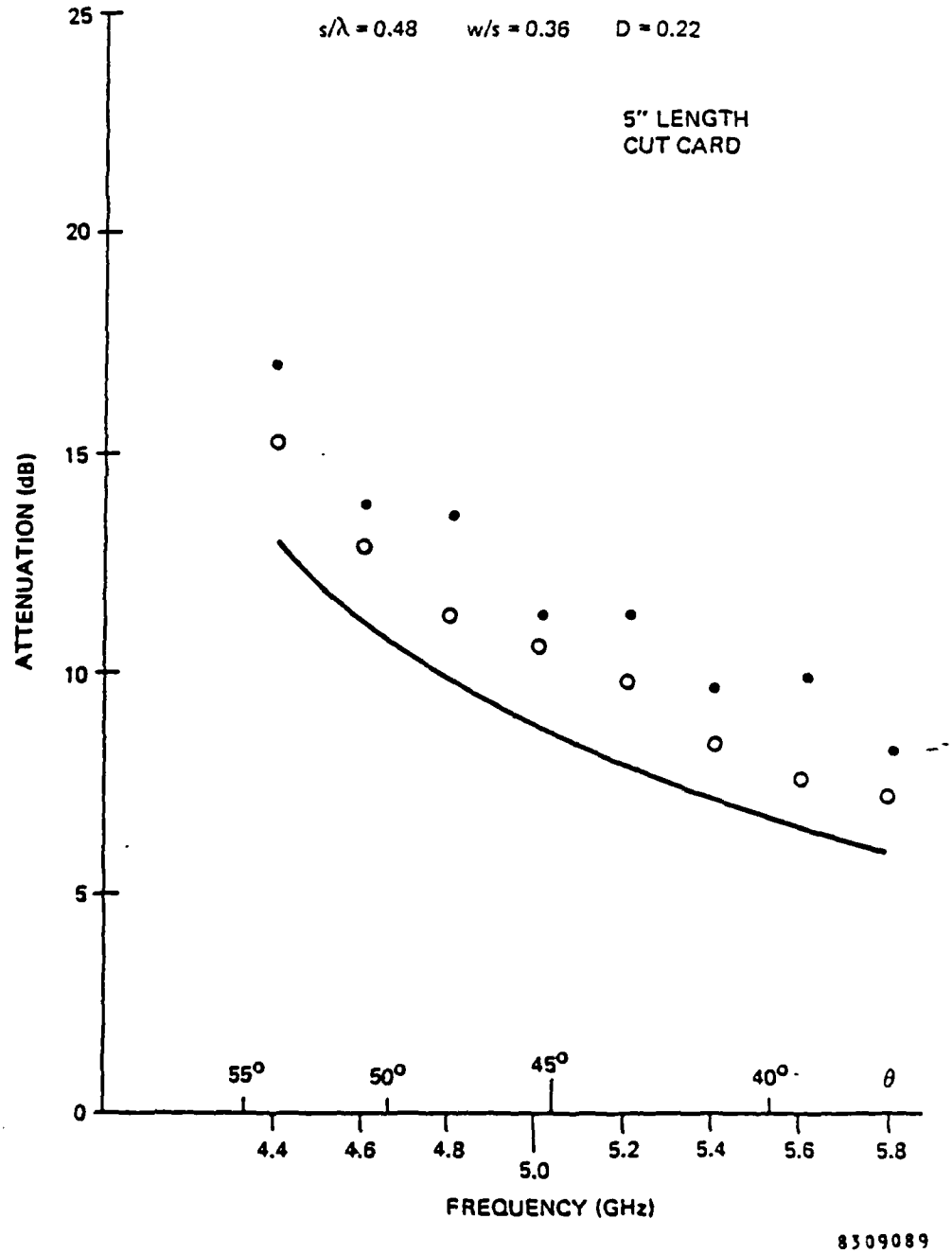

Figure 5-20. Measured Attenuation vs Frequency in Large Square Simulator for $s/\lambda = 0.48$, $w/s = 0.36$, $D = 0.22$

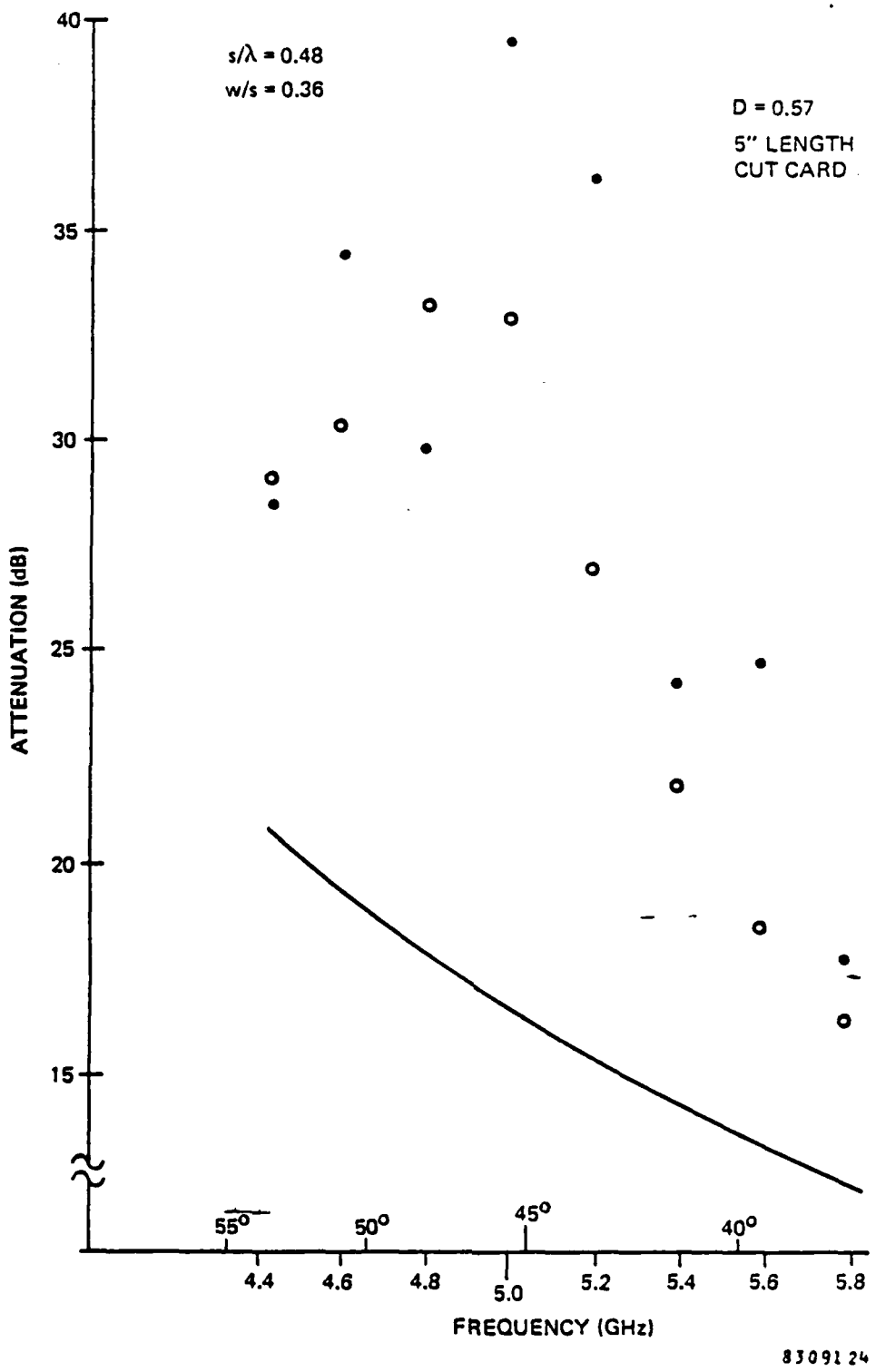

Figure 5-21. Measured Attenuation vs Frequency in Large Square Simulator for $s/\lambda = 0.48$, $w/s = 0.36$, $D = 0.57$

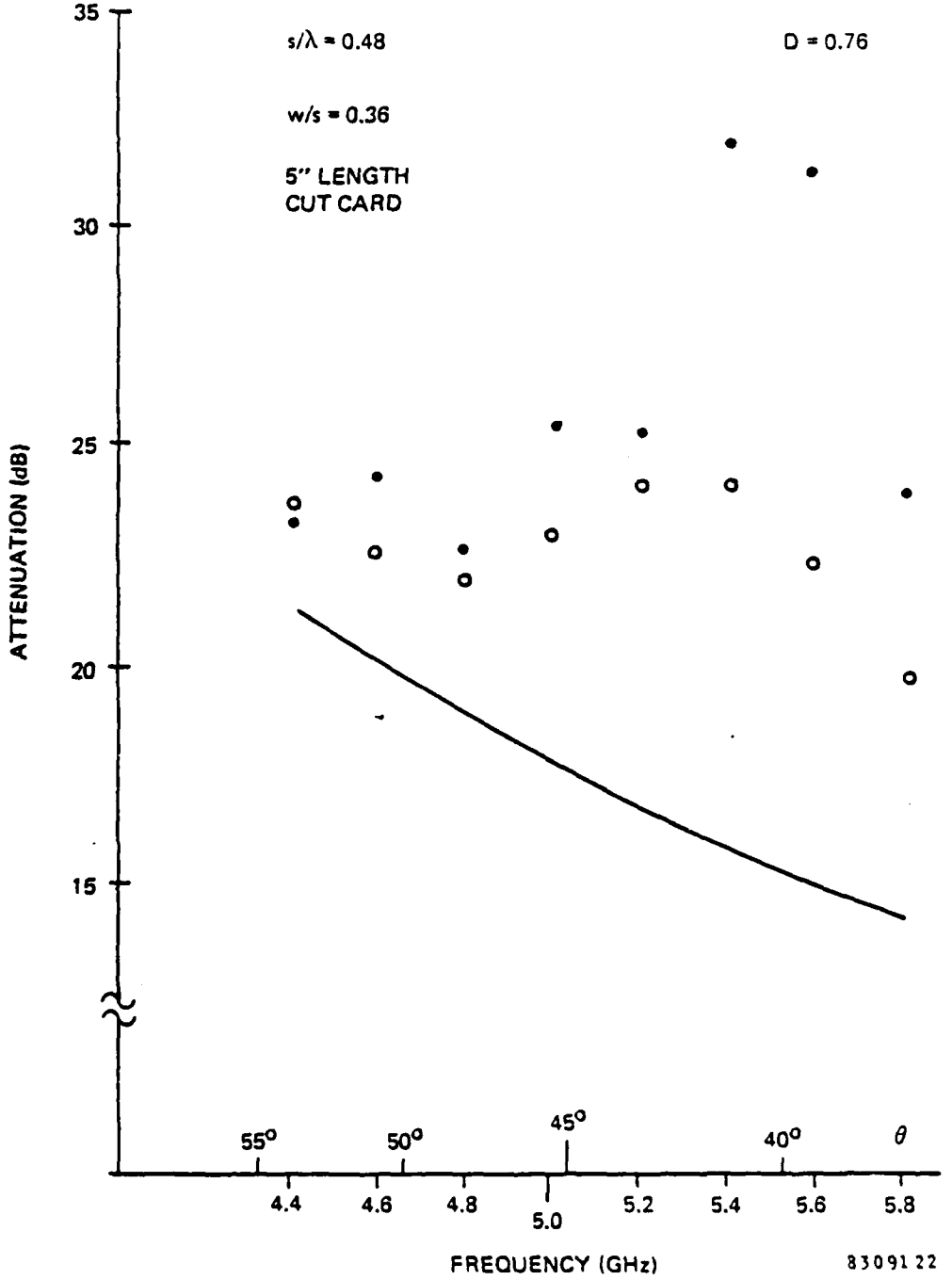

Figure 5-22. Measured Attenuation vs Frequency in Large Square Simulator for $s/\lambda = 0.48$, $w/s = 0.36$, $D = 0.76$

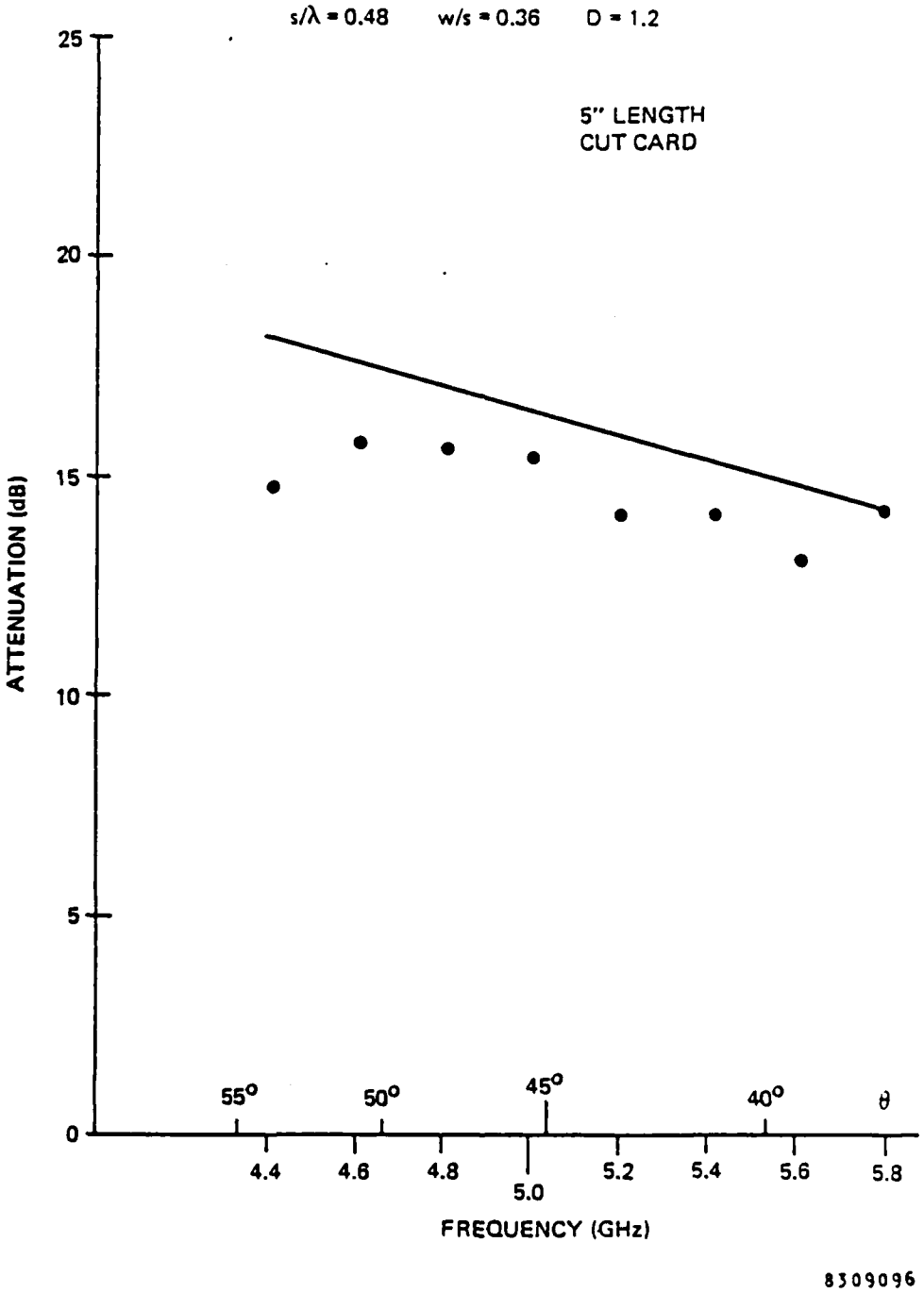

Figure 5-23. Measured Attenuation vs Frequency in Large Square Simulator for $s/\lambda = 0.48$, $w/s = 0.36$, $D = 1.2$

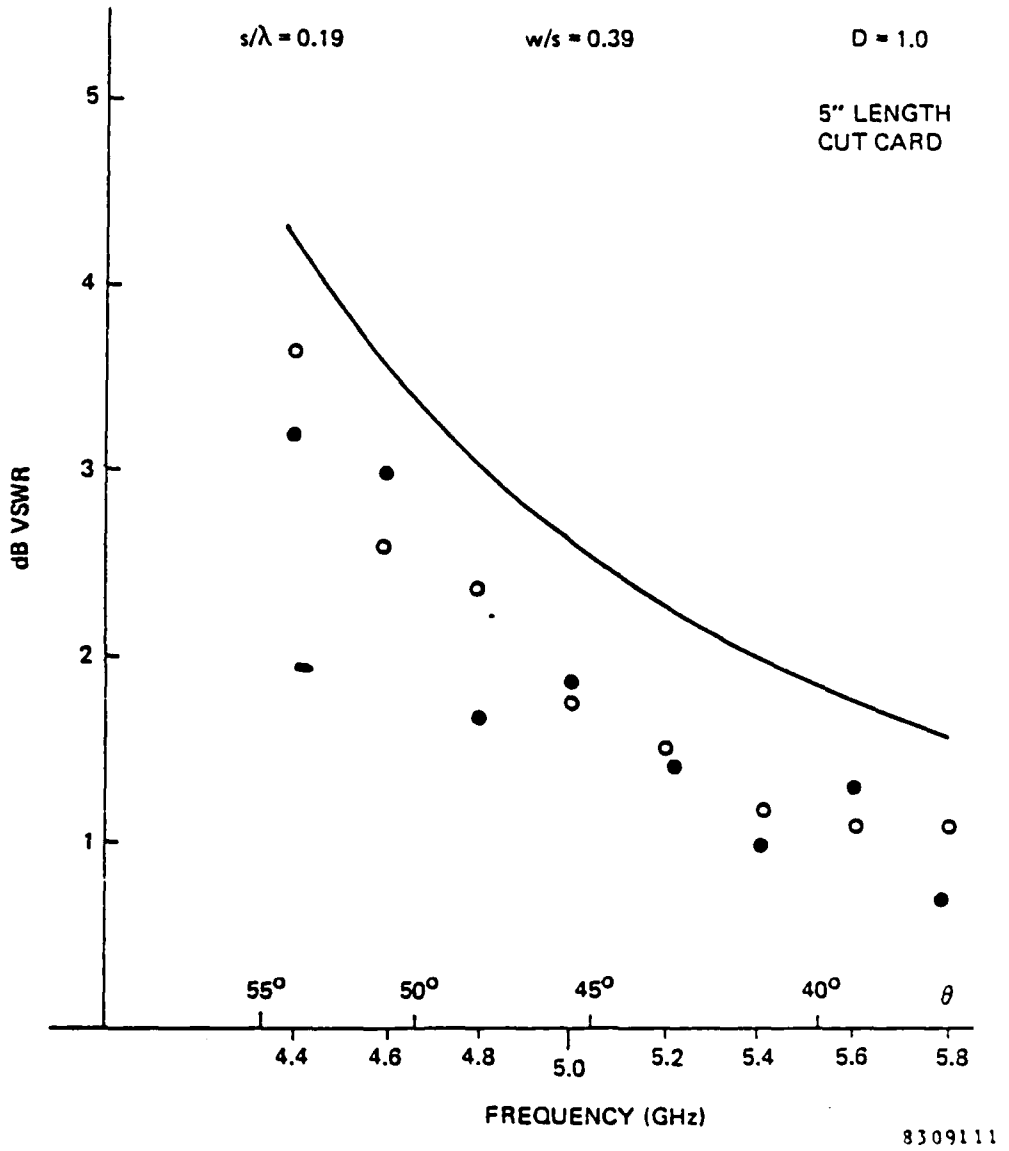

Figure 5-24. Measured VSWR vs Frequency in Large Square Simulator for $s/\lambda = 0.19$, $w/s = 0.39$, $D = 1.0$

confirmed the expectation that with small s/λ the attenuation of the inhomogeneous medium for moderate incidence angles is essentially the same as that of the ideal homogeneous medium. Figure 5-9, and Figures 5-10 through 5-13, illustrate this correspondence.

For the samples measured, this correspondence remains reasonably good for s up to about a quarter wavelength (Figures 5-14 through 5-16). With spacing increased further to 0.38 wavelength, some substantial changes are observed (Figure 5-19). A further increase to 0.48 wavelength yields a resonant-like enhancement of the attenuation for two of the four values of D measured (Figures 5-21 and 5-22).

Since the largest spacing used is less than a half wavelength, and the angle of incidence is less than 90°, it is believed that a grating lobe cannot exist in the samples measured. Therefore some other explanation is needed to account for the resonant-like enhancement. It is speculated that the A-wave/B-wave junction effect that appeared in the computed results in Figures 4-18, 4-19, 4-25 and 4-26 may be related to the resonant-like measured enhancement. The computed attenuation in the vicinity of that junction is unusually large.

The correspondence between the computed junction effect and the measured enhancement is not exact. For example, the computed junction effect requires a value for the susceptance ratio b that is between 0 and -1, while the b for the Figure 5-21 and 5-22 samples is -1.2, as determined from equation (90). However it should be

recognized that the approximate analysis in Section 4 is not accurate when the spacing s approaches a half wavelength. There is, at least, a rough correspondence in the sense that the more closely-spaced samples (which have still more negative values of b) have little or no such enhancement of attenuation. Furthermore the measured resonant-like enhancement occurs only for values of D fairly close to the 0.5 value that gives the computed junction effect. It should also be noted that the computations in Section 4 do not predict the net attenuation of the combined A and B waves, while the simulator measurements inherently provide a certain combination of the A and B waves.

The VSWR measurements of inhomogeneous axial-conductance samples in the large square TM-11 simulator have yielded results similar to those computed for a homogeneous medium, but with somewhat less VSWR. As can be seen from equation (32), a lesser VSWR is consistent with the effect that would be expected from the foam dielectric block in which the resistance strips were embedded for the simulator measurements. It is interesting that even for those samples having the resonant-like enhancement of attenuation, no unusual effect on measured VSWR was observed.

To summarize, measurements of inhomogeneous axial-conductance samples in the large square TM-11 simulator have yielded significant results for angles of incidence near 45° in the E plane. For the samples measured, the attenuation results are close to those computed for the ideal homogeneous medium when the resistance-strip spacing is less than a quarter wavelength but differ substantially for larger spacings. One sample (Figure 5-9) having $s/\lambda = 0.19$,

w/s = 0.17, and D near unity, is representative of the 5 x 5 foot panel in both its strip parameters and its printed construction.

(b) Small Square Simulator Results

One of the features anticipated for the axial-conductance angular filter is the avoidance of any spurious passbands at large incidence angles in the E plane. The analysis of the homogeneous and closely-spaced inhomogeneous media given in Sections 3 and 4 does not indicate the presence of any spurious passband. However, some experimental confirmation of this feature is desirable.

The 5 x 5 foot panel can yield some information about a possible spurious passband, but it is difficult to obtain accurate measurements close to grazing incidence with such a panel. On the other hand, a simulator using small square waveguide operating in the TM-11 mode can provide E-plane incidence angles close to grazing by operating at a frequency close to the cutoff frequency of the TM-11 mode. Such a simulator was used for this purpose in a previous angular-filter investigation for RADC (Ref. 10).

Figure 5-25 shows the small square waveguide simulator and some of its associated equipment. Long (five-foot) tapers in square waveguide are seen on each side of the space where the small square waveguide containing the sample would be. These tapers connect to the large square waveguides containing the TM-11 mode exciters.

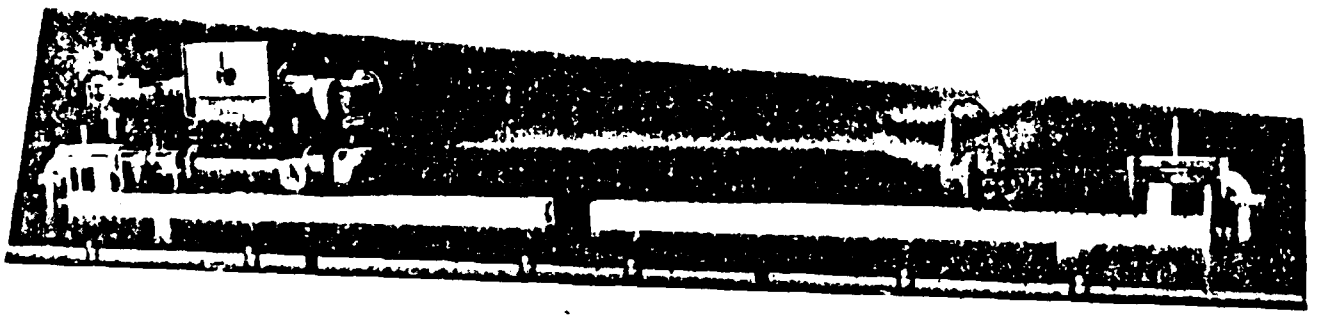

79G3112

Figure 5-25. Small Square Simulator System

Since the small square simulator operates close to cutoff, the incidence angle in the simulator is close to grazing incidence. Furthermore, the incidence angle can be changed substantially by making a relatively small change of frequency. Operating over a frequency range from 4.92 GHz to 5.65 GHz provides a range of incidence angle from 84° to 60° in the E plane.

Figure 5-26 shows the measured attenuation versus frequency for a printed sample having $s/\lambda = 0.18$ and $w/s = 0.17$, with $D = 1.0$ at 5.0 GHz. Also shown is a computed curve of attenuation that includes both the frequency and the resulting incidence angle in the simulator as inputs to the computation of attenuation. Equation (11) for the ideal homogeneous medium is used for this computation. It is seen that the measured attenuation is ten to fifteen percent less than the computed attenuation except very close to grazing incidence where the reflection loss becomes substantial. There is no indication of a spurious passband.

Figure 5-27 shows the measured attenuation versus frequency for a sample having $s/\lambda = 0.36$ and $w/s = 0.085$, with $D = 0.25$ at 5.0 GHz. This sample was made by removing certain resistance strips in the previous sample. Also shown is a computed curve based on equation (11) for a homgeneous medium. The measured attenuation is seen to be about ten percent less than the computed attenuation except very close to grazing incidence where the reflection loss becomes substantial. Again, there is no indication of a spurious passband.

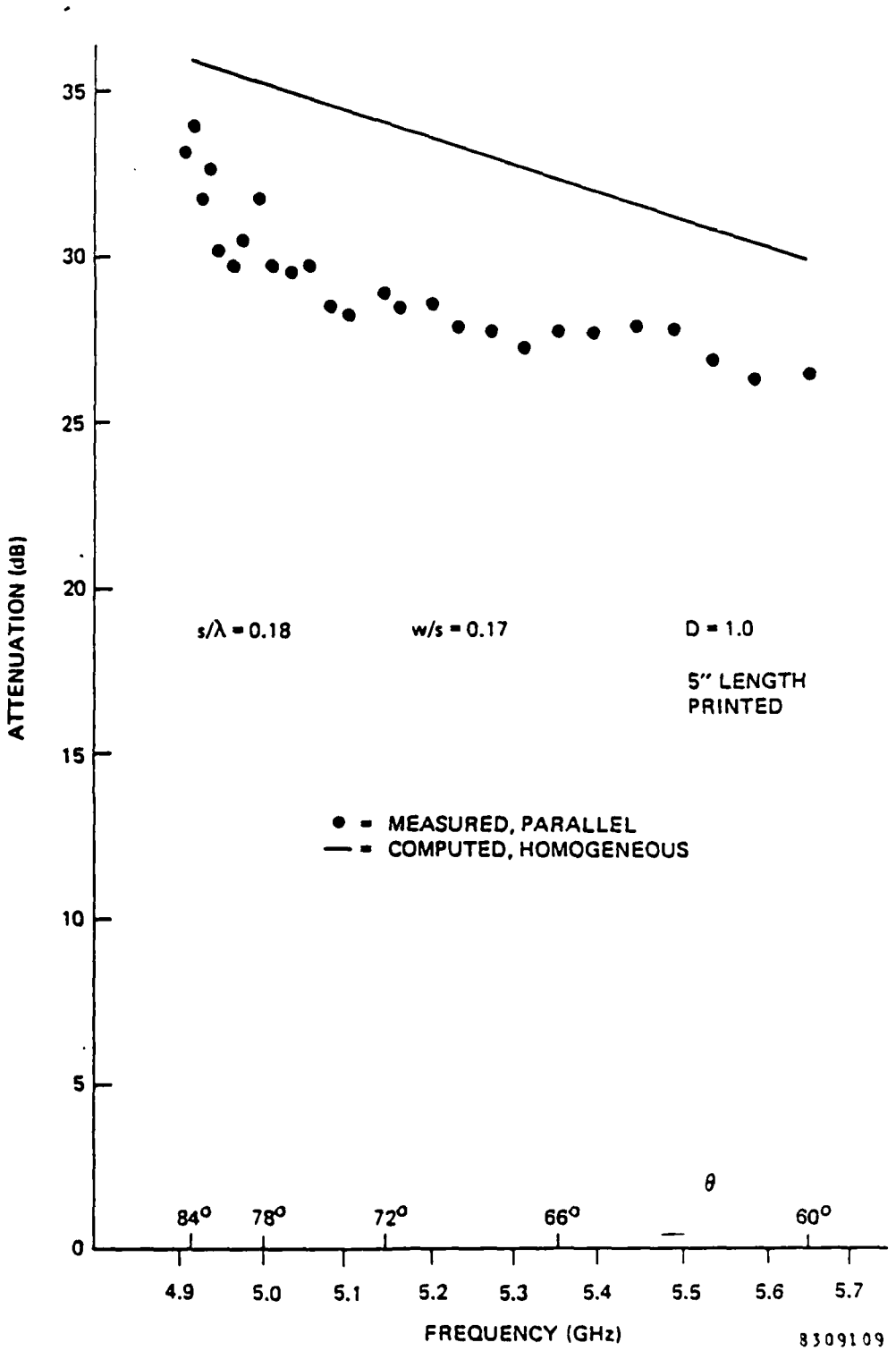

Figure 5-26. Measured Attenuation vs Frequency in Small Square Simulator for $s/\lambda = 0.18$, $w/s = 0.17$, $D = 1.0$

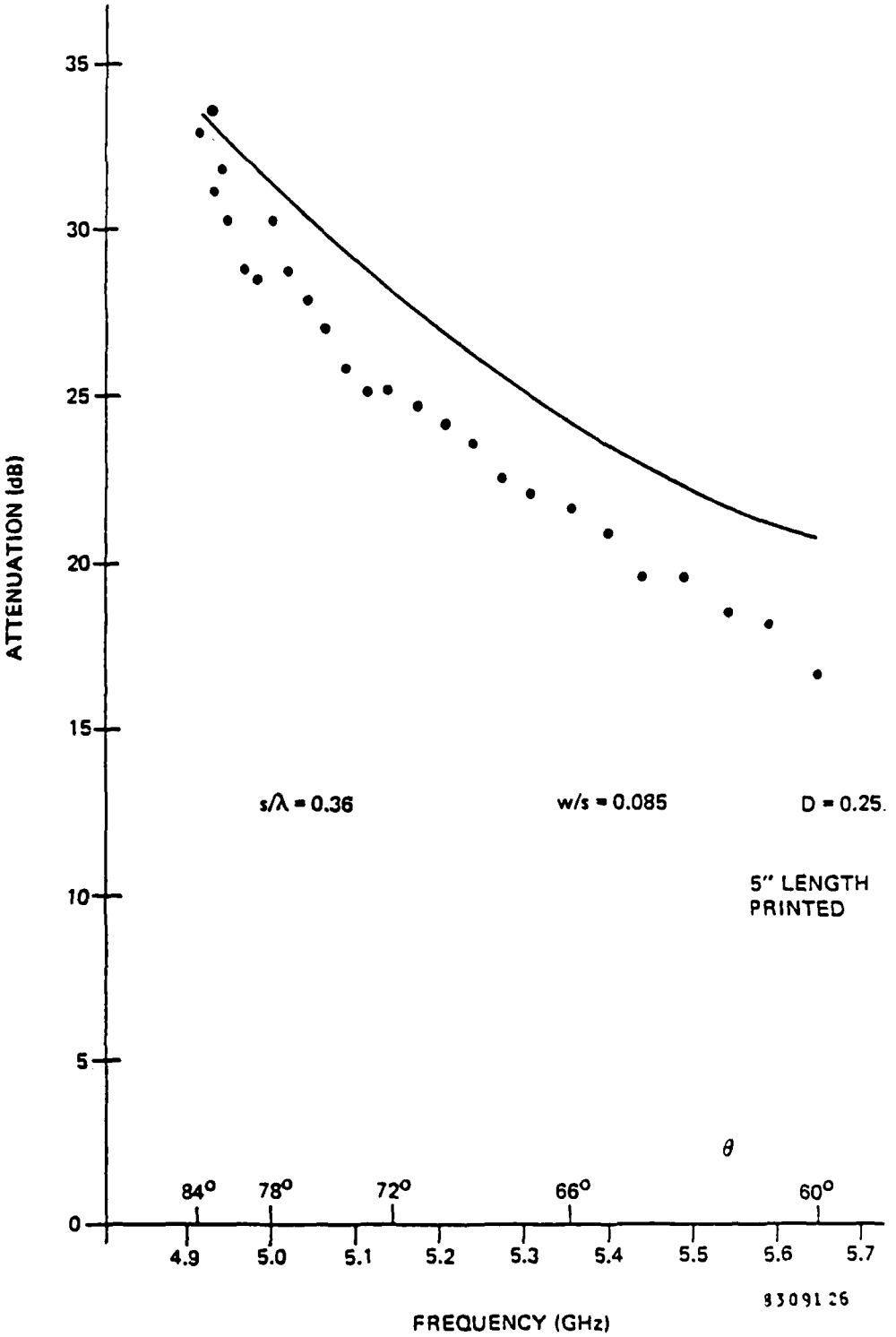

Figure 5-27. Measured Attenuation vs Frequency in Small Square Simulator for $s/\lambda = 0.36$, $w/s = 0.085$, $D = 0.25$

In addition to attenuation, the VSWR of each sample was measured over the frequency band. As was the case with the other square simulator, the measured VSWR is less than the VSWR computed from equation (20). The measured VSWR increases rapidly as the incidence angle approaches grazing, as expected.

Discussion of Small Square Simulator Results. The two samples tested in the small square simulator have yielded attenuation and VSWR results similar to, although somewhat less than, the results computed from the equations for a homogeneous medium. The first sample is a closely-spaced inhomogeneous sample having D = 1, while the second sample has substantial spacing and D = 0.25. Neither sample has shown any indication of having a spurious passband at large incidence angles. Although only these two samples were tested in the small square simulator, it appears reasonable to conclude that the behavior of an inhomogeneous axial-conductance medium at large incidence angles is not qualitatively different from its behavior at smaller angles.

5.4 SIMULATOR TEST CONCLUSIONS

Measurements of inhomogeneous axial-conductance samples in simulator waveguides have provided valuable information. The measured results for broadside incidence have correlated with the approximate formulas for broadside loss in Section 4.2, and have demonstrated that negligible broadside loss is available when s/λ and w/s are made sufficiently small.

The measured results for incidence near 45° in the E plane have shown that when s/λ is small the attenuation of the inhomogeneous medium is close to that given by the ideal homogeneous-medium analysis in Section 3. Larger values for s/λ yield results that deviate from those of the homogeneous medium. These measurements complement the inhomogeneous-medium analysis given in Section 4.3. The measured results from 60° to 84° incidence in the E plane show no evidence of a spurious passband; neither does the analysis of Sections 3 and 4.

The printed construction of some of the simulator samples yields results similar to the cut-card construction. While the cut-card construction permits a variety of small simulator samples to be obtained easily, it is a cumbersome approach to the construction of a 5 x 5 foot panel. The simulator measurements have indicated that a printed construction of the axial-conductance medium for the 5 x 5 foot panel should provide acceptable performance.

SECTION 6

CONSTRUCTION OF 5 X 5 FOOT FILTER

6.1 OBJECTIVES

An objective of this project is to construct an axial-conductance angular filter panel 5 x 5 feet in size. Its nominal midband frequency of operation is to be approximately 10 GHz. The panel is to be tested for its angular performance over a substantial frequency range; these tests will be described in Section 7.

Assuming that the spacing (s) between resistance strips is 0.2 inch, a 5 x 5 foot panel will have more than 70,000 strips. Cutting and inserting this large number of strips into the panel, although feasible, would clearly be a laborious process.

The printing technique, mentioned briefly in Section 5, would be more appropriate for making large numbers of axial-conductance elements if a process could be developed that is practical for a large size. Since another objective of this project is to identify and investigate a fabrication technique suitable for making large axial-conductance angular filters, the printing technique was selected for investigation and for construction of the 5 x 5 foot filter panel.

6.2 PRINTING THE STRIPS

(a) Screen Printing

A process known as screen printing is one that has the potential for printing a pattern of resistance strips on a large dielectric substrate. A typical screen printing process is shown in Figure 6-1. A polyester or stainless steel mesh is first coated with a gel. In the regions of the desired pattern, the gel is removed by a photo-etching process, leaving an open mesh. The screen with pattern is attached to a frame, and is placed on the dielectric substrate to be printed. The printing ink is placed on the screen and a squeegee is pulled across the screen, forcing the ink through the screen and transferring the pattern to the dielectric substrate. For a pattern consisting of resistance material a special resistive ink is used, as discussed later.

The 5 x 5 foot filter panel requires a set of printed dielectric substrates 5 feet long. Therefore a screen and frame 5 feet long was constructed. The screen is a polyester mesh with 64 wires per inch, supporting the gel containing the open printing pattern of parallel strips. The strip pattern has $s = 0.223$ inch and $w = 0.037$ inch. Thus $s/\lambda = 0.19$ at 10 GHz, and $w/s = 0.165$. The strip length is 5 inches, corresponding to the panel thickness that was chosen. Figure 6-2 shows this strip pattern. Figure 6-3 shows the screen and frame that was constructed.

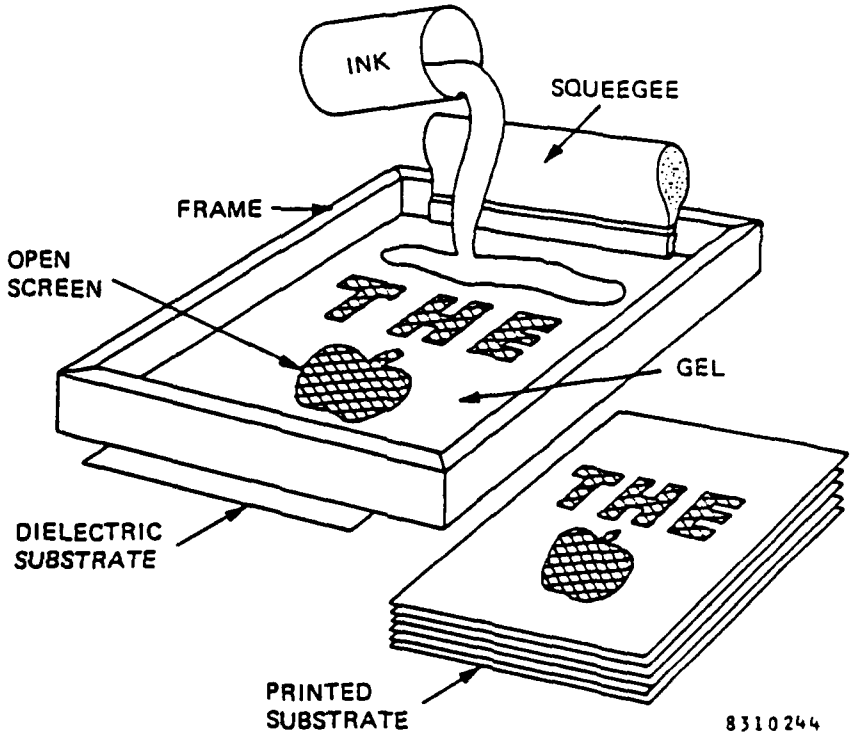

Figure 6-1. A Typical Screen Printing Process

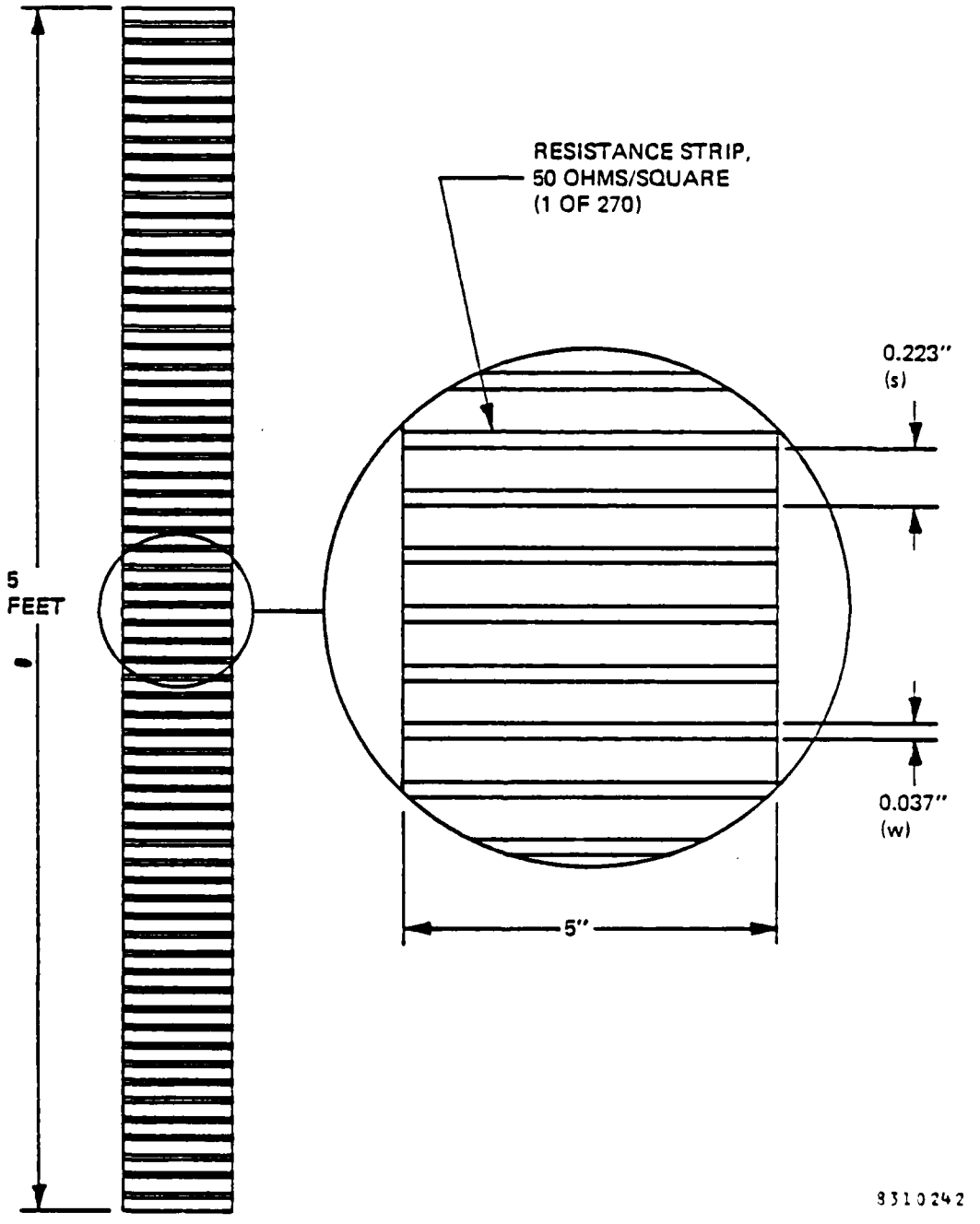

Figure 6-2. Pattern to be Printed on Dielectric Substrate

8312408

Figure 6-3. Screen in Frame

(b) Dielectric Substrate

The dielectric substrate for the filter panel should have the electrical properties of reasonably low dissipation (to minimize broadside loss) and reasonably low dielectric constant (to minimize reflection and anisotropy of transmission). The dielectric material should be strong, and available in thin sheets. It should be capable of providing a surface to which the resistive ink can adhere, and it should withstand the cure temperature of the ink.

The material chosen for the dielectric substrate in the 5 x 5 foot panel is polyester (Mylar) sheet, 0.005 inches thick. Its dielectric constant is approximately 2.8 and its loss tangent is approximately 0.01. It was obtained with a friction coating on the surface to provide acceptable ink adhesion. The 5 x 5 foot filter has 270 such sheets, each 5 feet long and 5 inches wide.

(c) Resistive Ink

Thick-film polymer inks are used to make low-cost electronic circuits. Either conductors or resistors can be obtained by screening an appropriate ink on a dielectric substrate. Many varieties of thick-film inks are available, and surface-resistance values from 10 ohms per square to 20 megohms per square are obtainable. A surface resistance of approximately 50 ohms per square is wanted for the 5 x 5 foot filter in order to obtain the optimum unity value for the axial loss tangent (D) when using the strip dimensions shown in Figure 6-2.

AD-A142 802 AXIAL-CONDUCTANCES ANGULAR FILTER INVESTIGATION(U) 3/3
HAZELTINE CORP GREENLAWN NY P W HANNAN ET AL. APR 84
6519 RADC-TR-84-80 F19628-81-C-0067

UNCLASSIFIED F/G 9/5 NL

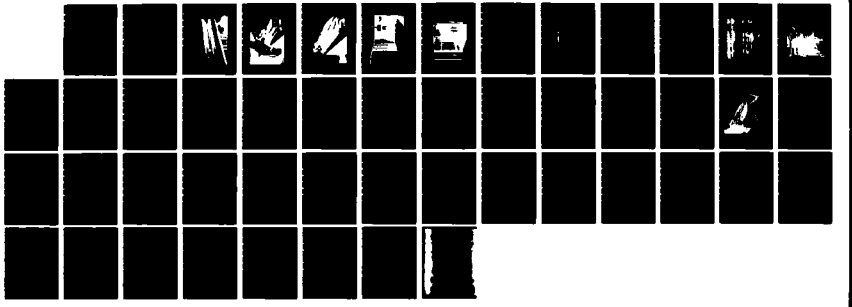

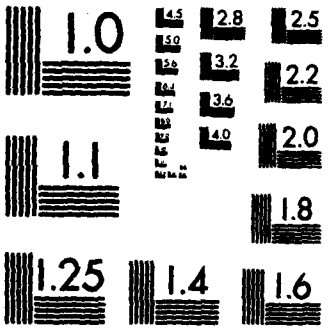

MICROCOPY RESOLUTION TEST CHART
NATIONAL BUREAU OF STANDARDS-1963-A

small sample of the ink has been satisfactory. It was found that the silver particles in the ink were too small.

Another ink, using only carbon particles, had been deemed acceptable on a sample basis, and was therefore obtained in large volume. However this, too, was found to be unsatisfactory, because its viscosity differed greatly from the earlier sample. A third ink, similar to the first one but with larger silver particles was then obtained. This ink, finally, proved to be satisfactory.

(d) Printing and Curing

Using the 5-foot screen, 5-foot polyester sheets, and the ink discussed above, a set of 270 printed sheets (plus some extras) were made for the 5 x 5 foot filter. Figure 6-4 shows the screen temporarily elevated above a 5-foot dielectric sheet which is held by a vacuum plate underneath. Figure 6-5 shows the squeegee being pulled across the screen to print one of the dielectric sheets. Figure 6-6 shows this printed sheet being lifted off the vacuum plate. Figure 6-7 shows several such sheets immediately after being printed.

Curing these printed sheets was accomplished in an oven. The curing temperature was approximately 150°C and the time was about one hour. Figure 6-8 shows a rolled-up sheet being cured in the oven.

After curing, about ten of the resistance strips in each sheet were measured for DC resistance. In some cases a sheet was found to have an average resistance sufficiently different from the desired value to be either given a

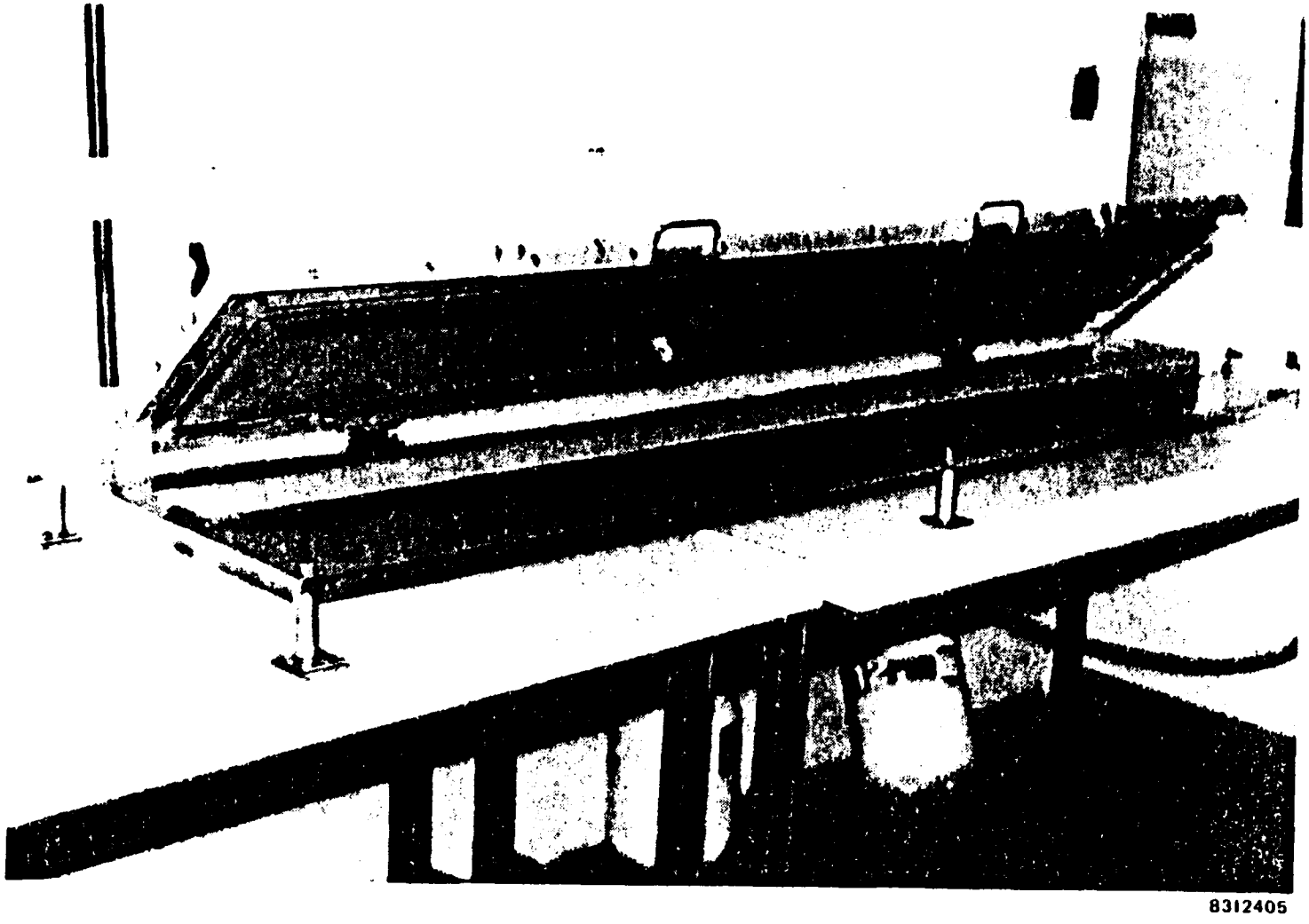

Figure 6-4. Screen, Dielectric Sheet, and Vacuum Plate

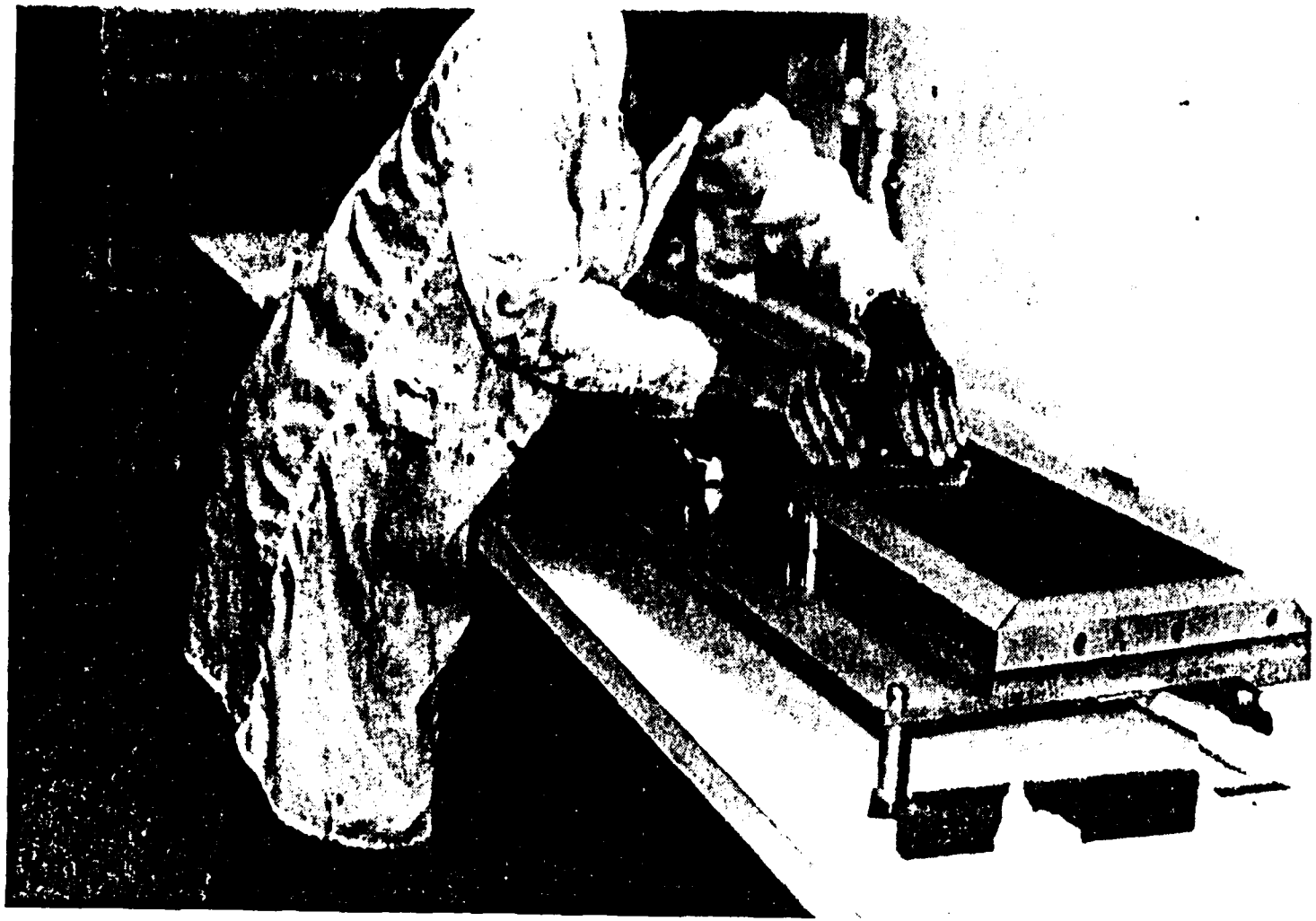

8312407

Figure 6-5. Printing One Five-Foot Sheet

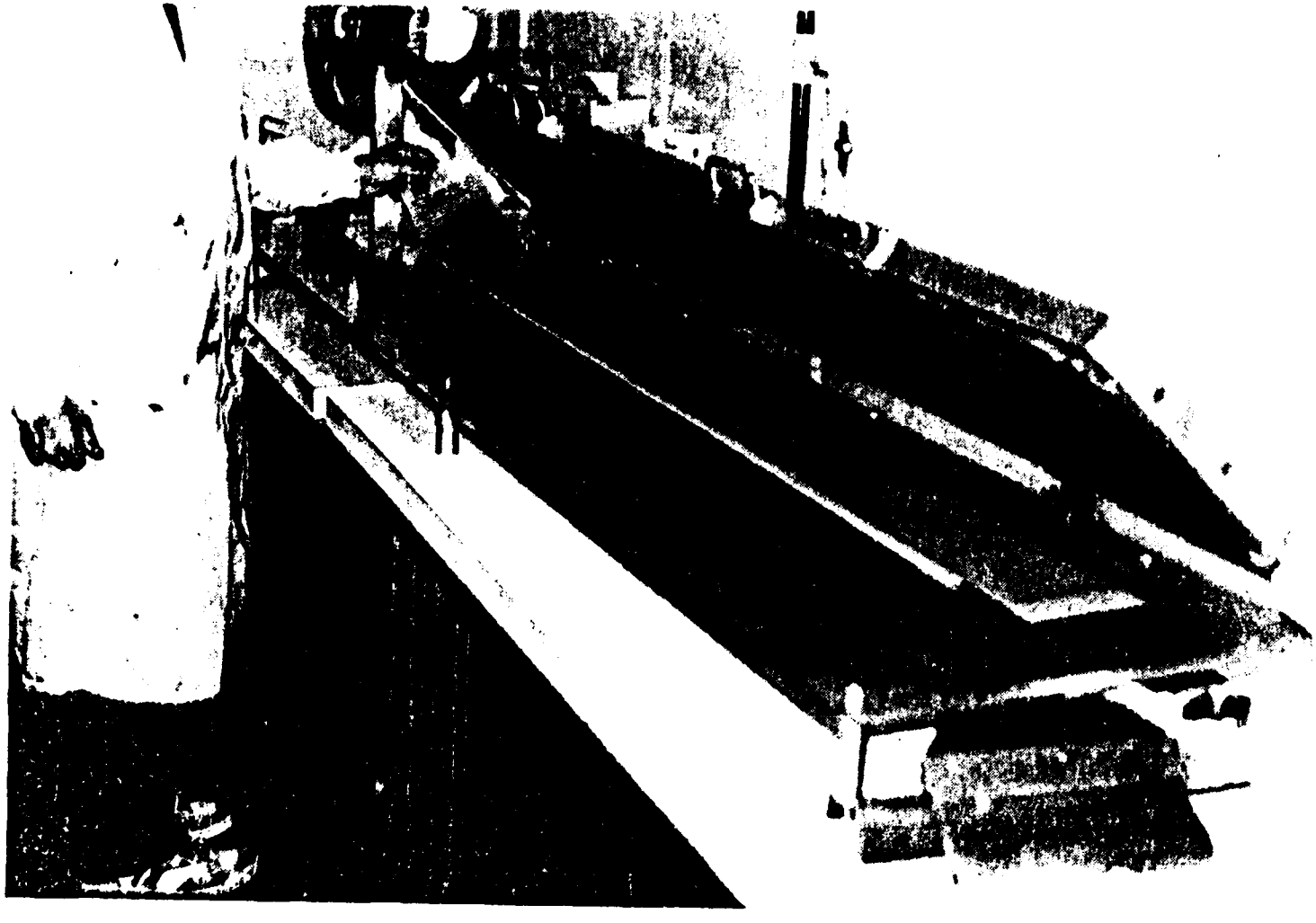

8312402

Figure 6-6. Printed Dielectric Sheet Being Removed From Vacuum Plate

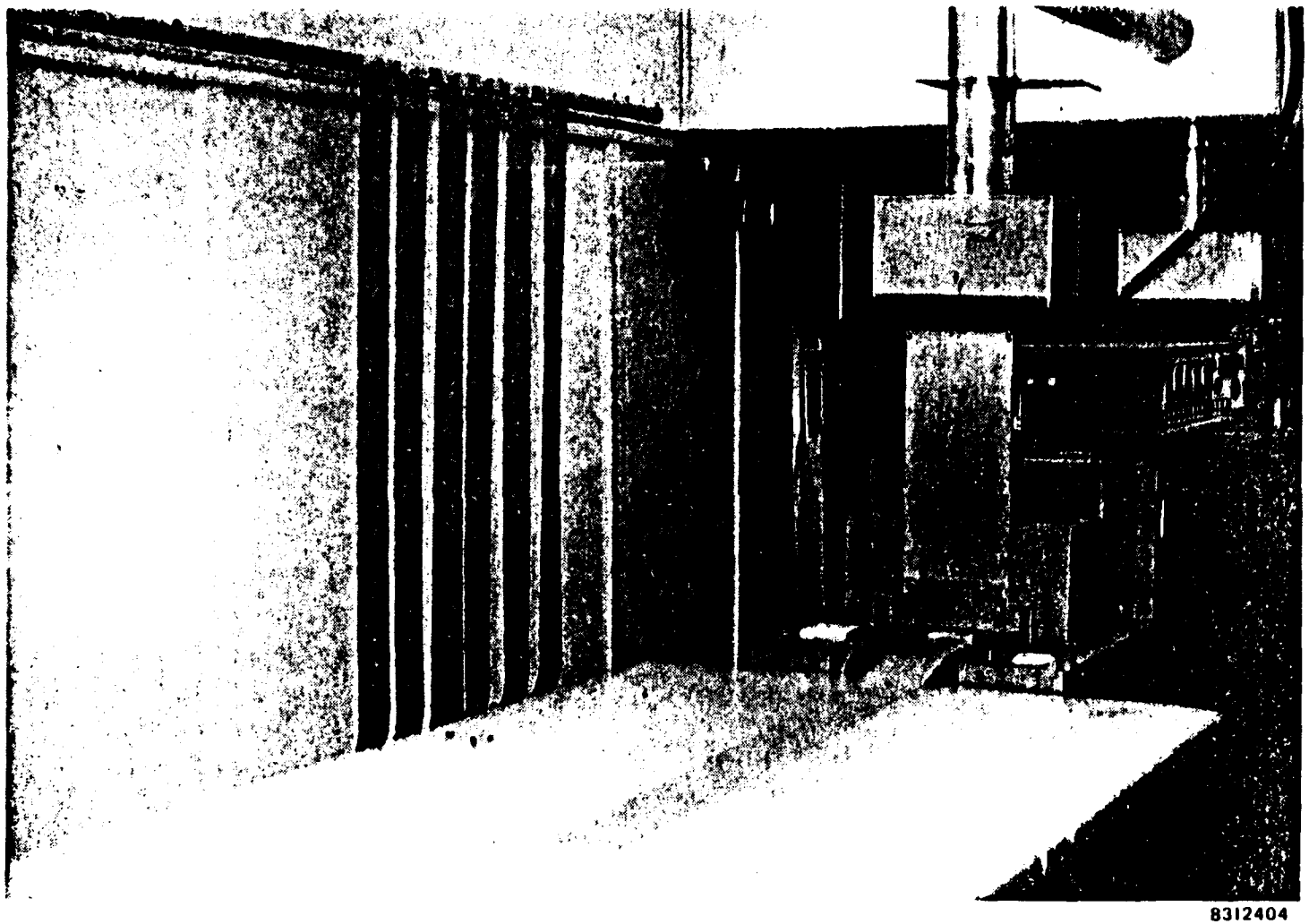

Figure 6-7. Sheets After Printing But Prior to Curing

8312403

Figure 6-8. Sheet Being Cured in Oven

further cure in the oven or to be discarded. In any one sheet the strips were generally found to have similar resistance values. Each sheet was also visually inspected for printing defects; any found were either corrected or the sheet was discarded. The net result is a set of 270 sheets having high probability that each resistance strip has a value of resistance reasonably close to the desired value. This is considered satisfactory for the axial-conductance angular filter because of its insensitivity to moderate deviations from the optimum value of axial loss tangent (D), and its inherent invisibility at broadside incidence.

6.3 ASSEMBLY OF FILTER PANEL

The 5 x 5 foot filter consists essentially of the 270 5-foot printed sheets in a 5-foot-wide stack, with sheet-to-sheet spacing s = 0.223 inch. To provide the correct spacing between the sheets, a foam slab, precut to the proper thickness, is placed between each adjacent pair of printed sheets. For mechanical and environmental integrity, a thin 5 x 5 foot fiberglass sheet is put on each of the two faces of the panel, and a thick fiberglass border is put around the four edges of the panel. Figures 6-9 and 6-10 show this assembly.

The actual construction proceeded as follows: First the alternating printed sheet and foam layers were stacked in a frame which has two fixed sides, one open side, and a movable plunger on the fourth side. The frame was located on a flat table that supported the stack of printed sheets and foam spacers. The plunger allowed the stack to grow without separation of its layers. Once all the layers were inserted, the plunger was tightened to eliminate excess air spaces in the stack.

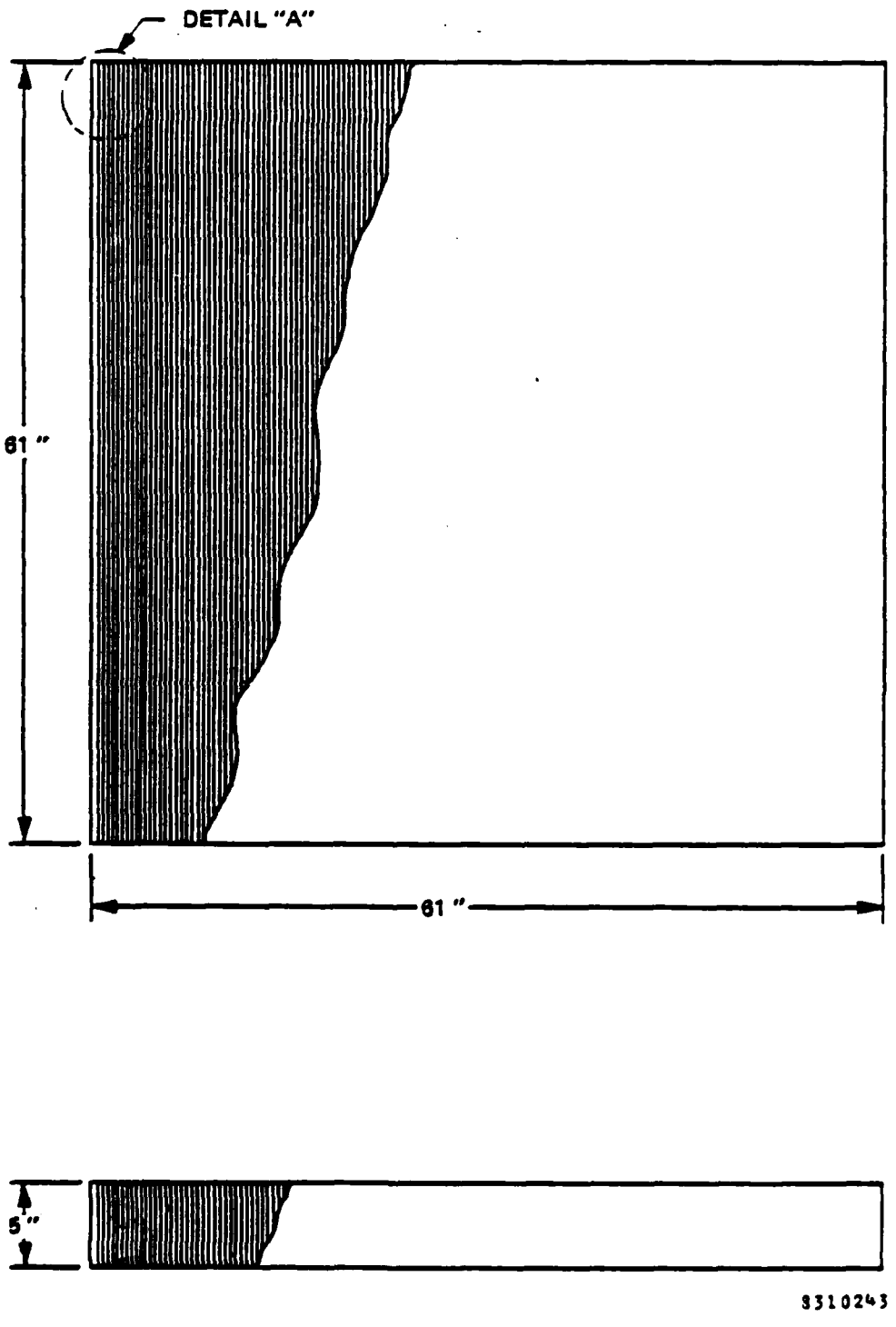

Figure 6-9. Overall Assembly of Filter Panel

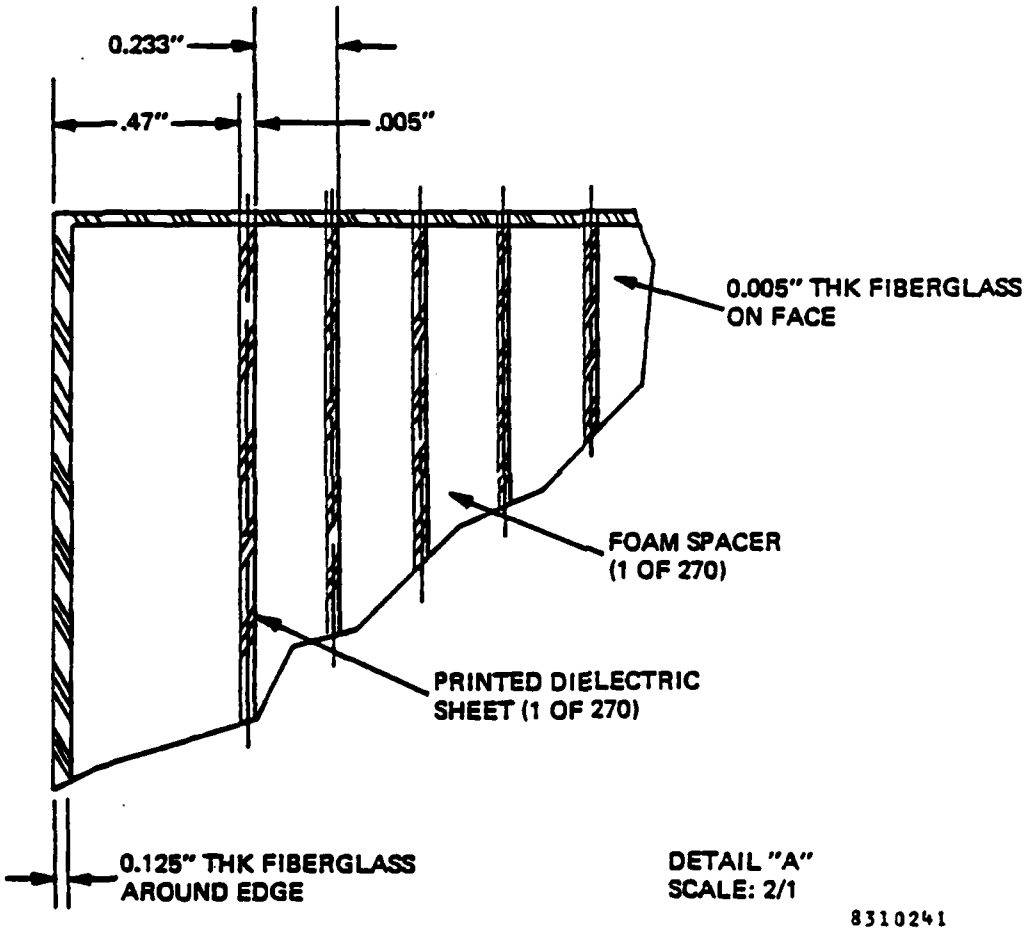

Figure 6-10. Detail Assembly of Filter Panel

Next, a thin fiberglass skin was applied to the top face of the assembly. Then the assembly was turned over and a second skin was applied to the opposite face. These skins were cured with the frame still in place. Next, the two edges of the assembly at right angles to the plunger were dressed with a thick layer of fiberglass to prevent the assembly from springing apart when the plunger was loosened. After loosening the plunger the two remaining edges of the panel were dressed with a thick layer of fiberglass, and the final curing was done. This completed the assembly of the filter panel.

Figure 6-11 is a photograph taken close to the face of the filter panel. It is interesting that the ends of the resistance strips can actually be seen through the thin translucent skin on the face of the panel. The complete 5 x 5 foot filter panel is shown in Figure 6-12.

6.4 DISCUSSION

A process for making the axial-conductance elements in large quantities was identified and investigated during this program. The process involves the screen printing of surface-resistance strips on large dielectric sheets. A hand-screening process, shown earlier in Figure 6-5, was considered appropriate for this project in which one filter panel was constructed. If a large number of filter panels were needed, an automated high-speed printing process involving a large initial cost could also be considered.

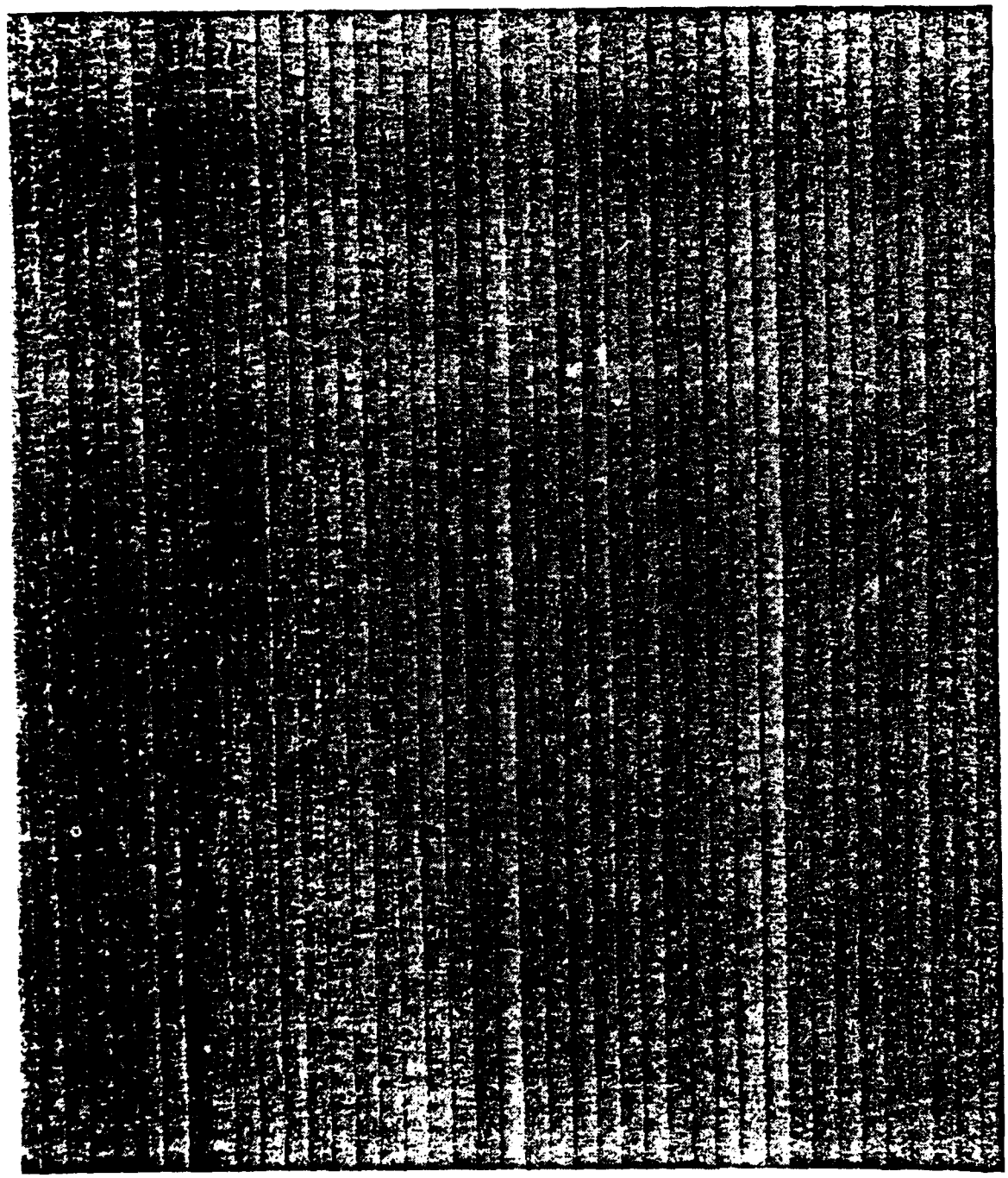

83H1303

Figure 6-11. Closeup View of Face of 5 x 5 Foot Angular Filter

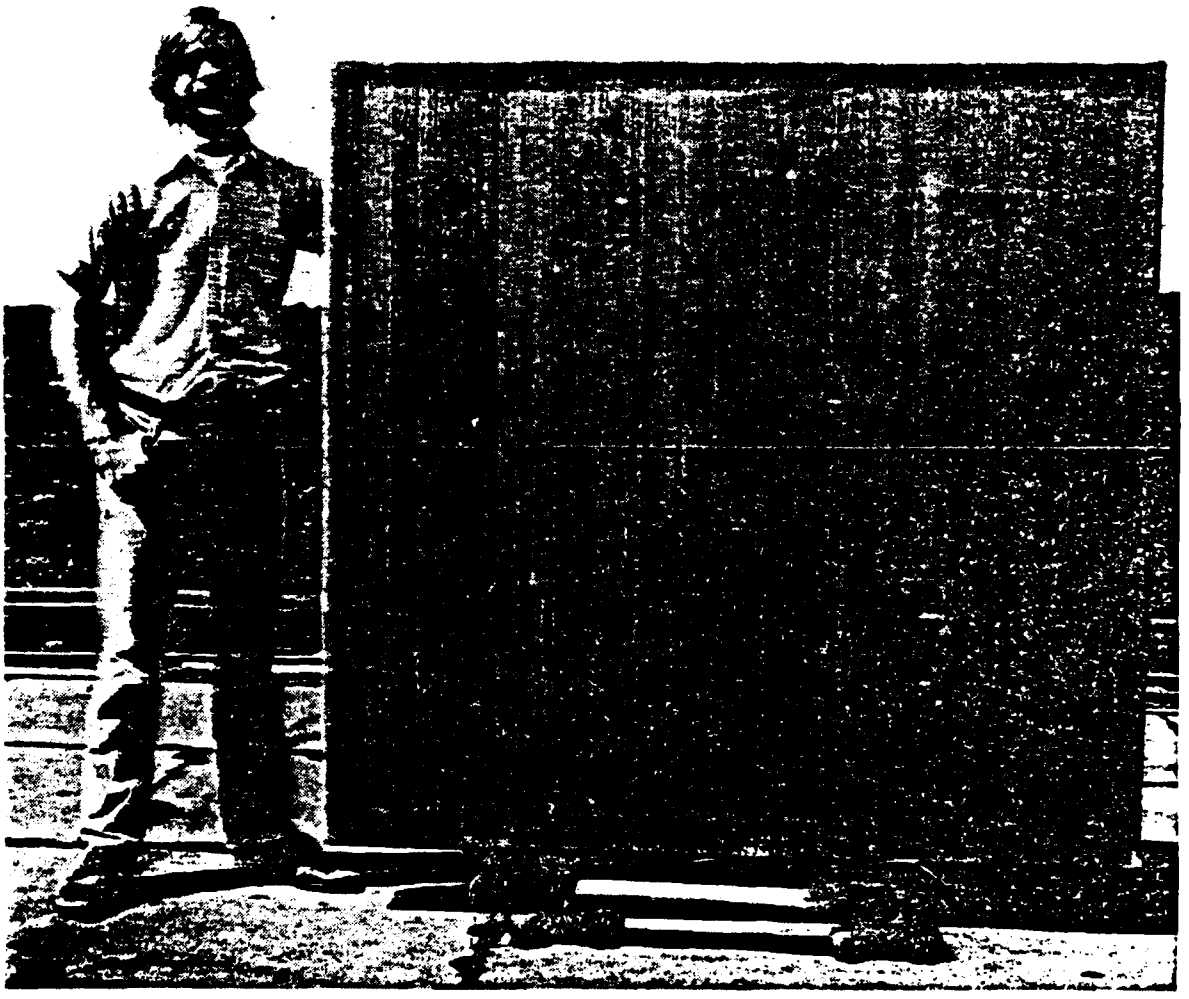

83H1302

Figure 6-12. 5 x 5 Foot Axial-Conductance Angular Filter

A large (5-foot long) screen with the desired resistance-strip pattern was constructed, and then was used to print the 270 thin dielectric sheets needed for the 5 x 5 foot angular-filter panel. The total number of resistance strips made in this way for the panel is over 70,000.

Various problems were encountered during the printing process, many of them related to the properties of the resistive ink. However these problems were resolved, and a 5 x 5 foot angular filter having the desired axial-conductance elements was successfully constructed.

SECTION 7

TESTS OF 5 X 5 FOOT FILTER

7.1 OBJECTIVES

Tests of the 5 x 5 foot axial-conductance angular filter have the principal objective of measuring its rejection versus incidence angle over a wide range of frequencies. Specifically, the filter panel was measured over a continuous range of E-plane incidence angles from 0° to about 45°. These measurements were made at three frequencies covering a two-octave frequency band.

A second objective of the tests is to demonstrate the effectiveness of the filter in reducing the wide-angle sidelobes of a microwave antenna in a situation where antenna/filter interaction could degrade performance. This was done by measuring the radiation pattern of an antenna/grating combination before and after the filter was placed in front of it.

7.2 MEASUREMENT OF REJECTION VS ANGLE

To measure the filter rejection versus incidence angle, the radiation pattern of a small horn was measured before and after combining it with the filter. This is indicated in Figure 7-1. A comparison of the two measured patterns gives an approximation to the reflection versus angle behavior of the filter.

The measured results at 5, 10, and 20 GHz are shown in Figures 7-2, 7-3, and 7-4, respectively. In each figure,

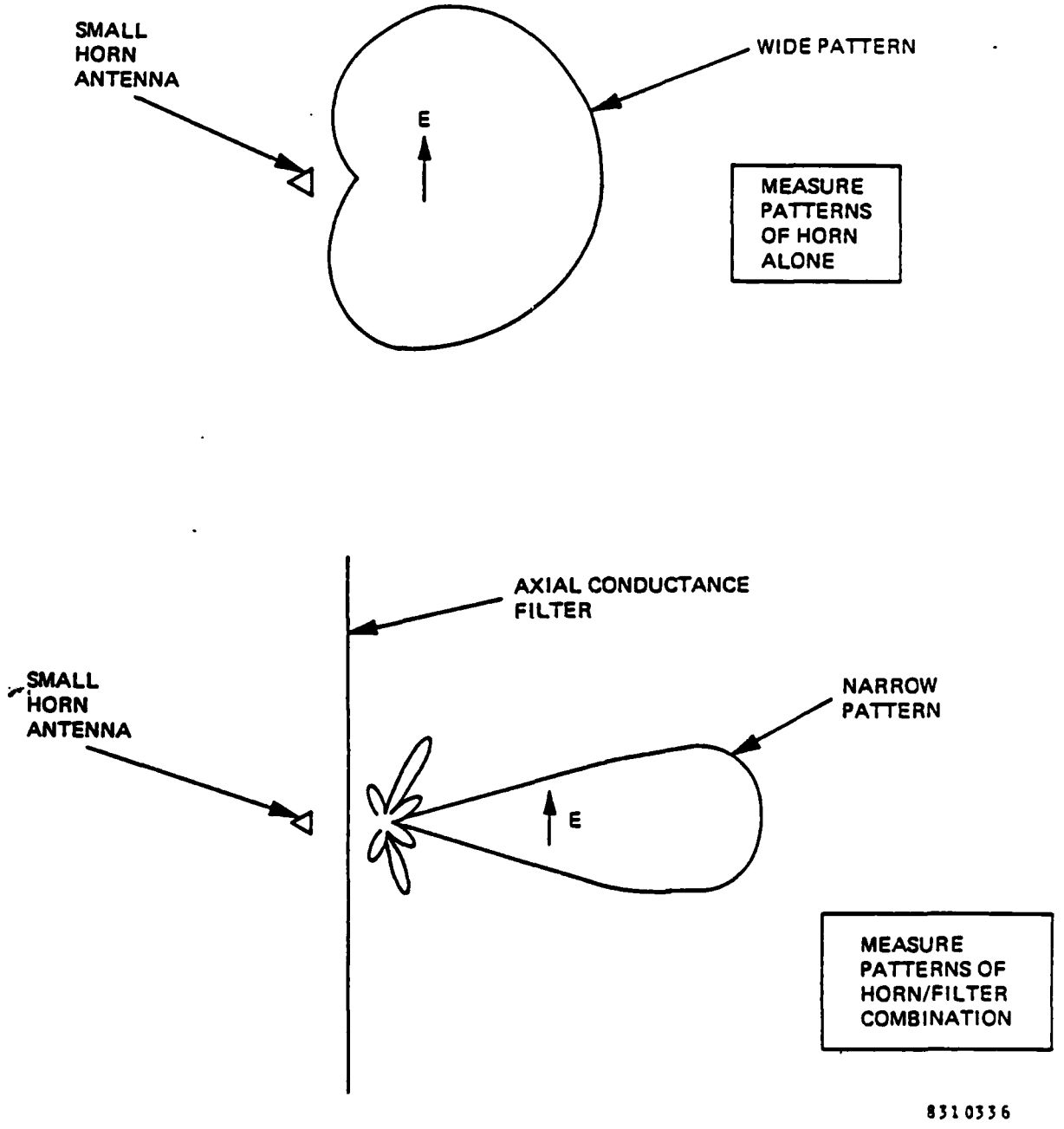

Figure 7-1. Arrangement for Measurement of Filter Rejection vs Incidence Angle

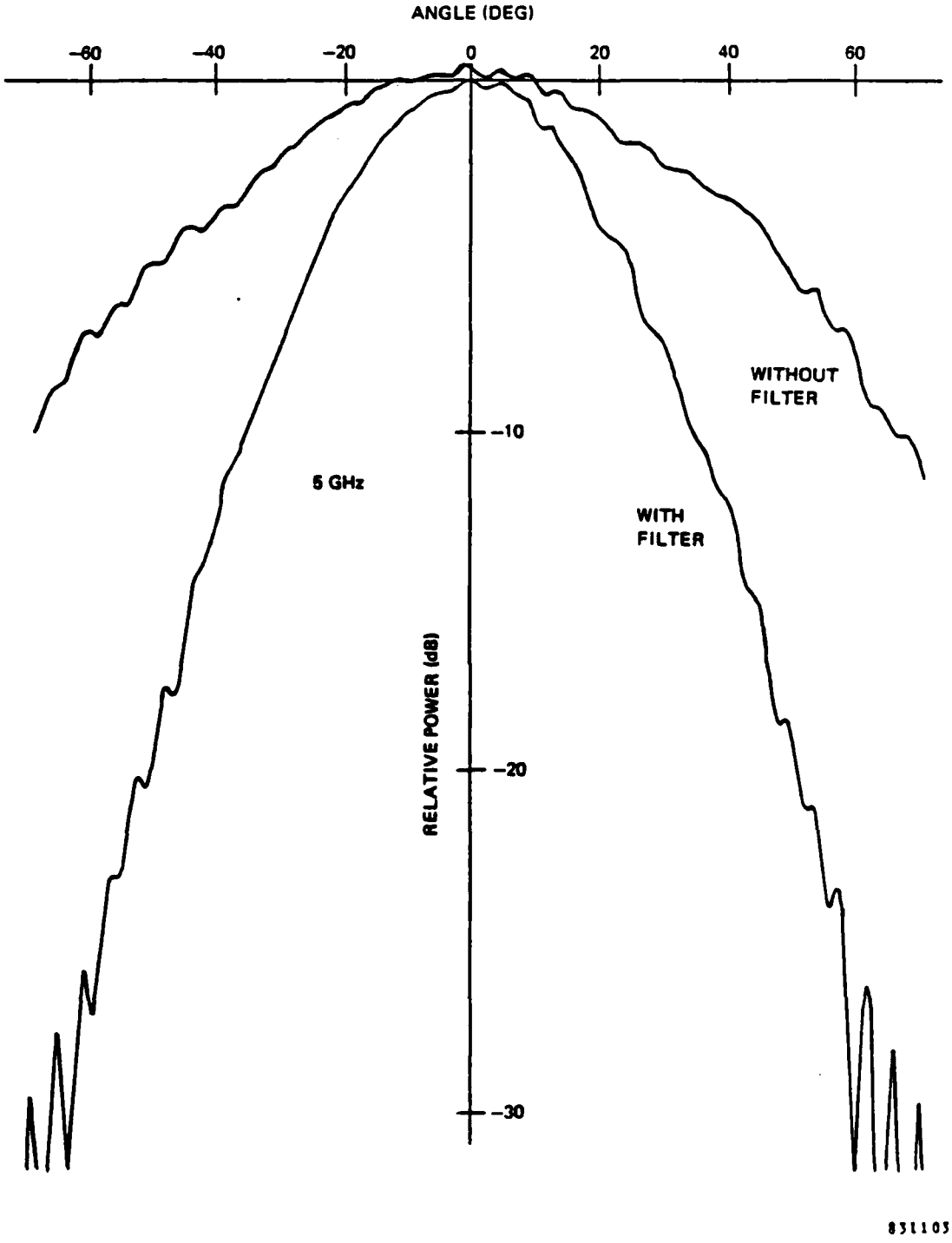

Figure 7-2. Measured Patterns of Horn Without and With Filter at 5 GHz

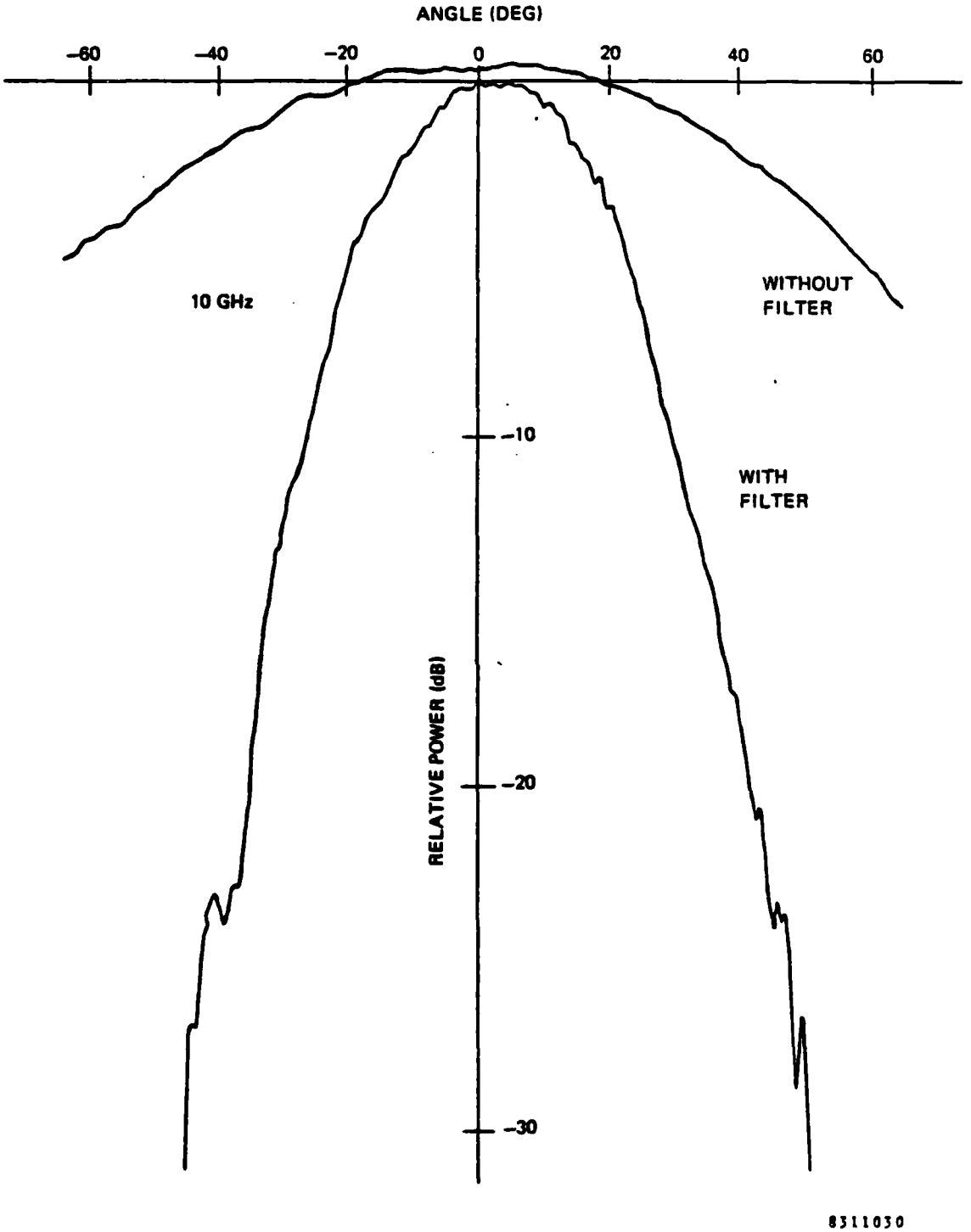

Figure 7-3. Measured Patterns of Horn Without and With Filter at 10 GHz

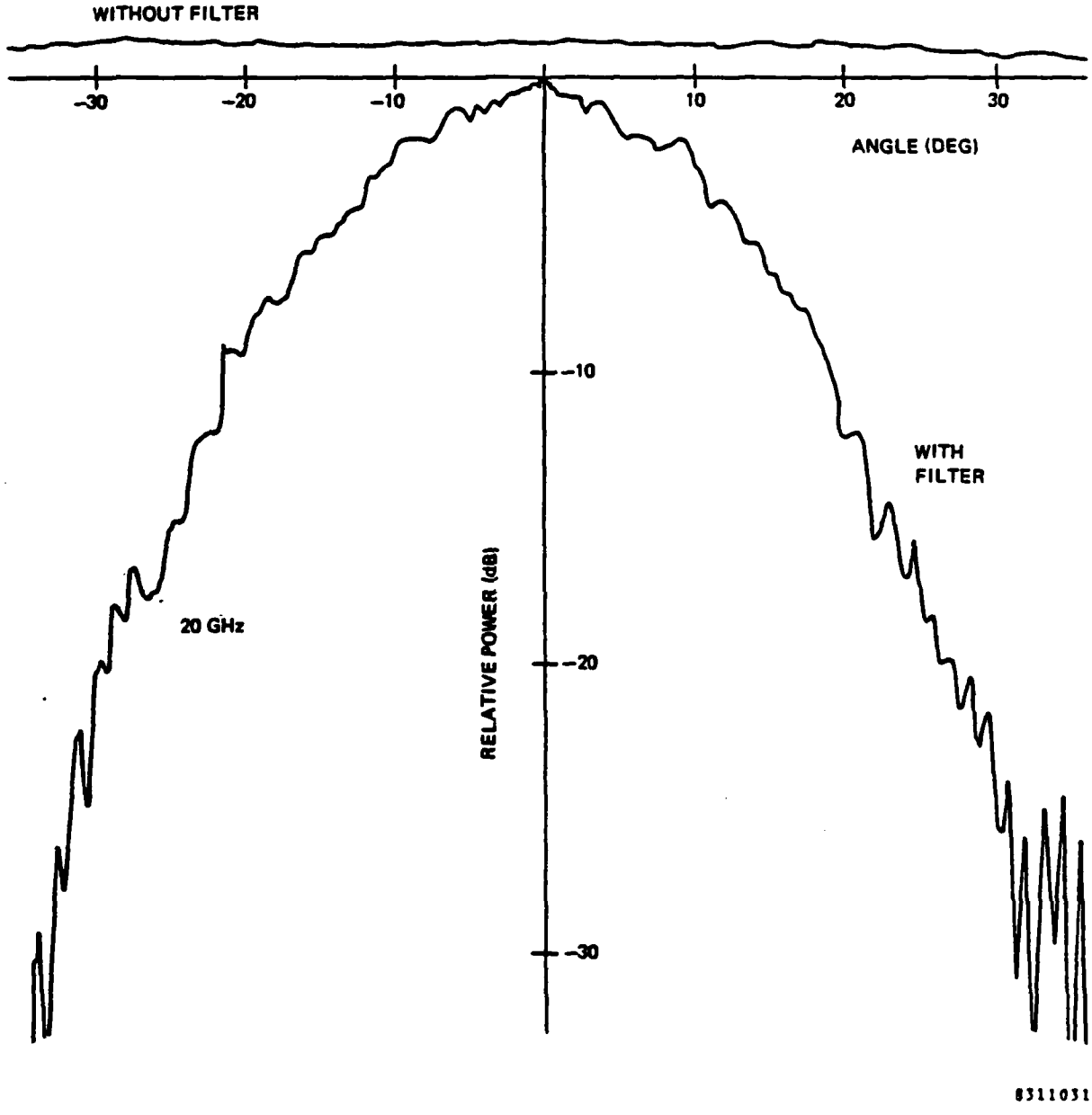

Figure 7-4. Measured Patterns of Horn Without and With Filter at 20 GHz

the wider pattern is that of the horn alone, and the narrower pattern is that of the horn/filter combination. The difference between peak levels of the two patterns is not significant, and is caused by level changes between the two conditions of measurement, as well as by some frequency-sensitive multiple reflections between the inner and outer faces of the panel. The w dimension of the resistive strips in the panel was oriented perpendicular to the E field of the horn, so any broadside loss of the inhomogeneous axial-conductance medium would not be included in these measured results (broadside loss is best measured by simulators, as in paragraph 5.2).

The filter rejection versus incidence angle is given approximately by the difference (in dB) of the two patterns when normalized to their peak values. Figures 7-5, 7-6, and 7-7 show this "measured filter rejection" versus angle, at 5, 10, and 20 GHz, respectively. Also shown in these figures is the rejection versus angle computed from equation (11) for a 5-inch-thick homogeneous medium (also see Figure 3-4). The computation is made with D = 1 at 10 GHz, and hence D = 2 at 5 GHz and D = 0.5 at 20 GHz. The measured rejection at 10 GHz is actually the average of measurements made at 9.5, 10.0, and 10.5 GHz.

It is seen that, at all three frequencies, the measured filter rejection has an angular variation similar to that of the computed homogeneous curve, but the measured rejection is somewhat less. One possibility that might account for this difference is the inhomogeneous construction of the axial-conductance medium in the actual filter. However the inhomogeneous-medium analysis given in paragraph 4.3 indicates that at 5 and 10 GHz where s/λ is about 0.1 and 0.2,

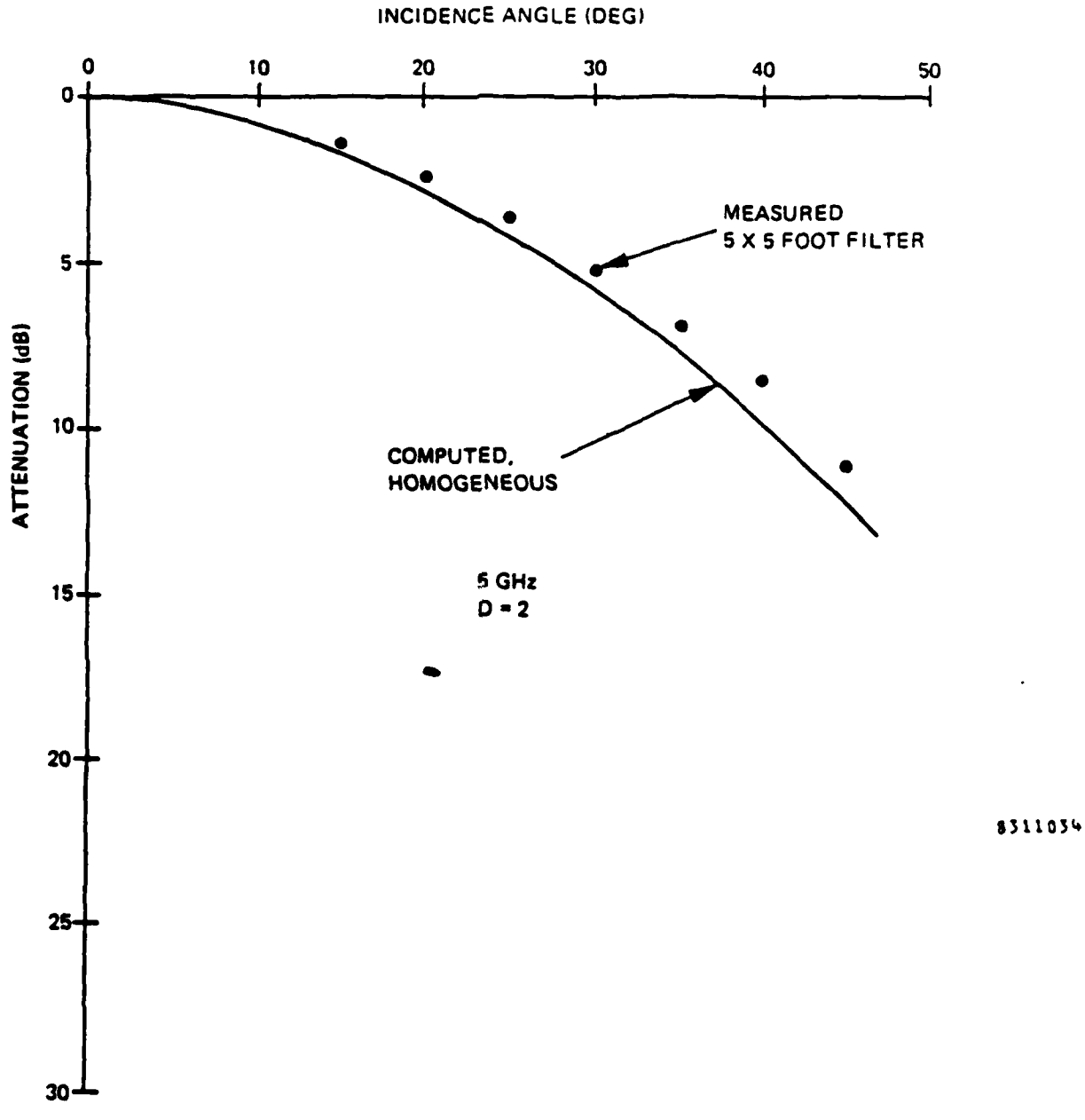

Figure 7-5. Filter Rejection vs Incidence Angle Derived from Measurements, 5 GHz

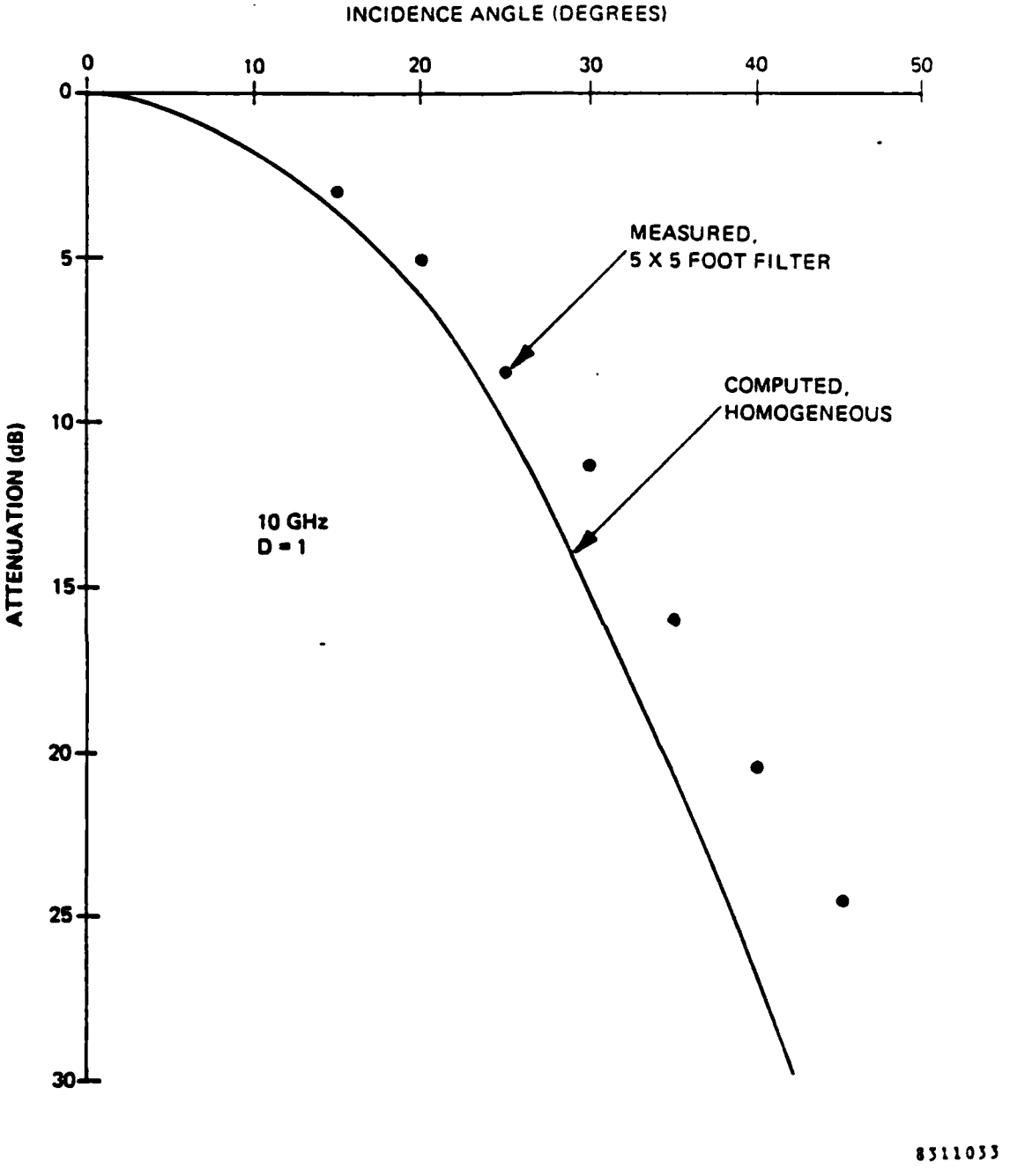

Figure 7-6. Filter Rejection vs Incidence Angle Derived from Measurements, 10 GHz

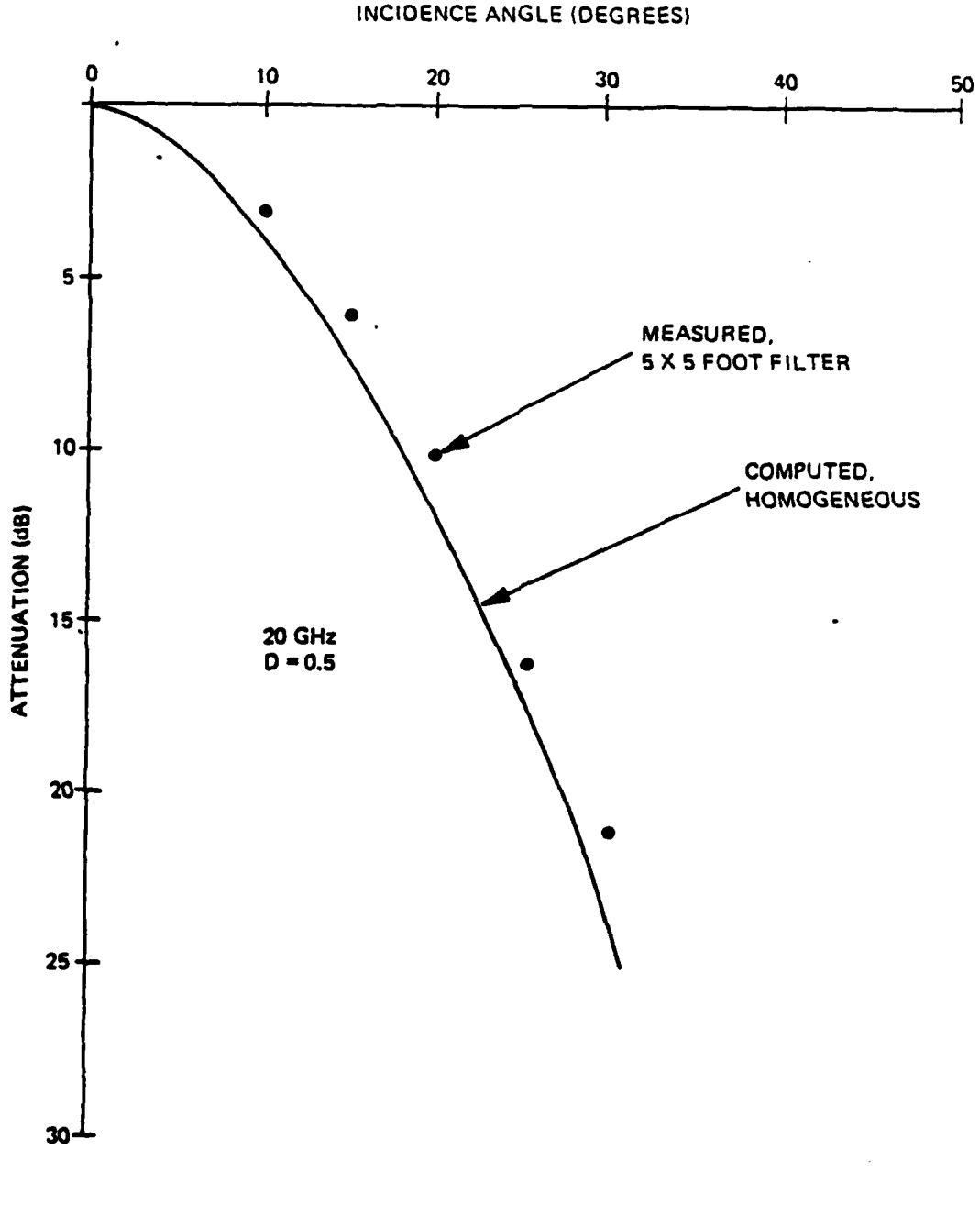

Figure 7-7. Filter Rejection vs Incidence Angle Derived from Measurements, 20 GHz

respectively, the inhomogeneous medium attenuation should be close to that of the homogeneous medium. The measurements in the large square simulator also gave good agreement with the homogeneous analysis when s/λ was 0.2 or less (see Figure 5-9).

Another possibility that might account for the difference between the measured and computed results is the difference in the wave geometry for the two cases. The computed result assumes a plane wave incident on the filter. The measurement, however, involves a small horn antenna near the filter.

Because of Fresnel diffraction, the signal coupled to the horn includes a range of incidence angles at the filter, rather than the single incidence angle that would correspond to a plane wave. This range of angles includes H-plane incidence (where the filter provides no rejection) as well as E-plane incidence. The net result, we suspect, is to introduce a kind of "leakage signal" in the measurement, causing the measured rejection to be somewhat less than both the computed rejection and the rejection measured in the large square simulator (which simulates an incident plane wave).

In spite of the quantitative difference between the measured results on the filter panel and the computed or the simulator results, the qualitative results are similar. The measured rejection increases continuously with E-plane incidence angle, as expected. The measured results show that the rejection increases approximately proportional to frequency over a two-octave band, as expected. The amount

of measured rejection provided by this filter panel at large incidence angles is substantial over the two-octave frequency band.

7.3 MEASUREMENT OF FILTER/ANTENNA INTERACTION

In a previous angular-filter investigation for RADC (Ref. 12), a metal-grid angular filter was placed in front of a reflector antenna and was shown to substantially reduce its wide-angle sidelobes. A grating was then put in the antenna aperture to create high grating lobes. When the metal-grid angular filter was placed in front of this assembly the grating lobes were reduced as expected, but some of the sidelobes closer to the main beam were increased substantially. This latter result was considered to be caused by the substantial grating-lobe energy being reflected by the metal-grid filter back to the antenna where it was then scattered into sidelobe energy, some of which was within the angular passband of the filter.

An advantage claimed for the axial-conductance angular filter is that its rejection is obtained by absorption rather than by reflection. Therefore it could be hoped that there would be little or no increase of any sidelobes when this filter is placed in front of the grating/antenna combination.

A measurement to support or refute this conjecture was made, using the same antenna and grating previously used with the metal-grid filter. Figure 7-8 shows the 40-inch reflector antenna with the axial-conductance angular filter panel in front, both attached to an antenna pedestal for measuring patterns. The grating was not present when this photograph was taken. Figure 7-9 shows the grating

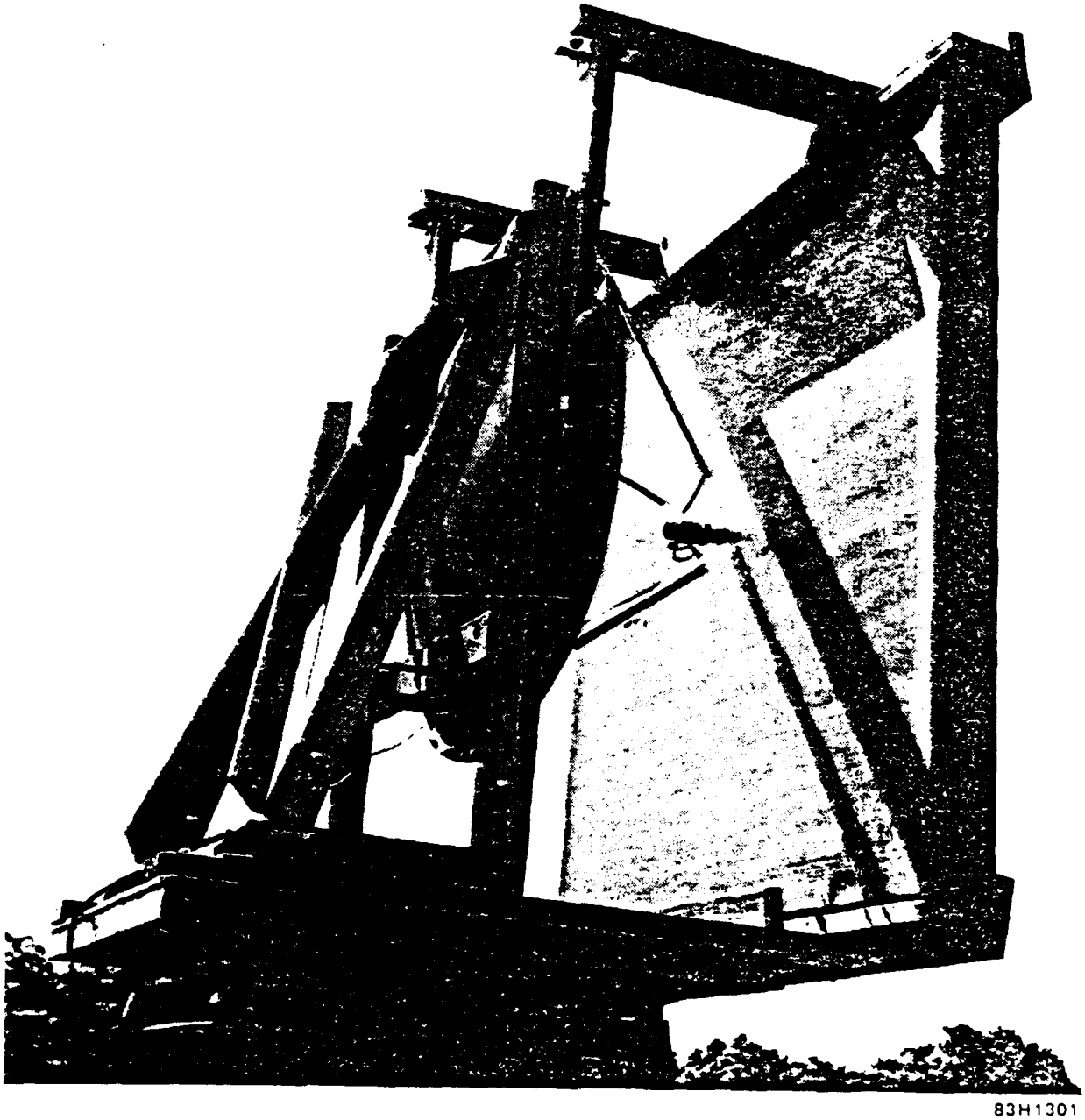

83H1301

Figure 7-8. Axial-Conductance Filter with Reflector Antenna on Antenna Range

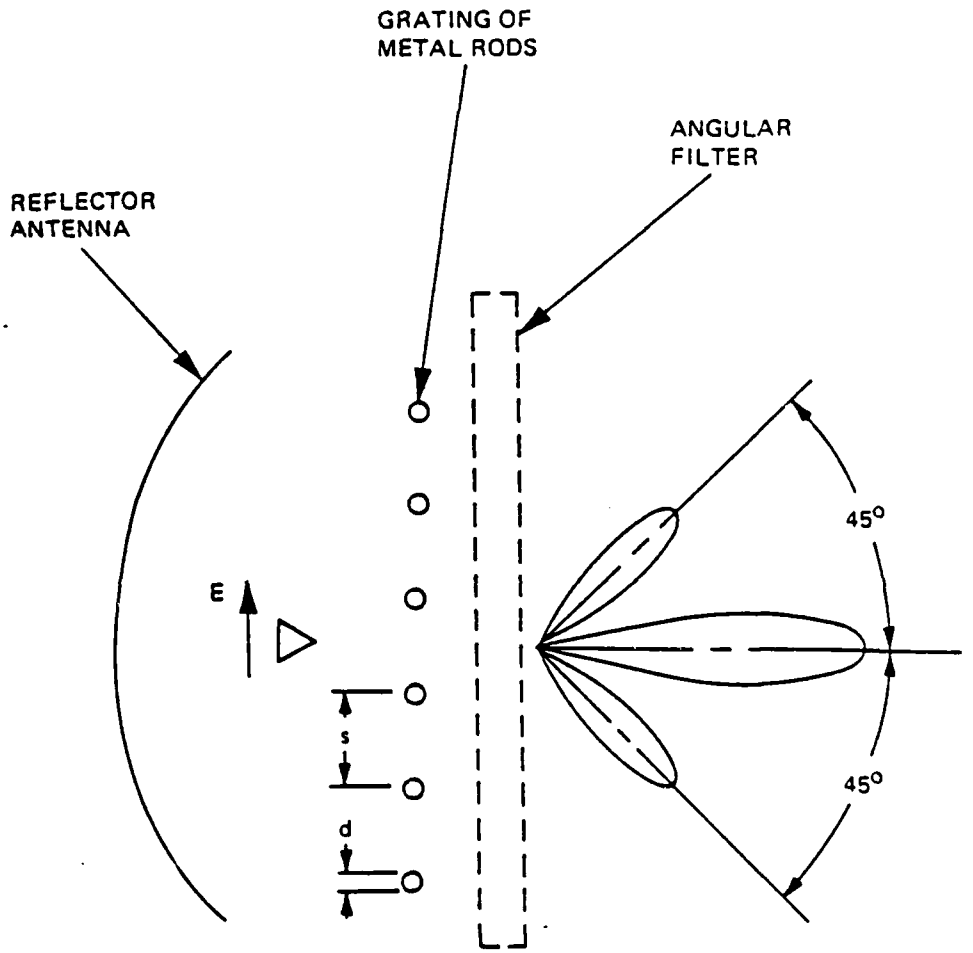

Figure 7-9. Grating/Antenna Combination

geometry, and the expected grating-lobe pattern of the antenna/grating combination before the filter is added.

Two patterns were measured at 10 GHz with the antenna/grating combination: one without the filter, and the other with the axial-conductance angular filter added to the assembly. These two patterns are shown superimposed in Figure 7-10. The dashed pattern is measured without the filter and exhibits large grating lobes in the vicinity of ±45°. The solid pattern is measured with the filter, and shows a major reduction of the grating lobes, as expected. Furthermore, it is seen that there is virtually no increase of the sidelobes at smaller angles. This latter result, which contrasts with the previous result obtained with the metal-grid angular filter, supports the viewpoint that the absorptive-type rejection provided by the axial-conductance angular filter is a significant desirable feature.

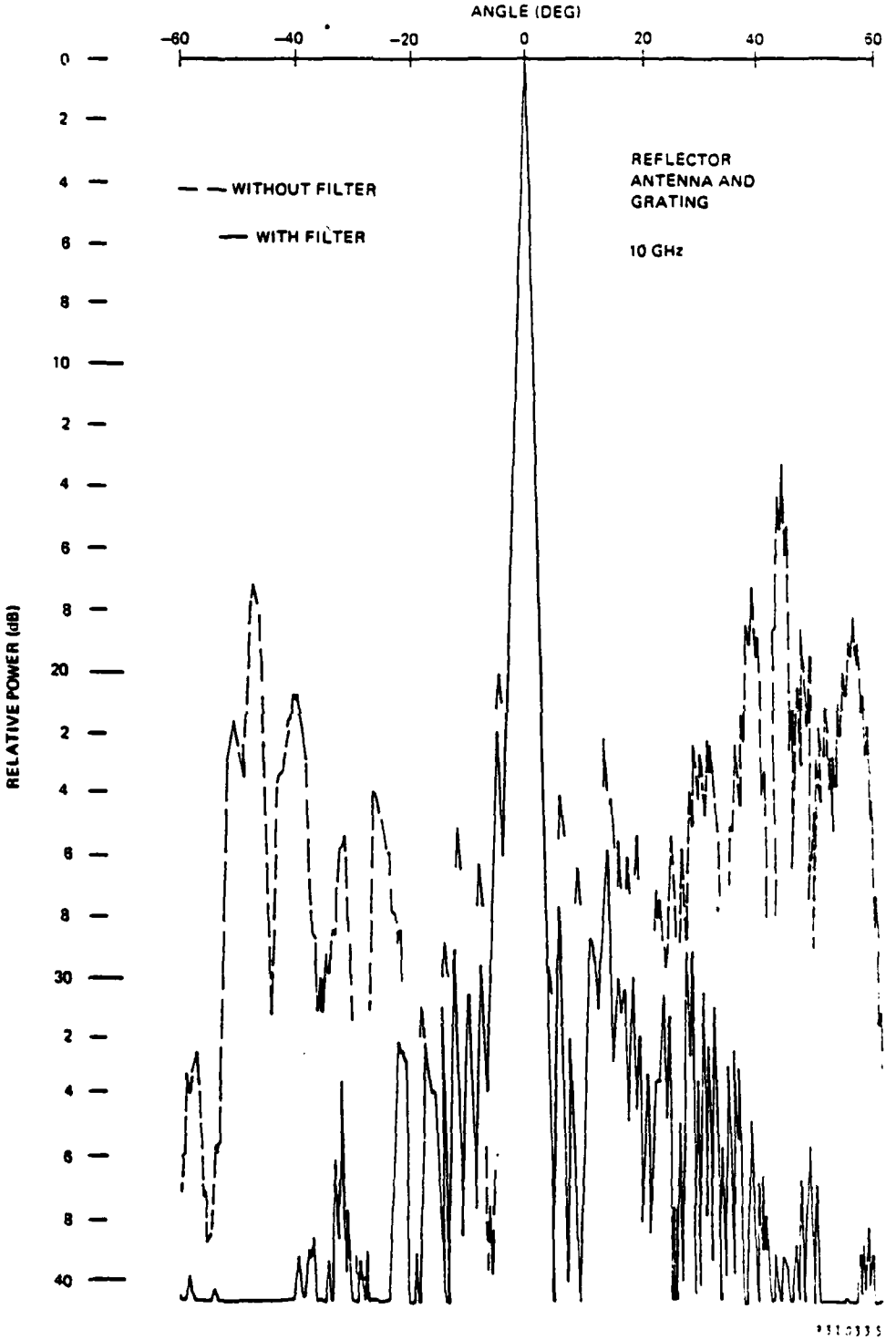

Figure 7-10. Measured Patterns of Grating/Antenna Combination Without and With Filter

SECTION 8

CONCLUSIONS

This report has described the results of an investigation of a new type of angular filter. The filter employs an axial-conductance medium that is essentially invisible at broadside incidence but provides rejection that increases with E-plane incidence angle (θ).

Features of this type of angular filter include an absorptive mechanism for providing the desired rejection, an insensitivity to dimensional or material tolerances, and a very wide frequency band of operation.

Homogeneous Medium. Analysis of an ideal homogeneous axial-conductance medium has shown that the optimum value for the axial loss tangent (D) is unity. With this value, the increase of filter attenuation with θ for small θ is maximized. Such a medium has an attenuation at $\theta = 45°$ of approximately 8 dB per wavelength of filter thickness, and the attenuation is approximately proportional to $\sin^2\theta$. Moderate deviations from the unity value for D have little effect on performance.

The addition of isotropic dielectric to the axial-conductance medium reduces the available attenuation, but transverse dielectric increases the attenuation. Either types of dielectric creates some reflection at broadside incidence.

Inhomogeneous Medium. A practical construction for the axial-conductance medium is an array of closely-spaced

axially-oriented strips of surface-resistance material. With this inhomogeneous configuration, however, there is some loss at broadside incidence. To keep the broadside loss small, the width (w) of the resistance strips must be kept small relative to the strip spacing (s) and relative to the wavelength (λ). Representative dimensions for small broadside loss are $w/s < 0.2$ and $w/\lambda < 0.02$.

Another effect of the inhomogeneous configuration is to modify the angular response of the medium. An analysis of this has been made, based on the concept that the essential effect of the inhomogeneous configuration is the introduction of inductance. This analysis has yielded the interesting result that two types of waves can exist in the inhomogeneous medium when only one wave is incident in the E plane.

One of the two waves (the A type) always has zero attenuation at broadside incidence. The other wave (the B type) has a non-zero attenuation for incidence near broadside, and is expected to be unexcited at broadside incidence. One of the two waves (A or B, depending on the value of D) exhibits a cutoff phenomenon versus frequency and incidence angle. When $D = 0.5$ the analysis yields discontinuous results indicating that enhanced attenuation may occur over a limited range of frequency and incidence angle.

The analysis has been extended to include the possibility of excess capacitance ($e > 1$) in the strip configuration, as well as the presence of transverse dielectric ($\varepsilon'_{tr} > 1$). Results indicate that when both are present and equal, the inhomogeneous medium should yield increased attenuation for both the A wave and the B wave. When only $e > 1$, the results indicate that enhanced attenuation of the

A wave may be possible over a limited frequency range near broadside incidence without introducing a reflection at broadside incidence.

When the spacing between the resistance strips is small compared with the wavelength, the inductive reactance introduced by the inhomogeneous construction may be small compared with the strip resistance. In this case the overall attenuation through the medium is likely to be determined primarily by the A-wave attenuation, which, with small inductance, is not very different from the attenuation of the equivalent homogeneous medium. Thus with small spacing the inhomogeneous medium should give an angular response similar to that of the ideal homogeneous medium. Results of the analysis have shown that for a typical example having $D = 1$ and w/s greater than 0.1, this desired performance occurs when s/λ is 0.25 or less.

Simulator Tests. Measurements of inhomogeneous axial-conductance samples have been made in wide rectangular waveguide operating in the TE-10 mode, representing broadside incidence. The results have verified that small loss at broadside incidence is obtained when w/s and w/λ are made sufficiently small. Reasonably good correlation with theoretical predictions of broadside loss was also obtained.

Inhomogeneous samples were also measured in a large square waveguide operating in the TM-11 mode, representing E-plane incidence angles near 45°. For those samples with spacing (s) up to about a quarter wavelength, the measured attenuation versus frequency showed reasonably good correspondence with the attenuation computed for a homogeneous medium. Thus these results verified the similar conclusion that was drawn from the inhomogeneous medium analysis.

For those large square samples having spacings larger than a quarter wavelength, the correspondence with the homogeneous computed attenuation became progressively poorer with increasing spacing. With $s = 0.48\lambda$ a resonant-like enhancement of attenuation was observed when D had values near 0.5. It is speculated that this result may be related to the discontinuous results obtained from the inhomogeneous medium analysis when $D = 0.5$.

Some inhomogeneous samples were also measured in a small square waveguide operating in the TM-11 mode, representing a range of incidence angles from 60° to 84°. The measured attenuation was somewhat less than the homogeneous computed attenuation, but exhibited similar trends. No evidence of a spurious passband at large incidence angles was observed. This confirms the analytical results, which also have not indicated the presence of a spurious passband.

The measured VSWR of all the square (oblique-incidence) samples was somewhat less than the homogeneous computed VSWR, but exhibited similar trends with incidence angle. As expected, the VSWR is near unity for small incidence angles, and it increases rapidly only when the incidence angle approaches grazing.

In general, the simulator tests of various samples of inhomogeneous axial-conductance media gave results that correlated with or complemented the analytical results. Two different constructions were used for the simulator samples: in one, the resistance strips were cut from commercially-available resistance card; in the other, a film of resistance strips was printed on thin dielectric sheets. The two constructions gave nearly the same results.

Construction of 5 x 5 Foot Filter. An axial-conductance angular filter designed for 10 GHz operation was constructed. This filter is 5 x 5 feet in aperture size, and is 5 inches thick. It comprises 270 parallel sheets of thin dielectric on which are printed a total of over 70,000 resistance strips.

A screen printing process using thick-film resistive ink was investigated and found to be practical for the 5 x 5 foot filter. A 5-foot long screen containing the desired strip pattern was constructed, and then was used to print the 270 sheets of dielectric. Problems with the resistive ink were encountered, but were satisfactorily resolved.

The 270 printed sheets of dielectric were alternated with foam spacers, and the resulting stack was encased within a fiberglass shell for mechanical integrity. The end result is a 5 x 5 foot angular filter having an inhomogeneous axial-conductance medium that is suitable for operation in a microwave antenna system.

Tests of 5 x 5 Foot Filter. Measurements were made of the filter rejection versus angle of incidence at 5, 10, and 20 GHz. The measured results were similar to the computed results for a homogeneous medium, but gave somewhat less attenuation. The difference is believed to be a consequence of the measurement configuration, which only approximated a plane wave incident in the E plane.

As expected, the measured rejection increases continuously with incidence angle. Also, as predicted, the rejection increases approximately proportional to frequency over the two-octave band of measurement. This filter provides a

significant amount of rejection at wide angles over a two-octave frequency band.

A measurement was also made of the effectiveness of the filter in reducing sidelobes of a microwave antenna in a situation where antenna/filter interaction could degrade performance. This situation was obtained by creating wide-angle sidelobes containing a substantial fraction of the antenna radiated power. As expected, the filter made a major reduction in the level of the grating lobes. Furthermore, there was virtually no increase in any of the narrow-angle sidelobes, even though substantial power was being rejected by the filter. This result supports the viewpoint that the absorptive-type rejection provided by the axial-conductive angular filter is a significant desirable feature.

Discussion. In many ways, the axial-conductance type of angular filter provides performance that complements that of a metal-grid type of angular filter. In some applications the metal-grid type would be preferred, while in other applications the axial-conductance type may be needed. In certain cases, it may be appropriate to use both types together. The investigation described in this report has defined the design and performance of an axial-conductance filter, and has shown that it is practical to construct in a size appropriate for application to microwave antennas.

SECTION 9

ACKNOWLEDGEMENTS

Contributions to the analysis were made by Dr. R. La Rosa and Dr. H. A. Wheeler. The computer solution of the equations was developed by C. Ruskowski. Simulator tests were performed by W. M. Roxbury. The printed construction of the axial-conductance medium for the 5 x 5 foot angular filter was suggested by T. C. Hana, managed by A. F. Clerihew, and performed by S. Yell.

SECTION 10

REFERENCES

Ref. 1 - R.J. Mailloux, "Synthesis of Spatial Filters with Chebyshev Characteristics", IEEE Trans. Antennas and Propagation, pp. 174-181; March, 1976.

Ref. 2 - J.H. Pozgay, S. Zamoscianyk, L.R. Lewis, "Synthesis of Plane Stratified Dielectric Slab Spatial Filters Using Numerical Optimization Techniques", Final Technical Report RADC-TR-76-408 by Raytheon Co., December, 1976.

Ref. 3 - J.H. Pozgay, "Dielectric Spatial Filter Experimental Study", Final Technical Report RADC-TR-78-248 by Raytheon Co., November, 1978.

Ref. 4 - A. C. Schell et al, "Metallic Grating Spatial Filter for Directional Beamforming Antenna" AD-D002-623; April, 1976.

Ref. 5 - R.J. Mailloux, "Studies of Metallic Grid Spatial Filters", IEEE AP-S Int. Symp. Digest, p. 551; 1977

Ref. 6 - E. L. Rope, G. Tricoles, O-C Yue, "Metallic Angular Filters for Array Economy", IEEE AP-S Int. Symp. Digest, pp. 155-157; 1976.

Ref. 7 - E. L. Rope, G. Tricoles, "An Angle Filter Containing Three Periodically Perforated Metallic Layers", IEEE AP-S Int. Symp. Digest, pp. 818-820; 1979.

Ref. 8 - R. J. Mailloux and P.R. Franchi, "Metal Grid Angular Filters for Sidelobe Suppression", RADC-TR-79-10; January 1979.

Ref. 9 - P. R. Franchi, R. J. Mailloux, "Theoretical and Experimental Study of Metal Grid Angular Filters for Sidelobe Suppression", IEEE Trans. Antennas and Propagation, pp. 445-450; May 1983.

Ref. 10 - P. W. Hannan, P. L. Burgmyer, "Metal-Grid Spatial Filter", Interim Technical Report RADC-TR-79-295 by Hazeltine Corp., July 1980.

Ref. 11 - P. W. Hannan and J. F. Pedersen, "Investigation of Metal-Grid Angular Filters", Proceedings of the 1980 Antenna Applications Symposium, Allerton Park, Illinois; September 1980.

Ref. 12 - P. W. Hannan, J. F. Pedersen, "Metal-Grid Spatial Filter", Final Technical Report RADC-TR-81-282, by Hazeltine Corp., November 1981

Ref. 13 - J. F. Pedersen, P. W. Hannan, "A Metal-Grid 5 x 5 Foot Angular Filter", IEEE AP-S Int. Symp. Digest, pp. 471-474; 1982.

Ref. 14 - J. Brown, "Microwave Lenses", Methuen and Co. Ltd., London, page 41; 1953.

Ref. 15 - G.G. MacFarlane, "Surface Impedance of an Infinite Parallel-Wire Grid at Oblique Angles of of Incidence", JIEE, Vol. 93, Pt 3A, pp 1523-1527; 1946.

Ref. 16 - M.I.Kontorovich, V. Yu Pretun'kin, N.A. Yesepkina, M.I. Astrakhan, "The Coefficient of Reflection of a Plane Electromagnetic Wave from a Plane Wire Mesh", Radio Engineering and Electronic Physics (USSR), Vol. 7, No. 2, pp 222-231; February 1962.

Ref. 17 - J. Brown, "Artificial Dielectrics Having Refractive Indices Less Than Unity", Proc. IEEE, Vol. 100, Pt 4, pp 51-62; 1953.

Ref. 18 - P. W. Hannan and M. A. Balfour, "Simulation of a Phased Array in Waveguide", IEEE Trans. Antennas and Propagation, pp 342-353; May 1965.

Ref. 19 - H. A. Wheeler, "A Survey of the Simulator Technique for Designing a Radiating Element in a Phased Array", Phased Array Antenna Symposium, Artech House, pp 132-148; 1970.

APPENDIX A

DERIVATION OF CURRENT FACTOR FOR PARALLEL STRIPS

BY H. A. WHEELER

MEMO TO: File

FROM: H. A. Wheeler

SUBJECT: The incremental capacitance of coplanar parallel strips.

Abstract. A grid of coplanar parallel strips causes an increment of capacitance if located in a plane wavefront with their width subjected to the E field. The amount is known from publications stemming from World War II. Another quantity is relevant to the dissipation in a thin strip of rather low but substantial surface resistance. This quantity is the greater capacitance terminating on the strip. A simple derivation by conformal mapping is presented, which yields both of these quantities. It is valid for strip width and spacing much less than the wave radianlength.

References.

[1] T. Moreno (ed.), "Microwave Transmission Design Data", Sperry Gyroscope Co.; 1944. (C window, p. 105, formula.)
[2] G. G. Macfarlane, "Quasi-stationary field theory and its application to diaphragms and junctions in transmission lines and waveguides", Jour. IEE, vol. 93, part IIIA, pp. 703-719; 1946. (Abstract of derivation of C increment by thin ridge between parallel planes.)
[3] N. Marcuvitz, "Waveguide Handbook", McGraw-Hill, Rad. Lab. Series, vol. 10; 1951. (C window, p. 218, formula.)
[4] J. Brown, "Microwave Lenses", Methuen/Wiley; 1953. (C strips, formula, p. 42.)
[5] R. E. Collin, "Field Theory of Guided Waves", McGraw-Hill; 1960. (Derivation of multiple grid of C strips, p. 539, complicated solution.)

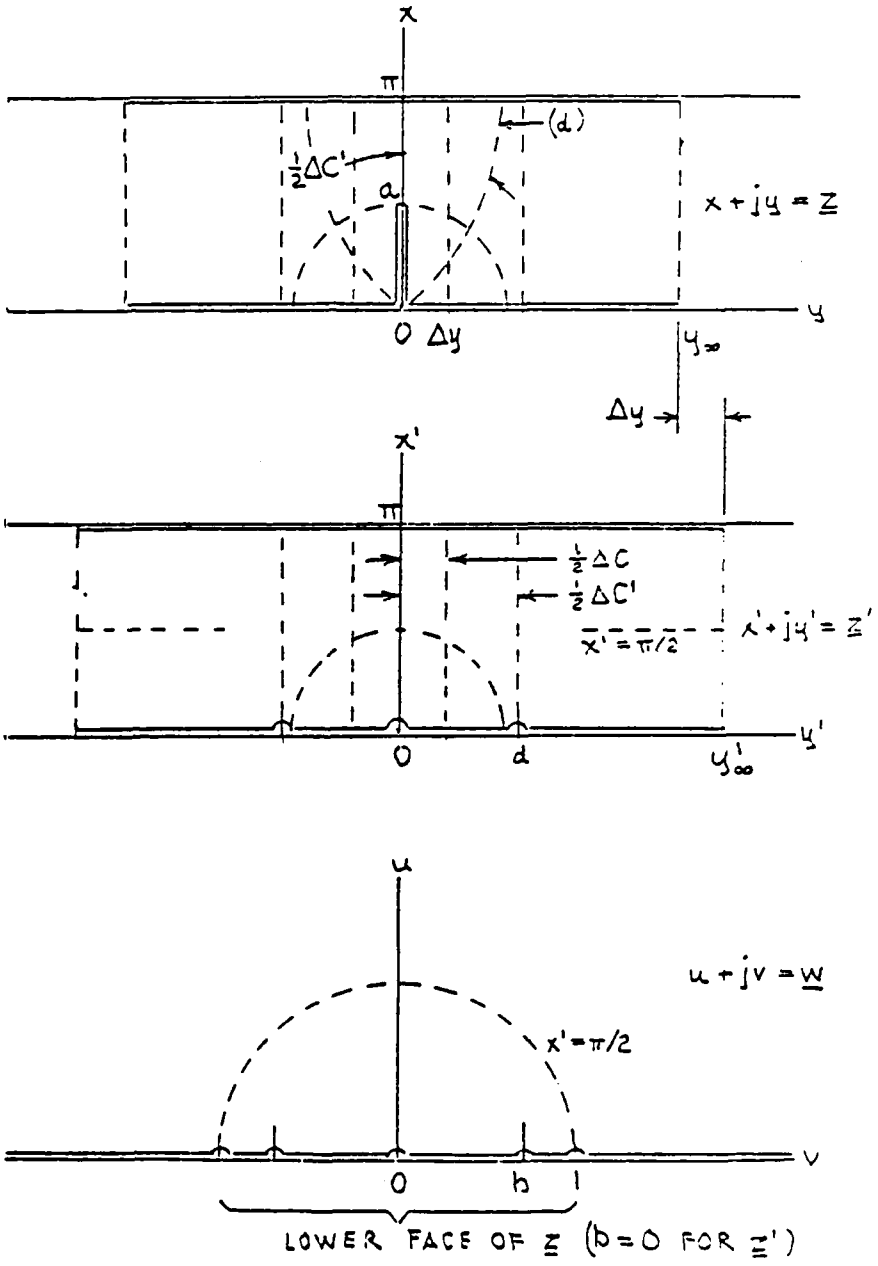
x
π
(d)
½ΔC'
a
x + jy = z
y
0 Δy
y∞
Δy
x'
π
½ΔC
½ΔC'
x' = π/2
x' + jy' = z'
y'
0
d
y'∞
u
u + jv = w
x' = π/2
v
0
b
1
LOWER FACE OF z (b = 0 FOR z')

The two-dimensional cross section in the $\underline{z}$ plane is bounded by the two planes of symmetry parallel to the length of the strips. The lower plane bisects the strip width. The upper plane bisects the strip separation.

2a = width; 2π = separation between centerlines.

The cross section in the $\underline{z}'$ plane includes the same space but without the strips (a = 0). The $\underline{w}$ plane has the bounded space mapped on half-space bounded by a single plane. It serves as an intermediary for relations between the $\underline{z}$ and $\underline{z}'$ planes, by the familiar polygon mapping of right angles and reversals.

These are the corresponding points on the three planes:

$\underline{z}$	a	0	$\pm y_\infty$
$\underline{z}'$	0	$\pm d$	$\pm y'_\infty$
$\underline{w}$	0	$\pm b$	± 1

The coordinates of the $\underline{z}'$ plane are orthogonal potential and flux, normalized to π potential. Those of the $\underline{w}$ plane are ratios.

The actual field is represented on the $\underline{z}$ plane. The image planes are horizontal conductors. The half-width of a strip appears as a vertical ridge on the lower conductor. Its height is a/π of the vertical separation.

The orthogonal field on the $\underline{z}'$ plane has width dimensions proportional to capacitance. An amount of capacitance per unit length is

$$\varepsilon_o(y'_2 - y'_1)/\pi \qquad (1)$$

The capacitance terminating on the ridge in the $\underline{z}$ plane is the amount in the corresponding width in the $\underline{z}'$ plane.

$$\Delta C' = \varepsilon_o \, 2d/\pi \qquad (2)$$

This is the quantity not described in the references.

The increment of capacitance caused by the ridge is defined in a manner that yields to simple formulation. A value of v (near ±1) on the $\underline{w}$ plane includes equal C on the $\underline{z}$ and $\underline{z}'$ planes. The corresponding (large) widths are defined respectively between $\pm y_\infty$ and between $\pm y'_\infty$. The latter is greater to include equal C without the ridge. The difference ($\Delta y = y'_\infty - y_\infty$) approaches a limiting value which represents the increment caused by the ridge:

$$\Delta C = \varepsilon_o \, 2\Delta y/\pi \tag{3}$$

The algorithm for computing this value is a feature of the present derivation.

Another feature is the current distribution on the ridge. The mean-square current is about 2/3 the square of the total current in the base of the ridge.

In the conformal mapping, there are two pairs of singluar points which appear at ±1 and ±b on the v axis. The former is a reversal with a π step on the $\underline{z}$ and $\underline{z}'$ planes. The latter is a right angle at the base of the ridge on the $\underline{z}$ plane. It is marked on the y' axis, but there is no discontinuity. A central point at 0 on the v axis marks a reversal at the top of the ridge ($x = a$).

The mapping gradient from the $\underline{w}$ plane to the $\underline{z}'$ plane is designed to provide the reversals with π steps at $\underline{w} = \pm j$ ($u = 0$, $v = \pm 1$).

$$\frac{d\underline{z}'}{d\underline{w}} = \frac{2}{\underline{w}^2 + 1} \tag{4}$$

The gradient from $\underline{w}$ to $\underline{z}$ has supplemental factors to provide the characteristics of the ridge, namely a reversal at $\underline{w} = 0$ and right angles at $\underline{w} = \pm jb$ ($u = 0$, $v = \pm b$).

$$\frac{d\underline{z}}{d\underline{w}} = \frac{2}{\underline{w}^2 + 1} \frac{\underline{w}\sqrt{1 - b^2}}{\sqrt{\underline{w}^2 + b}} \tag{5}$$

It includes also a constant factor to keep the steps equal to ±π. The latter simplifies to the former if $b = 0$, denoting the absence of a ridge.

The more general form can be integrated by transformation from Dwight 192.11, which is:

$$\int \frac{dx}{x\sqrt{a + x}} = -j\sqrt{\frac{2}{a}}\ \text{atan}\ j\sqrt{\frac{a + x}{a}} = \sqrt{\frac{2}{a}}\ \text{atanh}\sqrt{\frac{a + x}{a}} \qquad (6)$$

Substitute: $x \to \underline{w}^2 + 1$; $dx \to 2\underline{w}\, d\underline{w}$; $a \to -1 + b^2$; $a + x \to \underline{w}^2 + b^2$
Multiply by $\sqrt{a} = j\sqrt{1 - b^2}$ for π step at $\underline{w} = \pm j$

$$\underline{z} = 2\ \text{atan}\sqrt{\frac{\underline{w}^2 + b^2}{1 - b^2}} = j2\ \text{atanh}\sqrt{\frac{\underline{w}^2 - b^2}{1 - b^2}} \qquad (7)$$

$$b = 0: \quad \underline{z}' = 2\ \text{atan}\ \underline{w} = j2\ \text{atanh}\ \underline{w}/j \qquad (8)$$

Dimensions on the $\underline{z}$ and $\underline{z}'$ planes are evaluated by definite integrals on the v axis (u = 0).

$$\underline{z} = 2\ \text{atan}\sqrt{\frac{b^2 - v^2}{1 - b^2}} = j2\ \text{atanh}\sqrt{\frac{v^2 - b^2}{1 - b^2}} \qquad (9)$$

$$a = \underline{z}\Big|_b^0 = 2\text{atan}\frac{b}{\sqrt{1 - b^2}} = 2\ \text{asin}\ b\ ;\ b = \sin a/2 \qquad (10)$$

$$\underline{z}' = j2\ \text{atanh}\ v \qquad (11)$$

$$jd = \underline{z}'\Big|_o^b = j2\ \text{atanh}\ v \qquad (12)$$

$$d = 2\ \text{atanh}\ b = \ln\frac{1 + b}{1 - b}\ ;\ b = \tanh d/2 \qquad (13)$$

The difference of y and y' is evaluated in preparation for going to the limit.

$$y' = 2\ \text{atanh}\ v = \ln\frac{1 + v}{1 - v} \qquad (14)$$

$$y = 2\ \text{atanh}\sqrt{\frac{v^2 - b^2}{1 - b^2}} = \ln\frac{\sqrt{1 - b^2} + \sqrt{v^2 - b^2}}{\sqrt{1 - b^2} - \sqrt{v^2 - b^2}} \qquad (15)$$

$$y' - y = \ln \frac{1+v}{1-v} \frac{\sqrt{1-b^2} - \sqrt{v^2-b^2}}{\sqrt{1-b^2} + \sqrt{v^2-b^2}} = \ln \frac{1+v}{1-v} \frac{1-b^2-v^2+b^2}{\left(\sqrt{1-b^2} + \sqrt{v^2-b^2}\right)^2}$$

$$= \ln \frac{(1+v)^2}{\left(\sqrt{1-b^2} + \sqrt{v^2-b^2}\right)^2} = 2 \ln \frac{1+v}{\sqrt{1-b^2} + \sqrt{v^2-b^2}} \qquad (16)$$

Going to the limit, v = 1:

$$\Delta y = y'_\infty - y_\infty = 2 \ln \frac{1}{\sqrt{1-b^2}} = \ln \frac{1}{1-b^2}$$

$$= 2 \ln \frac{1}{\cos a/2} = 2 \ln \frac{1}{\operatorname{sech} d/2} = 2 \ln \cosh d/2 \qquad (17)$$

The current to one side of the ridge is measured by y' in the interval 0 to d. The current increases with decreasing x in the interval 0 to a.

$$x = 2 \operatorname{atan} \sqrt{\frac{b^2-v^2}{1-b^2}} \; ; \; \tan^2 x/2 = \frac{b^2-v^2}{1-b^2} \; ; \; \tan^2 a/2 = \frac{b^2}{1-b^2} \qquad (18)$$

$$\left(\frac{\tan x/2}{\tan a/2}\right)^2 = \frac{b^2-v^2}{b^2} = 1 - \left(\frac{v}{b}\right)^2 \qquad (19)$$

$$y' = 2 \operatorname{atanh} v \; ; \; \tanh y'/2 = v \; ; \; \tanh d/2 = b \qquad (20)$$

$$\left(\frac{\tanh y'/2}{\tanh d/2}\right)^2 = \left(\frac{v}{b}\right)^2 = 1 - \left(\frac{\tan x/2}{\tan a/2}\right)^2 \qquad (21)$$

A simple approximation can be based on small a/π and d/π:

$$(y'/d)^2 = 1 - (x/a)^2 \qquad (22)$$

(fraction of base current)^2 = 1 - (fraction of height)^2
average (current)^2 = $\frac{2}{3}$ (base current)^2

The principal ratio is a/π, the ridge height as a fraction of the space. These relations are expressed in terms of that ratio.

$$b = \sin a/2 = \sin(\pi/2)(a/\pi) \tag{23}$$

$$d/\pi = \frac{2}{\pi}\,\text{atanh}\, b = \frac{2}{\pi}\,\text{atanh}\,\sin(\pi/2)(a/\pi)$$
$$= \frac{2}{\pi}\,\text{asinh}\,\tan(\pi/2)(a/\pi) \tag{24}$$

$$\Delta C = \epsilon_o 2\Delta y/\pi = \epsilon_o \frac{4}{\pi} \ln \frac{1}{\cos(\pi/2)(a/\pi)} \tag{25}$$

$$\Delta C' = \epsilon_o 2d/\pi = \epsilon_o \frac{4}{\pi}\,\text{asinh}\,\tan(\pi/2)(a/\pi) \tag{26}$$

The principal relations can be appreciated by the approximations for a narrow strip ($a/\pi \ll 1$).

$$b = a/2 = d/2 \;;\; d/\pi = a/\pi \tag{27}$$

$$\Delta C = \epsilon_o \frac{\pi}{2}(a/\pi)^2 \;;\; \Delta C' = \epsilon_o 2(a/\pi) \;;\; \Delta C/\Delta C' = \frac{\pi}{4}(a/\pi) \tag{28}$$

As an example, compare the complete and approximate values for ridge height 1/2 the space height (as in the diagram).

$a/\pi = 0.5$	complete	approximate
$d/\pi = \frac{2}{\pi}\,\text{atanh}\,\sqrt{1/2} = \frac{1}{\pi}\ln(3+\sqrt{8})$	0.5611	0.5
d/a	1.1222	1.
$b = \sqrt{1/2}$	0.7071	0.7854
$\Delta C/\epsilon_o = 2\Delta y/2a = \frac{1}{\pi}\ln 4$	0.4413	0.3927
$\Delta C'/\epsilon_o = 2d/2a = \frac{2}{\pi}\ln(3+\sqrt{8})$	1.1222	1.
$\Delta C/\Delta C' = 2\Delta y/2d = \frac{\ln 2}{\ln(3+\sqrt{8})}$	0.3932	0.3927

The complete value is substantially different from the approximate, except for close agreement of $\Delta C/\Delta C'$ (near $\pi/8$).

This derivation for a single vertical ridge between parallel horizontal planes appear to be a simple one well adapted to the configuration. Earlier derivations are not completely reported, so a comparison is difficult. Macfarlane [2] describes one essential feature, taking the difference ΔC in the limit of two wide spaces with and without the ridge. The earlier derivations do not report $\Delta C'$ and the current on the faces of the ridge. This result was the direct motivation for the present study. It is relevant to a study being conducted by Peter W. Hannan.

MISSION
of
Rome Air Development Center

RADC plans and executes research, development, test and selected acquisition programs in support of Command, Control Communications and Intelligence (C^3I) activities. Technical and engineering support within areas of technical competence is provided to ESD Program Offices (POs) and other ESD elements. The principal technical mission areas are communications, electromagnetic guidance and control, surveillance of ground and aerospace objects, intelligence data collection and handling, information system technology, ionospheric propagation, solid state sciences, microwave physics and electronic reliability, maintainability and compatibility.

END

FILMED

8